UNIVERSITY OF CALIFORNIA

Santa Barbara

Fundamentals of Titanium Interactions with Nitrogen and Oxygen

A dissertation submitted in partial satisfaction of the

requirements for the degree Doctor of Philosophy

in Materials

by

Mayela Renata Aldaz Cervantes

Committee in charge:

Professor Anton Van der Ven, Chair

Professor Tresa Pollock

Professor Samantha Daly

September 2022

The dissertation of Mayela Renata Aldaz Cervantes is approved.

_____
Samantha Daly

_____
Tresa Pollock

_____
Anton Van der Ven, Committee Chair

August 2022

Fundamentals of Titanium Interactions with Nitrogen and Oxygen

by

Mayela Renata Aldaz Cervantes

This dissertation is dedicated to anyone who has not been allowed to thrive in science.

It was never your fault. You are more than enough. You belong.

Para Javier Arturo Aldaz García.

Mis éxitos siempre han sido y seguirán siendo también tuyos.

ACKNOWLEDGEMENTS

As my time as a graduate student nears its conclusion, I am thankful for the many people who have supported my journey in growing as a scientist, researcher, educator, and person. I must first thank my committee, Dr. Anton Van der Ven, Dr. Tresa Pollock, and Dr. Samantha Daly, for sharing their time and expertise with me and for their valuable contributions to the research discussed in this thesis.

I would like to acknowledge the funding sources that provided the financial support for myself and for the research discussed in this dissertation. This research project was funded by two National Science Foundation (NSF) grants: NSF DMR-1436154 and 1729166. My research would not have been possible without the facilities at UCSB under the MRSEC Program of the NSF under Award No. DMR 1720256, as well as the Nanostructures Cleanroom Facility within the California NanoSystems Institute (CNSI) where I used the Raman spectrometer. I am thankful for the UCSB Regents in Materials Fellowship, NSF Graduate Research Fellowship Program under Grant No. 1650114, and the UC President's Dissertation Year Fellowship which funded my time during graduate school, allowing for me to focus on my research and professional development without financial worries. I would also like to thank Dr. Michael Chabinyc for advocating for me to obtain three quarters of additional funding through departmental and Graduate Division financial support which provided enough time for me to complete this degree.

I am thankful for the amazing staff affiliated with the UCSB Materials Department, from the staff in the main and Structural offices to the fantastic support at the Microscopy and Microanalysis Facilities at CNSI. I would like to give a special thank you to Ali Todhunter, Stefani Juarez, Jocelyn Guzman, Alexandria Huddleston, Budd Jamieson, and Tawny

Hernandez for helping me so many times with shipping, funding, payments, software issues, and other things that sound simple but are crucial to a successful graduate student. Thank you for everything you do for our department. I would also like to thank Mr. Deryck Stave for his support and training in the technical equipment I used for my oxidation and diffusion couple experiments; Dr. Aidan Taylor for his patience in sharing his expertise in all things electron microscopy and helping me reach my personal record of making four TEM-ready specimens in eight hours; Mr. Mark Cornish for training me when I started my graduate career; Dr. Claire Chisholm for providing help when the TEM or FIB got angry at me; Dr. Rachel Schoeppner for her crucial help with my in situ Raman oxidation experiments, and Dr. Mike Gordon for his thoughtful discussions on and assistance with our Raman studies. I want to thank Dr. Yuan Wu and Dr. Paul Rottmann for the electron microscopy work they provided during different stages of this research project. I would also like to acknowledge all the UCSB workers who maintain the spaces that allow us to study and work, as well as all the essential workers who allow us to lead a comfortable life even through a pandemic. I hope their worth is recognized and our community supports their livelihood and safe working conditions moving forward.

These past seven years I had the pleasure and honor to mentor and teach over a hundred undergraduate and graduate students. I am thankful for each of them and for being able to witness and support their journeys in science. I would like to thank Ms. Sarah Löβlein for her contributions to the in situ Raman oxidation project during her summer internship in 2019. I am incredibly grateful to the wonderful staff at the Center for Science and Engineering Partnerships (CSEP) for allowing me to participate in their programs to educate and inspire the next generation of scientists and engineers, as well as Dr. Julie Standish and Dr. Dotti

Pak from the Materials Research Lab for allowing me to participate in fellowship panels and as a mentor in the Cooperative International Science and Engineering Internship program.

Thank you to my colleagues, especially Dr. Colin Stewart for being my oxidation buddy when I began my research, Dr. Daesung Park for his help with diffraction and spectroscopy analysis, and Dr. Collin Holgate for being a supportive and understanding friend through the highs and lows of graduate school (and life). I would also like to thank Dr. Harsha Gunda for being my titanium oxidation buddy, seminar partner, and wonderful collaborator. I am indebted to the friends I made along the way who continuously cheered for me and inspired me, as well as those whose friendship stood the test of time, distance, and busy schedules. Future Dr. Timnit Kefela, I am eternally grateful for our friendship and your unconditional support throughout this journey. You are next!

I would not be in graduate school without the educators who supported me and believed in me throughout my life. I especially want to thank Dr. Stephen Stafford at the University of Texas at El Paso (UTEP) who first introduced me to the wonders of materials science and continues to be a supportive mentor to this day.

Graduate school can be hectic and overwhelming, but nothing is ever worth sacrificing our physical and mental wellbeing. I am thankful to the staff at Student Health, Counseling and Psychological Services, Goleta Acupuncture Wellness Clinic and Acacia Counseling and Wellness for supporting me in maintaining my physical and mental health during my doctoral work. I am equally thankful for the gift of music which helped lift my spirits whether I was listening to songs in the student office, in lab, singing in the car, or playing my bass, uke, or violin.

A mis padres, gracias por su amor incondicional, por su apoyo y por las lecciones que me impartieron y siguen mostrando día con día. Su amor me ha guiado a convertirme en la persona que soy. Los amo y me falta vida para agradecerles todo lo que han hecho por mí. A mis hermanos, suegros, cuñados y demás familia, gracias por todo su apoyo y cariño siempre. A Ares, Ian, Dariana y Mariel, espero que este libro largo y aburrido (y el papelito que me van a dar por él) les motive a lograr cualquier meta que se propongan. Gracias por compartir mi alegría en completar el primer doctorado de la familia.

Andrés, I cannot imagine surviving this Ph.D. and pandemic (and wildfires and…) without you. You are the best human, life partner, friend, and study buddy. You are my favorite soul. I love you always.

Gracias infinitas a Dios y a mi Madre Santísima por todas sus bendiciones y permitirme lograr esta meta. Concédanme por caridad la gracia de servirles conforme a Su Voluntad y saber usar lo que he aprendido para bien y en servicio de mi hermana humanidad.

VITA OF MAYELA RENATA ALDAZ CERVANTES

August 2022

Education

Ph.D. Candidate in Materials, May 2018
University of California, Santa Barbara (UCSB)

Bachelor of Science in Metallurgical and Materials Engineering, May 2015
The University of Texas at El Paso (UTEP)
Graduated Summa Cum Laude with Honors Degree (i.e. completed 30+ honors credits)

Fellowships

- NSF Graduate Research Fellowship Program (GRFP) Fellow, Fall 2017 – Present
- UC President's Dissertation Year Fellowship, Fall 2020 – Summer 2021
- UCSB Materials' Regents Fellowship Award, Fall 2015 – Summer 2016
- UCSB Miguel Velez Fellowship Award, Spring 2016

Publications

- **Aldaz-Cervantes, M.*** & Kefela, T*. (2021). The mentorship toolkit: A resource guide for effective undergraduate mentoring in STEM. Center for Science and Engineering Partnerships, UCSB. *Equal contributions
- Gaytan, S. M., Cadena, M., **Aldaz, M.**, Herderick, E., Medina, F., & Wicker, R. (2013). Analysis of ferroelectric ceramic fabricated by binder jetting technology. In Proceedings of Solid Freeform Fabrication Symposium, Austin, TX (pp. 859-868).

Oral presentations

- **Aldaz-Cervantes, M.R.** & C.G. Levi. "In Situ Raman Spectroscopy Study of Titanium Oxidation in Low Oxygen Environments". Research seminar (virtual due to COVID-19 pandemic) on May 14, 2020 for Biological Nanostructures Lab at UC Santa Barbara.
- **Aldaz-Cervantes, M.R.** & C.G. Levi. "Oxidation Mechanisms of Titanium in Low Oxygen Environment". Research seminar on January 24, 2020 at Metallurgical, Materials, and Biomedical Engineering Department, The University of Texas at El Paso.
- **Aldaz-Cervantes, M.R.**, P. Rottmann, N.S.H. Gunda, A. Van der Ven & C.G. Levi. "Titanium Oxidation in Low Oxygen Environment". MS&T Conference on October 17, 2018 at Greater Columbus Convention Center, Columbus, OH.

Poster presentations

- **Aldaz-Cervantes, M.R.**, S.M. Löβlein & C.G. Levi. "In Situ Raman Studies of Titanium and Ti-2X (X = Al, Nb) Oxidation". Winter Study Group on High-Performance Materials on January 10-11, 2020 at University of California Santa Barbara.
- **Aldaz-Cervantes, M.R.**, P. Rottmann, N.S.H. Gunda, A. Van der Ven & C.G. Levi. "Identification of Titanium Suboxides Formed Under Low pO_2". Gordon Research Conference on Physical Metallurgy on July 6-12, 2019 at Southern New Hampshire University, Manchester, NH.

- **Aldaz-Cervantes, M.R.**, N.S.H. Gunda, A. Van der Ven & C.G. Levi. "Titanium Oxidation Under Low Partial Pressures of Oxygen". TMS Annual Meeting on March 12, 2019 at Henry B. Gonzalez Convention Center, San Antonio, TX.
- **Aldaz-Cervantes, M.R.**, N.S.H. Gunda, A. Van der Ven & C.G. Levi. "Oxygen Ordering in Titanium Oxidized at 800°C in Low Oxygen Environment". Microscopy & Microanalysis Facilities Open House on February 1, 2019 at University of California Santa Barbara.
- **Aldaz-Cervantes, M.R.**, N.S.H. Gunda, A. Van der Ven & C.G. Levi. "Oxygen Ordering in Titanium Oxidized at 800°C in Low Oxygen Environment". Workshop on Multi-Principal Element (MPE) Alloys on January 10, 2019 at University of California Santa Barbara.
- **Aldaz-Cervantes, M.R.**, N.S.H. Gunda, A. Van der Ven & C.G. Levi. "Oxidation of Titanium at 800°C in Low Oxygen Environment". Gordon Research Conference on Physical Metallurgy on July 22-25, 2017 at University of New England-Biddeford.
- **Aldaz-Cervantes, M.R.**, N.S.H. Gunda, A. Van der Ven & C.G. Levi. "Oxidation of Titanium at 800°C in Low Oxygen Environment". Winter Study Group on High-Performance Materials on January 2017 at University of California Santa Barbara.

Mentoring and teaching experience

- **Research Mentor** for Sarah M. Löβlein, Cooperative International Science and Engineering Internships, Summer 2019
- **Instructor** for Materials Science for high school students, School for Scientific Thought, Fall 2018
- **Graduate Mentor Coordinator and Science Communication Specialist**, Summer Institute for Science and Mathematics (SIMS), Summer 2017, 2018, and 2019
- **Mentor for Bridges to Doctorate Fellows**, Graduate Scholars Program, Fall 2018 – Spring 2019
- **Teaching Assistant** for MATRL100C, Materials Department, Fall 2018

Awards

- Materials Department Service Award, for outstanding contributions to departmental diversity and to the microscopy facility, Summer 2021
- University Award of Distinction, for outstanding contributions to campus and community life, Spring 2020
- Gordon Research Conference on Physical Metallurgy, Best Poster Award Runner-Up, Summer 2019
- Art of Science Competition, 2nd Place, Winter 2019, Micrograph exhibited at Santa Barbara Museum of Art & UCSB Library

Research experience

Center for the Advancement of Space Safety and Mission Assurance Research El Paso, TX
Undergraduate Research Assistant 10/13- 05/15

- Performed non-destructive testing for the failure analysis of Space Shuttle Columbia.

Massachusetts Institute of Technology (MIT) Cambridge, MA
MIT Summer Research Program Intern Summer 2014 and 2013

- Developed hydrogels and scaffolds with tunable biological properties for liver cells through techniques including Michael-type addition, stereomicrolithography, and soft lithography.

W.M. Keck Center for 3D Innovation El Paso, TX
Undergraduate Research Assistant 03/13 – 06/13

- Applied principles of binder jetting and sintering to build samples with powdered materials such as barium titanate in an ExOne M-Lab machine.

Work experience

Freeport McMoran El Paso Copper Refinery El Paso, TX
Process Engineer Intern 05/15 – 08/15

- Supervised the quality of the copper sheets produced from novel titanium blanks by bend tests and metallographic analysis and re-designed copper anode rack for improved efficiency.

UTEP University Career Center El Paso, TX
Peer Career Advisor for the College of Engineering 02/12 – 03/13

- Provided engineering students with information about career-related subjects such as résume reviewing, career planning, and job interviews on a one-on-one basis and to small groups.

Professional affiliations and service

Volunteered over 300 hours through undergraduate and graduate education on and off-campus to support diversity, equity, and inclusion in STEM through outreach, workshops, fellowship and grad school panels, and mentorship.

- The Minerals, Metals, and Materials Society (TMS)
- Society for the Advancement of Chicanxs/Hispanics and Native Americans in Science (SACNAS) – UCSB Graduate Chapter
- Women in Science and Engineering (WiSE) – UCSB
- Grads for Implicit Bias Education (GIBE) – UCSB
- Graduate Students for Diversity in Science (GSDS)
- Alpha Sigma Mu Metallurgical Honor Society
- Tau Beta Pi Engineering Honor Society

ABSTRACT

Fundamentals of Titanium Interactions with Nitrogen and Oxygen

by

Mayela Renata Aldaz Cervantes

Titanium is a lightweight and attractive metal for use in aerospace, chemical processing, and biomedical industries due to its high strength-to-weight ratio, good oxidation and corrosion resistance, as well as biocompatibility. One important problem with the use of titanium is the embrittlement that accompanies its incorporation of interstitials, most notably oxygen and nitrogen. Since titanium readily dissolves both nitrogen and oxygen, understanding these reactions is fundamental to develop strategies to minimize contamination or to take advantage of these reactions to form nitrides, oxides, or oxynitrides that may exhibit interesting properties for energy storage, biomedical, coatings, or other applications. This research is motivated by the need for improving the fundamental understanding of titanium interactions with nitrogen and oxygen and the nature of its developed phases.

Reaction studies were performed at 800°C (to remain in the hcp Ti phase) using argon-based environments with three distinct low partial pressures of nitrogen and oxygen. These experiments were performed in two furnace configurations, one of which allowed monitoring of scale evolution in situ using Raman spectroscopy. Characterization of the developed scales relied on scanning and transmission electron microscopy, energy dispersive spectroscopy, focused ion beam, X-ray diffraction, electron diffraction, and Raman spectroscopy.

Across environments used, the microstructures show the formation of layered structures with varying porosity throughout. When fast-cooling specimens in the gettered Ar environment (the lowest partial pressure used), the scale consists of mainly nitride phases. Slow-cooling enables the formation of a N-rich hcp-based phase, an oxynitride (TiN_xO_y) phase, Ti_2O_3 in a corundum structure, Magnéli phases, and rutile. Ultra-high purity Ar studies show an additional range of oxygen orderings in the substrate when slow-cooling the specimen after the desired dwell time.

Analysis of the specimens exposed to gettered and ultra-high purity Ar also shows the formation of twinned fcc TiN or oxynitride structures and an orientation relationship between the fcc phase and the underlying hcp Ti substrate. Partial dislocations are proposed to play a role in the hcp Ti to fcc TiN/TiN_xO_y transformation and potentially in the formation of voids at the metal-scale interface. Reacting titanium to a $1\%O_2$-Ar environment hinders the formation of nitride or oxynitride phases and develops multiple layers of rutile.

In situ experiments proved rutile formation occurs at the exposure temperature rather than during cooling and shows coloration changes in the surface throughout the reaction. Blisters also appeared in between the outermost rutile scales and developed at temperature rather than from CTE mismatch between the oxide and metal during cooling.

This dissertation has contributed to the understanding of titanium reactions with nitrogen and oxygen at high temperatures and low partial pressures. The experimental approaches used can be applied towards studying further complex systems either in Ti-based alloys or in other systems such as complex concentrated alloys (CCAs).

Glossary of Abbreviations

APB	Anti-phase boundary
BCC	Body-centered cubic (crystal structure)
BF	Bright field (imaging mode)
BSE	Backscattered electrons (imaging mode)
CTE	Coefficient of thermal expansion
CTEM	Conventional transmission electron microscopy
DF	Dark field (imaging mode)
DFT	Density functional theory
EDX	Energy dispersive X-ray spectroscopy
EELS	Electron energy loss spectroscopy
EFTEM	Energy-filtered transmission electron microscopy
ELNES	Energy loss near edge spectra
ERR	Energy release rate
FCC	Face-centered cubic (crystal structure)
FIB	Focused ion beam
HAADF	High-angle annular dark field (imaging mode)
HCP	Hexagonal close-packed (crystal structure)
IFL	Interfacial layer
IL	Inner layer
IO	Inner oxide
LPSO	Long period stacking ordering (LPSO) structures
NW	Nanowhisker
OL	Outer layer
OO	Outer oxide
PBR	Pilling-Bedworth ratio
PX	Polycrystalline
RS	Raman spectroscopy
SAED	Selected area electron diffraction
SE	Secondary electrons (imaging mode)
SF	Stacking faults
SEM	Scanning electron microscopy
STEM	Scanning transmission electron microscopy
SX	Single cystal
PX	Polycrystalline
TEM	Transmission electron microscopy
TGO	Thermally-grown oxide
UHP	Ultra high purity
XPS	X-ray photoelectron spectroscopy
XRD	X-ray diffraction

Table of Contents

1 Introduction

Titanium is a lightweight and attractive metal for use in aerospace, chemical processing, and biomedical industries due to its high strength-to-weight ratio, good oxidation and corrosion resistance, as well as biocompatibility [1]. Despite decades of research, titanium is a relatively modern metal whose use and manufacturing were popularized in the 1970's and for which there is still an expanding science and technology knowledge base. One important problem with the use of titanium is the embrittlement that accompanies its incorporation of interstitials, most notably oxygen and nitrogen [1,2].

Titanium metal and the ores from which it is extracted are fairly abundant resources. However, titanium alloys are expensive due to their costly extractive and processing requirements. Once processed into an ingot, 15-40% of titanium scrapped is due to oxygen and nitrogen contamination resulting in detrimental mechanical properties [3]. It is important to note that oxygen is not always undesirable and is also used as an intentional alloying element in titanium alloys to provide interstitial strengthening. Since titanium readily dissolves both nitrogen and titanium, understanding these reactions is fundamental to develop strategies to minimize contamination or to take advantage of these reactions to form nitrides, oxides, oxynitrides, or related phases that may exhibit interesting properties for energy storage, biomedical applications, and coatings, among others.

This research is motivated by the need for improving the fundamental understanding of titanium interactions with nitrogen and oxygen and the nature of the phases formed from these reactions. Group IV elements in the periodic table are characterized for the highest solubility for oxygen among the transition metals, with Ti reaching a maximum 33 at% O concentration in the hcp phase at temperatures above and below the β transus temperature

(882°C) [4,5]. Its solubility of nitrogen, albeit lower than oxygen, is still a notable 15-22 at% N [6–8]. While it is well known that the most stable oxide of Ti is titanium dioxide (TiO_2) in its rutile form, there are additional metastable forms of the dioxide (e.g. anatase and brookite) as well as a multitude of suboxides ranging from Ti_6O to Ti_nO_{2n-1}, where $4 \leq n \leq 10$. While the Ti-N system exhibits fewer phases, exploring the Ti-N-O composition space expands the potential metastable and stable phases that can be formed. Given this wide range of possible phases, it can be hypothesized that layered scales of nitride, oxynitride, and/or oxides with different compositions and crystal structures could be formed by altering the oxygen and nitrogen potential at the reaction front of titanium metal.

The overarching goal of this dissertation is to test this hypothesis by performing reaction studies using argon-based environments with several low partial pressures of nitrogen and oxygen. Because it is extremely challenging in practice to get pure O_2 with no residual N_2 in the gas, this research will examine the effect of the relative O_2:N_2 ratios on the developed phases and their mechanisms of formation. These experiments were performed in two distinct furnace configurations, one of which allows monitoring of scale evolution in situ using Raman spectroscopy. The two main guiding questions to be examined in the context of the available phase equilibria are as follows:

1. What phases form in the reactions of each partial pressure used and what are their crystal structures?
2. How do these phases form and evolve as a function of time?

This research will focus on a temperature range in which the stable form of titanium remains in the hcp α-Ti phase, to avoid the complications introduced by the β (bcc) → α (hcp) transformation.

A review of the current literature and knowledge gaps on titanium oxidation, nitriding, and the Ti-N-O system, with its thermodynamic and kinetic considerations, is included as background in Chapter 2, leading to a statement of the research problem and solution approach. Chapter 3 describes the experimental and characterization techniques used for the tube furnace and Raman spectroscopy studies and to perform the phase analysis required for this research. Additionally, some of the experimental challenges associated with this topic are discussed, as well as showing how microstructures were validated as reliable.

Given the different experimental conditions used, a schematic summarizing the materials, experimental setup, gas environments, cooling, identified phases, and resulting microstructures for each chapter is shown in Figure 1.1. The order of these chapters goes from lowest to highest partial pressures of nitrogen and oxygen used.

Chapter 4 will begin by examining the results of the tube furnace studies using a gettered Ar environment (the lowest partial pressure of all three gas environments used) with a parallel flow to the specimen loading direction and by fast-cooling specimens. These specimens show the formation of nitride phases almost exclusively. A rocksalt TiN forms above the hcp Ti substrate with an orientation relationship of $[\bar{1}2\bar{1}0]$ in α-Ti and [110] in the fcc TiN. The TiN in the scales is twinned with a twin axis of [110] and {111} twin plane. There are small voids in between the scale and substrate. Two specimens made with the same experimental conditions (25 h dwell time) show slight variations where one of them forms a Magnéli (Ti_4O_7) scale above the TiN layer of the developed scale and the other one only forms nitride phases. There is also evidence of a 2-phase region where ε-Ti_2N forms along the TiN phase in both of the 25 h specimens.

Using the same gas environment, Chapter 5 will discuss tube furnace studies of titanium in gettered Ar using a counter flow and a slow-cooling method. Despite using the same environment as Chapter 4, these specimens enable the formation of lower oxides (Ti_2O_3 and Magnéli) and an fcc rocksalt Ti oxynitride phase with nanoporosity within its scale. These specimens have an outer oxide of rutile in the 9 h and 25 h specimens. The orientation relationship between the fcc oxynitride and hcp Ti substrate remains in a similar manner to that of the fast-cooled specimens discussed in Chapter 4. Voids appear throughout the specimen and the factors that may influence their formation are discussed.

Increasing the interstitial content, Chapter 6 will discuss the results of heating stage experiments under Raman spectroscopy using an ultra-high purity (UHP) Ar environment. The specimens will result in layered microstructures comparable to the 9 h specimen from Chapter 5. The general microstructure for these specimens is a solid solution and α”-like phase in the substrate, with one or two fcc oxynitrides layered above the metal, and an outer layer composed of porous rutile. The hcp-fcc orientation relationship remains. A slow-cooled specimen provides evidence for a wide range of oxygen orderings within the substrate as well as Magnéli phase formation in the outermost rutile scale. The Raman spectra proves the formation of rutile at the dwell temperature rather than during cooling or at any other stage of the reaction.

For Chapter 7, titanium specimens were exposed to a 1%O_2-Ar environment which resulted in the formation of layered rutile scales. Given the N_2:O_2 ratio in this gas, there is no formation of nitrides, oxynitrides, nor lower oxides (aside from an hcp-based α”-like oxygen ordered phase in the substrate). Blisters are seen in the in situ specimen which develop from growth stresses during the dwell stage of the heating stage experiment.

The conclusions and broader impacts of this work, as well as suggestions on future directions for research on these topics, are discussed in Chapter 8.

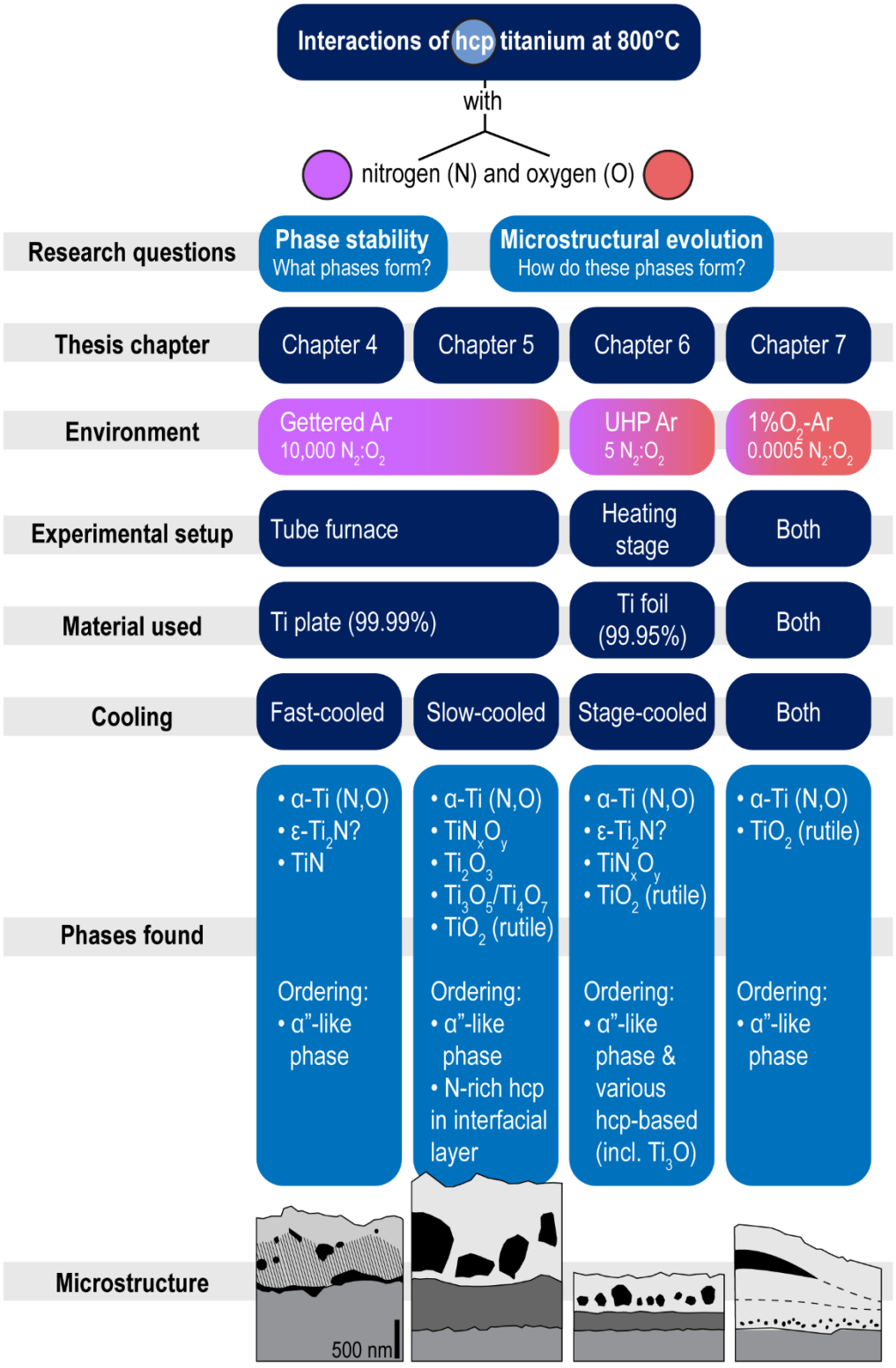

Figure 1.1. Schematic summarizing this research project's experimental conditions and results, as well as which thesis chapter covers each set of data.

2 Background

While much of the commercial applications of titanium are in its dioxide form used in cosmetics, paint, photocatalysis, and other applications, titanium alloys are attractive structural materials due to their high strength-to-weight ratio, low density, and corrosion resistance. The wide range of microstructures and properties achievable in Ti alloys are largely a result of its existence of two allotropic forms, namely α (hcp) and β (bcc), and the transformations between them. Titanium alloys are used in a variety of applications from eyeglass frames to sporting goods and biomedical implants. The majority of titanium used in the aerospace industry includes alloys for fan blades in aircraft engines, or for airframe components in military aircraft. Its use, however, is mostly restricted to low-temperature sections of engines in commercial aircraft due to its limited mechanical properties and environmental degradation at high temperatures. Titanium is a highly reactive metal that readily forms a passive, protective oxide at low temperatures, giving it excellent corrosion resistance. At temperatures above ~500°C, depending on the type of alloy, the oxide layer dissolves into the titanium and enables inward continuous oxygen infusion.

For structural alloys based on α–β or β microstructures the incorporation of oxygen and nitrogen promotes the formation of an embrittled "α case" owing to the role of oxygen and nitrogen as α-stabilizer elements [2]. Oxygen, nitrogen and carbon, which are highly soluble in titanium [9,10], are known to improve the strength of titanium alloys but significantly reduce ductility [11,12]. The embrittlement from these interstitials and the associated lower oxidation resistance restrict the use of titanium alloys in high temperatures. With the longstanding interest in increasing the temperatures and reducing the overall weight of aircraft engine components, it is desirable to understand and mitigate the environmental

limitations to the use of Ti alloys. While components made of titanium alloys are restricted to fan blades in turbine engines where temperatures are below 500°C, it is important that these metal alloys are able to withstand increases in operating temperatures. Furthermore, titanium oxides, nitrides, and oxynitrides are of interest in wide-ranging applications, from batteries to photocatalysis to biomedical applications. A thorough understanding of the fundamental interactions between titanium, nitrogen, and oxygen provides important information for many technological developments whether the goal is to hinder or promote the formation of different phases for optimal performance. A fundamental understanding of titanium interactions with nitrogen and oxygen at high temperature can provide guidance for improving alloying strategies for high temperature applications and for tailoring synthesis of different Ti-O, Ti-N or Ti-N-O phases.

Due to the complexity of the processes and crystal structures of interest to this dissertation, the basics of titanium metallurgy and interactions with the more soluble interstitials, namely oxygen and nitrogen, will be discussed. A literature review of oxidation, nitriding, phase diagrams, and other relevant topics will follow.

2.1 Titanium metallurgy

Titanium exhibits a low-temperature hexagonal close-packed (hcp) α phase and a high-temperature body-centered cubic (bcc) β phase with a phase transformation between them at 882°C [13]. To avoid β phase formation that would further complicate analysis, this dissertation will focus on pure titanium comprised only of α phase and the terms “hcp Ti” and “α-Ti” will be used interchangeably to refer to this hexagonal phase. The lattice parameters for α-Ti are a = 0.295 nm and c = 0.468 nm for a c/a ratio of 1.586, at variance with the ideal c/a ratio for hcp structures of 1.633 [14]. (In comparison, the cubic β phase has

a lattice parameter of 0.332 nm, with an interatomic distance of 0.234 nm along the close packed direction.) These crystal structures are shown in Figure 2.1.

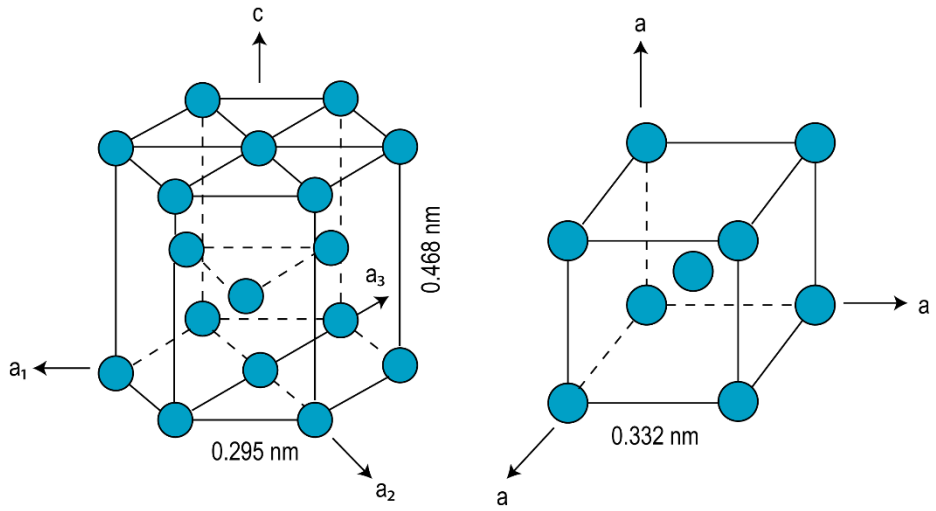

Figure 2.1. Crystal structures for low-temperature α-titanium with an hcp structure (left) and the higher-temperature β-titanium with a bcc structure (right). Figure adapted from [14].

The properties of titanium alloys are dependent on the relative amounts of α and β phases in their microstructures at the use temperature, as well as their morphology. Titanium alloys are classified as: commercially pure, alpha (α) and near-alpha (near-α), alpha-beta (α-β), and metastable beta (β) [15]. Most titanium alloys contain at least a small amount of β for microstructural control.

Alloying elements are categorized in terms of their effect on the stabilization of either alpha or beta phases, reflected in the trend of the beta transus temperature with the elemental addition. Alpha stabilizers, as their name indicates, stabilize the alpha phase, and consequently increase the beta transus temperature. Alpha stabilizers include: aluminum, oxygen, nitrogen, and carbon. Beta stabilizers are elements that will decrease the beta transus temperature of the titanium alloy. Niobium, molybdenum, and vanadium are some examples of beta stabilizers. Other elements may not show a clear stabilizing effect and will be considered neutral, such as Sn, Si and Zr.

2.2 Interstitial diffusion and effects in α-Ti

Interstitial diffusion in titanium is of crucial importance in tailoring and preserving its optimal mechanical properties, particularly since carbon, nitrogen, and oxygen are known to promote the formation of the brittle α case in α/β or β titanium alloys. This oxygen-rich layer is undesirable due to the ensuing embrittlement and is removed during titanium processing [16–21]. Interstitials have been shown to increase strength and reduce ductility in titanium (Figure 2.2).

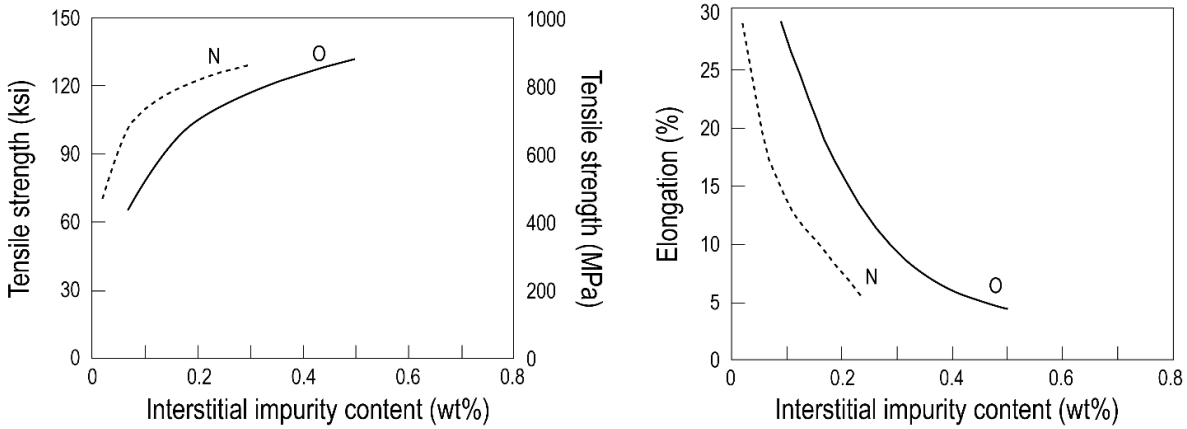

Figure 2.2. Effect of interstitial addition to the mechanical properties of titanium. Figure from [15] which is adapted from [22].

Interstitial content is therefore carefully controlled depending on the alloy's intended purpose. Since oxidation of titanium involves simultaneous oxide growth and significant oxygen diffusion into the metal, it is important to understand interstitial diffusion into the metal during this process. Interstitials in α-Ti dissolve in the octahedral sites in the hcp structure and their diffusivities are one to two orders of magnitude larger than the self-diffusivity of Ti [23]. While they mainly occupy octahedral sites, interstitials are thought to travel through other metastable sites (mainly tetrahedral, hexahedral, and crowdion) during interstitial diffusion in hcp Ti [24,25]. These computational studies proposed diffusion pathways for interstitials in hcp titanium and calculated their diffusivities along the a and c-

axes. Given the hcp structure of Ti, its interstitial diffusivities are anisotropic – meaning their values are different when diffusing along the a or c-axis of the hcp Ti lattice. The incorporation of these interstitials has been shown to distort the hcp cell most significantly along the c lattice, thus increasing the c/a ratio of a "pure" α-Ti without interstitials and suggesting anisotropy in the oxygen diffusion in hcp Ti.

The Ti-O and Ti-N phase diagrams will be discussed in detail later in this chapter, but they generally agree on high oxygen and nitrogen solubility in hcp Ti. Notably, α-Ti shows a higher solubility of O than for other interstitials at the same temperature. The oxygen solubility in hcp titanium at 800°C (the temperature used for most oxidation studies in this dissertation) is ~33 at% [5,13] whereas the nitrogen solubility is 15-22 at%, lower but still substantial [8,9]. This high solubility for several interstitials complicates the isolation of each element and the impact it has on titanium oxidation when studying this process experimentally. Furthermore, since interstitials are light elements, the analysis and quantification become complicated and limits the extent of our understanding of the oxidation process. This is one of the potential explanations for the discrepancies between the interstitial diffusivities reported in computational and experimental studies, briefly discussed below.

Previous experimental diffusivities for oxygen and nitrogen in hcp titanium (Figure 2.3) disagree depending on the experimental environment, temperature ranges, and initial metal purity used [23,26–34]. It is suggested that diffusion coefficients for oxygen may be strongly impacted by the presence and concentration of various impurities, such as carbon and nitrogen [23]. From Nakajima and Koiwa's literature survey [23], the reported diffusivities at 800°C for oxygen are in the order of 10^{-14}-10^{-13} m^2/s and around 10^{-15} m^2/s for

nitrogen in hcp titanium suggesting that nitrogen diffusion is slower than that of oxygen. Since these are values from different experiments and methods, Bregolin et al. [35,36] provide a nuclear reaction analysis of oxygen and nitrogen in hcp titanium using similar methods. The activation energies and diffusivities are reported in Table 2.1 and also suggest that diffusivity of N is slower than O in hcp Ti at 800°C, although error ranges provided allow for variation in these values.

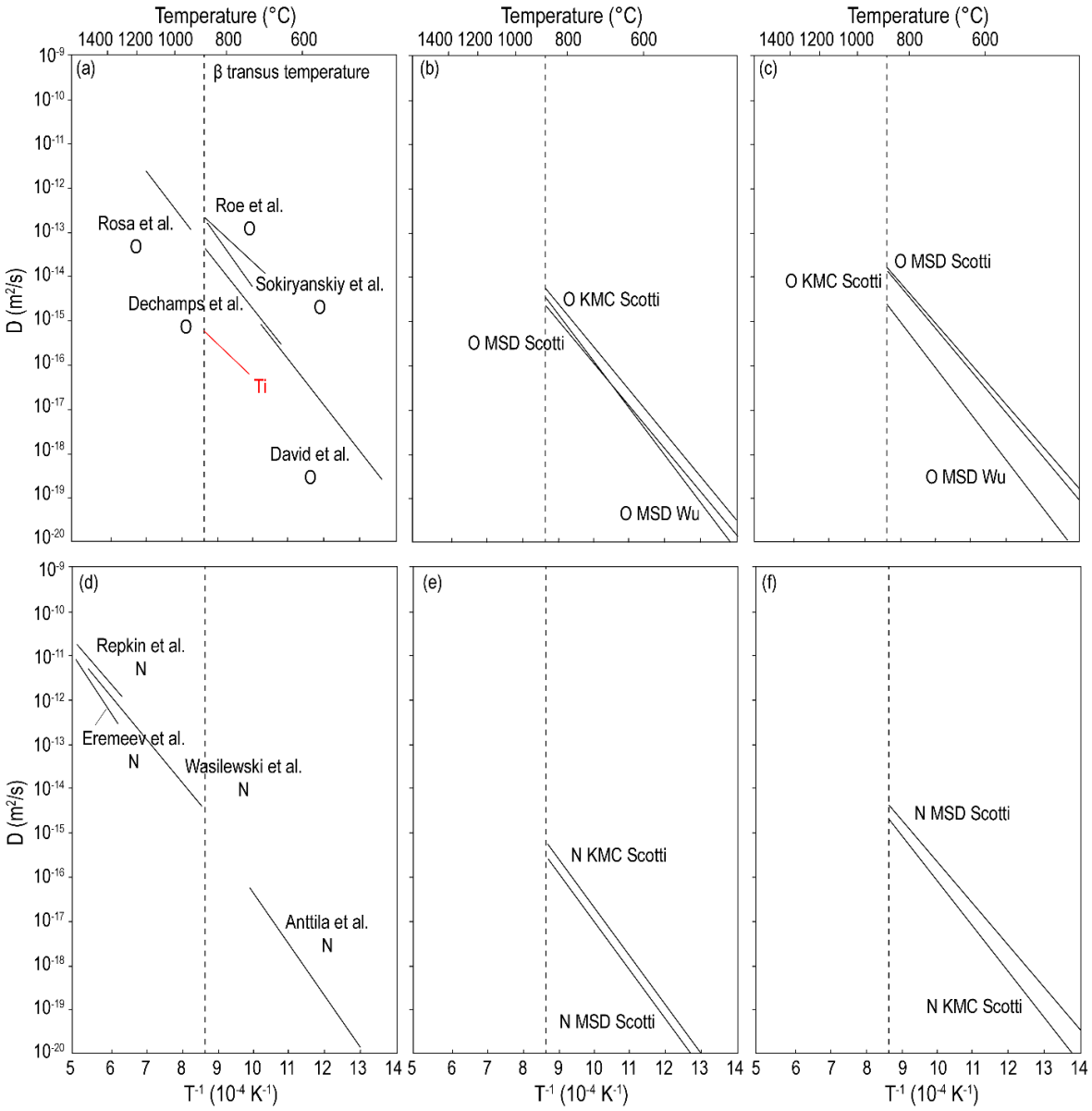

Figure 2.3. Diffusivities in hcp Ti for (a-c) oxygen and (d-f) nitrogen from (a, d) a literature survey of experimental data [23] and from computational studies [24,25] for (b, e) the direction perpendicular to the basal plane of hcp Ti and (c, f) parallel to the basal plane. The self-diffusivity in polycrystalline titanium from [23] is shown in red in (a) as reference.

Table 2.1. Activation energies and diffusivity values for N and O in hcp titanium from [35,36].

Interstitial	N [36]	O [35]
Temperature (K)	673 – 1023	623 – 873
Q (eV)	1.8977 ± 0.2	1.752 ± 0.5
Q (kJ/mol)	183 ± 2	169 ± 50
D_o (m^2/s)	$1.1 \pm 0.8 \times 10^{-7}$	$2 \pm 1 \times 10^{-7}$
D at 800°C (m^2/s)	1.36×10^{-16}	1.2×10^{-15}

2.3 Titanium-oxygen-nitrogen binaries, ternary, and crystal structures

In developing an understanding of titanium oxidation, it is important to first understand the thermodynamics associated with the titanium-oxygen, titanium-nitrogen, and titanium-oxygen-nitrogen system. Phase diagrams are valuable tools to determine which phases are expected to be stable at equilibrium. While oxidation is typically a non-equilibrium process and metastable phases must be considered, phase diagrams allow for a baseline of which phases might form during or after oxidation.

2.3.1 Titanium-oxygen phase diagrams

Different versions of the titanium-oxygen phase diagram have been published based on experiments [13,37] as well as from first-principles calculations [5,38]. Four of the most recent Ti-O phase diagrams (including a metastable diagram) are shown in Figure 2.4. Some of the inconsistencies between phase diagrams include: (1) expected equilibrium phases, (2) solubility ranges, and (3) invariant reaction temperatures. The multiple structures of Ti oxides are described in Section 1.3.2. The phase diagram reported by Okamoto [13] in Figure

2.4(c) contrasts with that of Murray and Wriedt [37] in Figure 2.4(a) most significantly in the exclusion of the Ti_3O and Ti_2O phases within the α-Ti phase field. For a thorough assessment of the thermodynamic knowledge on the Ti-O system (including a list of all experimental observations and methods) the reader is referred to the work by Cancarevic et al. [39] on which Okamoto's phase diagram is largely based. Additionally, there are two full phase diagrams from computational studies: one equilibrium phase diagram and a metastable one suppressing the ω phases [5]. These computational diagrams do not include the liquid phases. The experimental and computational phase diagrams differ in which phases are expected to be in equilibrium at different temperatures and compositions, solubility ranges, and invariant reaction temperatures.

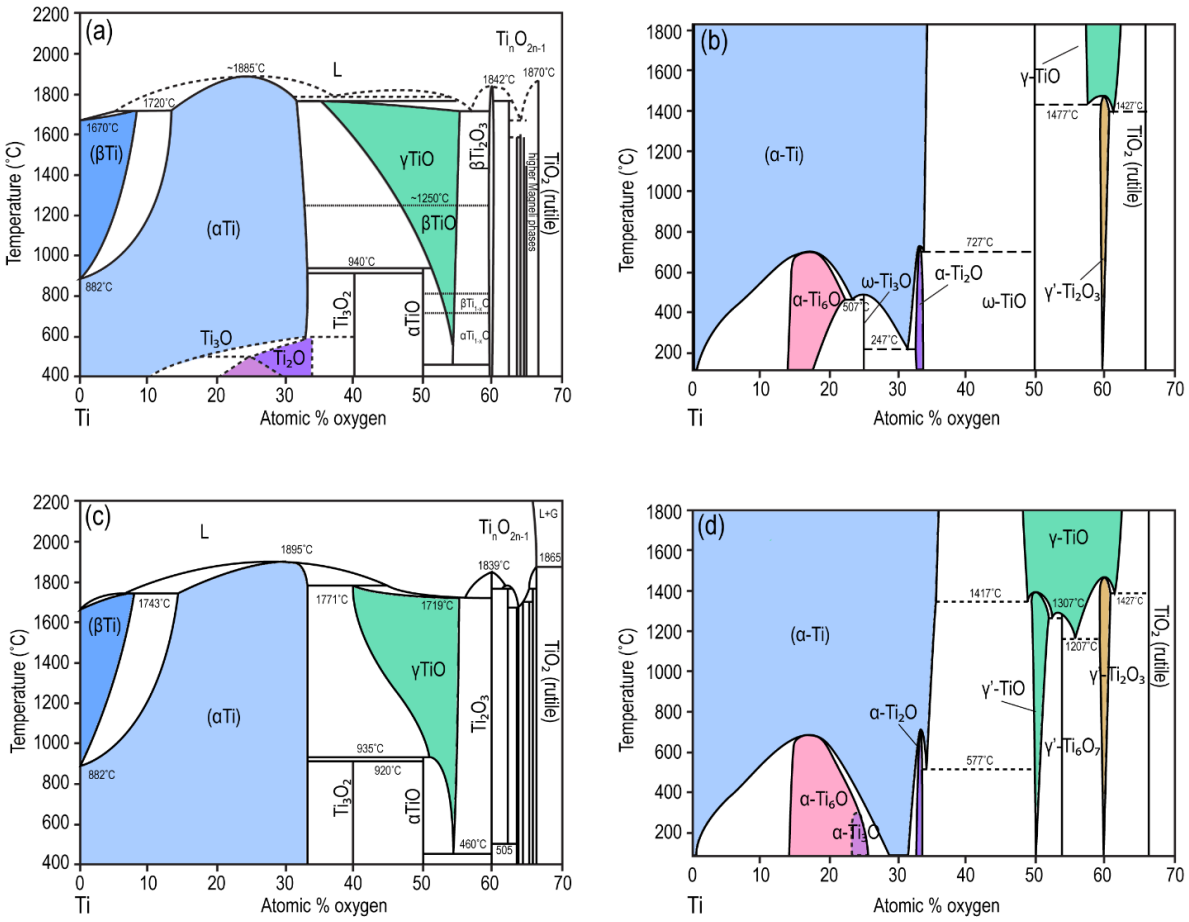

Figure 2.4. Binary Ti-O phase diagrams from experimental data from (a) [37], (c) [13] and from computational studies [5] (b) in equilibrium and (d) metastable diagram suppressing ω oxide phases. Images adapted from the citations listed before. Colored regions denote single phases. Note: Computational phase diagrams do not include the β phase.

2.3.2 Titanium oxide crystal structures

One of the challenges of studying the titanium-oxygen system is the large number of feasible metastable and stable oxides [5,13,37]. The relevant crystallographic information for a subset of these oxides is shown in Table 2.2 and Table 2.3. While there are many thermodynamically-stable and metastable titanium oxides, these can be divided into five broad categories:

1. **hcp-based suboxides.** These have oxygen contents below the oxygen solubility limit of 33 atomic percent oxygen for hcp titanium. These oxides include: Ti_6O, Ti_3O, and

Ti_2O, which also show a significant solubility range. The only difference between these is the ordering of the oxygen interstitials which occupy octahedral sites within the hcp titanium lattice. This dissertation will refer to these phases as α-Ti_6O, α-Ti_3O, and α-Ti_2O since they are based on the α-Ti crystal structure. While experimental evidence exists for the three oxides, they are not included as stable structures in all the Ti-O phase diagrams shown in Figure 2.4. Okamoto [13] removes it due to lack of sufficient experimental confirmation from oxidation studies, while Murray and Wriedt [37] include α-Ti_2O and α-Ti_3O but not α-Ti_6O, which is only included in the phase diagram based on computational work [5]. α-Ti_6O has been observed experimentally albeit not in oxidized titanium specimens, but in alloys prepared by reacting titanium with titanium dioxide powders [40]. Based on the available literature, Ti_2O has two proposed crystal structures: one where oxygen occupies every interstitial layer [5] (hereby referred to as α-Ti_2O) and one where oxygen occupies every other interstitial layer [37] (hereby referred to as α" phase as described by Yamaguchi [40]). A side-view of the crystal structures of these hcp-based Ti oxides is shown in Figure 2.5. The stacking of Ti and O layers in hcp and hcp-based oxides as well as the oxygen ordering within the interstitial layer for α-Ti_6O, α-Ti_3O, and α-Ti_6O is detailed in Figure 2.6.

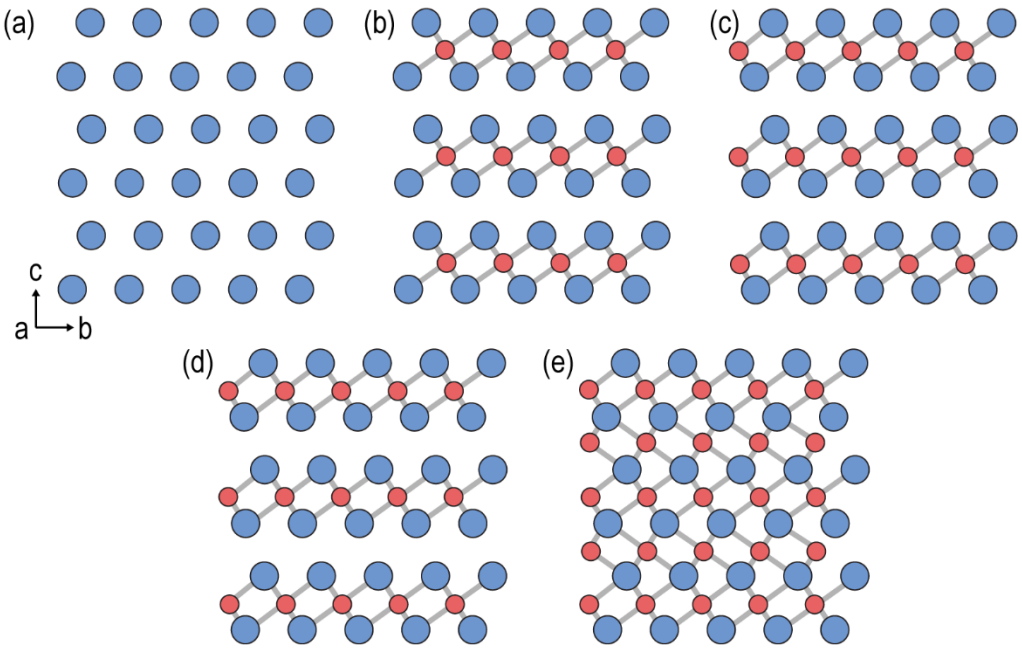

Figure 2.5. Side-view of hcp-based crystal structures in the Ti-O system looking down the [100] axis. Blue circles denote Ti atoms and red circles indicate O atoms. The structures shown are (a) α-Ti, (b) α-Ti_6O, (c) α-Ti_3O, (d) staged Ti_2O (also called α") and (e) α-Ti_2O.

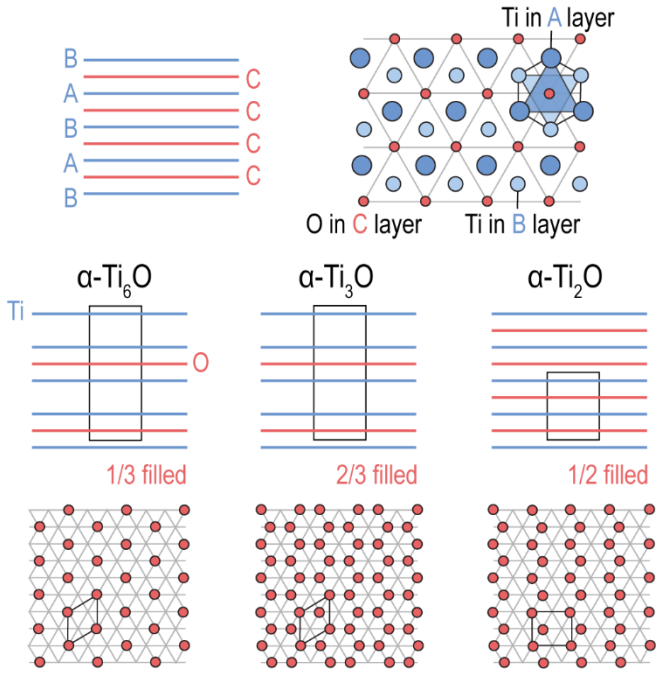

Figure 2.6. Schematic showing the stacking of α-Ti with all the possible Ti and O sites and the hcp-based suboxides from first-principles calculations by Gunda et al. [5]. Oxygen atoms (red circles) are all in octahedral sites. The schematics of the suboxides show the oxygen ordering in the interstitial layer and their occupancy is shown in text. Image adapted from [5].

2. **Omega (ω) suboxides.** Gunda et al. [5] predicts these to be the equilibrium suboxide structures instead of the hcp-based suboxides listed above. These structures have two honeycomb layers of titanium where pyramidal sites can be occupied by oxygen. These oxides include: ω-Ti_3O and ω-TiO shown in Figure 2.7. The ω-TiO phase has been observed experimentally but was referred to as ϵ-TiO and was not produced by titanium oxidation [41].

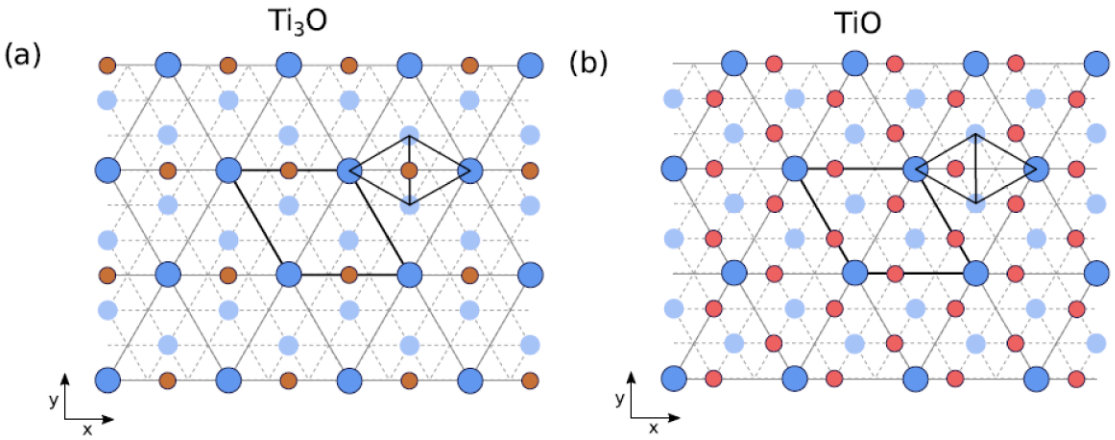

Figure 2.7. Schematics showing the ordering of Ti and O atoms in the triangular layers of ω-based Ti suboxides from first principles calculations [5]. Image from [5].

3. **Rocksalt-based (fcc) oxides.** These oxides are based on the NaCl rocksalt structure with a titanium sublattice and an oxygen sublattice (Figure 2.8). The main difference resides on vacancy orderings and whether there are vacancies in the titanium sublattice, oxygen sublattice, or both. These phases include: a high-temperature γ-TiO (disordered vacancies on both sublattices), a low-temperature stoichiometric γ'-TiO (ordered vacancies on both sublattices and is also referred to as α-TiO), γ'-Ti_6O_7 (ordered vacancies on both sublattices) and γ'-Ti_2O_3 (ordered vacancies in Ti sublattice only). Anatase, a polymorph of TiO_2, could be described as a rocksalt with an fcc oxygen sublattice with Ti ordered in half of the octahedral sites [5], but for

simplicity, it will be considered a tetragonal and discussed in the TiO_2 polymorphs section.

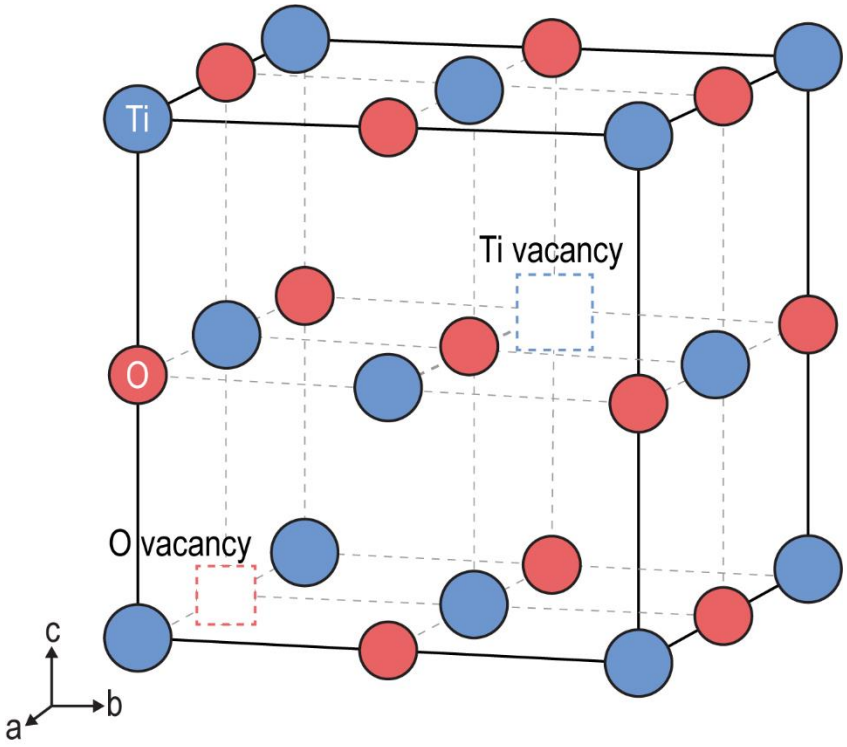

Figure 2.8. Schematic of a rocksalt-based Ti oxide showing Ti (blue) and O sites (red) with one vacancy in each sublattice. The difference between rocksalt oxides is whether the Ti or O sublattice have any vacancy orderings.

4. **Oxides with oxygen in hcp orderings.** This includes corundum Ti_2O_3 and rutile TiO_2 phases (Figure 2.9), as well as the Magnéli phases (Ti_nO_{2n-1}). These latter phases can be thought of as rutile with shear defects as seen in Figure 2.10.

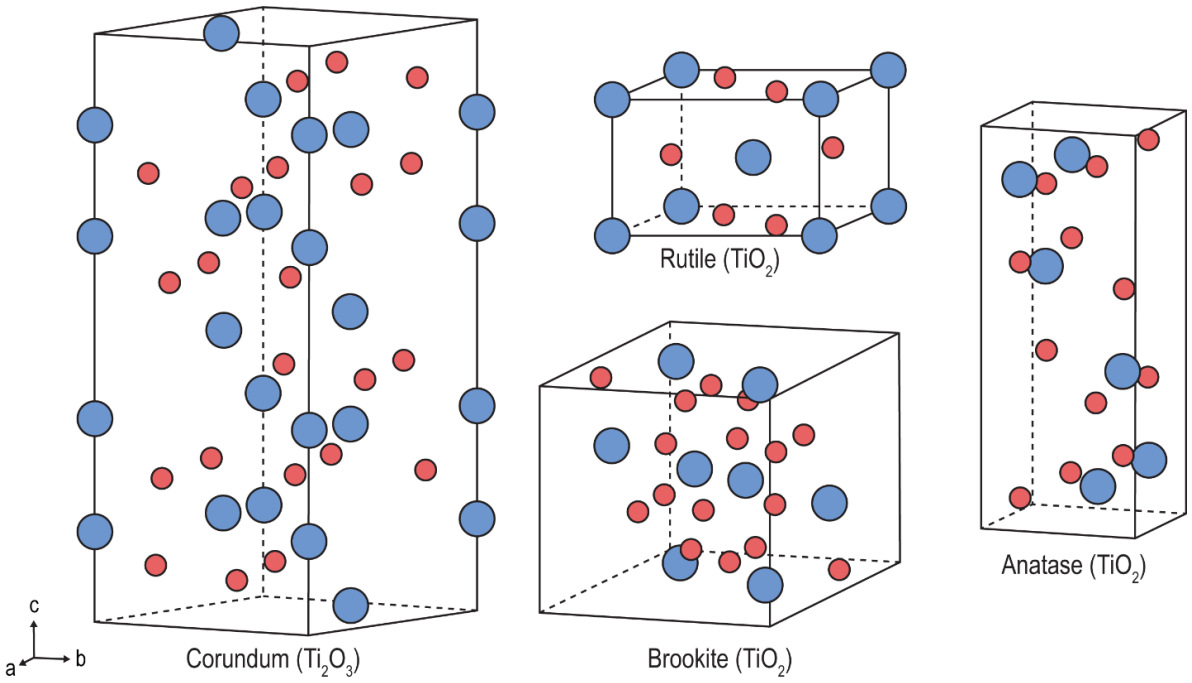

Figure 2.9. Crystal structures for Ti_2O_3 in its corundum crystal structure and the polymorphs of TiO_2: rutile, brookite, and anatase.

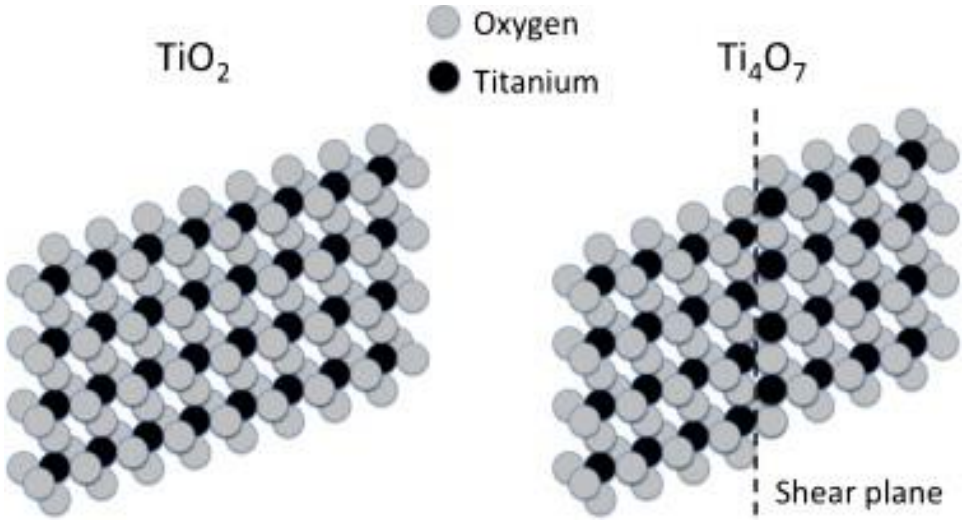

Figure 2.10. Example of a Magnéli phase (Ti_4O_7) from edge-sharing TiO_2 with face-sharing shear plane. Image from Walsh and Wills [42].

5. **Titanium dioxide (TiO_2) polymorphs.** Titanium dioxide has three common polymorphs: anatase (tetragonal), rutile (tetragonal), and brookite (orthorhombic) as shown in Figure 2.9. In titanium oxidation, most oxide scales are composed mainly of

rutile despite anatase expected to be more energetically favorable from DFT calculations [43–48]. Depending on the application, anatase or rutile will be the preferred reaction product. In biomedical applications, anatase has been shown to be more biocompatible and is thus a desirable phase [49,50].

Table 2.2. Subset of titanium oxide phases and their crystallographic information based on the highest quality or most recent reference phase on ICSD or referencing the relevant first principles-based work.

Oxide	**Phase**	**Composition at% O**	**Bravais lattice**	**Pearson symbol**	**Space group**	**ICSD**	**Source**
Ti	α	0-33	hcp	*hP*2	$P6_3/mmc$	253841	[51]
Ti_6O	α	~14-22	hcp	*hP*14	$P\bar{3}1c$	23576	[52]
Ti_3O	α	20-30	hcp	*hP*16	$P\bar{3}1c$	24082	[53]
	ω	25	hcp	-	-	-	[5]
Ti_2O	α	25-33.4	hcp	*hP*3	$P\bar{3}m1$	23574	[52]
	α	~33-35	hcp	-	-	-	[5]
Ti_3O_2	-	40	hcp	*hP*5	*P*6/*mmm*	-	[54]
TiO	α	50	Monoclinic	m*S20*	*C*12/*m*1	15327	[55]
	γ’	40-55.3	fcc (rocksalt)	*cF8*	$Fm\bar{3}m$	56612	[56]
	ω or ϵ	50	hcp	*hP*6	$P\bar{6}2m$	196273	[41]
Ti_2O_3	Corundum	60	Trigonal	*hR*10	$R\bar{3}c$	1462	[57]
	Rocksalt w/vacancies	~60-61	fcc (rocksalt)	-	-	-	[5]
Ti_3O_5	Magnéli	62.5	Monoclinic	*mC*32	*C*2/*m*	75193	[58]
Ti_4O_7	Magnéli	63.64	Triclinic	*aP*44	$P\bar{1}$	16297	[59]
TiO_2	Rutile	66.5-66.7	Tetragonal	*tP*6	$P4_2/mnm$	257864	[60]
	Anatase	66.7	Tetragonal	*tI*12	$I4_1/amdZ$	159910	[61]
	Brookite	66.7	Orthorhombic	*oP*24	*Pbca*	154605	[62]

Table 2.3. Lattice parameters and unit cell volumes for a subset of titanium oxides based on the phases with most experimental evidence.

Oxide	ICSD	Composition at% O	a (Å)	b (Å)	c (Å)	Volume (Å^3)	Vol/Ti atom (Å^3)
α-Ti	253841	0-33	2.95	2.95	4.68	35.32	17.66
Ti_6O	23576	~14-22	5.06	5.06	9.48	210.20	17.52
Ti_3O	24082	20-30	5.14	5.14	9.53	218.20	18.18
Ti_2O	23574	25-33.4	2.96	2.96	4.83	36.65	18.33
α-TiO	15327	40-55.3	5.86	9.34	4.14	215.99	21.59
Ti_2O_3	1462	60	5.16	5.16	13.61	313.60	26.13
Ti_3O_5	75193	62.5	9.83	3.79	9.97	371.12	30.93
Ti_4O_7	16297	63.64	5.60	7.13	12.47	466.10	29.13
TiO_2 (rutile)	257864	66.5-66.7	4.60	4.60	2.96	62.74	31.37

2.3.3 Titanium-nitrogen phase diagrams

The study of the titanium-nitrogen system encounters similar experimental challenges to those encountered in the titanium-oxygen system, especially since nitrogen is an even smaller atom than oxygen and thus more difficult to quantify. Many of the reported Ti-N phase diagrams have dashed lines indicating that further research is required to confirm the phase fields for different nitrides. This hinders ascertaining the solubility ranges of different fields and which phases are included. Figure 2.11 shows the binary T-N phase diagrams from experimental and computational studies. Phase diagrams from computational studies do not show the β-Ti nor liquid phases due to difficulties in incorporating those phases to the calculations.

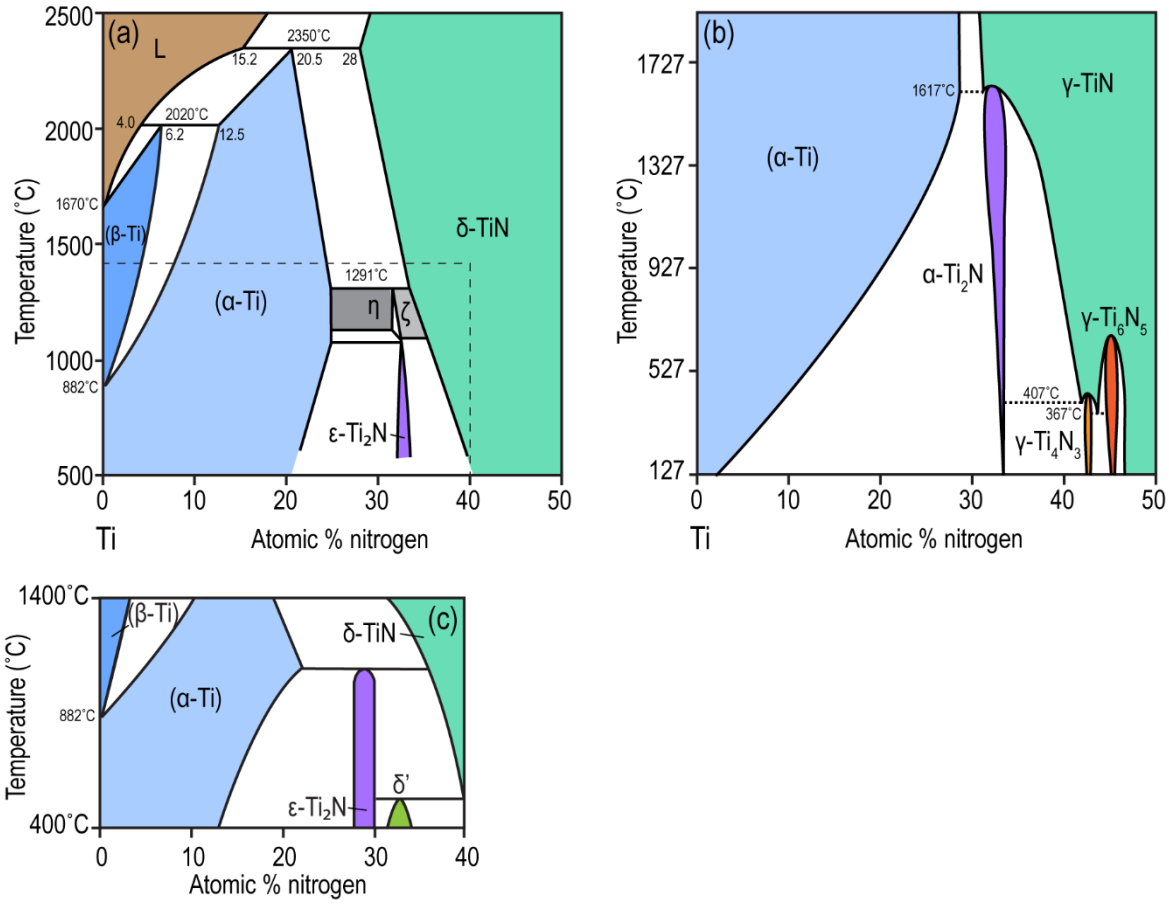

Figure 2.11. Binary Ti-N phase diagrams from (a, c) experimental data [9] and (b) computational studies [8]. Colored regions denote single-phase regions. β-Ti and liquid phases are not included in (b). These phase diagrams are adapted from (a) [63], (b) [8], and (c) [7].

All three iterations of the phase diagram indicate the formation of ε-Ti_2N and δ-TiN at 800°C although they show different solubility ranges. The latest experimental phase diagram [7] only shows Ti_2N, TiN and δ' (a tetragonal Si_2Th structure) nitrides removing the η and ζ phases proposed in 1992 [63]. The binary from first-principles [8] proposes additional phases γ-Ti_4N_3 and γ-Ti_6N_5 where γ denotes vacancy-ordered rocksalt phases. All of these phases and their corresponding crystallographic information will be discussed in the following section.

At 800°C, the expected solubility of nitrogen is ranges from 15 to 22 at% N which is substantially lower than oxygen's expected solubility of 33 at% O in hcp Ti. At this

temperature, the first phase expected to form first in the Ti-N system is Ti_2N while in the Ti-O system, the first thermodynamically-stable phase would be TiO. This suggests that the Ti_2N phase is stable at higher temperatures than its equivalent composition Ti_2O. Overall, there are fewer titanium nitride phases reported than there are titanium oxides.

2.3.4 Titanium nitride crystal structures

Nitrogen, like oxygen, energetically favors octahedral sites in hcp titanium. However, the orderings of these nitrogen atoms differ from those of oxygen in the phases with equivalent compositions (e.g. Ti_2N vs Ti_2O). The stacking and orderings of the analogue ε-Ti_2N and α" (staged Ti_2O) are compared in Figure 2.12. Although ε-Ti_2N is a tetragonal structure, it can be thought of as an ordering of N and vacancies over the octahedral sites of hcp Ti with the Ti positions slightly shifted as can be appreciated from the crystal structure comparison.

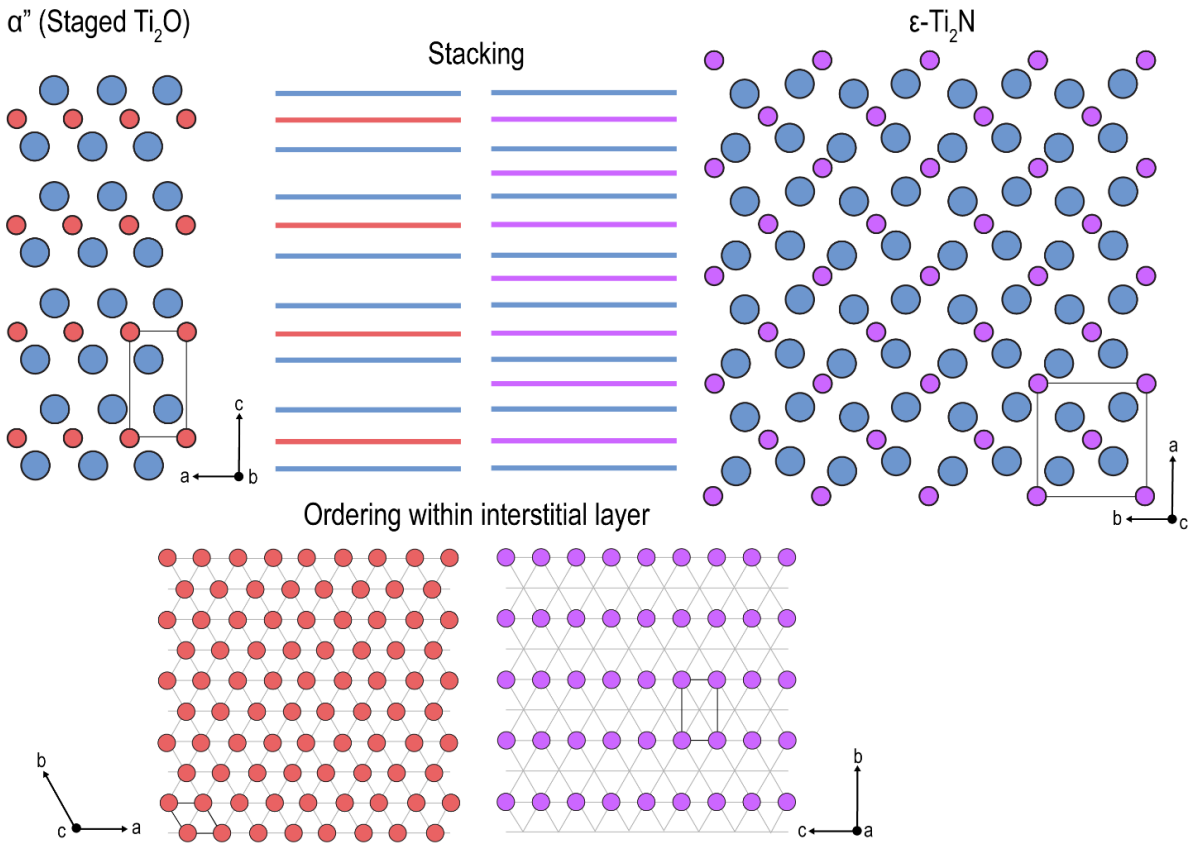

Figure 2.12. Crystal structures, stacking, and ordering comparisons for α" (staged Ti_2O) and ε-Ti_2N.

There are fewer titanium nitride phases reported than there are titanium oxides. Reported titanium nitride phases are: Ti_2N (sometimes referred to as ε-Ti_2N, anti-rutile tetragonal structure), δ' (a tetragonal Si_2Th structure), and TiN (rocksalt structure). Computational studies [8] predict two additional titanium nitrides: γ-Ti_4N_3 and γ-Ti_6N_5, where γ denotes a vacancy-ordered rocksalt phase. The crystallographic information for nitride phases in shown in Table 2.4 and Table 2.5. The crystal structures for ε-Ti_2N and TiN are shown in Figure 2.13.

Table 2.4. Titanium nitride phases and their crystallographic information based on the highest quality or most recent reference phase on ICSD or referencing the relevant first principles-based work.

Nitride	at% N	Bravais lattice	Pearson symbol	Space group	ICSD	Source
ε-Ti_2N	~33	Tetragonal	*tP*6	$P4_2/mnm$	180520	[64]
δ’	38	Tetragonal	*tI*12	$I4_1/amd$	180521	[64]
η-Ti_3N_{2-x}	~40	Trigonal[1]	-	$R\bar{3}m$	-	[65]
ζ-Ti_4N_{3-x}	~43	Trigonal	-	$R\bar{3}m$	-	[66]
γ-Ti_4N_3	~43	fcc (rocksalt)	-	-	-	[8]
γ-Ti_6N_5	~46	fcc (rocksalt)	-	-	-	[8]
δ-TiN	30-55	fcc (rocksalt)	*cF*8	$Fm\bar{3}m$	1547	[67]

Table 2.5. Lattice parameters and unit cell volumes for a subset of titanium nitrides based on the phases with most experimental evidence.

Nitride	ICSD	Composition at% N	a (Å)	b (Å)	c (Å)	Volume (Å^3)	Vol/Ti atom (Å^3)
ϵ-Ti_2N	180520	33	4.98	4.98	3.06	75.89	18.97
TiN	1547	30-55	4.24	4.24	4.24	76.17	19.04

[1] According to Lengauer, this phase could be indexed as a rhombohedral or hexagonal unit cell as well.

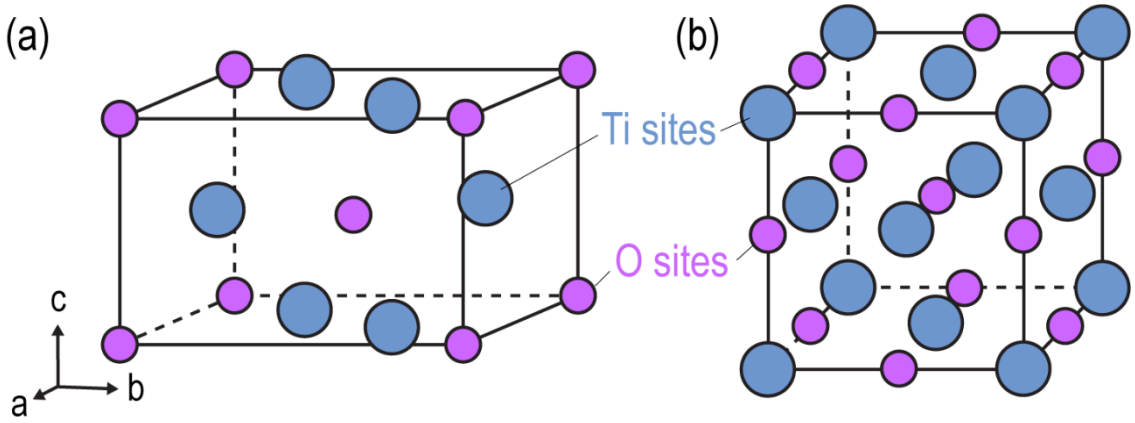

Figure 2.13. Schematic showing the main titanium nitrides expected to form at 800°C: (a) a tetragonal ϵ-Ti_2N with an anti-rutile structure and (b) rocksalt TiN.

The methodology that was used to synthesize the reference nitride phases used in this chapter are shown in Table 2.6. This information is included so that potential contaminants or additional reaction products can be taken into consideration when using these for phase identification.

Table 2.6. Experimental methods used to generate ICSD phases from the Ti-N system used as reference.

Phase	**ICSD**	**Source**	**Method**
α-$TiN_{0.17}$	644765	[68]	Arc-melted Ti sponge and TiN formed by reacting Ti with purified N_2 gas at 1250°C to desired composition. Mixtures were then annealed at 900°C in a sealed, evacuated silica tube for a month.
ϵ-Ti_2N	180520	[64]	Combustion synthesis of nitrogen and 99.27% pure Ti powder homogenized by annealing in vacuum at 1400°C for 24 h and hardened in air
δ’	180521	[64]	
δ-TiN	1547	[67]	Single crystals made by zone melting, zone annealing, and annealing crystal growth methods of $TiN_{0.9}$

2.3.5 Titanium-nitrogen-oxygen phase diagram

Once more than one interstitial is considered, the analysis and quantification of the different phases becomes more complex. In the case of the Ti-O-N ternary system, there are few phase diagrams available [69–76]. Since TiO and TiN are both rocksalt structures, titanium oxynitrides are sometimes referred to as a TiO-TiN solid solution. Other terms used for oxynitrides are TiN_xO_y and TiN_xO_{1-x}. Most of these phases are typically a rocksalt structure and are anticipated to have a wide composition range that allows for vacancies in the N/O sublattice and Ti sublattice. A rocksalt crystal structure for a Ti oxynitride and a partial ternary phase diagram based on binaries at 800°C are shown in Figure 2.14.

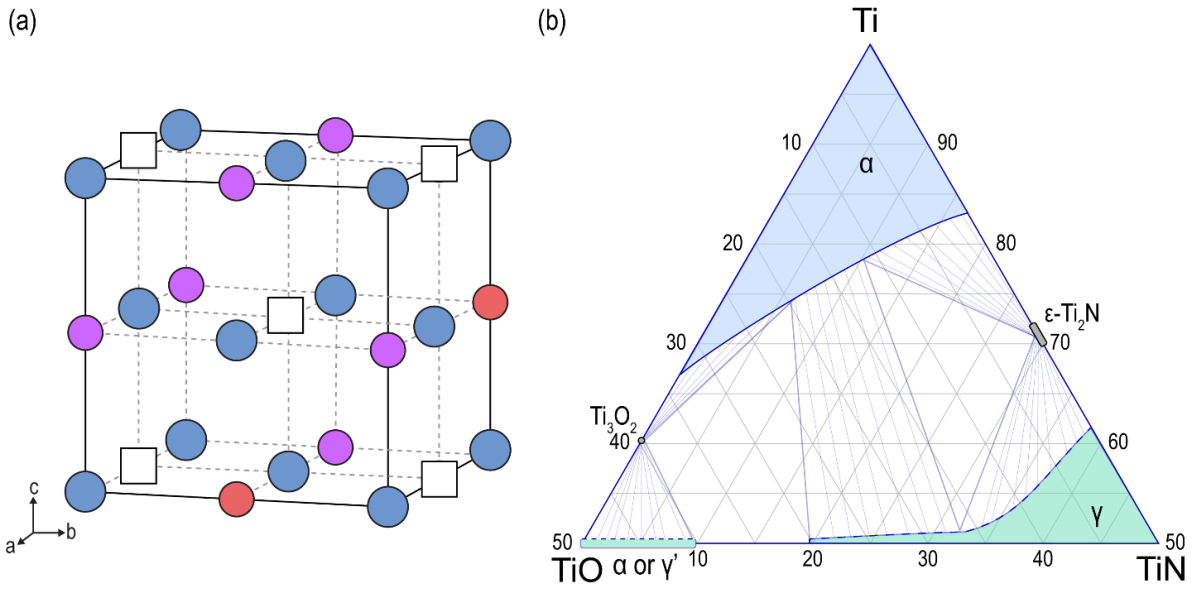

Figure 2.14. (a) Crystal structure for rocksalt-based Ti oxynitride where blue atoms are Ti, red atoms are O, purple atoms are N and boxes represent vacancies. (b) Partial Ti-N-O phase diagram at 800°C based on the binaries from [7] for Ti-N and [13] for Ti-O. Tie lines and dashed lines for α-TiO and γ-TiN are speculative of potential solubilities and should not be relied on as factual.

Compiling experimental evidence for various Ti-N-O ternary phases, Figure 2.15 includes the binary phases expected at 800°C and the ternary phases that have been observed experimentally before.

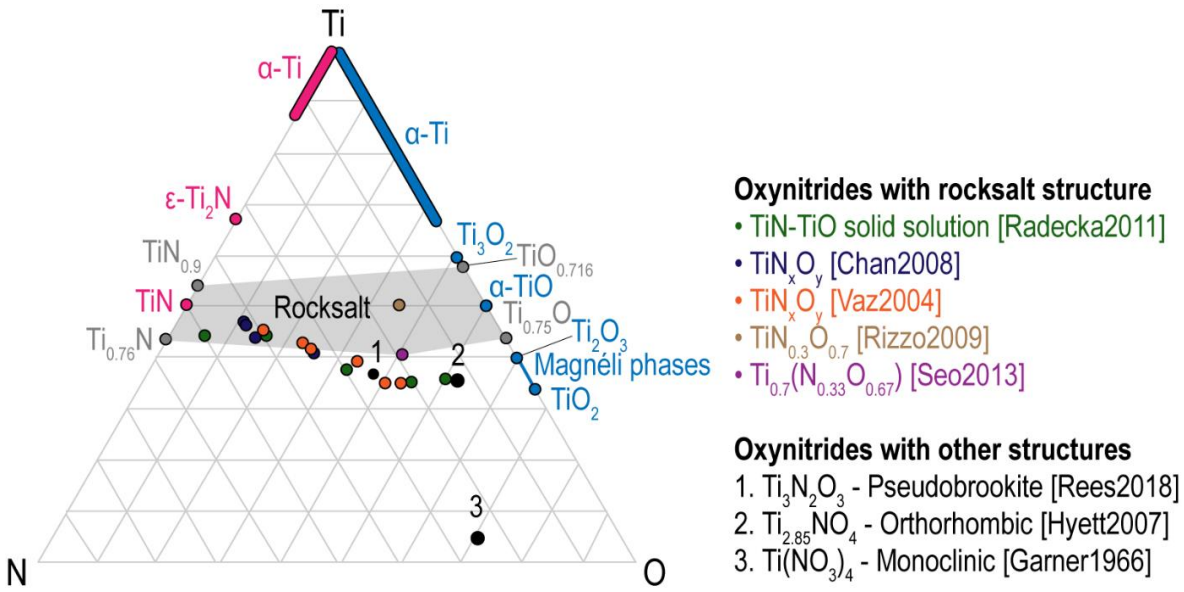

Figure 2.15. Schematic partial Ti-N-O phase diagram showing the binary phases expected at 800°C for Ti-N in pink and Ti-O in blue. Shaded gray area indicate regions where rocksalt (gray) is expected from Rees et al. [74]. Additional colored points show ternary phases with rocksalt structure [69–73] and numbered points indicate oxynitrides with other crystal structures [74–76].

One of the most recent ternary Ti-N-O phase diagrams available (Figure 2.16) was calculated at 650°C in ThermoCalc using a thermodynamic database [77]. Notably, this iteration shows a significant composition range for nitrogen and oxygen in the fcc rocksalt oxynitride phase labelled here "$Ti(N_yO_{1-y})_{1\pm x}$".

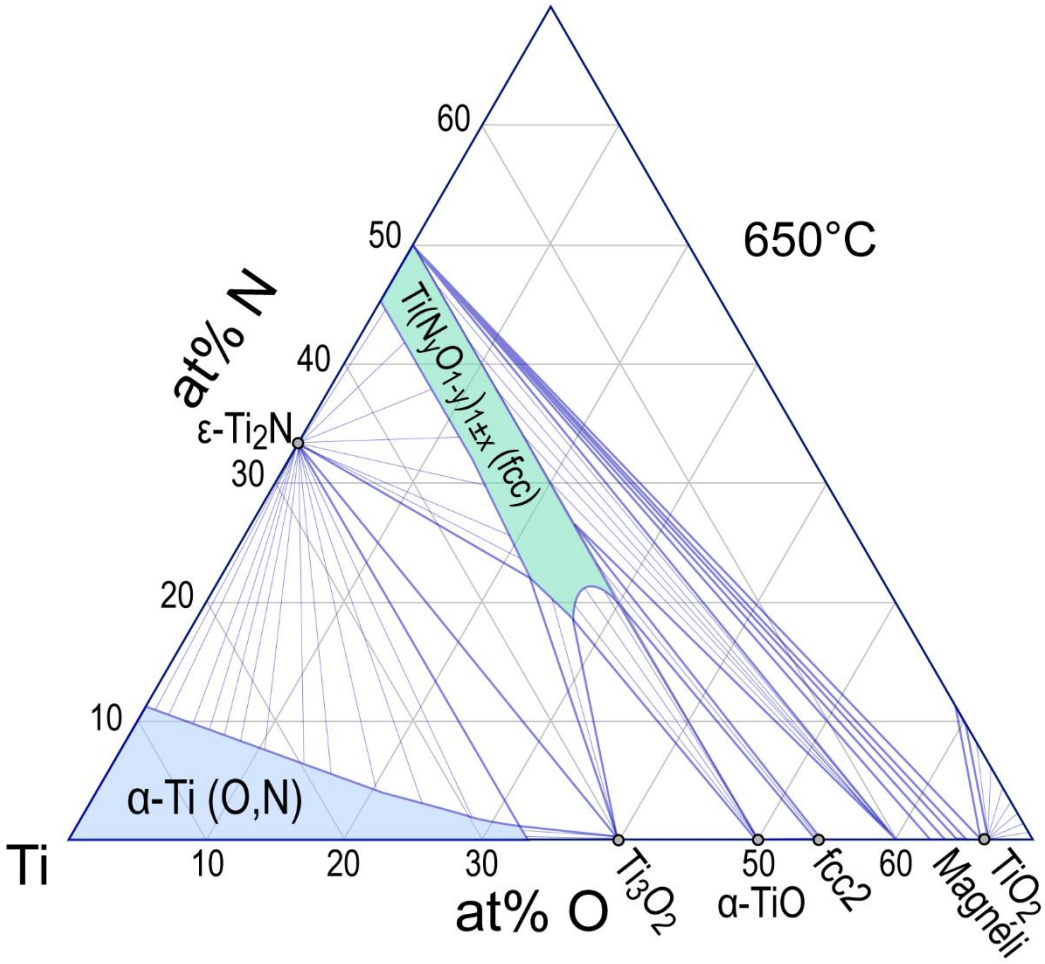

Figure 2.16. Partial ternary Ti-N-O phase diagram at 650°C showing wide solubility of N and O in α-Ti and fcc rocksalt oxynitride phase. Adapted from Dupressoire et al.'s [77] diagram calculated using ThermoCalc and the TCTI1 database.

2.3.6 Ti-N-O (oxynitride) crystal structures

Since TiO and TiN are both rocksalt structures, titanium oxynitrides are sometimes referred to as TiO-TiN solid solution. Other terms used for oxynitrides include TiN_xO_y and TiN_xO_{1-x}. Most of these phases are typically a rocksalt structure and have a wide composition range as shown in the Ti-N-O phase diagrams (Figure 2.14 for crystal structure and Figure 2.16 for solubility range of oxynitride phase).

Ti oxynitrides show a decreasing symmetry in their crystal structures with increasing O content. Oxynitride phases from literature show this trend in their composition and crystal structure as evidenced in Table 2.7. It is important to note that none of these reference oxynitrides were formed from exposing titanium metal to argon environments as in this work. However, oxynitrides have been reported to form in oxidation studies of various titanium alloys. The rocksalt TiN_xO_y phase that will be used as a reference throughout this work (i.e. $Ti_{0.7}(N_{0.33}O_{0.67})$ from [73]) was formed by exposing TiO_2 nanoparticles to NH_3/N_2 gas at 800°C.

Table 2.7. Titanium oxynitride phases and their crystallographic information based on the highest quality or most recent reference phase on ICSD.

Phase	at% N	at% O	Bravais lattice	ICSD	Source
$Ti_{0.7}(N_{0.33}O_{0.67})$	19.4	41.2	fcc (rocksalt)	426340	[73]
$Ti_{2.85}O_4N$	12.7	51.0	Orthorhombic	173420	[75]
$Ti(NO_3)_4$	23.5	70.6	Monoclinic	26639	[76]

Abdallah et al. [78] shows a thorough exploration of nitride and oxynitride formation in a Ti2642S alloy, but there are no similar explorations in pure titanium that deal with phases formed from exposure to an environment with both N and O simultaneously. TiN_xO_y phases reported by Tkachuk et al. [79] were formed by introducing a molecular N_2 environment ($pN_2 = 10^5$ Pa) at 850-950°C and subsequently an O_2 environment in various partial pressures to isolate the effects of nitrogen exposure from reactions with oxygen.

2.3.7 fcc titanium and long period stacking ordering (LPSO) structures

Previous work on titanium thin films [80–84] and in carbo-oxidized titanium [85] has shown the formation of an fcc-based Ti phase that has puzzled researchers since hcp should be a more energetically favorable structure for Ti than fcc. Traylor et al. [81] provide a

thorough literature review of the different fcc phases that have been reported for titanium. Further illustrating the complexities of understanding titanium oxidation, the fcc phase has been sometimes attributed to the formation of an fcc titanium hydride (either δ-TiH_2 or γ-TiH) explained by hydrogen pick-up during experimental methods used such as FIB sectioning.

From in situ TEM studies of Ti in Nb-Ti-Si based alloys, the hcp to fcc Ti formation has been observed and was proposed to include additional intermediate structures along the hcp to fcc transformation pathway [86]. These intermediate structures were identified as long period stacking ordering (LPSO) structures similar to 9R and 18R orderings. These phases were not identified as oxides, nitrides, or oxynitrides, but rather as titanium transforming from hcp to fcc.

2.4 Oxidation of titanium

The oxidation of titanium and its alloys has been studied for over five decades, yet the reported results are difficult to consolidate due to experimental variations in titanium purity, initial sample thickness, and oxidative environment [39]. Titanium, as will be evident throughout this work, is very sensitive to variations in experimental parameters including, but not limited to, titanium purity, sample preparation, environment, and thermomechanical history [39]. Understanding of titanium oxidation is further complicated by the fact that oxidation encompasses two simultaneous processes: oxide scale formation and growth, and significant oxygen dissolution into the substrate – particularly in α-Ti (Figure 2.17). This complex mechanism has provided challenges into the study of oxygen diffusion and oxidation in titanium since the effects and contribution of each process to the oxidation mechanism is difficult to isolate experimentally.

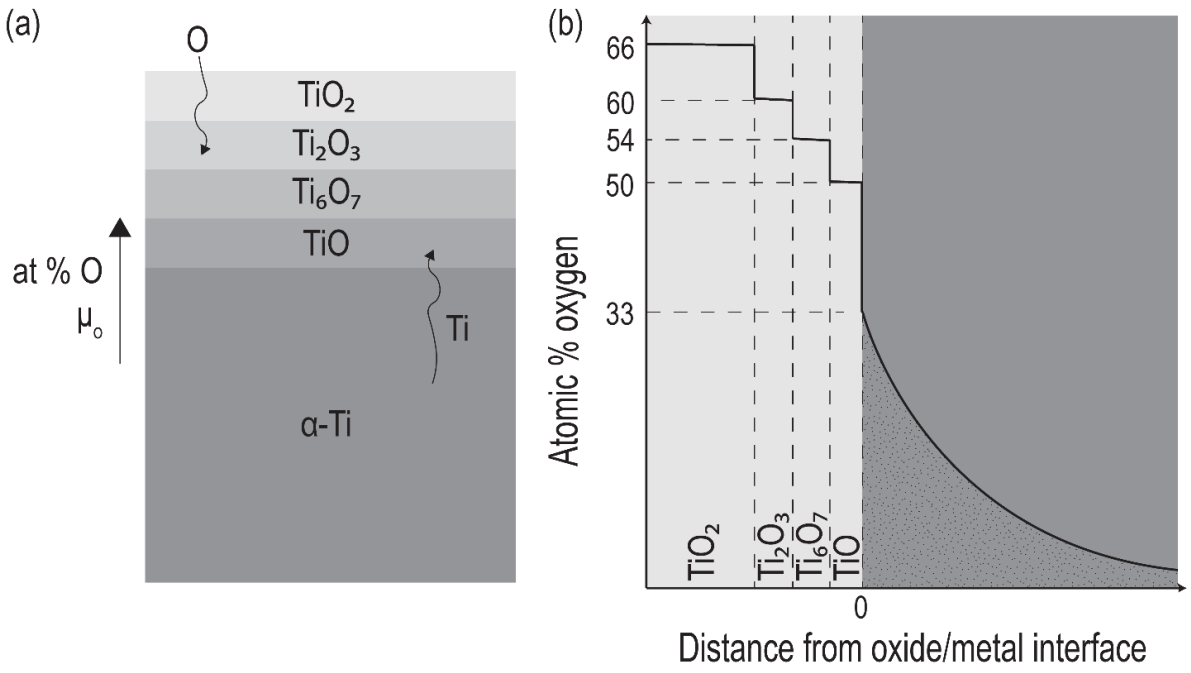

Figure 2.17. Idealized scenario showing oxide layers expected for oxidation of titanium at 800°C showing the (a) expected microstructure and (b) corresponding oxygen concentration profile.

From previous oxidation studies, it is known that titanium readily forms a dense titanium dioxide (TiO_2) layer (usually in its rutile crystal structure) despite the many thermodynamically feasible oxides with lower oxygen content than rutile. This rutile layer is known to form at room temperature with a thickness of a few nanometers when exposed to air or aqueous solutions [87]. This native oxide is dissolved into the metal substrate upon heating thus changing the purity of the titanium and altering its initial properties. From the Ellingham diagram of titanium oxides (Figure 2.18), the required equilibrium partial pressures to form any of the lower titanium oxides are extremely low [88]. This would suggest that even if lower oxides were to form during initial stages of oxidation, they should transform to rutile. While a useful reference, Ellingham diagrams are calculated based assuming stoichiometric compositions, meaning that they do not account for oxygen dissolved in Ti or solubility ranges in the oxides. In the Ti-O system, as has been mentioned

before, interstitial solubility plays an important role and these thermodynamic references should be used with caution.

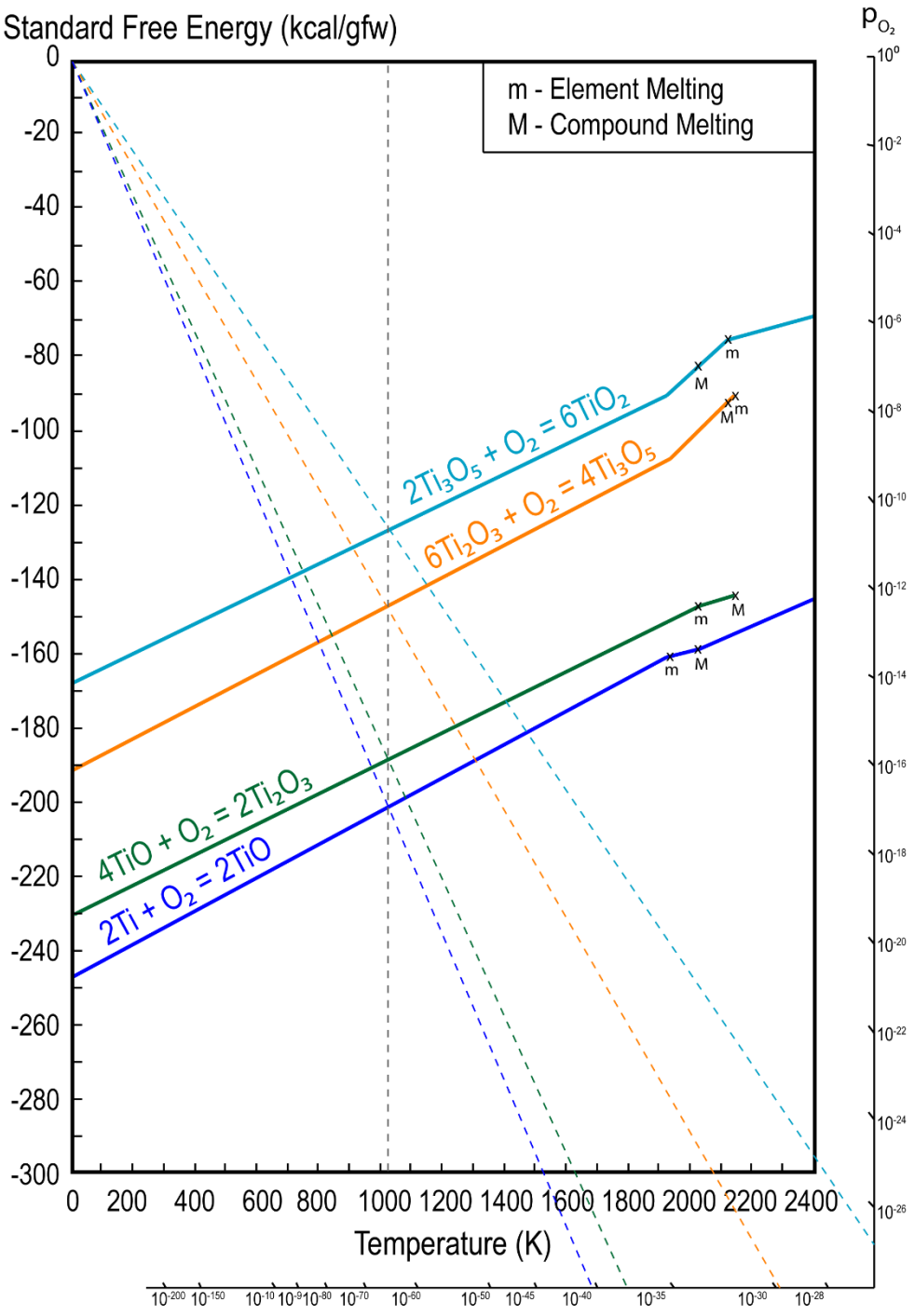

Figure 2.18. Ellingham diagram for various titanium oxidation reactions. These reactions start with the formation of TiO from Ti metal and sequential oxidations until TiO_2 formation. Adapted from reference Ellingham diagrams [88]. Dashed lines indicate the equilibrium pressure for oxide formation at 800°C.

2.4.1 Titanium oxidation in air and oxygen-rich atmospheres

From previous oxidation studies, titanium is known to develop a rutile (TiO_2) oxide scale whenever oxidized in air despite the many oxides that are thermodynamically feasible [89–91]. Between the temperatures 600-1000°C, the oxidation of titanium follows parabolic rate law [92], but this rate combines two distinct processes: (1) oxide formation and growth and (2) the oxygen dissolution into the metal. The mass change for this parabolic oxidation rate is then described by

$$\frac{\Delta m}{A} = k_p(oxide\ growth)\sqrt{t} + k_p(dissolution)\sqrt{t}$$

where Δm corresponds to the mass change (typically gain) from the oxidation process, A is the surface area of the specimen over which oxidation occurs, k_p is the parabolic rate constant (or 'scaling constant', and t is time [93].

Since only rutile is found when oxidizing in air, it is hypothesized that if TiO (or another lower oxide) were to form first, sequential oxidation would occur until all oxide is transformed into rutile. The morphology of the rutile scale observed varies between studies, leading to a few proposed oxidation mechanisms for hcp titanium. Oxidation studies have been done for the early stages of oxidation [94,95] and for long-term exposures [29,89,92,96–101].

As is typical in metal oxidation, the oxidation process in titanium begins by the adsorption of oxygen onto the metal surface by physisorption. These oxygen molecules dissociate into oxygen atoms or anions for oxide formation or dissolution into the metal. The oxidation process in titanium is dominated by outward Ti diffusion and inward O diffusion [89,90,102], but the oxidation mechanism is still only partially understood.

In general, only rutile formation is reported when oxidizing titanium in air, pure oxygen or O_2/Ar mixtures [89–91,96,100]. Kofstad et. al. [89] reported the formation of two rutile scales, a dense outer layer and an apparently porous inner layer which presumably had recrystallized. The columnar outer scale grows from outward Ti diffusion while the internal scale forms from inward O diffusion. By metallographic analysis, hardness measurements, and X-ray diffraction, it is proposed that the oxidation mechanism of titanium in air involves the following steps: (1) oxygen saturation to ~25 at % O at the metal surface after 1 h above 900°C at which point Ti converts to β and α would only be present at the surface once oxygen is incorporated, (2) further oxygen dissolution increases localized stresses and strains and leads to cracking in developing oxide scales, and (3) a titanium oxide (tentatively TiO) forms by nucleation and immediately oxidizes to rutile TiO_2. Due to cracking in the oxide scales, it is hypothesized that oxygen would continue to permeate through the porous oxygen scale and contribute to further oxide growth at the boundary with the metal.

Lopes Gomes and Huntz [90] reported the formation of stratified and layered oxide scales when oxidizing titanium in a pure oxygen atmosphere from 600 to 800°C. During the initial stages, the kinetics is reported to be parabolic and is ascribed to the formation of a compact outer oxide scale. After reaching an oxygen content above 25.9 at% in the titanium substrate, the stresses are expected to increase along with the oxide growth. While they report 25.9 at% O as a saturation point, this is below the predicted 33 at% solubility of oxygen in α-Ti at 600-800°C. This could be attributed to difficulties in measuring oxygen content in the titanium system, particularly since this study did not attempt quantification and relied on X-ray diffraction for phase identification.

The study then proposed that once the initial oxide reaches a critical thickness, the stresses increase enough to initiate fracture. The formation of the first crack denotes the transition from parabolic to pseudolinear kinetics where the porous oxide scale allows for steady-state oxygen permeation. These cracks (formed parallel to the surface) serve as short transport pathways where there is oxygen transport through the open crack and surface diffusion on the crack surfaces. Titanium can no longer diffuse outwards through these cracks to form and grow oxide scales. The number of oxide layers formed was correlated to small changes in the slopes of the kinetic curves obtained during the oxidation process. A schematic of this proposed oxidation mechanism in shown in Figure 2.19.

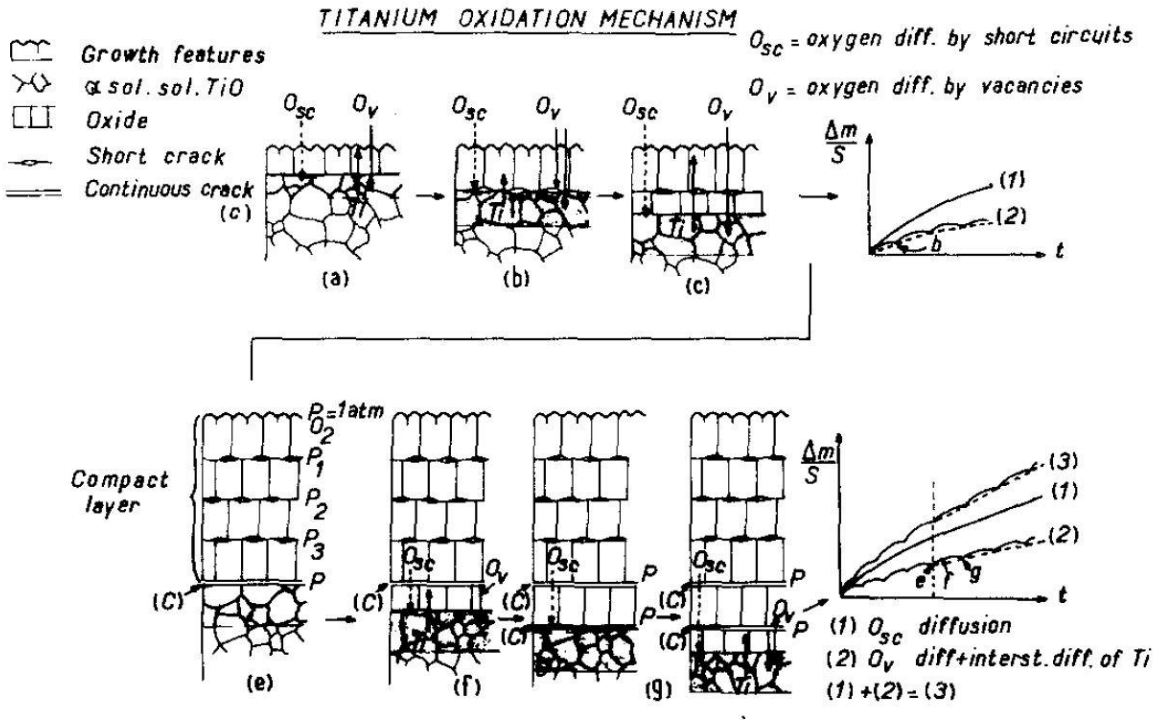

Figure 2.19. Titanium oxidation mechanism described by Lopes Gomes and Huntz [90] showing the different microstructural features of the oxidized specimens and proposed mass gain curves. Images from [90].

The morphology of many thin oxide scales was later confirmed by Bertrand et al. [91], who found an external scale of equal thickness layers (made of stoichiometric rutile)

and an internal oxide scale with coarse recrystallized grains (composed of nonstoichiometric oxide). An example of two such microstructures is shown in Figure 2.20.

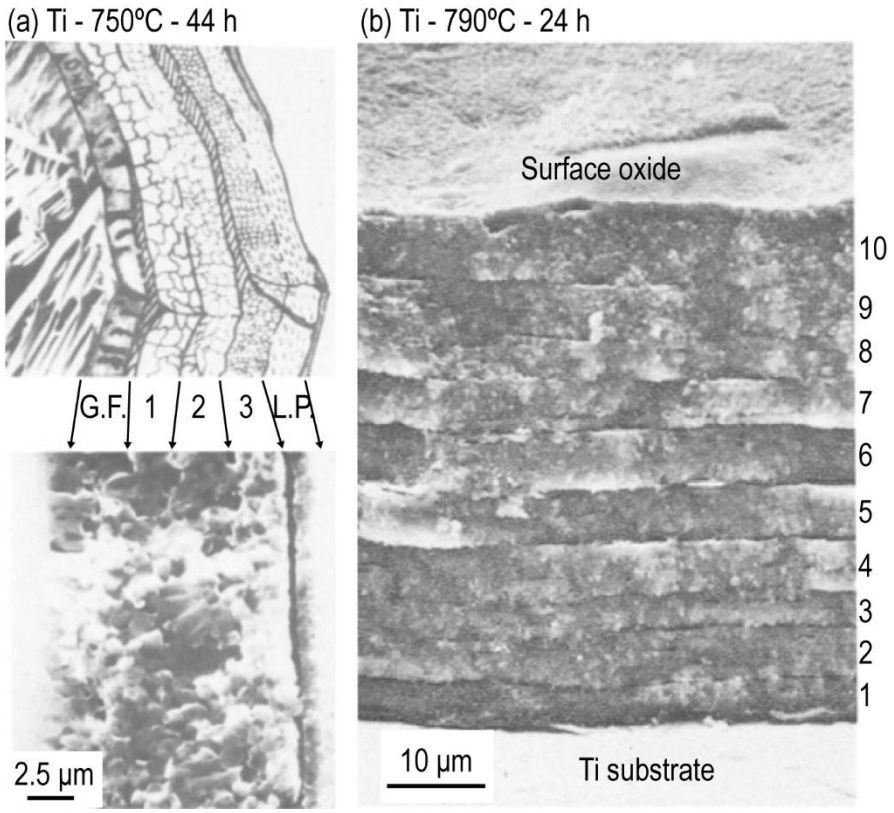

Figure 2.20. Examples of oxide morphology from titanium oxidation studies under (a) pure oxygen atmosphere [90] and (b) pO_2=105 Torr (~0.14 atm) [91]. G.F. stands for "growth features", numbers denote distinct oxide layers, and L.P. designates the oxide layer grown during the "linear period" of oxidation. Images from the cited sources and annotated by the author.

Bertrand et al. [91] proposed four different explanations for the oxide morphologies obtained:

1) Increase in stresses due to the Pilling-Bedworth ratio (PBR) of 1.75 associated to the formation of rutile from titanium (PBR values for all oxides are shown in Table 2.8). These compressive stresses would cause the oxide scale to separate from the metal, leaving a fresh titanium surface, which would then be oxidized. This process would repeat itself until many oxide layers form.

2) Oxygen dissolution into the metal leads to changes in titanium lattice parameters which lead to stress buildup and the detachment of a layer of Ti solid solution. This distinctive layer would subsequently be quickly oxidized.
3) If the scale is built up by titanium ion diffusion outwards then metal vacancies would be produced at the metal-oxide interface. After sufficient production of these vacancies, these interfacial vacancies could cluster and cause the periodic stripping of the metal – exposing a fresh metallic surface for oxidation.
4) Cooling of the oxidized specimens might contribute to additional stresses and stratification processes. However, it is unlikely that this would explain the repeated layers of oxide seen after oxidation.

Table 2.8. Pilling-Bedworth ratios for a subset of titanium oxides calculated assuming formation from hcp Ti. Values suggest compressive stress generation in all oxides since PBR > 1.

Oxide	Pilling-Bedworth ratio (PBR)
Ti_6O	1.02
Ti_3O	1.00
Ti_2O	1.04
TiO	1.22
Ti_2O_3	1.51
Ti_6O_7	1.39
TiO_2 (rutile)	1.78
TiO_2 (anatase)	1.99

Interestingly, the stratification of stable rutile layers seems to disappear with increasing temperature at which point a single compact scale is formed. These studies

provide supporting evidence to the oxidation mechanism proposed by Kofstad et. al [89] and further demonstrate the impact that experimental factors such as temperature, oxygen pressure, sample thickness and geometry, and thermomechanical history can have on the resulting microstructures and oxidation behavior in titanium.

Imbrie and Lagoudas [103] further supports the two rutile oxide scale structure, but adds that the porous inner layer seemed to have pore size be a function of distance from the metal-oxide interface.

2.4.2 Titanium oxidation in low partial pressures of oxygen

Oxidation studies for pure titanium in low partial pressures are more limited than those done in air due to their more relevant technical applications. The formation of titanium oxides other than rutile has been reported in oxidation studies in low partial pressures of oxygen at room temperature [104], where reactions are limited by the low temperature, and above 1300°C [92], where β-Ti forms and influences the oxidation process. Oviedo [104] reports the formation of thin oxide films (7 Å total thickness) primarily composed of TiO, but also showing the presence of TiO_2, Ti_2O_3, and Ti_3O_5 at pressures below 10^{-6} Torr (~10^{-9} atm). Kofstad [92] claims "all the oxides of titanium" (Ti_2O, TiO, Ti_2O_3, Ti_3O_5, and TiO_2) form when oxidizing at pressures below 10^{-3} Torr (~10^{-6} atm) O_2 and temperatures above 1300°C when titanium will have transformed into β. The phase identification relied on metallography and XRD so there is the possibility that phases were not properly identified using solely those techniques.

2.4.3 Growth stresses

In high-temperature oxidation of metals, stresses are known to generate within the oxide as it grows. These are referred to as growth stresses. When cations are mobile, as is the case in titanium oxidation, these growth stresses must relax so that contact is not lost between metal and scale and ion transport may continue. If the scale does not relax, voids may form at the metal-oxide interface and begin separating the oxide scale from the metal surface [93]. Growth stresses can arise from a variety of situations including volume differences between the initial metal and final oxide, compositional changes in alloy or scale, epitaxial stresses, and even geometry [93]. Most observations of the impact of stresses on titanium oxidation have remained qualitative and are usually ascribed to the large PBR value for titanium to rutile transformation which would result in a compressive stress in the oxide scale. Growth and thermal stresses manifest through delamination cracks in the oxide, separating oxide from metal, as well as plastic deformation in either substrate or oxide. To the author's knowledge there are no systematic studies on the stress evolution and associated mechanisms during titanium oxidation.

2.5 Nitrogen effect on titanium oxidation

Titanium oxidation studies that have used nitrogen-containing gas mixtures (e.g. 20%N_2-O_2) have reported a reduction in oxygen dissolution in the metal substrate, as well as decreased oxide formation from what is sometimes called the "nitrogen effect" [77,78,105–109]. While the exact mechanism for this effect is still debated, proposed hypotheses for the reduced oxidation are:

1. Reduced oxygen solubility resulting from nitrogen dissolution into the substrate [77,105–107].

2. Formation of a nitride layer between the substrate and oxide scales that acts as a diffusion barrier to oxygen ingress into the substrate [77,78,105–108].

In cases where there is rutile formation, nitrogen is believed to decrease the oxygen vacancy concentration in the rutile scale [105].

When comparing the results of oxidizing titanium and its alloys under different environments, it has become clear to the community that the presence of nitrogen in the oxidizing environment can have a significant impact on oxidation response. The main effects that have been observed are the decrease in oxidation rates when oxidizing in N_2-O_2 and the formation of a stable titanium nitride layer between the metal substrate and oxide scale which is believed to affect cation or anion transport. Göbel et al. [109] studied the oxidation of pure titanium at 800°C under dry and humidified Ar-20%O_2 and N_2-20%O_2 environments. In this case, the effect of nitrogen had a minimal impact on the kinetics as mass gain decreased only slightly. However, the oxide scale formed was significantly thinner in nitrogen-containing environments (120 μm vs 200 μm in the Ar-20%O_2) as seen in Figure 2.21.

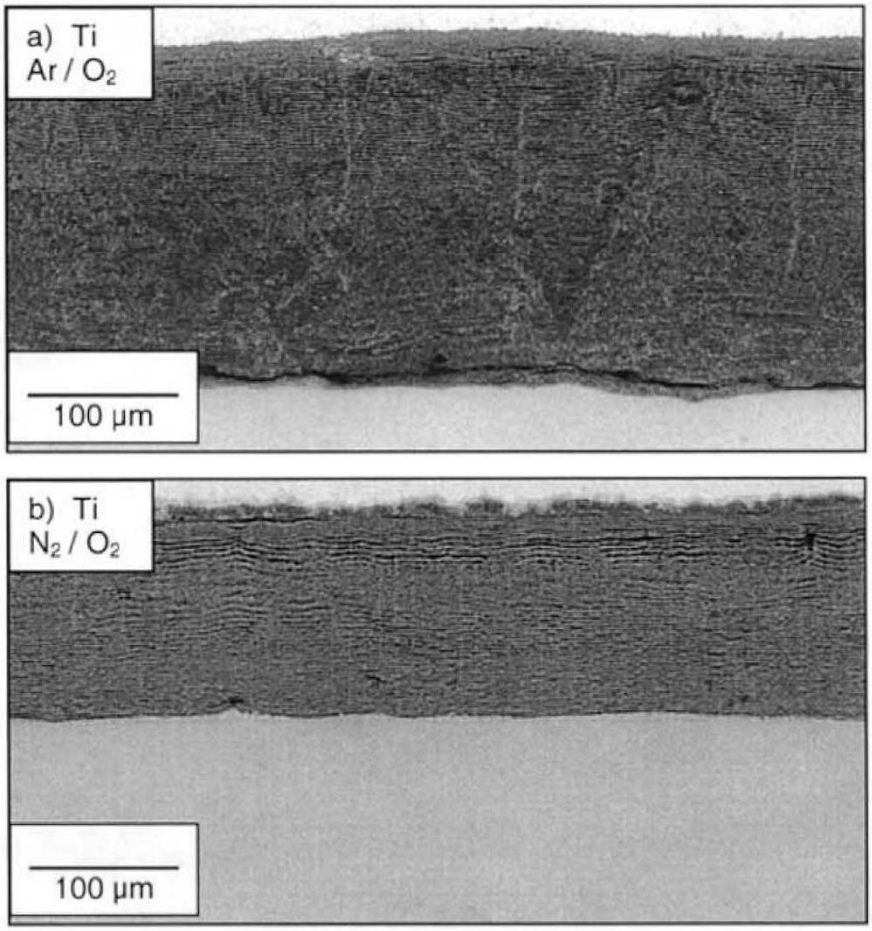

Figure 2.21. SEM cross-sectional micrographs of pure Ti oxidized at 800°C for 150 h under (a) Ar-20%O_2 and (b) N_2-20%O_2. Image from [109].

No continuous nitrogen-rich layer was found in any of the oxidation scenarios for titanium, although a thin scale of Ti_2N was found in the Ti-4Nb, an α-β alloy (Figure 2.22). Since microhardness diffusion profiles in titanium did not significantly change with environment, it was suggested that the nitrogen presence only affects the outer oxide growth without substantially influencing the inward oxygen diffusion process, although oxygen ingress greatly reduced in the Ti-4Nb specimen when exposed to Ar/N_2 gas [109].

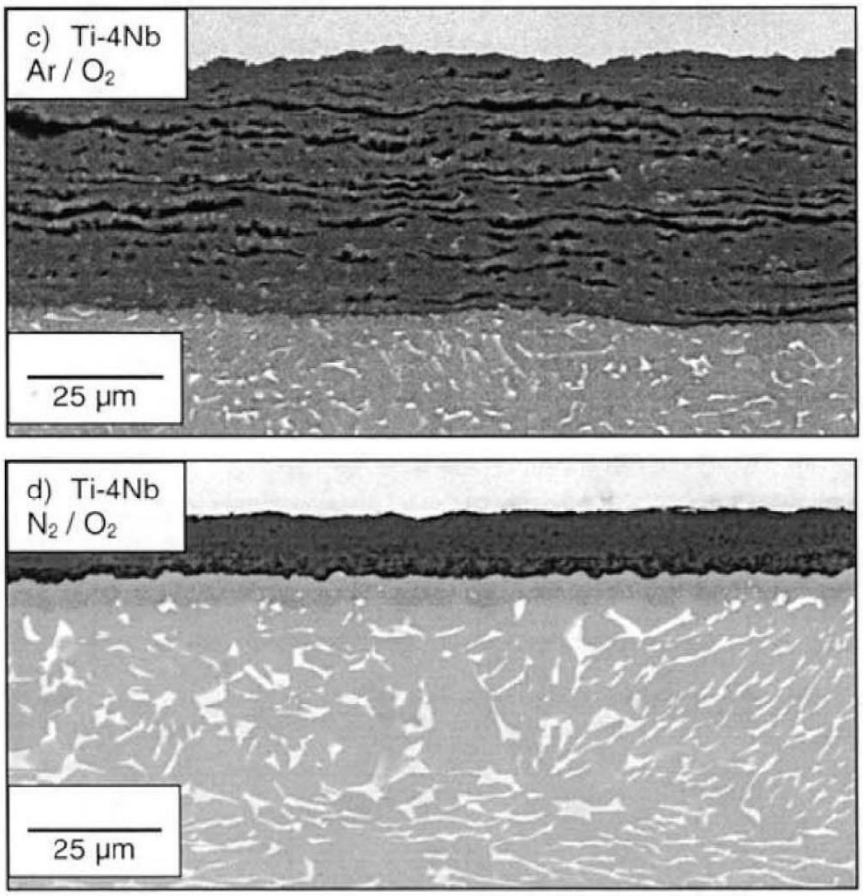

Figure 2.22. Cross-sectional SEM micrographs of Ti-4Nb oxidized at 800°C for 150 h under different gas environments. Figure from [109].

Hanrahan and Butt [110] studied Ti-Ta alloys of various concentrations of which the lowest was Ti-5Ta. While the paper does not specify initial alloy phase, this alloy is most likely in β phase since alloys were processed at 900°C at which Ti-5wt%Ta would be bcc [111]. In oxidizing this alloy at 800°C, oxidation rates and weight gains were lower in N_2-20%O_2 environments than in Ar-20%O_2. In nitrogen-containing environments, the formation of a nitride layer resulted in less oxygen dissolution into the metal (which they qualitatively interpreted from thinner α-phase layers underneath the metal-oxide interface). They proposed that nitride layers acted as diffusion barriers to oxygen dissolving into the substrate but did not impede the outward diffusion of metal ions which might continue oxide formation or

growth. Throughout the studies of the different alloys, both Ti_2N and TiN were identified and proposed to have similar effects to the titanium oxidation response. Additionally, scale adhesion seemed to improve in nitrogen-containing environments than in pure oxygen or argon-oxygen mixtures.

Extending into more complex alloys, oxidation of titanium alloys in nitrogen-containing environments have also shown the formation of titanium nitride layers at the alloy-oxide interface [78,112]. These nitrides are not always continuous layers, but all seem to act as an oxygen-diffusion barrier when formed as a dense, continuous layer. A more recent study [78] has identified Ti_2N, TiN, and TiN_xO_y as reaction products from oxidation of a Ti-2642-S alloy in synthetic air. Since this study relied on EELS and these layers were 10-30 nm thick, it is possible (and perhaps even likely) that previous oxidation studies have not properly observed nor identified the phases of the nitrogen-containing layers in the past. While the alloy-oxide interface looked different depending on the environment used, the oxide scale itself seemed to retain similar morphologies regardless of nitrogen presence in the oxidizing environment. In this study, the nitrogen-containing layers were also observed to decrease oxygen dissolution into the alloy.

2.6 Titanium nitriding

When looking at the Ellingham diagram as an initial reference point (Figure 2.23), the equilibrium partial pressures required for oxide and nitride formation are both extremely low

suggesting that they can readily form even at relatively low partial pressures of N_2 and O_2.

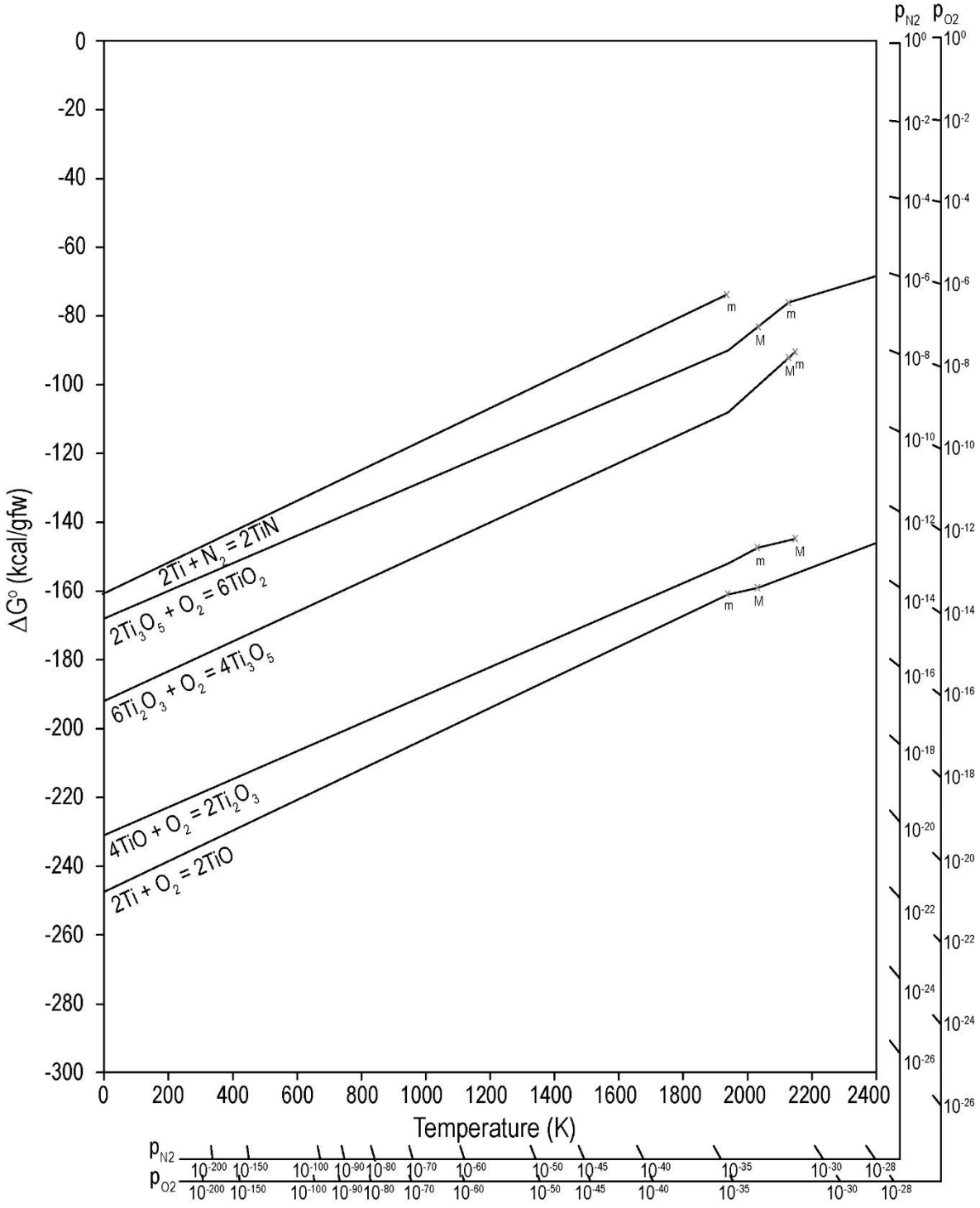

Figure 2.23. Ellingham diagram for various Ti nitriding and oxidation reactions. Adapted from reference Ellingham diagrams [88].

Titanium nitriding is typically used to improve the surface properties of titanium alloys by depositing titanium nitrides or nitriding the surface via gas nitriding, plasma nitriding, laser nitriding, or ion nitriding [113–115]. A thorough review of nitriding titanium alloys can be found in Zhecheva et al.'s article [114]. The process of nitriding titanium is dominated by inward N diffusion and the formation of Ti_2N and TiN, as well as of a solid solution of hcp Ti with dissolved N (Figure 2.24). Given the fewer nitride phases available compared to Ti oxides, the resulting microstructures are much simpler than those of titanium oxidation, but the high solubility of nitrogen continues to occur simultaneously to the nitride formation and growth as in the case of Ti oxidation.

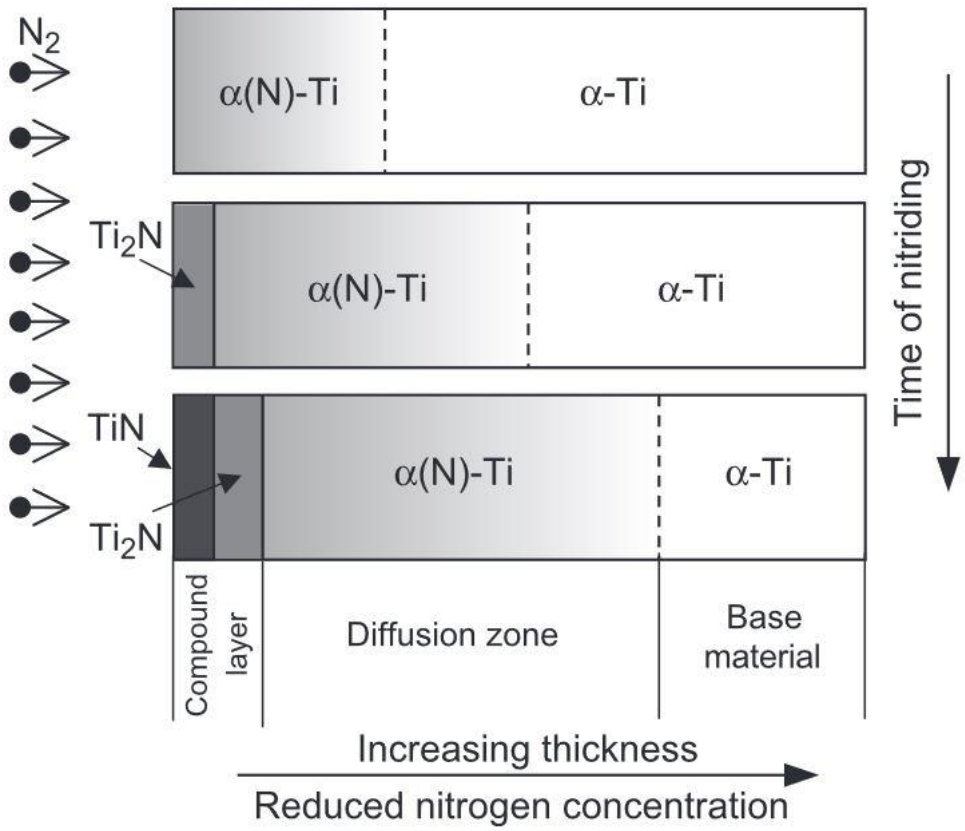

Figure 2.24. Schematic showing the formation and growth of nitride layers during titanium nitriding from [114] adapted from [116].

When calculating the Pilling-Bedworth ratios for nitride formation, the values suggest compressive stress generation since Ti_2N and TiN show a PBR of 1.06 and 1.07 respectively. These are slightly higher PBR values than that of the hcp-based suboxide Ti_2O (PBR = 1.04) shown in Table 2.8.

Table 2.9. Pilling-Bedworth ratios for a subset of titanium nitrides calculated assuming formation from hcp Ti. Values suggest compressive stress generation in both nitrides since PBR > 1.

Nitride	Pilling-Bedworth ratio (PBR)
ε-Ti_2N	1.06
TiN	1.07

2.7 Titanium oxynitride formation

Titanium oxynitrides, as noted before, have been observed in titanium oxidation studies using nitrogen-containing environments [78] and in two-step oxynitriding studies [79]. A predominance diagram at 650°C was calculated using ThermoCalc and provides useful information regarding which phases are expected to be thermodynamically stable at various partial pressures of oxygen and nitrogen (Figure 2.25). In higher partial pressures of nitrogen than oxygen, the expected structure would be a α-Ti (O,N) solid solution with layers of Ti_2N, the fcc oxynitride phase, some of the lower oxides (depending on the partial pressures used), and the outermost scale would be composed of rutile. With higher partial pressures of oxygen than nitrogen, no nitride phases would be expected to form and the resulting microstructure would be composed of various oxide layers with different compositions and crystal structures.

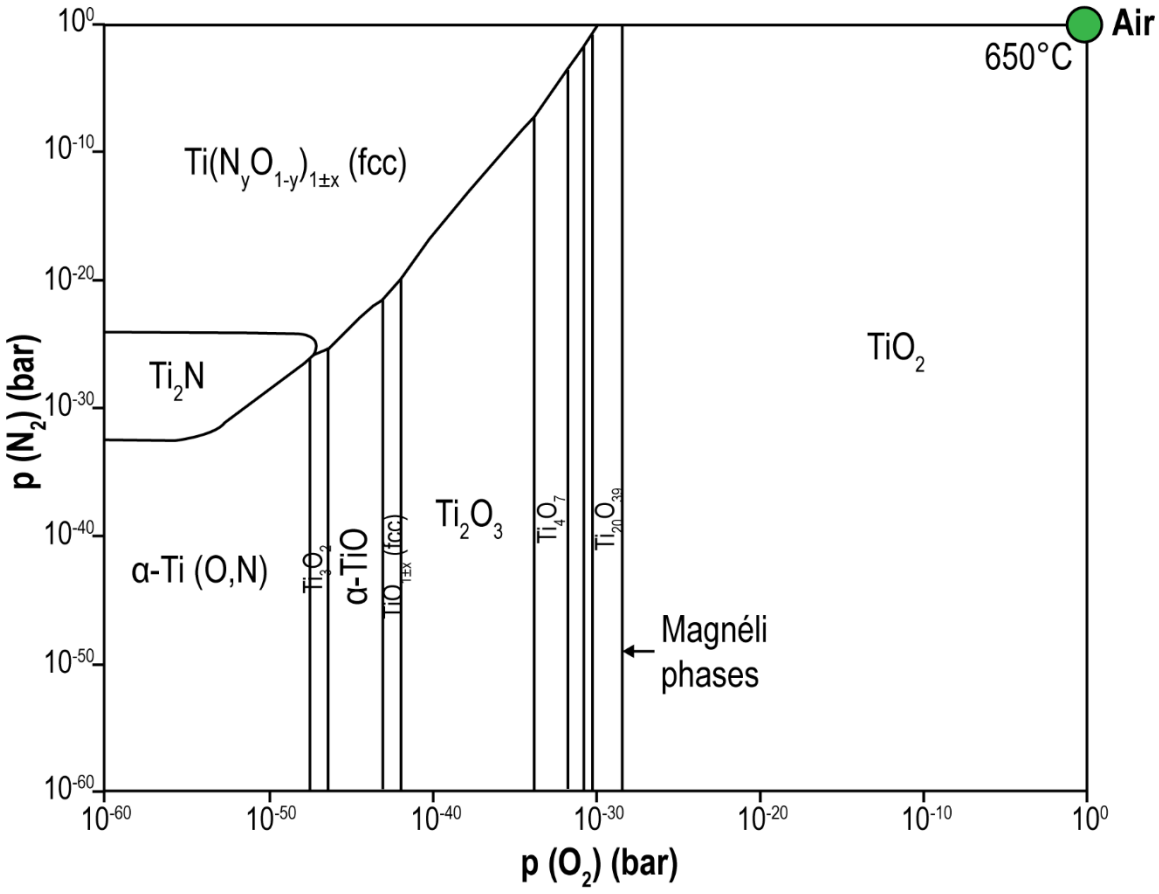

Figure 2.25. Predominance diagram showing which phases would be favored to form under various partial pressures of nitrogen and oxygen. The green circle in the top right corner shows the position for partial pressures in air. Adapted from Dupressoire et al.'s [77] diagram calculated using ThermoCalc and the TCTI1 database.

In understanding the mechanisms of oxynitride formation, however, most of the studies rely on oxidizing titanium nitrides. In general, these microstructures form layered rutile scales and a thin gray film suspected to contain TiN_xO_y, TiO, Ti_2O_3, Magnéli phases, and substoichiometric rutile [117]. No sufficient characterization was provided for these phase identifications, but the thin gray film showed poor adhesion and was proposed to contribute to the periodic exfoliation of the oxide scales. The mechanism of formation is represented in Figure 2.26.

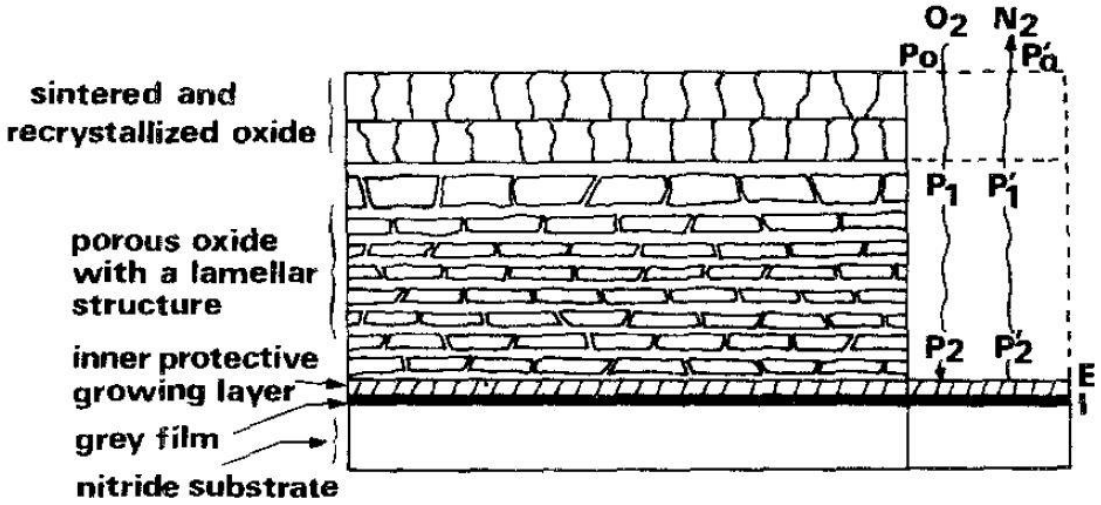

Figure 2.26. Mechanism of TiN_x oxidation from reacting TiN_x in low partial pressures of oxygen. Figure from [117].

More recent studies identify the formation of a mixed oxynitride/oxide layer with two different species of oxynitride from XPS analysis [118]. Other studies only identify rutile as a reaction product when reacting in air above 700°C [119]. Notably, the researchers from this work noted that the process was dominated by inward oxidation and that the porosity they observed in the scales could have occurred from nitrogen release during the oxidation process.

2.8 Tweed structures in titanium alloys

Tweed contrast, or microstructures, is part of a set of features referred to as "pre-martensitic effects" which have been observed in a variety of alloy systems. Tweed or tweed-like microstructures appear in materials systems that undergo ordering transformation, spinodal decomposition, GP zone formation, ω-phase (hcp) formation, or martensitic transformations [120]. The formal definition of tweeding was proposed by Robertson and Wayman [120] building on Laughlin et al.'s [121] initial definition and described tweed as "linear variations of contrast which lie nearly parallel to the traces of {110} planes in a

nominally cubic solid solution, and which obey extinction rules consistent with shear displacements on {110} planes in $< 1\bar{1}0 >$ directions" with minor modifications applied to non-cubic systems. The microstructure and schematic highlighting the striations along the {110} planes in a cubic β-NiAl material is shown in Figure 2.27.

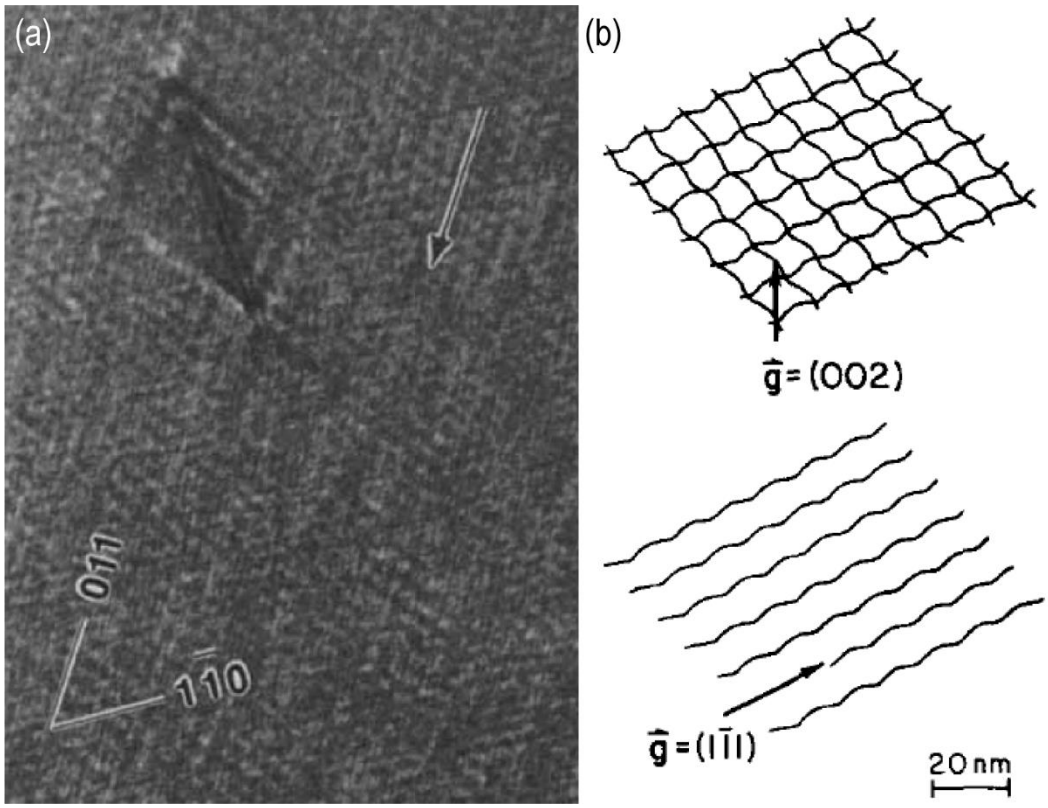

Figure 2.27. (a) Bright-field image of a tweed microstructure in β-NiAl with striations parallel to the designated traces of (011) and (0$\bar{1}$1) planes. Adapted from [120]. (b) Schematic of <110> tweed microstructures showing a [110] zone axis of an fcc material. Adapted from [121].

The origin of these tweed microstructures has been attributed to the formation of precipitates or laths along elastically soft directions (sometimes coinciding with the orientations of twin boundaries) [122,123], as well as to decomposition of a solid solution phase [124,125], GP zone formations [126], or strain-type transitions [127–129].

In titanium alloys in particular, tweed microstructures are observed in shape memory alloys [128] as well as in TiNb and TiNi alloys with O additions [130–133]. The addition of

an interstitial alloying element results in the appearance of strain nanodomains which enable the formation of tweed microstructures instead of a forward martensitic transformation. In β metastable titanium alloys, striations forming a tweed-like structure were determined to form from two distinct intermediate structures forming in the β phase between that of the expected β, α, or ω phases by atomic displacements distorting the $\{110\}_\beta$ and $\{112\}_\beta$ planes [134].

2.9 Raman studies of titanium oxides and nitrides

Raman spectroscopy is a non-destructive technique based on the interaction of light and the chemical bonds of a material that can give information on chemical structure, crystallinity, stress state, and phases. In the Ti-O system, Raman has been used primarily to distinguish between polymorphs of titanium dioxide: anatase, rutile, and brookite during electrochemical synthesis [135], in heat-treated nanophase titanium dioxide [136], in hydrothermal treatments of titania nanotubes [137], and in titanium oxidized using an oxygen plasma treatment [138]. While the Raman spectrum of Ti_2O_3 is known [135], the spectra of lower titanium oxides are not readily available in databases or literature with the exception of Magnéli phases [139]. Since rutile is the main oxidation product of titanium, the Raman modes and corresponding Raman shifts are shown in Table 2.10.

Table 2.10. Raman modes of rutile and reported Raman shifts from literature.

Assigned mode	Ekoi et al. (cm^{-1})	Ma et al. (cm^{-1})	Arsov et al. (cm^{-1})
B_{1g}	143.2	140.2	143
Multi-phonon process	232.4	235.5	236
E_g	446.6	445.8	447
A_{1g}	609.8	609.8	612
B_{2g}	-	825.5	826

Rutile has four Raman active modes: B_{1g}, E_g, A_{1g}, and B_{2g} (Figure 2.28 for spectra and Figure 2.29 for physical meaning of each active mode). The first three modes are mainly associated with the symmetric stretching vibration, symmetric bending vibration, and the anti-symmetric bending vibration of the O-Ti-O bonds, respectively [140,141]. In addition to these four bands, rutile shows a broad peak around 232 cm^{-1} referred to as second-order scattering [142] which is a result of multi-phonon scattering. Ekoi's study [138] showed the formation of lower Ti oxides from XRD analysis, but only rutile was observed from Raman spectroscopy. However, the E_g and A_{1g} bands of this spectrum were shown to be affected by experimental parameters such as input power, chamber pressure, and crystallite size. E_g has also been shown to be sensitive to oxygen deficiency within rutile [136]. During in situ Raman using heat, Raman bands have been noted to shift to lower frequencies with increasing temperatures [143].

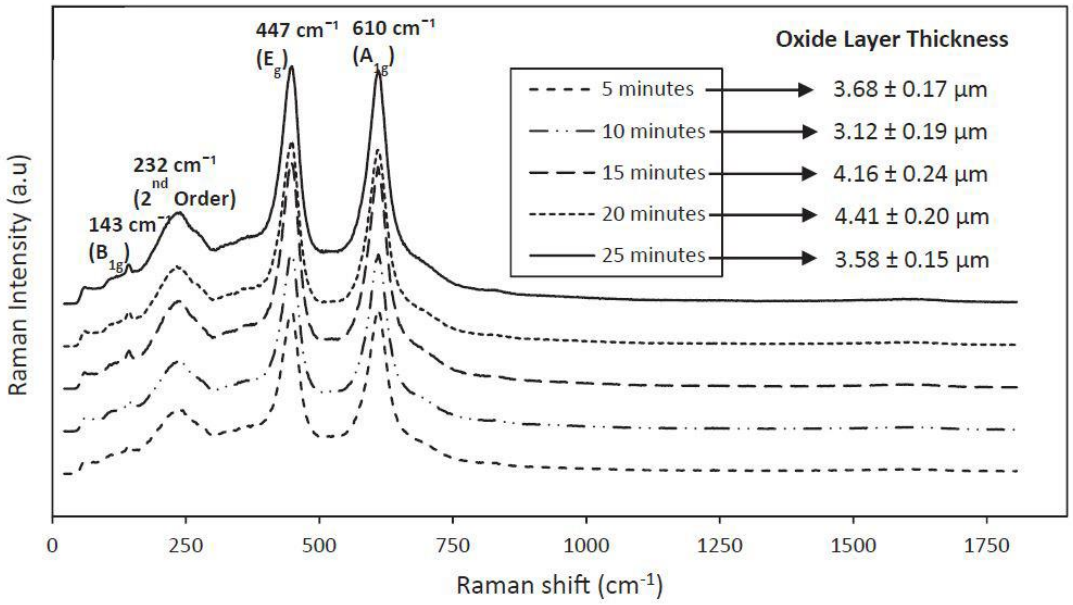

Figure 2.28. Raman spectra of rutile with increasing oxidation time from Ekoi et al. [138].

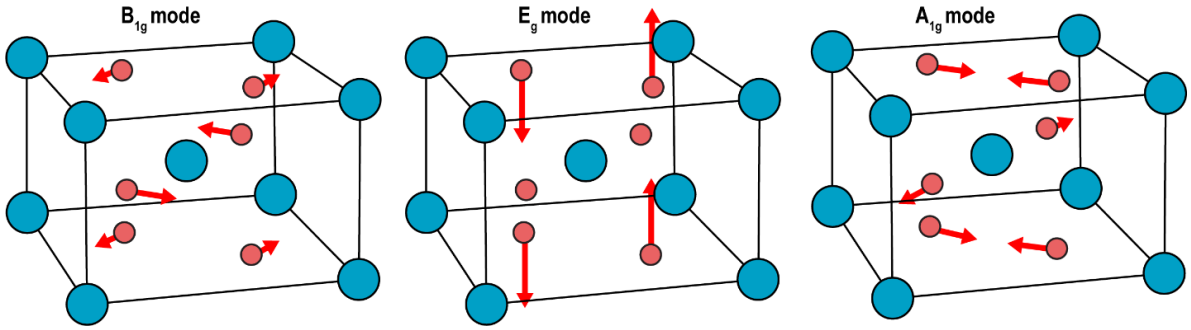

Figure 2.29. Rutile crystal structures showing oxygen motion associated with the Raman modes. Adapted from [144].

When using Raman spectroscopy for titanium nitrides, only TiN is reported in literature at stoichiometric and non-stoichiometric compositions [145,146]. The peaks in the TiN Raman spectrum (Figure 2.30) are not as clearly defined as those in rutile.

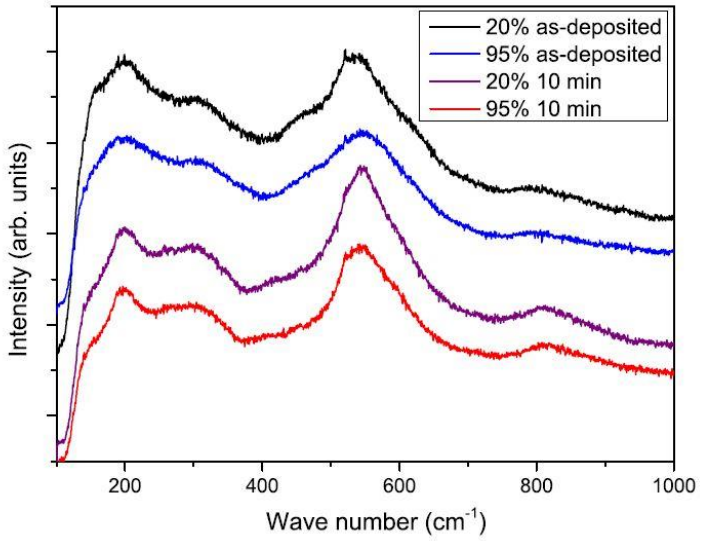

Figure 2.30. Raman spectra of TiN_x deposited at 20% or 95% nitrogen flow rate shown as-deposited and after 10 min of annealing at 700°C. Figure from [146].

2.10 Problem statement and research approach

As the previous review illustrates, there are many issues that complicate the understanding of titanium reactions with nitrogen and oxygen. Due to the reactivity of titanium and the experimental challenges associated with understanding the interactions of light elements with titanium, this research aimed to integrate computational predictions [5,8,147] and experimental work to determine which phases form during titanium exposure to nitrogen and oxygen and the mechanisms by which they form.

The objective of this research is to carefully investigate the reactions of titanium with nitrogen and oxygen at high temperature through ex situ and in situ reaction studies where (a) interstitial content is limited in the reacting gas environments, (b) titanium remains in the hcp α phase, and (c) multiscale characterization is done to identify the developed phases. In studying the microstructural evolution of these specimens, the phase stability will be

explored in three gases with varying O_2:N_2 ratios that have not been traditionally used in previous oxidation or oxynitridation studies.

The fundamental scientific contributions from this research in defining the phase stability and microstructural evolution in titanium reacting with nitrogen and oxygen at high temperature are expected to improve guidelines to develop strategies for improved oxidation resistance such as coating or alloy development. A secondary benefit would be in providing additional considerations for future interstitial interaction studies of materials with significant interstitial solubility such as the emerging complex concentrated alloys (CCAs) based on refractory metals.

3 Experimental Methods

Nominally pure titanium specimens from a plate and foil were exposed to three distinct Ar-based environments with low partial pressures of N_2 and O_2 to identify phase stability and elucidate microstructural evolution. Two different furnace configurations were used, one of which allowed for in situ monitoring of the scale evolution using Raman spectroscopy. The experimental methods for these reaction studies of titanium with nitrogen and oxygen and relevant characterization techniques are detailed below.

3.1 Experimental challenges

Before elaborating on the methodology used for this research project, it is important to acknowledge the experimental challenges inherent to the titanium-nitrogen-oxygen system which complicate the understanding of titanium reactions with interstitials. The most critical challenge is the significant oxygen and nitrogen dissolution into the metal preceding and concurrent with oxide or nitride formation and growth. This high solubility of interstitials makes it difficult to isolate the effects of scale formation vs interstitial dissolution, though efforts have been previously made to address this issue [109]. In terms of identifying the phases produced during these reaction studies, there are two significant challenges in studying the titanium-nitrogen-oxygen system:

1. Difficulty in quantifying oxygen and nitrogen content within oxide scales through conventional techniques such as X-ray energy dispersive spectroscopy (EDS) due to significant reabsorption into the substrate of low energy X-rays generated by interstitials [148].

2. Similarities between the crystal structures of the many thermodynamically stable and metastable titanium oxides, nitrides, and oxynitrides [4,7,8,77] that impact the effectiveness of diffraction analysis.

Titanium has also been reported to have an extreme sensitivity to experimental parameters such as initial material purity, thermomechanical history, exposure to different environments, and surface preparation [39]. This has made it difficult to consolidate findings from various titanium oxidation studies over the years since the changes in conditions greatly impact what would be considered the "true" oxidation mechanism inherent to pure titanium metal. In practice, truly pure titanium is not achievable since it will always have varying amounts of oxygen, nitrogen, carbon, and hydrogen – all of which alter its performance and properties[2].

An unexpected but significant challenge encountered in this project is the impact of nitrogen on the oxidation behavior and phase formation in titanium. While care was taken to minimize oxygen and other interstitial contents in the gas environments used, the ppm levels of nitrogen present in the argon and gettered argon used were sufficient to react with the titanium metal and form nitrogen-containing layers. The investigation thus shifted from studying titanium oxidation exclusively to studying titanium interactions with nitrogen and oxygen at high temperature.

[2] A note on hydrogen: While inert gas fusion is able to detect and quantify hydrogen in the bulk titanium pieces used (Table 3.1), the techniques used to analyze the resulting microstructures in this study do not allow for hydrogen analysis. SIMS was attempted to address this issue, but results were inconclusive due to the possibility of hydrogen, carbon, nitrogen, and oxygen all reacting with titanium metal. Although this thesis focused on nitrogen and oxygen, both hydrogen and carbon could potentially also play a role in the titanium reactions and merit further study with the appropriate techniques.

3.2 Materials and specimen preparation

3.2.1 Titanium preparation

A commercially pure (99.999% metals basis) titanium plate, 100 mm x 100 mm x 3.175 mm thickness, was purchased from Alfa Aesar (Ward Hill, MA) and sectioned into 12.7 x 12.7 mm squares using electrical discharge machining (EDM). The chemical compositions measured by inert gas fusion of this Ti metal and alloys made for this research project are shown in Table 3.1.

Table 3.1. Chemical composition for titanium used for oxidation studies.[3]

Metal	Al	Nb	H (ppm)	C (ppm)	N (ppm)	O (ppm)	Ti
Ti plate	< 50 ppm	< 100 ppm	9	< 20	< 20	160	Bal
Ti foil	-	-	-	40	60	700	99.95%

The individual Ti squares were subsequently ground with 320 grit SiC paper, polished with a 9 μm diamond solution, and chemomechanically polished with a 30% H_2O_2 – colloidal silica solution following the standard Ti 3-step polishing method [149] to achieve an appropriate finished surface for reaction experiments. Samples were rinsed with distilled water between each step and cleaned ultrasonically in isopropyl alcohol for ten minutes after the final polishing step.

For in situ reaction experiments, which will be described later, the mass of the specimen was restricted to 76.5 milligrams and the height of the specimen was not to exceed 3.4 mm due to size constraints from the heating stage. Titanium foils (4 mm x 4 mm x 50 μm

[3] Titanium foil composition given is from the certificate of analysis provided by Alfa Aesar. Remaining compositions are from inert gas fusion of specimens conducted by ATI Specialty Alloys and Components. Values in ppm are denoted by weight basis.

thickness) were used to fit these heating stage specifications. These specimens were polished only with 1 μm diamond slurry to avoid significant loss of thickness. The diamond slurry was sufficient to provide a polished surface adequate for Raman spectroscopy. The chemical compositions of both Ti plate pieces and Ti foil are detailed in Table 3.1.

3.3 Exposure procedures for reaction studies

Polished titanium specimens were exposed to gas environments with different N_2:O_2 ratios with an aim to study the phase stability of nitride, oxynitride, and oxides, as well as to understand the microstructural evolution during these reactions. The major steps of the experimental procedure are summarized in Figure 3.1.

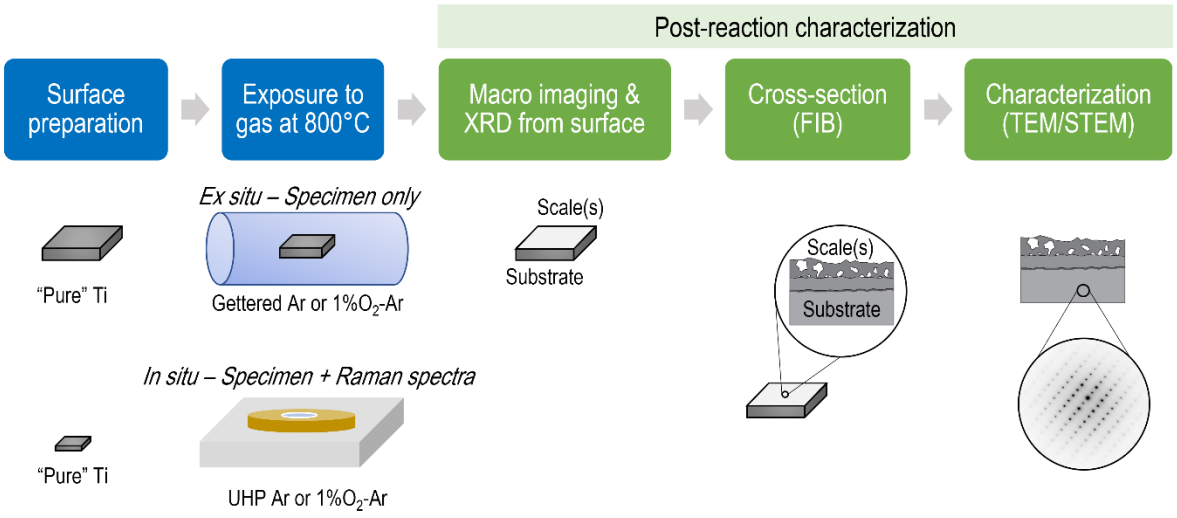

Figure 3.1. Summary of experimental procedure for ex situ and in situ reaction studies and relevant characterization of developed scales post-treatment. The ex situ and in situ setups are shown in more detail in Figure 3.2 and Figure 3.5 respectively. Post-reaction characterization steps apply to specimens from both types of reaction studies.

3.3.1 Ex situ experiments in tube furnace using low partial pressures of oxygen

Polished and clean titanium substrates were placed on a flat alumina boat, separated by a Ta foil to avoid interactions, and loaded into a tube furnace (CM Furnaces, Bloomfield, NJ) with a 76 mm diameter fused silica tube (Figure 3.2).

Figure 3.2. Tube furnace setup for ex situ furnace experiments.

The specimen setup, illustrated in Figure 3.3, was then attached to a set of alumina tubes that enabled insertion and extraction into the stabilized hot zone.

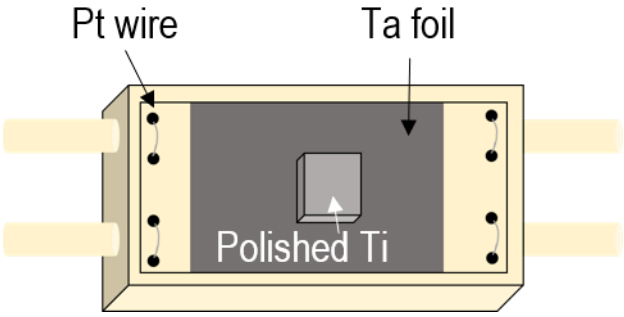

Figure 3.3. Setup for specimen holder on tube furnace using a dense alumina crucible tied onto alumina rods with platinum wire.

The tube furnace was then sealed, evacuated, and flushed with gettered argon gas until oxygen content in the environment reached at least 10^{-10} ppm O_2. Oxygen values were read from an oxygen analyzer with a solid state zirconia (ZrO_2) sensor (Model 2A by Centorr Vacuum Industries, Nashua, NH). Titanium chips were used as a gettering agent to purify the argon gas. The tube furnace was heated to the temperature of interest (800°C) and the specimen was inserted into the hot zone once the temperature and environment stabilized. This was done manually using a push-rod holding the alumina tube supports, sealed through an appropriate feedthrough. Specimens were cooled by ejecting the specimen from the hot zone over two minutes to avoid severe spallation and leaving to cool in a gettered argon flow

parallel to the loading direction (hereafter “fast-cooled in parallel Ar flow”). Once the specimen cooled, the argon flow was shut off and the specimen retrieved for microstructural characterization.

Another configuration used involved a gettered Ar flow counter to the loading direction. These specimens were slow-cooled (~10°C/min cooling rate based on furnace temperature over time) by leaving the specimen in the hot zone after the desired dwell time and cooling in the flowing Ar (hereafter “slow-cooled in counter Ar flow”). When using a 1%O_2-Ar gas for ex situ studies, the flow used was a parallel flow and the specimens were fast-cooled (as close as possible to a quench given the furnace setup[4]) as described for the “fast-cooled in parallel Ar flow” setup. These specimens generated by any of these configurations will be referred to as having been produced via “ex situ” furnace studies. The furnace setup with the two relevant gas flow directions discussed is shown in Figure 3.4.

[4] Since the specimen was ejected from the hot zone at 800°C over 2 minutes, an approximate cooling rate would be ~250°C if it is assumed that the Ti specimen cools to 300°C at the end of those 2 minutes of ejection. The actual temperatures are not known since thermocouples were not installed near the Ti specimen to avoid potential contamination from the thermocouple wires.

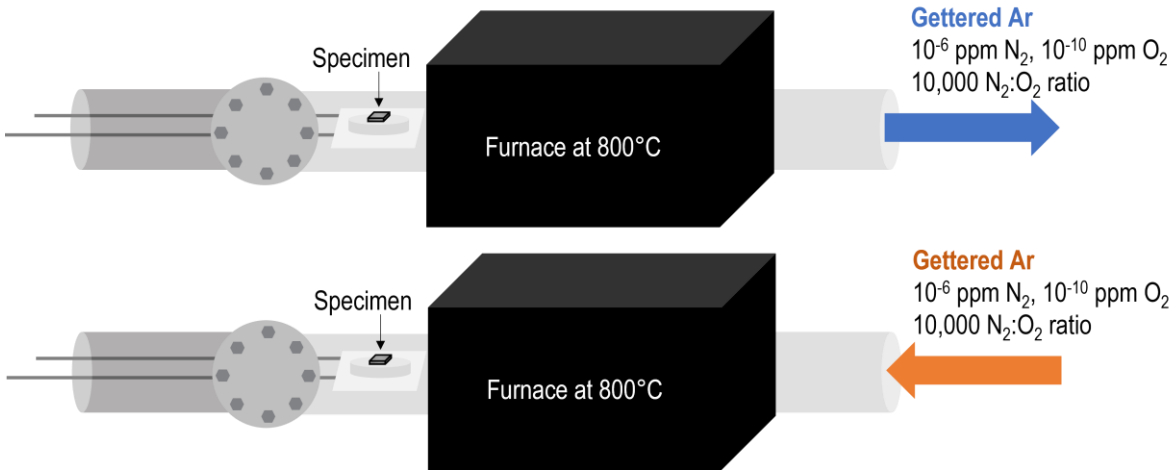

Figure 3.4. Furnace setup used for "ex situ" studies showing the (top) "fast-cooled in parallel Ar" setup and the (bottom) "slow-cooled in counter Ar" setup. Note the arrow indicating opposite Ar flow directions.

3.3.2 In situ experiments using Raman spectroscopy

"In situ" experiments were conducted using a Linkam TS1500 heating stage under a Raman spectrometer Horiba Jobin Yvon T64000 open-frame confocal microscope with a triple monochromator, liquid nitrogen-cooled CCD array detector, and a laser of 488 nm (Ar+ source). The setup for the heating stage, microscope, and laser configuration is shown in Figure 3.5.

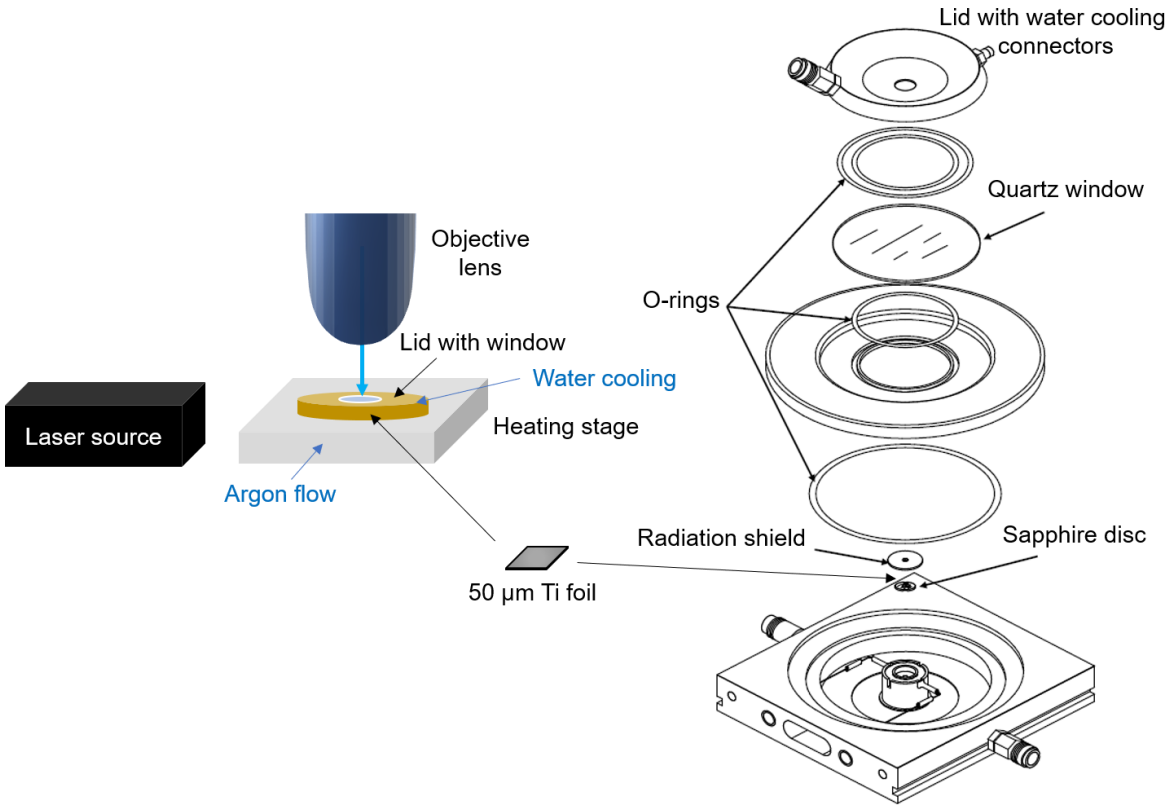

Figure 3.5. Setup for in situ Raman spectroscopy studies using Linkam TS1500 heating stage. Diagram on the right taken from the Linkam TS1500 user manual.

The polished titanium foils were placed on top of a sapphire disk inside the ceramic crucible of the heating stage. There was no evidence of reaction between the metal and the sapphire base. The ceramic crucible was covered with a radiation shield (an alumina disk with a small hole in the center to allow for viewing) and the stage's chamber was sealed with its lid. The stage was then carefully moved under the microscope's optical lens. An ultra-high purity argon tank (AirGas, 1 ppm O_2, 5 ppm N_2) or a 1%O_2-Ar mixture were used to establish the reacting environment within the chamber using a continuous flow of 25 mL/min. This flow was selected to avoid overworking the heating elements and to prevent the specimen from moving significantly during the reaction. A water-cooling system was used to maintain the stage cool to the touch.

Once the gas environment and water-cooling systems were stabilized, the stage was moved to allow for viewing of the specimen through the stage's lid and radiation shield. After focusing the sample via the optical microscope, the stage was programmed with the desired heating schedule. Using LabSpec6, a Raman spectroscopy software, spectra were taken every five minutes using a 488 nm laser line and 5s acquisitions. Due to the design of the heating stage, specimens could not be inserted at temperature and had to be heated along with the stage before reaching the desired dwell temperature. Similarly, the cooling was done either by programming a desired cooling rate, or by "fast-cooling" when shutting off the heating stage after the desired dwell time (~125°C/min cooling rate based on the heating stage temperature). Since an optical microscope is attached, optical images were taken between Raman spectra acquisition to record coloration changes on the surface during heating, dwell, and cooling stages of each experiment. An example of the most used heating profile for in situ studies is shown in Figure 3.6. For other dwell times, the same heating and cooling rates were used.

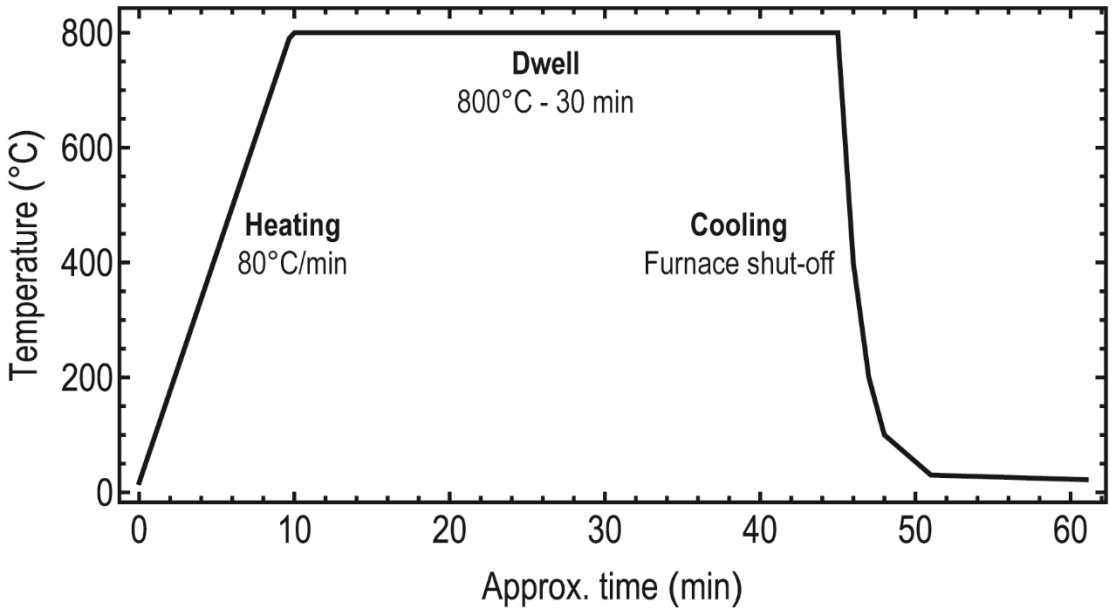

Figure 3.6. Example of heating profile for in situ studies done in the Linkam TS1500 stage.

Due to the thermal expansion associated with the heating process and potential stresses and scale growth induced by oxidation, the microscope stage holding the heating stage and specimen had to be adjusted periodically to ensure the microscope was focused on the surface. Given the 488 nm wavelength from the laser, the depth of penetration into the specimen for Raman acquisition can range from 761 nm to 3.2 μm. This allows for the detection of phases developing underneath the surface given these have Raman active modes. Failure to adjust the focus before acquiring a spectrum resulted in erroneous intensities that could lead to misinterpretation of the oxide evolution. While the intensities cannot be interpreted properly without focus adjustment, qualitative analysis of which Raman modes appear are still valid. Qualitatively, the heating and dwell stages show similar trends in both methods, but the spectra from cooling are significantly different in the intensities of the rutile peaks when not adjusting the focus on the specimen surface properly.

After exposure to the desired environment, Raman shifts in the experimental spectra were adjusted using a silicon piece as reference by adjusting the Raman shift of the post-reaction foil spectra by the value needed to center the silicon peak at 521 cm^{-1}. This was done to ensure consistency in the Raman shifts between experiments.

A summary of the interstitial contents in the gas environments for ex situ and in situ studies is given in Table 3.2. The oxygen content from the gettered Ar was analyzed using an oxygen analyzer attached to the gettering furnace. Given the lack of a nitrogen analyzer in the lab, the nitrogen content given in the table relies on values given from analysis provided by the gas suppliers. In the case of gettered Ar, the oxygen values were consistently 10^{-10} ppm O_2 or lower. At 800°C and using titanium chips as a gettering agent, the manufacturer (Centorr Industries) specified the oxygen and nitrogen content in the gettered Ar gas could

reach values of 10^{-10} ppm O_2 and 10^{-6} ppm N_2. Since the oxygen values reached that ideal scenario, the nitrogen content in the gettered Ar gas was assumed to be close to that specified by the gettering furnace manual.

Table 3.2. Nitrogen and oxygen contents for the three different gas environments used in oxidation studies. Oxygen content for gettered Ar was measured using an oxygen analyzer while the nitrogen content was inferred from the gettering furnace and oxygen analyzer manual based on the experimental setup used. Oxygen and nitrogen values for UHP and 1%O_2-Ar gases were obtained from the supplier (AirGas).

Gas environment	Oxygen content (ppm)	Nitrogen content (ppm)	O:N ratio	pO_2 (Pa)	Used in reaction studies
Gettered argon	10^{-10}	10^{-6}	0.0001	10^{-11}	Ex situ
Ultra high purity (UHP) argon	1	5	0.2	0.1	In situ
1%O_2-Ar	10^4	5	2000	1000	Ex situ + in situ

3.4 Microstructural characterization

3.4.1 Specimen preparation post-reaction studies

After exposure to the controlled environments, specimens were photographed using a Nikon camera to document color and general appearance of the surface. X-ray diffraction was performed on the surface of the entire specimen to determine which phases might be present throughout the developed scale. Once these two steps were completed, the "reacted specimens" (referring to specimens that were exposed to any of the gas environments) were mounted in aluminum stubs and sputtered with gold/palladium for scanning electron microscopy. Due to the delicate nature and small thicknesses (typically <2 μm per layer) of

the produced scales, cross-sections were avoided and direct focused ion beam (FIB) liftouts from the surface were favored to best analyze the resulting microstructures.

3.4.2 X-ray diffraction of reacted surfaces

Using a Cu-Kα beam, X-ray diffraction (XRD, Philips XPERT) was performed on the reacted specimens in the range $14° \leq 2\theta \leq 90°$. This provided preliminary information for phase identification throughout the scales and into the metallic substrate below. Phase identification was performed using the PANalytical X'Pert High Score software, or comparing the experimental patterns to those from phases in the Inorganic Crystal Structure Database and CIF files from first-principles calculations from N.S. Harsha Gunda et al. [5,8], converted to XRD patterns in VESTA [150].

Lattice parameter changes from XRD patterns were calculated using Bragg's equation to determine the interplanar spacing of a crystal:

$$2d\sin\theta = n\lambda$$

where d is the interplanar spacing, θ is the glancing angle of incidence, n is the diffraction order, and λ is the wavelength (Cu-Kα for the X-ray diffractometer used).

For the hexagonal crystal structure (relevant to hcp Ti peaks), the interplanar spacings from Bragg's equation can be used to determine the lattice parameters with the following equation:

$$\frac{1}{d^2} = \frac{4}{3}\left(\frac{h^2 + hk + k^2}{a^2}\right) + \frac{l^2}{c^2}$$

For the tetragonal crystal structure (relevant to rutile TiO_2 and ε-Ti_2N peaks):

$$\frac{1}{d^2} = \frac{h^2 + k^2}{a^2} + \frac{l^2}{c^2}$$

Using the known plane indices and the calculated d value from the peak of interest's 2θ angle and the wavelength λ from the X-ray incident beam (1.54 Å), the lattice parameters can be calculated and compared to their initial values. The changes calculated can show whether there has been an expansion or contraction of the lattice along a particular axis. In this system, for example, expansion along the c-axis of hcp Ti is expected when incorporating interstitials into the lattice.

3.4.3 Scanning electron microscopy of reacted surfaces and cross-sections

Reacted specimens were sputtered using a gold/palladium mixture to prevent drift of the specimen during imaging. Specimens were imaged using an FEI XL30 Sirion FEG Digital Electron Scanning Microscope (ThermoFisher Scientific, Hillsboro, OR), an FEI Nova Nano 650 FEG SEM, and a ThemoFisher Apreo C LoVac FEG SEM using secondary electrons for surface morphology analysis and backscattered electrons for elemental and diffraction contrast. Imaging of the surface was typically conducted at 10 kV.

3.4.4 Transmission electron microscopy imaging

Cross-sections were obtained from an FEI DualBeam Helios 600 (Hillsboro, OR) with a gallium ion beam for transmission electron microscopy analysis and mounted on copper grids. Copper grids were preferred due to the lack of overlap between the Cu-K signal and the elements to be analyzed in the reacted specimens (mainly titanium, oxygen, and nitrogen). FEI 200 kV Tecnai G3 Sphera and FEI Talos transmission electron microscopes were used for bright-field and dark-field imaging. STEM HAADF imaging was done using the Talos instrument.

3.4.5 Electron diffraction for phase identification

A 200 kV FEI Tecnai G2 Sphera TEM was used for selected area diffraction studies to analyze the crystal structure of different regions in the cross-sections of reacted specimens. An aluminum reference specimen was used to calibrate the camera length to ensure accurate scaling of experimental diffraction patterns. Whenever possible, at least three distinct diffraction patterns from different zone axes were recorded from each region to enable proper phase identification. Selected area diffraction patterns were obtained from various points in the metal substrate and from each developed layer from reaction studies. Diffraction patterns from interfaces and the neighboring layers were also obtained to identify any orientation relationships between different phases.

3.4.6 Energy dispersive X-ray spectroscopy and electron energy loss spectroscopy

A 200 kV FEI Talos with SuperEDX detectors was used for STEM EDX map acquisition. An area that covered all developed layers and a significant portion of the metal substrate was used for map acquisition. Signal parameters were adjusted as necessary, and scans were run for at least 15 minutes in each specimen to ensure a good signal-to-noise ratio. Analysis and quantification of these maps was done using ThermoFisher's Velox 2.13 software. Using the initial map and Velox software, many types of analysis can be done post-acquisition such as extracting line scans or obtaining compositions of specific areas. To improve the quality of qualitative STEM EDX maps in the Velox software, the following corrections were used:

- Schreiber-Wims model [151]: An empirical model with improved accuracy for transition metal and metal-oxides.
- Lamellae thickness was assumed to be approximately 100 nm.

- Density of 4.5 g/cc (accurate for titanium metal but only approximate for any nitride, oxide, or oxynitride phase[5]).

Additionally, pre-filtering and post-filtering were also applied to the STEM EDX elemental maps when obtaining semi-quantitative compositions in Velox. As a reminder, STEM EDX should not be used for quantification of light elements, particularly in the Ti system where N and O have significant peak overlap with Ti despite any corrections done to improve signal and data representation. Compositions will be reported throughout this dissertation using atomic percentages. The "optimized spectrum fit" feature from the Velox software was also used. Care was taken when selecting the elements used for quantification. For this, each area of interest was selected and the peaks of the resulting spectrum verified manually to ensure a true signal from the elements of interest and eliminating the influence of artifacts such as internal fluorescence peaks, sum or pileup peaks, and escape peaks. STEM EDX elemental maps shown will be based on net intensity maps obtained from Velox rather than atomic percent maps unless otherwise noted.

When quantifying compositions for elemental maps, error bars shown in the figures throughout the thesis were extracted from those given by the Velox software. According to their manual, their error calculations combine an estimate of the peak fit according to the cross-section model used and a deconvolution error. In an attempt to gauge the values of their error estimates, an alternative error calculation was performed. Two different line scans are shown below (Figure 3.7) with the top line scan using the compositions from area

[5] The lowest reported density for the relevant Ti phases is for rutile (TiO_2) at 4.25 g/cc [152,153] and highest is for titanium nitride (TiN) at 5.21 g/cc [153] giving a ±15% variation in the possible densities of relevant phases. Since scales are thin (sub-micron) and the bulk of the specimen remains in α-Ti phase, the assumed density of 4.5 g/cc is adequate for software corrections. No oxynitride densities were found in literature.

quantification and the error bars from the Velox software[6]. The line scan below this was constructed from obtaining horizontal line scans (~300 nm long) in the area of interest and displaying the average value of these compositions as the composition of the desired region. From these compositions, the standard deviation was calculated, and the line scans and errors compared to each other.

[6] This line scan is the same as the one discussed in Chapter 4, specifically in Figure 4.4.

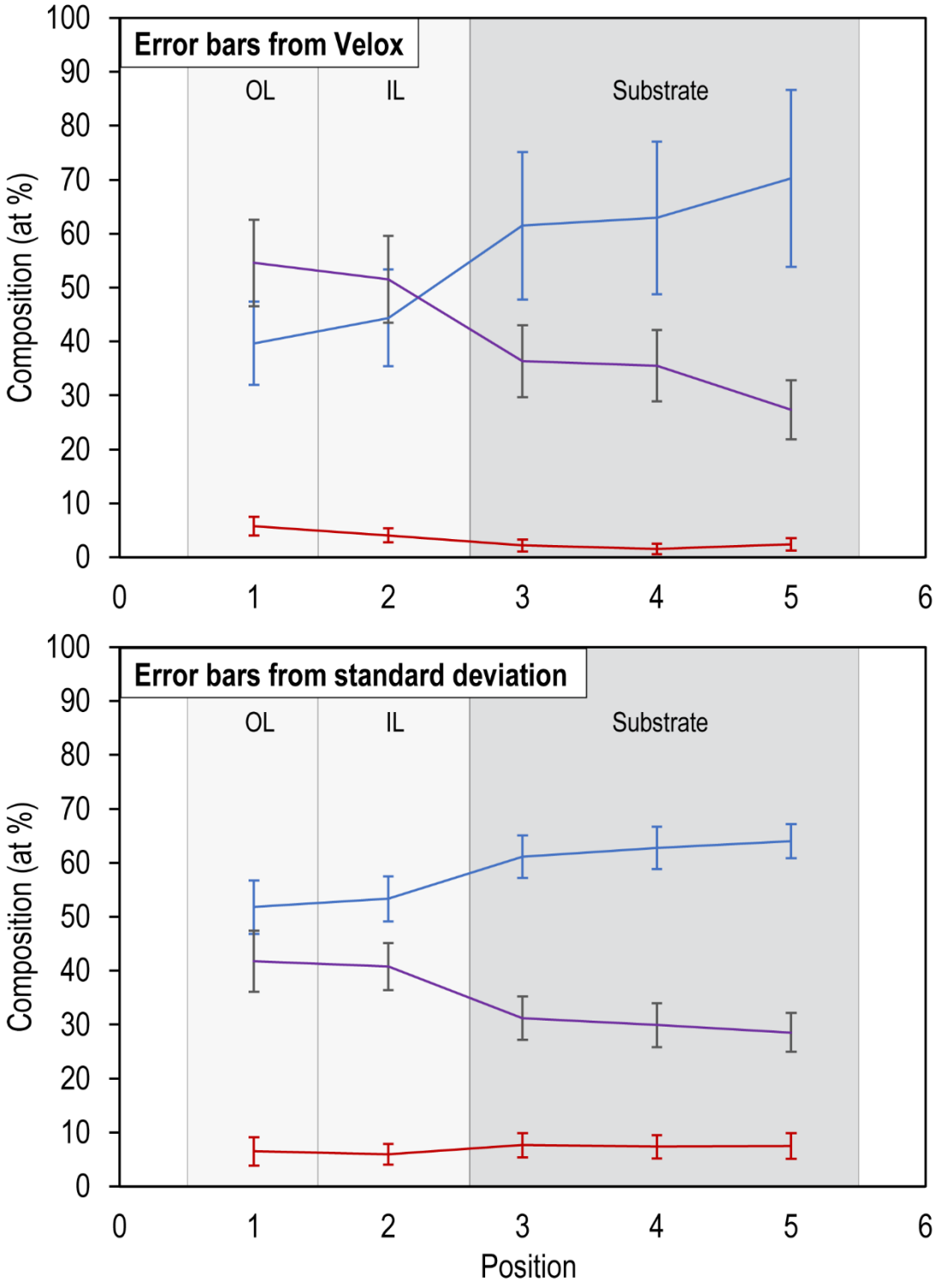

Figure 3.7. Line scans obtained from Velox through (top) area quantification and showing error bars calculated by the Velox software, and (bottom) by averaging horizonal line scans and calculating the standard deviation from this set of compositions for each area of interest.

Table 3.3. Compositions and error estimates for Ti exposed to gettered Ar for 25 h at 800°C and fast-cooled. Top values are using area quantification and error values from Velox (top of Figure 3.7) and bottom values are from averaging horizontal line scans in the areas of interest and obtaining standard deviation values (bottom of Figure 3.7).

	Ti		N		O	
	At %	**Error (%)**	**At %**	**Error (%)**	**At %**	**Error (%)**
OL	39.7	7.7	54.6	8.0	5.8	1.7
	51.8	4.9	41.7	5.7	6.5	2.7
IL	44.4	8.9	51.5	8.0	4.1	1.3
	53.3	4.2	40.7	4.4	5.9	1.9
Metal (x=0)	61.5	13.7	36.4	6.7	2.2	1.1
	61.1	4.0	31.2	4.1	7.7	2.2
Metal (x=500 nm)	62.9	14.1	35.5	6.6	1.6	1.0
	62.7	3.9	29.9	4.1	7.4	2.2
Metal (x=1000 nm)	70.3	16.4	27.4	5.5	2.4	1.2
	64.0	3.2	28.5	3.6	7.5	2.4

While the composition and error values are somewhat different with these two methods, the compositions are comparable to each other when accounting for the error estimates and are still within the composition ranges expected for the various phases that these will be identified as in the corresponding content chapter. It is important to recall that compositions given from STEM EDX should be considered qualitative given the light nature of the elements of interest (i.e. nitrogen and oxygen) and the difficulty of measuring these accurately with EDX. In the systems of interest, there are peak overlaps between both nitrogen and oxygen with titanium L-peaks that further complicate a true quantification of the interstitial content in the layers developed during oxidation. Electron energy loss spectroscopy (EELS) provides much more sensitivity and will be used when composition must be determined.

EELS was used to provide supporting evidence for the unexpected presence of nitrogen detected during STEM EDX analysis and to attempt quantification of the regions

with nitrogen and oxygen. EELS eliminates the peak overlap between nitrogen and oxygen with titanium in EDX and is preferred as a chemical analysis method for light elements. A FEI Titan 300 kV FEG TEM/STEM with a Gatan EELS detector was used for EELS analysis to acquire energy loss near-edge structures (ELNES) spectra Collective and convergence semi-angles were 10.5 and 18.9 mrad respectively. Spot measurements were taken at the various layers of the resulting microstructures using a 3 mm aperture, an energy dispersion of 0.3 eV/channel, 0.0001s exposure and 100 frames for acquisition of spectra containing the zero-loss peak and the Ti, N, and O core edges for quantification. For acquisition of the core loss spectra, an exposure of 10s and 10 frames was used for the eV range where Ti-$L_{3,2}$ (456-462 eV), N-K (402 eV), and O-K (532 eV) core edges are found. For ELNES acquisition, a 1 mm aperture, 0.05 eV/channel dispersion, 0.001s exposure and 100 frames were used to image the same Ti, N, and O edges. Energy dispersions given in eV/channel were adjusted to the values specified to improve resolution for low-loss energy resolution and for acquisition of relevant core edges. Short exposures and the addition of several frames from the same area were favored in low-loss regions to improve signal-to-noise ratio and avoid significant damage to the measured specimens and instrument.

3.4.7 Raman spectroscopy during in situ reaction experiments

Raman spectroscopy was done using a Horiba Jobin Yvon T64000 open-frame confocal microscope with a triple monochromator, and liquid nitrogen-cooled CCD array detector. The laser used was from an Ar+ source and had a 488 nm wavelength. To allow for enough space between the microscope stage and objective for heating stage placement, a 50x ultra-long working distance objective was used when recording Raman spectra during in situ oxidation experiments. Spectra were identified using Bio-Rad's Know-It-All database or

references from literature. For phases that had no reported spectrum in literature, their expected Raman modes were computed by uploading their crystal structures to the Symmetry Adapted Modes module in the Bilbao Crystallographic Server to identify whether any (and how many) modes would be expected based on the crystal structure alone [154].

3.5 Experimental validation and preliminary observations

This section will provide a few examples of microstructures developed during preliminary reaction studies before the ex situ furnace study parameters were established. While not all of the specimens included in this section will be discussed in the thesis, they provide an important example of the sensitivity that titanium shows when using different experimental parameters that might not be expected to make a significant impact in less reactive material systems. Before analyzing the results of titanium reactions with nitrogen and oxygen in the upcoming chapters, it is important to establish a few observations from these preliminary studies.

During initial ex situ studies in a tube furnace with flowing gettered argon, several different polishing procedures were tested for titanium surface preparation. Different specimen holder configurations, gas flows, and cooling methods were also assessed. The key result from the initial set up of the experimental ex situ procedure was the drastically different resulting microstructures even when using the same dwell temperature and time as evidenced in Figure 3.8.

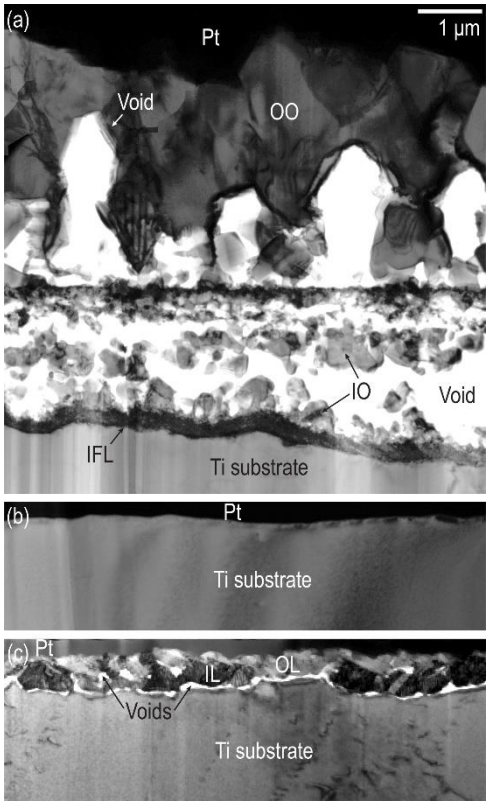

Figure 3.8. Bright field CTEM images of microstructures of Ti exposed at 800°C for 25 h and cooled by and cooled by (a) “slow-cooling in counter Ar flow”, (b) “fast-cooling in parallel Ar flow”, and (c) “fast-cooling in parallel Ar flow”.

These specimens were cooled in different ways: (i) by leaving the specimen in the hot zone, shutting off the furnace, and leaving to cool in a gettered Ar flow anti-parallel to the loading direction (hereafter “slow-cooled in counter Ar flow”) as in Figure 3.8a, (ii) by ejecting the specimen from the hot zone and leaving to cool in a gettered argon flow anti-parallel to the loading direction (“fast-cooled in counter Ar flow”) as in Figure 3.8b, and (iii) same as (ii) but with the argon flow parallel to the loading direction (“fast-cooled in parallel Ar flow”) as in Figure 3.8c. This highlights the high sensitivity of titanium to its thermomechanical history and the difficulty in capturing the reaction process accurately.

In the specimens that form a scale (Figure 3.8a and Figure 3.8c), two key features are the formation of distinct layers and the presence of voids of varying sizes and locations

within the reacted specimen. These features will be seen and explored in the upcoming chapters. One interesting result, however, was that one of the specimens showed no scale nor visual evidence of spallation (Figure 3.8b). This suggested that any scale formed at temperature had dissolved back into the metal substrate. This specimen prompted the in situ experiments to elucidate *when* oxide formed and whether any of it dissolved back into the substrate at temperature or during cooling. To best capture the microstructure at the dwell temperature, ex situ studies used a fast-cooling where the specimen was extracted from the hot zone over two minutes (to reduce spallation) and left to cool in the flowing gas. This minimized significant additional phase transformations during cooling and allowed for analysis of the reactions at high temperature.

Initially, post-exposure microstructures were cross-sectioned with a diamond blade for SEM analysis. Significant spallation and breakage occurred despite infiltrating the surface with epoxy and taking other precautions to preserve the metal-scale interface. An example of this is shown in Figure 3.9.

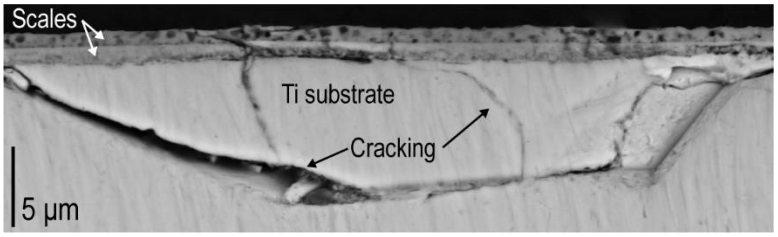

Figure 3.9. Backscattered SEM micrograph of a cross-section of a Ti specimen from early ex situ studies showing significant cracking throughout the developed scales and within the metal substrate. This specimen was exposed at 800°C for 9 h and fast-cooled in flowing gettered Ar.

This cracking could be explained partly by the embrittlement associated with high concentrations of interstitial contents in titanium metal, which would be expected in the conditions used for these studies. Other specimens cross-sectioned in this manner showed spallation within the metal substrate as well as of entire regions of developed scales. Since

scales were typically under 5 μm-thick and to preserve the metal-oxide interface, cross-sections were obtained using FIB liftout techniques moving forward.

Finally, it was important to verify that the microstructures obtained were reproducible and representative of the experimental parameters used despite the sensitivity and variability of titanium when changing experimental conditions. Several of the experiments were run three different times with different titanium specimens and resulted in similar microstructures ensuring that the microstructures formed were reliable. While there was slight variation between them, the morphologies and phases in the final microstructures were equivalent. Significantly, the microstructures obtained during ex situ and in situ experiments are also comparable despite being made using different equipment and gas environments (Figure 3.10).

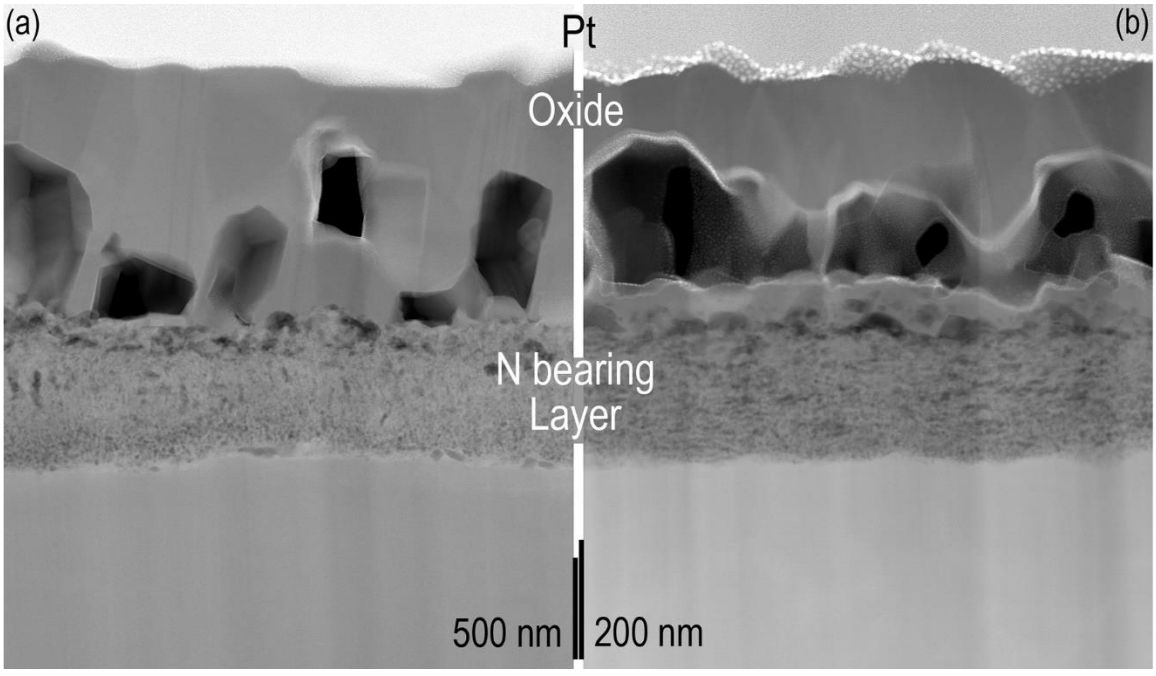

Figure 3.10. Scales formed in (a) a furnace experiment with flowing gettered Ar with a hold time of 9 h, and (b) a similar scale formed in the in situ Linkam furnace experiment with ultra-high purity Ar after 30 min dwell at 800°C.

The scales generated and microstructures are similar despite the differences in environment and dwell times. The difference in layer thicknesses is easily attributed to the different interstitial contents in the two different gas environments (gettered argon for ex situ and UHP Ar for in situ in the specimens shown in Figure 3.10). The scale from the in situ specimen shown is thinner because of a shorter exposure time in a higher O and N content compared to the ex situ studies.

In summary, microstructures were validated in several ways and features observed such as pores and developed scales should be interpreted as stemming from the Ti-N-O system and its reactions rather than from artifacts introduced from contamination in specimen preparation or experimental procedures. A list of all Ti specimens discussed in this dissertation is included in Table 3.4.

Table 3.4. List of Ti specimens discussed throughout the dissertation and their relevant experimental conditions.

Type of study	Equipment used	Environment	Material	Dwell T (°C)	Cooling method	Dwell times (Specimen name)	Text in
Ex situ	Tube furnace	Gettered Ar	Ti plate	800	Fast-cooled (FC)	1 h (T71) 9 h (T73) 25 h (T75)	Ch. 4
Ex situ	Tube furnace	Gettered Ar	Ti plate	800	Slow-cooled (SC)	1 h (T41) 9 h (T43) 25 h (T45b)	Ch. 5
In situ	Heating stage under RS	UHP Ar	Ti plate	800	Furnace-cooled	5 min (D805) 30 min (D8030) 130 min (D80130)	Ch. 6
					10°C/min	240 min (D81)	
Ex situ	Tube furnace	1%O_2-Ar	Ti foil	800	Fast-cooling (FC)	1 h (TO11) 9 h (TO13)	Ch. 7
In situ	Heating stage under RS	1%O_2-Ar	Ti foil	800	Furnace-cooled	30 min (M8030F)	

4 hcp Titanium under Parallel Flow Gettered Argon at 800°C (Fast-Cooled) in Tube Furnace

This chapter will explore the reactions of titanium in a gettered Ar gas environment where the partial pressure of N_2 is higher than the partial pressure of O_2 (N_2:O_2 ratio = 10,000). Following the **fast-cooled in parallel flow** setup, specimens were exposed to flowing gettered Ar at 800°C for 1, 9, and 25 h. While titanium reactions with gases containing oxygen usually form rutile or other oxides at high temperatures, these specimens mainly form nitride scales with a strong orientation relationship between the hcp Ti substrate and the rocksalt TiN outer scale. TiN grains are first seen at the 9 h dwell time showing diamond-shaped voids between these grains and the metal substrate underneath. The specimens that form layered scales (all except 1 h specimen) show porosity in a variety of sizes, morphologies, and locations. The observations from these experiments and their characterization suggest that α-Ti may form an ordered phase with nitrogen in the substrate in addition to α-Ti (N) solid solution and scales with coherently strained ε-Ti_2N and a twinned rocksalt TiN with an [011] twin axis and {111} twin planes. The phase identification and proposed growth mechanisms will be described in this chapter.

4.1 Results and discussion

The specimens generated under these experimental conditions formed layered microstructures with an outer δ-TiN layer and an inner two-phase region with ε-Ti_2N and δ-TiN. The microstructures for these specimens and proposed phase identification are shown in Figure 4.1. The substrate shows evidence for the existence of a solid solution of α-Ti with disordered nitrogen and the possibility of an ordered phase based on the α-Ti structure

(labelled as α”-like phase in Figure 4.1). These specimens mainly formed nitrides, suggesting that nitride formation takes precedence over oxide formation in these experimental conditions. Specimens were held at 800°C for 1, 9, and 25 h. Two specimens were made at 25 h where one of them showed an O-rich outer scale. This additional specimen will be discussed in an appendix at the end of this chapter. This section will discuss the phase identification of the resulting layers, the orientation relationship between the hcp Ti substrate and scale, porosity, and proposed mechanisms for these features. Since the 1 h specimen shows no scale and the 9 h specimen shows evidence for the same phases as the 25 h, the 25 h specimen will be discussed in detail as a case study.

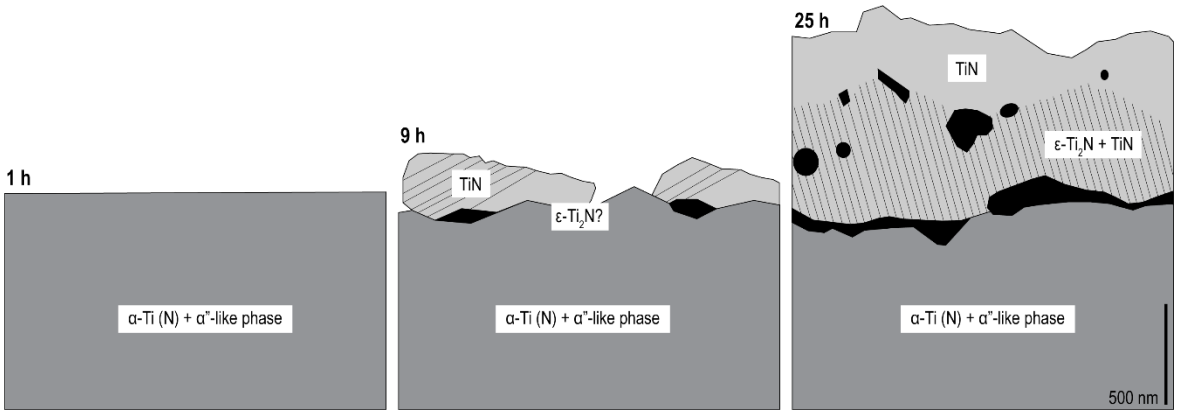

Figure 4.1. Schematic for microstructures generated from fast-cooled Ti specimens exposed to gettered Ar at 800°C for (left) 1 h, (middle) 9 h, and (right) 25 h.

4.1.1 Phase identification

Using the methodology for ex situ oxidation studies detailed in Chapter 3, polished titanium pieces were oxidized in gettered argon with a parallel flow at 800°C for 1 h, 9 h, and 25 h and fast-cooled by ejecting the specimens from the hot zone after the desired dwell time. The surface morphology of these specimens (Figure 4.2) showed several islands of faceted crystals (300-800 nm grains) for the 1 h specimen, sawtooth-like grains (720 nm – 1.5 μm at the base and 300-650 nm in height) in the 9 h, and elongated faceted grains (1-3 μm in length

and 300-500 nm thick) in the 25 h specimen. The 1 h specimen shows step-like facets on the surface underneath the islands of crystals. Small round particles (45-70 nm) are visible in the 1 and 9 h surfaces dispersed randomly throughout the surface.

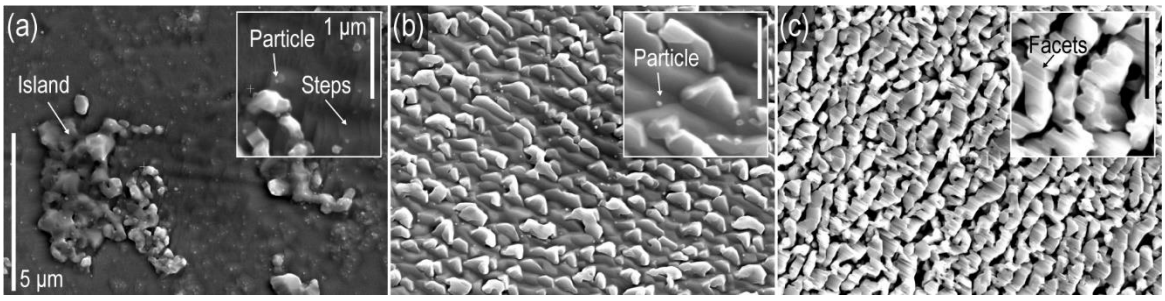

Figure 4.2. Top-view SE SEM micrographs of Ti oxidized ex situ at 800°C in gettered Ar for (a) 1 h, (b) 9 h, and (c) 25 h.

The cross-sections of these specimens (Figure 4.3) reveal no noticeable scale in the 1 h (top row of Figure 4.3); single grains (largest grain shown is 960 nm x 320 nm) with parallel features growing on the metal surface at the 9 h with small voids (~150 nm) growing at the metal-scale interface (middle row of Figure 4.3); and a two-layered scale with large grains (~650 nm) and voids within the scale (~230 nm) and at the metal-scale interface (70-170 nm in height) in the 25 h (bottom row of Figure 4.3);.

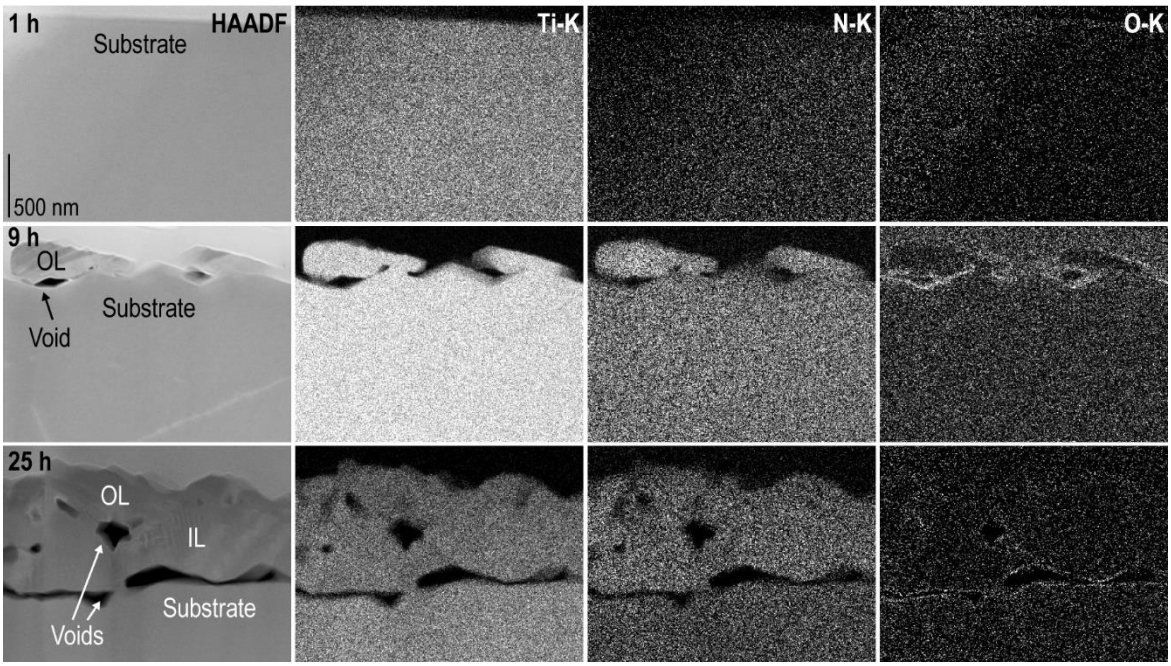

Figure 4.3. STEM HAADF cross-sectional micrographs and corresponding STEM EDX elemental maps for Ti foil exposed at 800°C in gettered Ar for (top row) 1 h, (middle row) 9 h, and (bottom row) 25 h showing Ti, N, and O signal. Features and scales are labelled in the HAADF images where OL is "outer layer" and IL is "inner layer".

In the 25 h, the scale is labelled as OL for 'outer layer' and IL for 'inner layer' (Figure 4.4). Aside from the presence of voids between these layers, they can also be distinguished by their microstructural features: OL is flat while IL shows a tweed-like pattern. Interestingly, elemental maps and line scans from STEM EDX (Figure 4.4) show there is no significant concentration of oxygen that would suggest the formation of rutile, which readily forms on Ti, or any other oxide. There is only a slight concentration of oxygen along the edges of pores and the scale. When looking at the nitrogen signal, however, the scale shows a slightly higher concentration of N than what the metal substrate shows. Using 100 nm x 100 nm squares to quantify the different regions of the microstructure, the oxygen values remain well below 10 at% O throughout the specimen while nitrogen values go from 27 at% N within the substrate to 55 at% N in the outer layer. While these values should not be relied on as absolute quantification, they provide important information to identify which

phases have formed from reactions in the gettered Ar and suggest that only nitrides are forming under these experimental conditions.

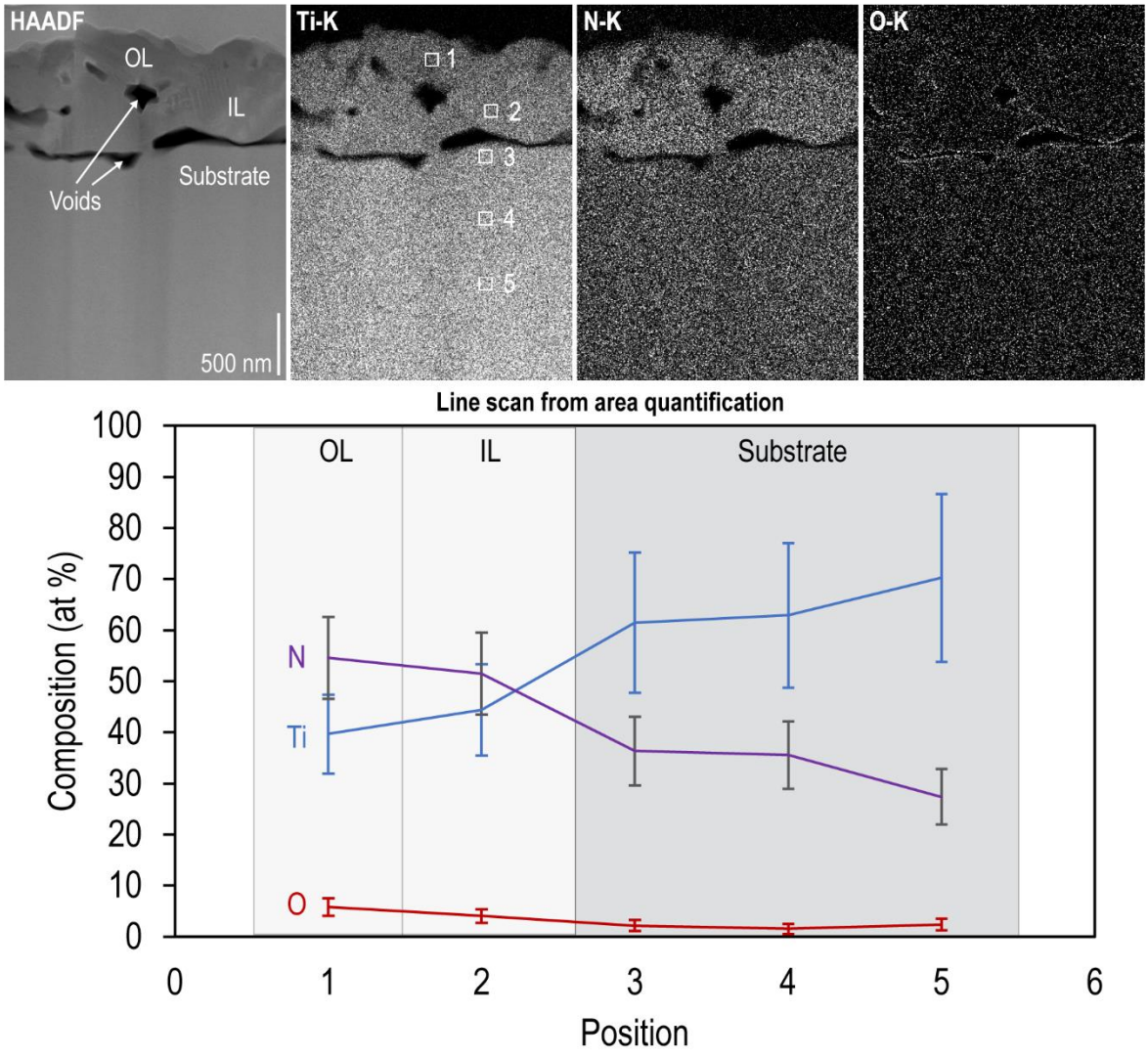

Figure 4.4. Cross-sectional micrographs from STEM HAADF and corresponding STEM EDX elemental maps. Areas used for quantification are shown in the Ti-K elemental map and its values were used to construct the line scan below. N values are highest within the scale and decrease going into the substrate. Oxygen values remain low throughout the specimen although they are slightly higher in the scale than in the substrate.

X-ray diffraction patterns from the surface of the three dwell times (Figure 4.5) show no rutile peaks in the 1, 9, and 25 h specimens which differs from the expectation of rutile formation in most titanium oxidation conditions. The 1 h specimen shows an XRD pattern

that is similar to the reference Ti foil XRD pattern suggesting that the N and O ingress has not been significant enough to change the lattice parameters of the α-Ti in this specimen. The most intense peaks in all three dwell times correspond to α-Ti peaks, but these shift to lower 2θ angles at 9 h and 25 h. This shift to a lower 2θ angle can be explained by a c-axis expansion from the shift in the $(0002)_\alpha$ peaks. This is expected upon incorporation of N and/or O into octahedral sites of α-Ti as a solid solution. The $(10\bar{1}3)_\alpha$ peak is the most intense in all three specimens which could also be explained by lattice changes from interstitial ingress into α-Ti. At 25 h, there are additional peaks to the α-Ti ones which can now be compared to nitride phases (Figure 4.6).

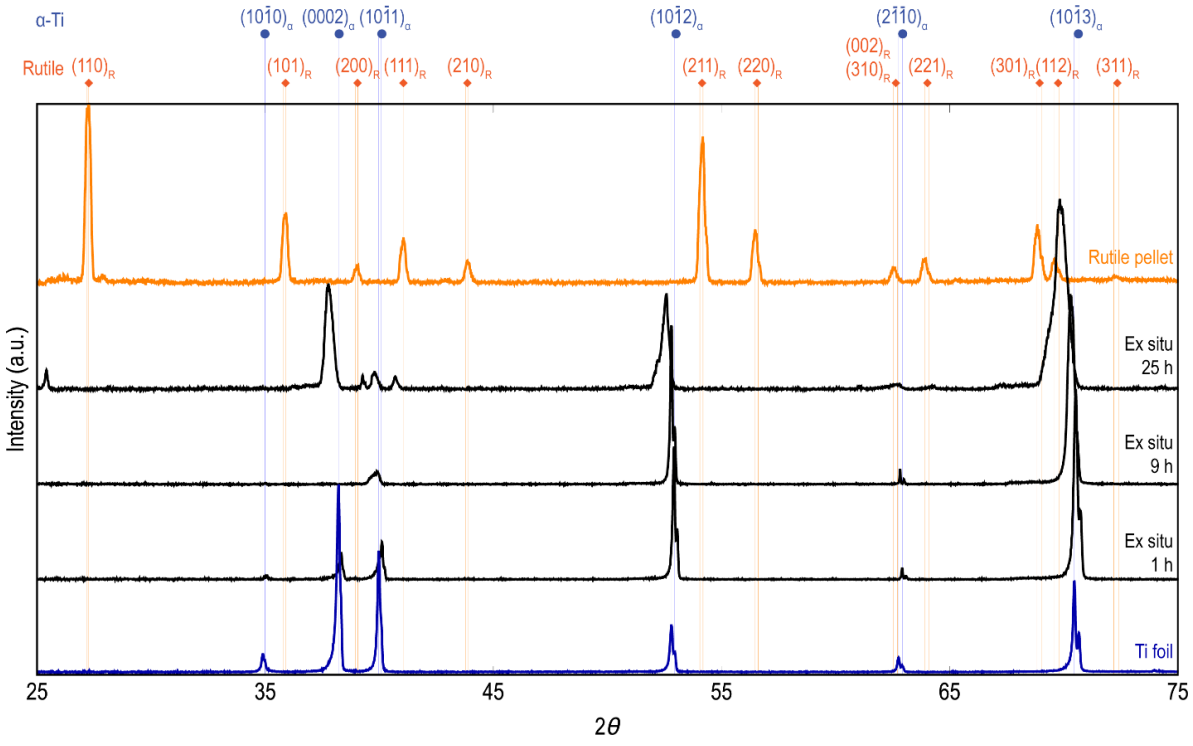

Figure 4.5. (Black spectra) XRD patterns from the surface of Ti specimens oxidized ex situ in gettered Ar at 800°C for 1 h, 9 h, and 25 h. Reference XRD patterns from rutile (top orange) and polished titanium foil pre-oxidation (bottom blue) are shown. Thin lines in orange and blue are extended from the reference spectra to the top of the plot to indicate the relevant planes for each phase's expected peaks. Future XRD patterns will show these guidelines whenever relevant to avoid repetition of the reference spectra.

In the 25 h specimen (which shows the largest shifts and peaks other than α-Ti), X-ray diffraction from the surface shows large peaks corresponding to α-Ti positions shifted to lower 2θ angles (Figure 4.6). The $(0002)_\alpha$ peak shift corresponds to a c lattice parameter of 4.76 Å, which is a 1.6% expansion from the initial hcp titanium. The c expansions for hcp-based suboxides and solid solutions with N and O are shown in Table 4.1. The observed expansion is lower than both solid solutions reported in the ICSD database. This could be explained by a lower interstitial content than in either of those reference phases and by considering the possibility that both nitrogen and oxygen are present in the substrate thereby affecting c expansion as well. The $(10\bar{1}3)_\alpha$ peak is the highest and shifts significantly to a lower 2θ value of 69.82° in this specimen. The interplanar spacing for this plane is 1.3455 Å, a 1.02% increase over the 1.3319 Å spacing of hcp Ti with no interstitial content.

Both nitrides, ε-Ti_2N and δ-TiN, are identified in smaller peaks (Figure 4.6). While these peaks are small, the ε-Ti_2N peaks can be seen shifted slightly from the ideal positions. This could be explained if tetragonal ε-Ti_2N grows with coherent strain from the hcp Ti. TiN peaks are labelled in the position where they would be expected but no significant peaks are visible in the experimental pattern (Figure 4.6). This, however, does not mean that there is no TiN formation, as will be seen in electron diffraction, but is rather the result of a thin TiN layer compared to the substrate thickness and XRD interaction volume.

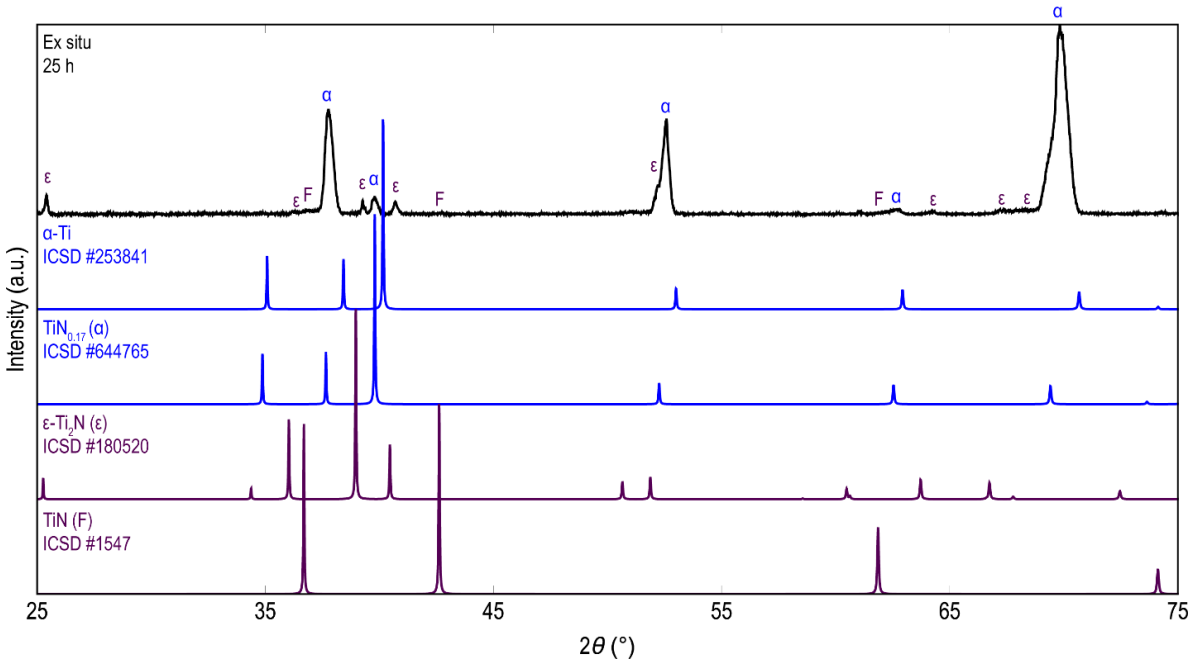

Figure 4.6. Comparison of experimental pattern from 25 h specimen to possible titanium phases from ICSD. α denotes α-Ti peaks, ε denotes ε-Ti_2N, and F indicates fcc rocksalt TiN peak positions.

Table 4.1. c-axis expansions of hcp-based suboxides compared to α-Ti where SS stands for solid solution.

Phase	**c expansion (%)**
α-Ti	0.00
α-Ti_6O	1.28
α-Ti_3O	1.82
α-$TiN_{0.17}$ (SS)	1.99
α-$TiO_{0.325}$ (SS)	2.03
α" (Staged Ti_2O)	3.21

Electron diffraction from the different regions of the specimen helps clarify identification of the phases that have formed throughout the layers. In examining the metal substrate, two different orientations were used to obtain electron diffraction patterns (Figure

4.7 and Figure 4.8) and were subsequently compared to hcp-based suboxides, solid solutions with N and O individually, and the nitride with lowest N content, ε-Ti_2N. The first zone axis (Figure 4.7) shown corresponds to $[\bar{1}2\bar{1}0]_\alpha$ and the equivalent directions for the other phases are shown in simulated SAED patterns with gray backgrounds. In the experimental pattern, the reflections show fairly even intensities although there are some alternating increases in intensity as can be seen with $(000\bar{1})_\alpha$ being dimmer than the $(000\bar{2})_\alpha$reflection. In α-Ti and its suboxides, the $(000\bar{1})_\alpha$ reflection is forbidden and can be seen marked as a double diffraction spot in yellow. The α" phase, which has oxygen ordered in every other interstitial layer, allows for these reflections.

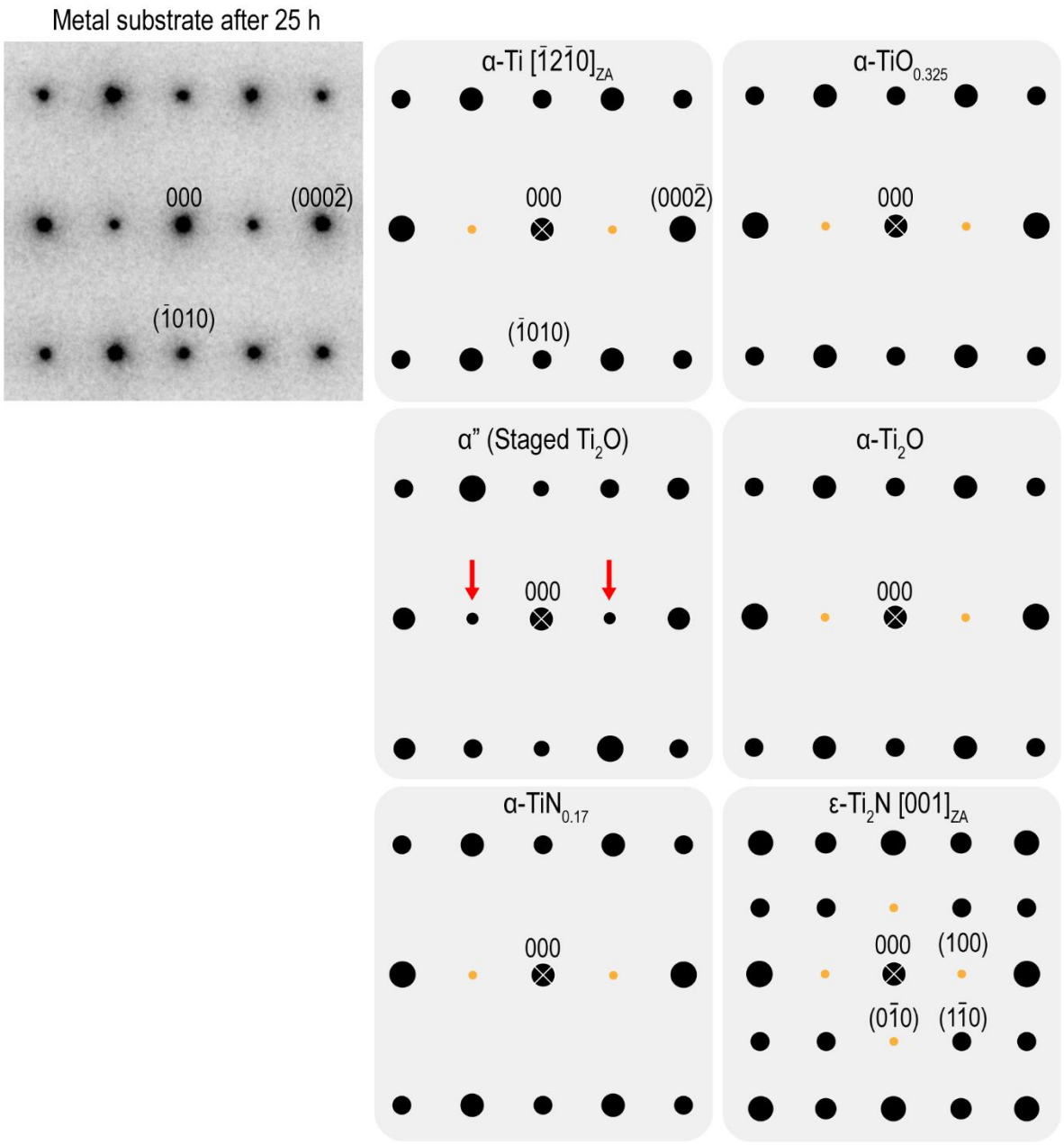

Figure 4.7. Experimental SAED from the metal substrate of titanium exposed to gettered Ar at 800°C for 25 h and fast-cooled. Indices shown correspond to α-Ti along a [$\bar{1}2\bar{1}0$] zone axis. Yellow spots represent forbidden or double diffraction spots and red arrows highlight when these forbidden spots become expected. Schematics of simulated suboxide, solid solution, and nitride SAED patterns are shown with gray backgrounds.

Along the [$\bar{5}7\bar{2}3$] zone axis (Figure 4.8), the experimental pattern is once again closest to the α" phase simulated pattern. α-Ti, the α-$TiO_{0.325}$ and α-$TiN_{0.17}$ solid solutions, and α-Ti_2O all lack a few of the reflections that are clearly seen in the experimental pattern.

The presence of the reflections that are forbidden in α-Ti suggests that the metal substrate has interstitials ordering in some way that breaks the symmetry of the hcp Ti lattice. The α" phase does this by ordering oxygen every other interstitial layer. It is possible that, rather than randomly distributing in the octahedral sites of α-Ti, nitrogen segregates to every other interstitial layer. Oxygen may also incorporate in this manner into the hcp Ti lattice albeit in much smaller quantities than nitrogen.

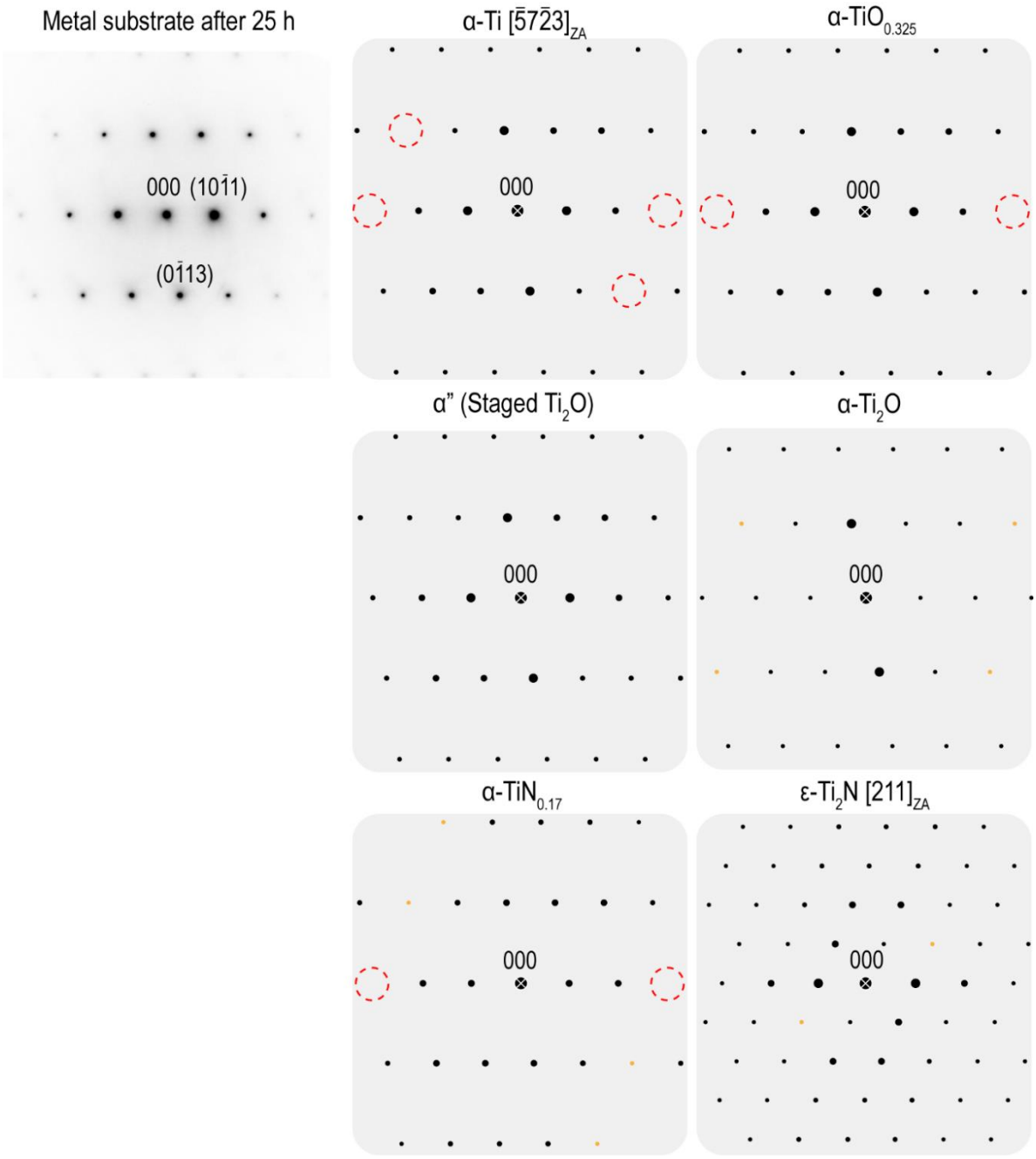

Figure 4.8. Experimental SAED from the metal substrate of titanium exposed to gettered Ar at 800°C for 25 h and fast-cooled. Indices shown correspond to α-Ti along a [$\bar{5}7\bar{2}3$] zone axis. Yellow spots represent forbidden or double diffraction spots. Schematics of simulated suboxide, solid solution, and nitride SAED patterns are shown with gray backgrounds.

Electron diffraction from the outer scale matches a twinned rocksalt structure (Figure 4.9). As mentioned before, rocksalt structures for the Ti-N-O system can be TiN, TiO, or TiN_xO_y with the additional possibility of vacancy over the N or O fcc sublattice. Given the

elemental maps from this specimen, it is likely that this phase is δ-TiN since its composition is ~55 at% N and ~6 at% O. It is possible that TiN has some O solubility, but since this is potentially low, this phase will be referred to as TiN rather than an oxynitride. The experimental pattern, simulated pattern showing the twinned SAED and its corresponding crystal structure is shown in Figure 4.9.

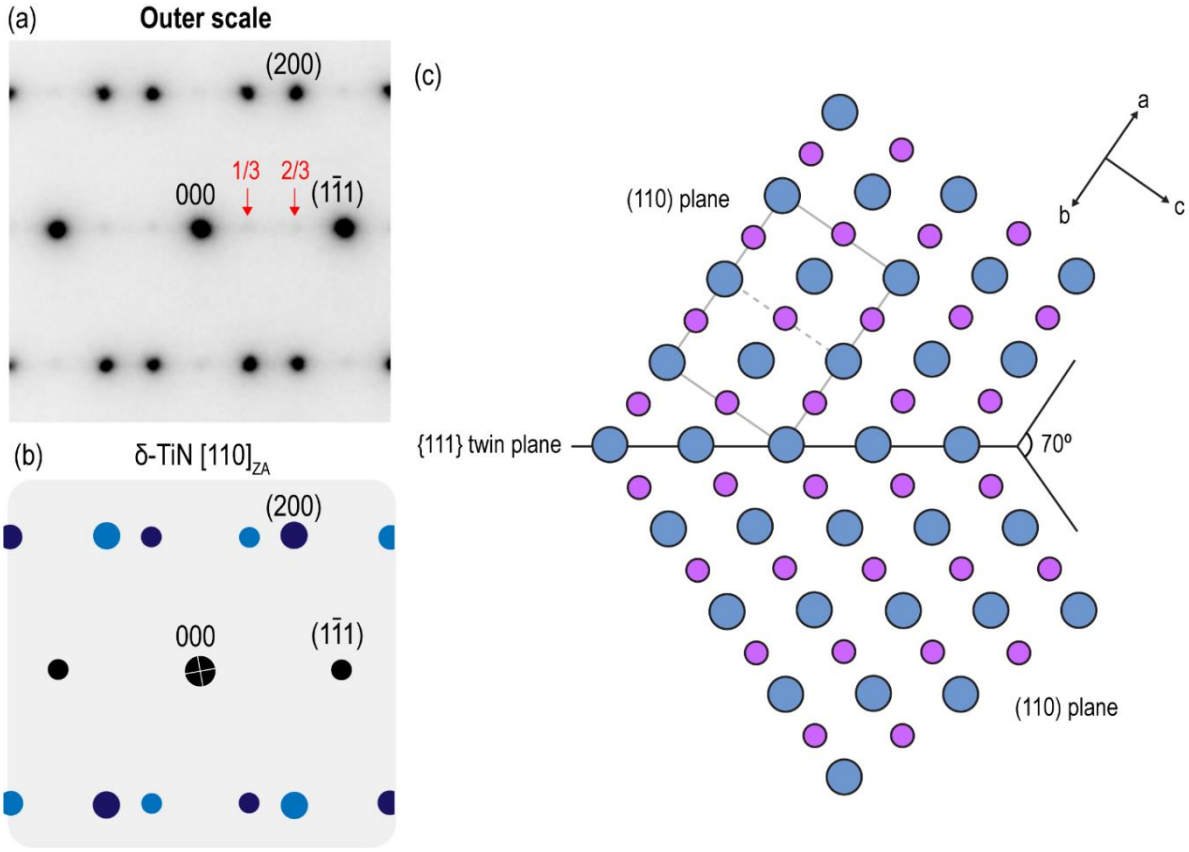

Figure 4.9. (a) Experimental SAED from outer layer with δ-TiN $[110]_{ZA}$ indices labelled and additional spots at 1/3 and 2/3 highlighted by red arrows, (b) simulated pattern for a twinned δ-TiN along the [110] zone axis. Black reflections are the same in both orientations whereas the dark blue and light blue denote the original and twinned reflections respectively. (c) Schematic of the crystal structure that would explain a twinned rocksalt with a [110] twin axis and a {111} twin plane.

The formation of twins in TiN has been observed in TiN thin films deposited onto graphite by chemical vapor deposition [155] where at temperatures below 950°C, TiN crystals grow mainly with twins rather than as single crystals. This suggests that it there is sufficient thermal energy to overcome the energetic cost of twin boundaries that form due to

kinetic processes. These twins form at these temperatures during the growth stage. They report multiply twinned particles (MTPs) and laminated twinned particles (LTPs) as opposed to the single twins observed in the experimental pattern in Figure 4.9. It could be that these twin boundaries are kinetically trapped and that exposure to elevated temperatures allows for the energy cost of these twin to be easily overcome.

In the experimental pattern (Figure 4.9), there are additional faint reflections at $\frac{1}{3}(1\bar{1}1)_{\text{fcc}}$ spots. These same reflections have been observed in two different systems: during in situ TEM studies of the hcp Ti to fcc Ti transformation in a Nb-Ti-Si alloy [86] and in TiCN synthesized by hot pressing mixtures of TiC and TiN powders [156]. While the spots in TiCN are attributed to double diffraction [156], the in situ studies [86] propose the formation of intermediate structures along the transformation pathway from hcp to fcc. They identify these as long period stacking ordered (LPSO) structures closest to the 9R rhombohedral crystal structure. An additional periodic structure that matches the expected stacking of an 18R structure forms before the 9R structure, but the reflections corresponding to this are not seen in this particular specimen. The transformation pathway from hcp to fcc is proposed by Ma et al. [86] to occur through lateral movement of growth ledges by partials with Burgers vectors of $\boldsymbol{b} = \frac{1}{3} < 1\bar{1}00 >_{\text{hcp}}$ along $\{0001\}_{\text{hcp}}$ planes or $\boldsymbol{b} = \frac{1}{6} < 112 >_{\text{fcc}}$ along $\{111\}_{\text{fcc}}$ planes.

In situ studies of the Nb-Ti-Si alloy discussed in the previous paragraph [86] ruled out the influence of oxygen on the formation of these LPSO structures, but it is unclear whether nitrogen was considered since their EELS work did not include the 400 eV region where the N-K edge would appear. Based on the evidence from literature and the specimens from this research project, it is unlikely that these additional reflections (Figure 4.9) are double

diffraction spots. Given the presence of twins in the outer scale and the dislocations in the substrate, it is possible that there are stacking faults or local changes in the stacking which can show reflections that would match LPSO structures. The formation of the LPSO structures could arise from the deformation induced by introducing interstitials into hcp Ti rather than from forming oxide or nitride phases. If a new phase is forming, it is possible that this is a metastable nitride and more work would be required to determine whether any metastable Ti-N phases match these additional reflections.

The final region to be analyzed in this specimen for phase identification is the "inner layer (IL)". The electron diffraction pattern from this region and its relevant simulated SAED patterns are shown in Figure 4.10. The inner layer is a layer of grains above the metal substrate with parallel features that can be seen throughout the lamella. The region shown in the BF micrograph (seen in the top left corner of Figure 4.10) shows a light and dark region, where the parallel features and tweed-like microstructure can be appreciated. The outer layer was shown first because the twinned rocksalt spots can once again be seen in the SAED pattern from the tweed-like IL region (the spots highlighted by red arrows in Figure 4.10 show which spots arise from twinned TiN reflections and an overlay of patterns illustrating this is shown in Figure 4.11).

While the major reflections are accounted for from the substrate and twinned TiN, there are additional faint reflections in a row in between the major α-Ti substrate spots (Figure 4.10). To identify these spots, all solid solutions, hcp-based orderings, and ε-Ti_2N phases were analyzed (Figure 4.10c-f). The rocksalt-based phases, Ti_4N_3 and Ti_6N_5, proposed by computational work [8] were also included in attempts to index these diffraction patterns. ε-Ti_2N can account for all of the α-Ti and most of the additional faint reflections. It is

proposed that the difference in electron diffraction patterns could arise from the formation of a coherently-strained tetragonal phase similar to ε-Ti_2N or a different tetragonal phase. Given the tweed-like microstructure and the XRD evidence for a tetragonal phase, one possibility is that the inner layer has a rocksalt TiN matrix and that the tweeding arises from rocksalt TiN (or N-rich TiN_xO_y) precipitates with tetragonal distortion. In α-Ti_2O (Figure 4.10f), one zone axis shows similar rows of faint reflections along the $[001]_{ZA}$ (based on a supercell from DFT calculations [5]) but this orientation does not correspond to the equivalent $[\bar{1}2\bar{1}0]_{\alpha}$ orientation and its major Ti reflections have different lattice parameters than those from the experimental pattern. If this inner layer is identified as a two-phase region with fcc TiN and tetragonal ε-Ti_2N (or a similar tetragonal phase), the tweed-like structure could be explained by an fcc TiN matrix and tetragonal embryos forming. A similar microstructure can be seen from fct embryos in an fcc matrix in an Fe-Pd alloy [157].

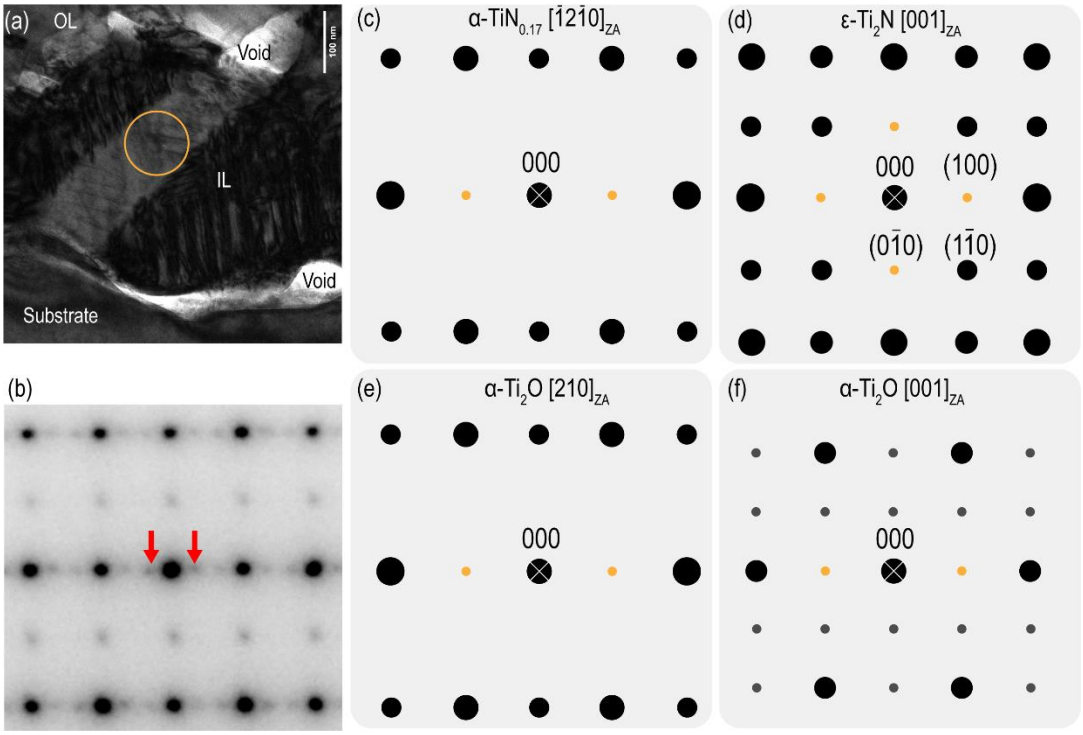

Figure 4.10. (a) CTEM BF micrograph of the inner layer highlighting where the (b) experimental SAED was obtained within this grain. (c-f) Simulated SAED patterns.

This experimental pattern shows a continuous orientation relationship between hcp Ti and the two nitrides since Ti reflections remain in the same positions through the SAED patterns of the substrate and inner layer. An ordered off-stoichiometric α' phase has been proposed to form from supersaturated α-Ti (N) solid solution before reaching equilibrium ε-Ti_2N [158] which could explain the differences between the simulated ε-Ti_2N pattern and the reflections from the experimental one since the spots would fit a tetragonal structure. The equivalent zone axis for the α-Ti $[\bar{1}2\bar{1}0]_{ZA}$ in ε-Ti_2N is the $[001]_{ZA}$. This relationship and an ε-Ti_2N layer that is coherent with hcp Ti has also been reported in oxidation in air of a Ti-0.5Nb-0.5Si (in wt%) alloy [159]. It is still possible that the tweed microstructure arises from strain or atomic displament considerations, or that the tetragonal precipitates form along the elastically soft directions, but the available evidence from this specimen is not sufficient to clarify its origin. However, colleagues at UCSB have observed tweed microstructures in Ti-

Nb-O systems with the precipitates in that system growing along the $[110]_{\beta}$ direction, which corresponds to the hcp habit planes, instead of the elastically soft direction of [100] typically seen in bcc systems.

4.1.2 Orientation relationship and possible growth mechanisms

An interesting feature of this specimen is the strong orientation relationship between the metal substrate and the scale that grows above it. For simplicity, the relationship between the outer scale and metal substrate will be analyzed. This overlay suggests that Ti atoms remain in essentially the same positions from the metal substrate into the outer scale where a twinned rocksalt TiN forms. The spots to the immediate left and right of the Ti reflections (overlay pattern in Figure 4.11) stem from the twinned rocksalt phase and are slightly misaligned from the α-Ti reflections. This will be a recurring feature in Ti exposed to other environments explored in this research project. Additionally, this orientation relationship can also be seen when sampling other substrate and outer scale regions in the cross-section of the 25 h specimen. Furthermore, an orientation relationship remains when looking at the same layers using different zone axis.

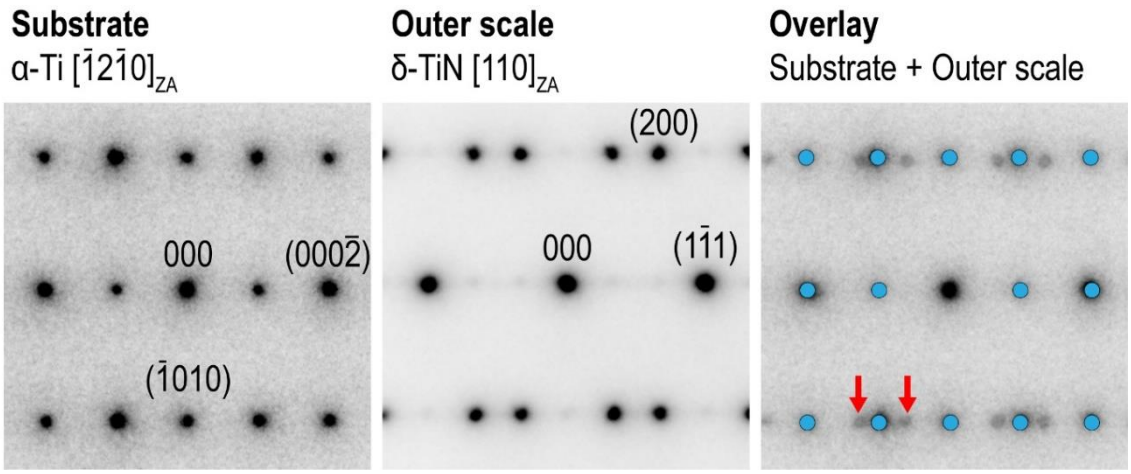

Figure 4.11. Experimental SAED from the metal substrate and the outer layer using the same tilt on the specimen holder. The overlay of the outer scale SAED pattern in transparency over the metal substrate SAED pattern is shown on the right. Red arrows highlight reflections from outer scale and blue circles indicate reflections from α-Ti solid solution.

The same orientation was used for obtaining electron diffraction patterns of these regions from all three dwell times (Figure 4.12). The twinned rocksalt can also be seen in the 9 h specimen albeit at a different angle compared to the underlying α-Ti substrate showing that the TiN can grow in different ways on the hcp Ti lattice.

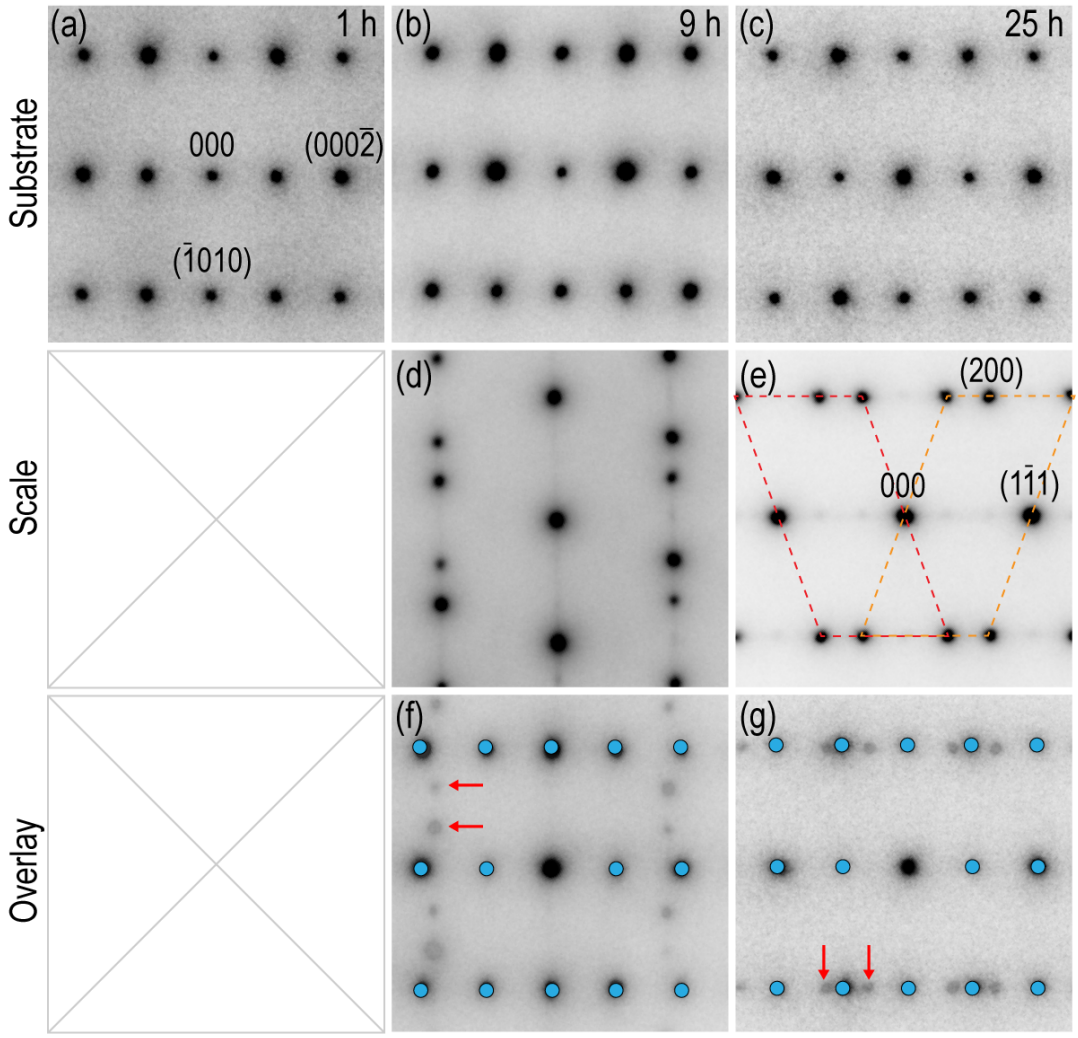

Figure 4.12. SAED patterns from metal substrate and scale regions of Ti oxidized ex situ at 800°C for (a) 1 h, (b, d, f) 9 h, and (c, e, g) 25 h. (f, g) show the overlay of scale SAED pattern in transparency over the metal substrate SAED pattern. Red arrows highlight fcc reflections and blue circles indicate reflections from α-Ti solid solution. Indices in (a) correspond to an α-Ti $[\bar{1}2\bar{1}0]_{ZA}$ and indices in (e) correspond to a rocksalt pattern with $[110]_{ZA}$. Both rocksalt patterns are twinned as highlighted by dashed lines in (e).

With Ti atoms remaining in position, the relevant orientation of TiN growing on hcp Ti is shown in Figure 4.13 based on the 25 h specimen. In this scenario, the ABAB stacking of hcp Ti is changed to an ABCA stacking with N in the interstitial layers to form rocksalt TiN where the $\{0001\}_{\alpha}$ plane lines up with a $\{111\}_{\delta}$ plane. This transformation can be accomplished by partial dislocations.

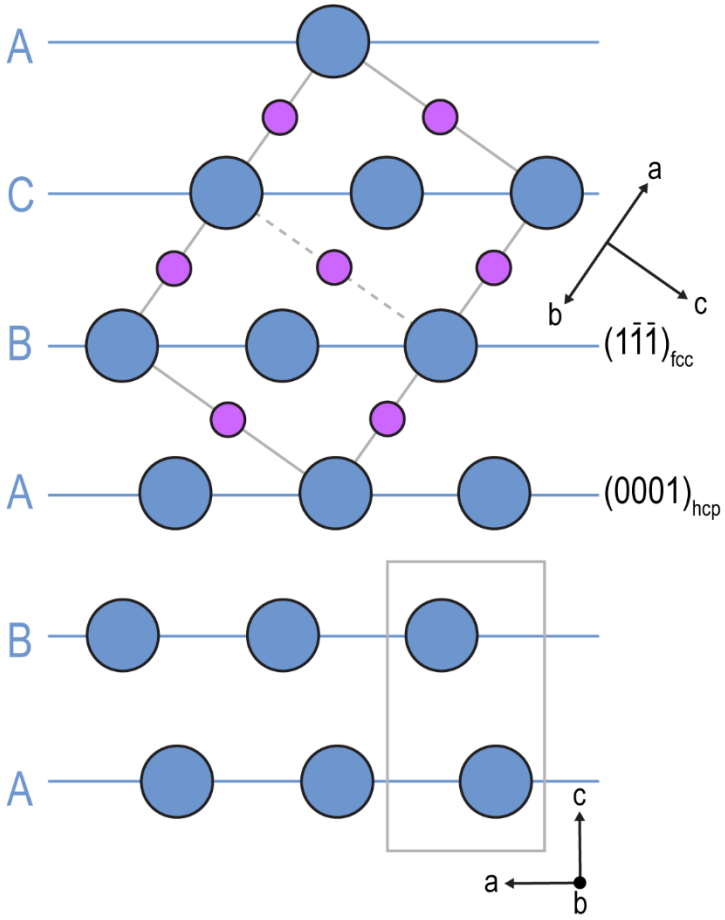

Figure 4.13. Schematic showing the orientation relationship between the hcp Ti substrate (ABAB stacking) looking down the $[\bar{1}2\bar{1}0]$ direction and the rocksalt TiN outer layer (ABCA stacking) along the [110] direction. The {0001} planes from hcp correspond to the {111} planes from fcc stacking. Blue atoms are Ti and purple atoms are N.

Transformations from hcp to fcc crystal structures have been observed before and are often explained through the movement of Shockley partial dislocations and the formation of stacking faults (SFs) as is the case with cobalt [160]. Through partials and SFs, the stacking of one crystal structure can lead to the formation of another, for instance going from ABAB (hcp) to ABCA (fcc) as in Figure 4.13. Other proposed models involve overlapped stacking faults [161], a combination of stacking faults and growth ledges [162,163], or the nucleation of intermediate structures [86,164,165].

Since the hcp to fcc transformation and twinning can both occur through the movement of partial dislocations, two possible growth scenarios are detailed in Figure 4.14. The first scenario shows only inward N diffusion while the second scenario accounts for a possible outward Ti diffusion that will be further discussed in the next section. In both scenarios, partial dislocations disrupt the ABAB stacking of the hcp titanium substrate and result in the formation of a rocksalt TiN and its twin divided by a twin boundary. As inferred from the experimental SAED patterns and supported by literature, these dislocations would move along the $\{0001\}_{hcp}$ and $\{111\}_{fcc}$ planes. The resolved shear stress for a partial dislocation 1/6 <110>{111} in TiN has been estimated to be 13.8 GPa from in situ indentation and first principles calculations [166]. The second scenario includes the formation of vacancies that would arise from an outward Ti diffusion larger than the inward N diffusion.

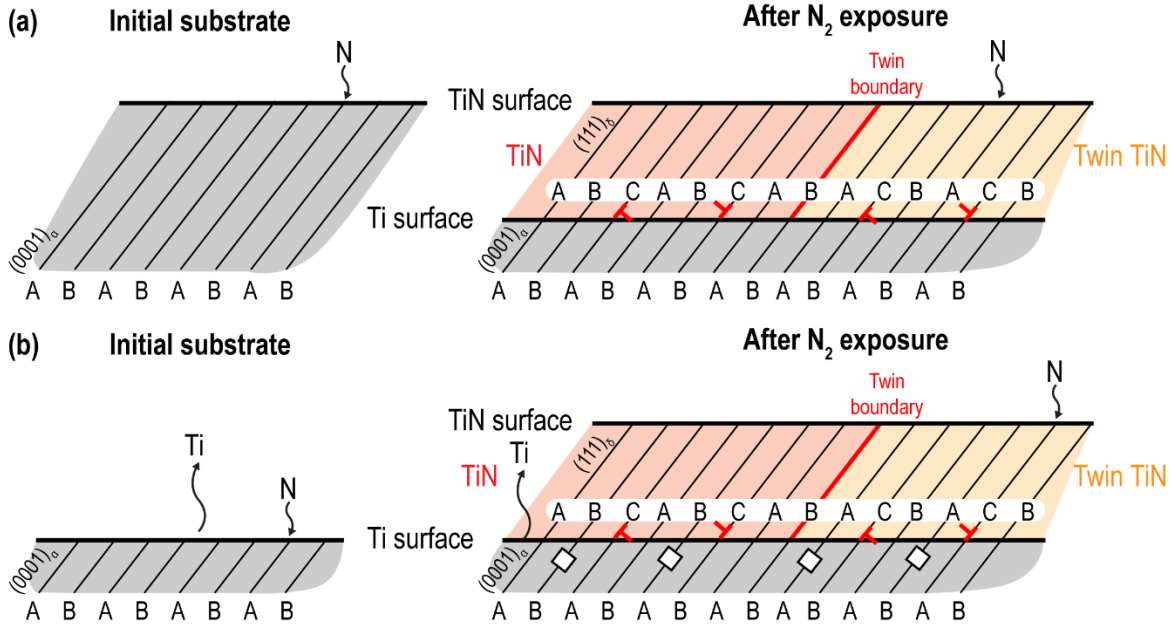

Figure 4.14. Possible growth scenarios for TiN and twin TiN grains on top of hcp Ti substrate by partial dislocations assuming (a) only N ingress or (b) N ingress with a larger Ti outward diffusion which may leave vacancies behind in the substrate. Note the change in initial metal surface depending on the scenario.

4.1.3 Void formation and growth mechanisms

While pores have been reported in oxidation of Ti, there have been fewer observations of void formation in nitriding of titanium [167]. However, it is clear that voids form alongside TiN as seen from the cross-section of the 9 h specimen (Figure 4.3). This section will discuss the different scenarios that could explain void formation in this materials system.

Given the PBR values for nitride formation, the scales formed in these fast-cooled Ti specimens are expected to develop significant compressive stresses. These compressive stresses are likely inhomogeneous and tend to vary along the scale position due to relative rates of nitrogen (or oxygen) and metal diffusion to internal grain boundaries [168]. As described by Evans et al. [168], the typical response for brittle coatings with compressive stress is fracture or spallation, both of which require an initial interface separation. Spalling, then, can occur from void formation at the interface reaching a critical size. Void formation at the interface is usually attributed to vacancy condensation from asymmetrical cation and anion fluxes, but since grain boundaries and interfaces can act as sinks for these, an alternative void formation source stems from residual local tensile stresses at the interface – typically in the presence of boundary waviness.

CTEM BF and STEM DF images of the 25 h specimen shows the extent of the voids and tweed-like microstructures throughout the specimen (Figure 4.15). The cross-section shows there are significant defects (likely dislocations) in arrays within the substrate. These seem to align with step-like regions of the metal-scale interface but not with the presence of the voids at the metal-scale interface. While the voids along the metal-scale interface may seem like spallation, there are several regions where the inner layer is contiguous to the

substrate. Additionally, there is no evidence of cracking in the cross-section, and the void morphology along the interface does not match the morphology of the inner layer, which would be the case from spallation. These voids, instead, show growth towards the scale or towards the substrate depending on which region of the cross-section is observed. The voids at the outer-inner scale interface have a more equiaxed morphology.

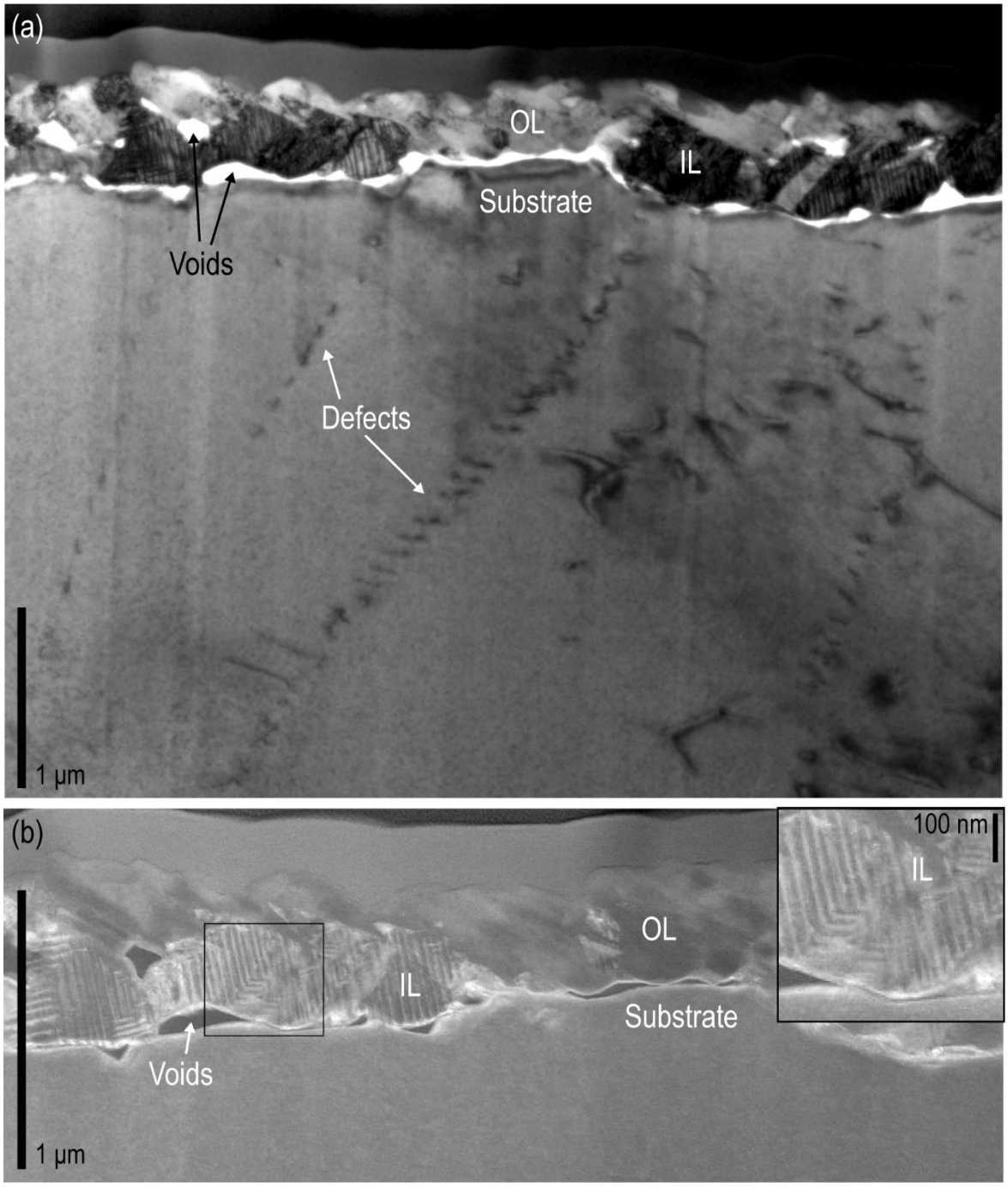

Figure 4.15. (a) CTEM BF image of the specimen's cross-section showing microstructural features: voids and defects in substrate. (b) STEM DF image of the cross-section showing the voids throughout the substrate and tweed-like patterns in the inner layer (IL).

The cross-section shown in Figure 4.15 also reveals regions where there is no inner layer (two-phase region of ε-Ti_2N and δ-TiN) and the outer layer (δ-TiN) is immediately above the substrate (although separated by voids). This suggests the possibility of α-Ti

transforming to fcc δ-TiN first and the appearance of the two-phase inner layer occurring afterwards in the microstructural evolution.

The volume expansion from transforming α-Ti into both ε-Ti_2N and rocksalt TiN is given in Table 4.2. As can be seen in the table, the volume change is large when transforming from hcp Ti into either of the nitrides but there is no significant volume change from transforming from ε-Ti_2N to δ-TiN. Since there are voids between the inner and outer layers, a simple volume expansion explanation does not suffice to explain the presence of voids from these experimental conditions.

Table 4.2. Normalized volumes and volume expansion in % relative to the initial volume of α-Ti for ε-Ti_2N and δ-TiN.

Phase	**Vol/Ti atom**	**Volume expansion (%)**
α-Ti	17.66	0
ε-Ti_2N	18.97	7.4
δ-TiN	19.04	7.8

In trying to explain void formation from a diffusion standpoint, there are two main possibilities: an inward N-dominant mechanism and an outward Ti-dominant mechanism (Figure 4.16). An outward Ti diffusion would be necessary to explain void formation but there is a scarcity of work discussing this in the literature since our current understanding of Ti nitriding relies on inward N-dominant mechanisms.

Voids have been observed in TiN from reacting titanium metal with a nitrogen atmosphere at 800-1200°C and in films generated from DC arc plasma jet [167,169]. Tamaki and others [167] observed three regions in the specimen: a two-phase region with α-Ti and ε-Ti_2N (A region), a two-phase region of ε-Ti_2N and δ-TiN (B region) and an outer layer of δ-

TiN (C region) and reported void formation throughout the B region and to a lesser extent in C region. McDonald and Wallwork [169] observed voids in the outer regions of the TiN scales, which formed at all temperatures tested. They proposed that outward Ti diffusion would be required to explain this porosity thought they admitted it was unclear as to why vacancies would condense to form pores rather than migrate to the free surface. Their reactions were determined to be dominated by inward N diffusion, but a small amount of outward Ti diffusion was proposed to explain the porosity found.

Assuming an equilibrium layer structure from the Ti-N phase diagram, the two different scenarios can be represented by the N and Ti fluxes drawn in Figure 4.16. For voids to form, an outward Ti diffusion would have to be larger than the inward N diffusion. This, again, could only partially explain the voids at the metal-scale interface but not the voids between the inner and outer layers. Furthermore, these do not contribute to our understanding of the peculiar void morphology at the metal-scale interface although asymmetrical fluxes could lead to different void morphologies (Figure 4.17). Additionally, the diffusivities reported from literature (Table 4.3) suggest that the Ti diffusion would be slower than the N diffusion throughout all possible phases of α-Ti (N), ε-Ti_2N and δ-TiN at 800°C.

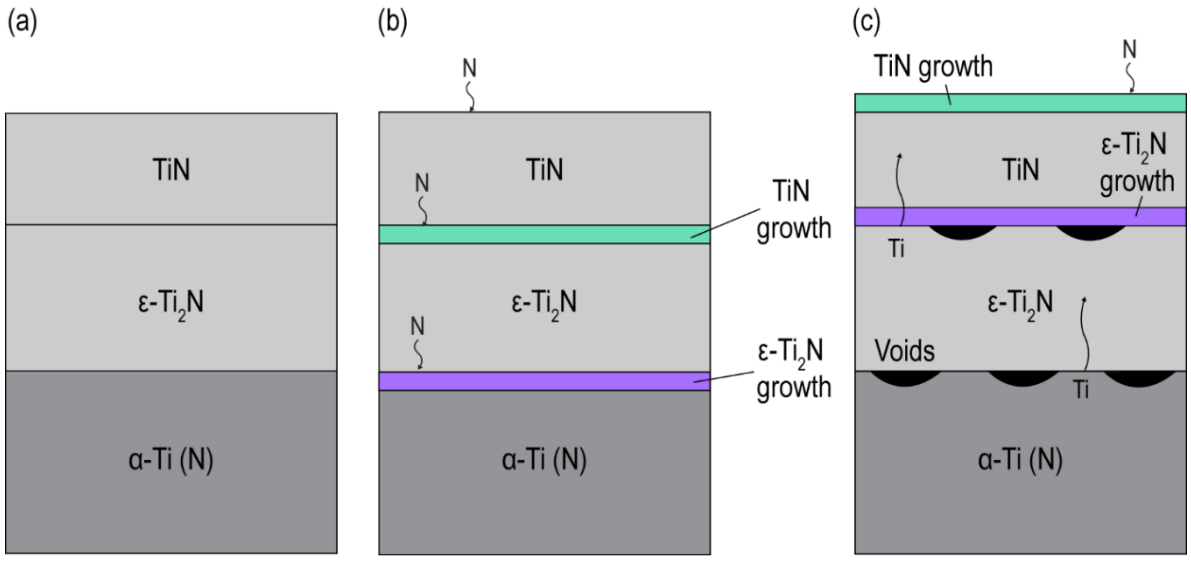

Figure 4.16. Schematics showing the (a) equilibrium layer structure at 800°C and nitride and void growth when Ti-N reactions are (b) dominated by inward N diffusion, or (c) outward Ti diffusion.

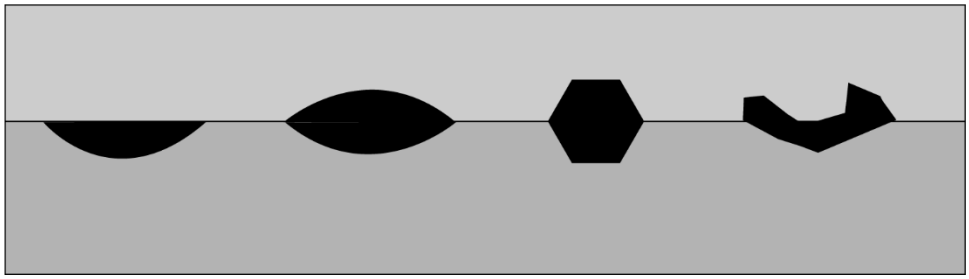

Figure 4.17. Examples of void morphology with the rightmost being representative of void morphology from the metal-scale interface in the specimen discussed in this chapter.

Table 4.3. Self-diffusivity of Ti and diffusivities of N through α-Ti and relevant nitrides.

Diffusing element	In phase	D at 800°C (m^2/s)	Reference
Ti	α-Ti	4×10^{-17}	[23]
N	α-Ti	1.4×10^{-16}	[36]
N	(α-Ti)	3.4×10^{-15}	[115]
N	ε-Ti_2N	1.4×10^{-14}	[115]
N	δ-TiN	1.6×10^{-16}	[115]

An alternative explanation would be considering the effects of grain boundary diffusion [119,170]. Void formation was attributed to the release of nitrogen during oxidation of TiN films, where grain boundaries provided a short diffusion path for oxidation [119]. Furthermore, the anisotropic nature of hcp Ti could also play a role in the location and size of voids forming due to the diffusivities in hcp Ti typically being faster parallel to the c-axis than to the a-axis. These two considerations would suggest that larger voids would form near or on grain boundaries.

In the analogue 25 h specimen from the appendix, the substrate was exposed from scale spallation occurring near the corner of the specimen. Since the substrate and inner layer are comparable, it can be inferred that this surface morphology would be representative of the one in the 25 h specimen discussed until now. From the cross-section of this specimen and the surface SEM of the substrate underneath the scale (Figure 4.18), it could be assumed that dislocations (seen in the substrate as dislocation ledges) may contribute to the understanding of the void formation mechanism. The surface displays varying depths that

form stair-like structures. If extracted from the top as would be done from FIB, these ledges would likely form V-shapes comparable to the V-shapes of the pores forming at the metal-scale interface seen in cross-section. While this is speculative, dislocations could explain the magnitude of these pores since an asymmetrical flux approach and a volume expansion change cannot on their own.

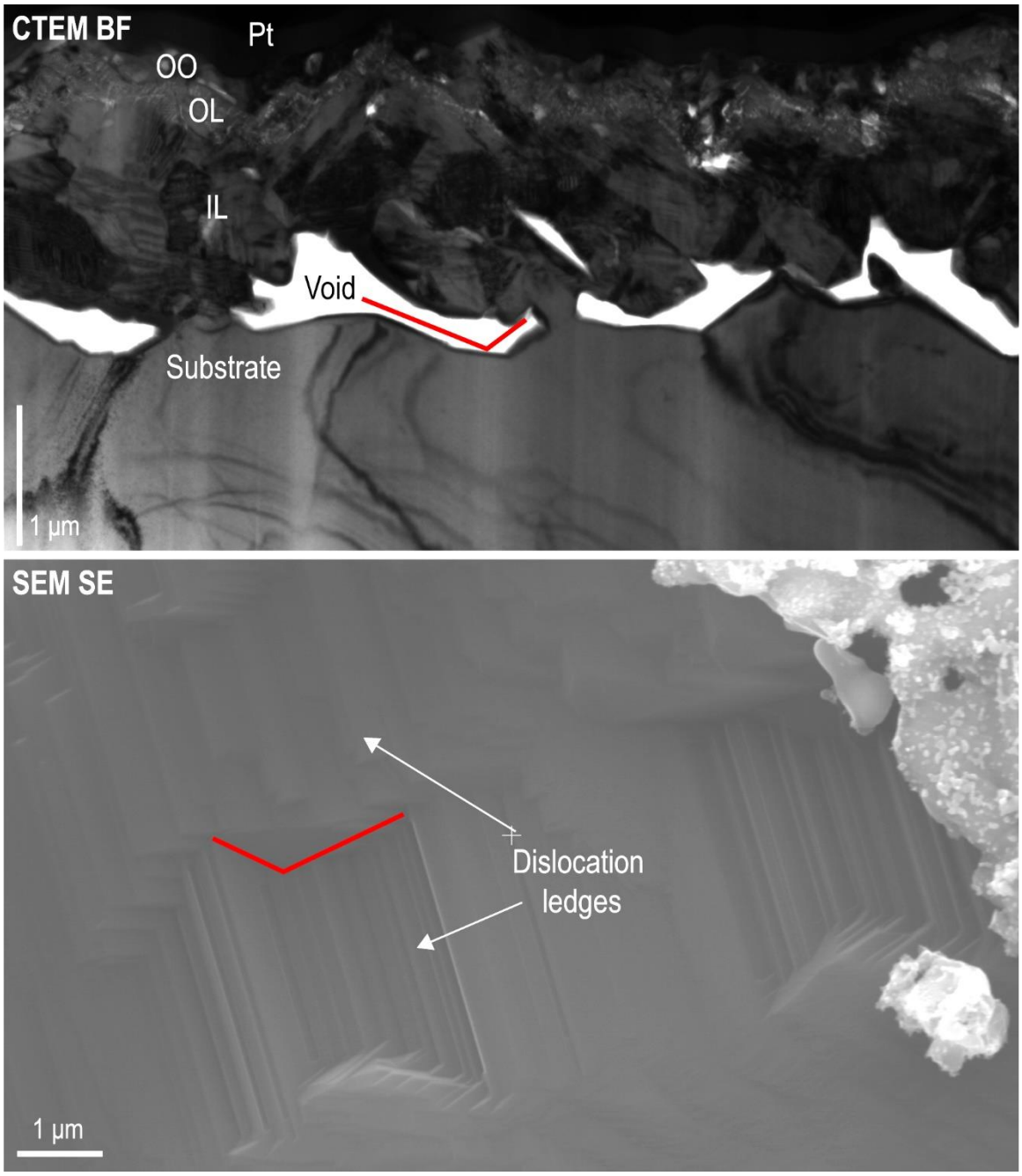

Figure 4.18. CTEM BF micrograph showing the analogue 25 h specimen which grows an O-rich outermost scale (OO). The inner scales and morphologies match the previous 25 h. SEM SE shows the substrate from a region where the scales spalled off. This region shows dislocation ledges which show similar shapes to the voids seen in cross-section at the metal-scale interface.

A final mechanism to be considered for void growth is the formation of porous zones seen in oxidation of pure metals (Figure 4.19) [93]. As growth stresses in the oxide arise, the scale must relax these stresses to maintain contact with the metal underneath. If the scale

does not lose contact with the substrate, voids may form at the metal-scale interface. The outward cation diffusion continues along with inner oxygen diffusion through the voids, which more readily occur along grain boundaries of the compact outer oxide scale. While a similar process could also occur with nitriding, the elemental maps from the specimens in this chapter also show oxygen concentration along the voids at the metal-scale interface. This suggests that the void formation and growth mechanism in this system likely involves a complex interplay with nitrogen and oxygen that contributes to the presence of voids at the metal-scale interface and in between the outer and inner layer.

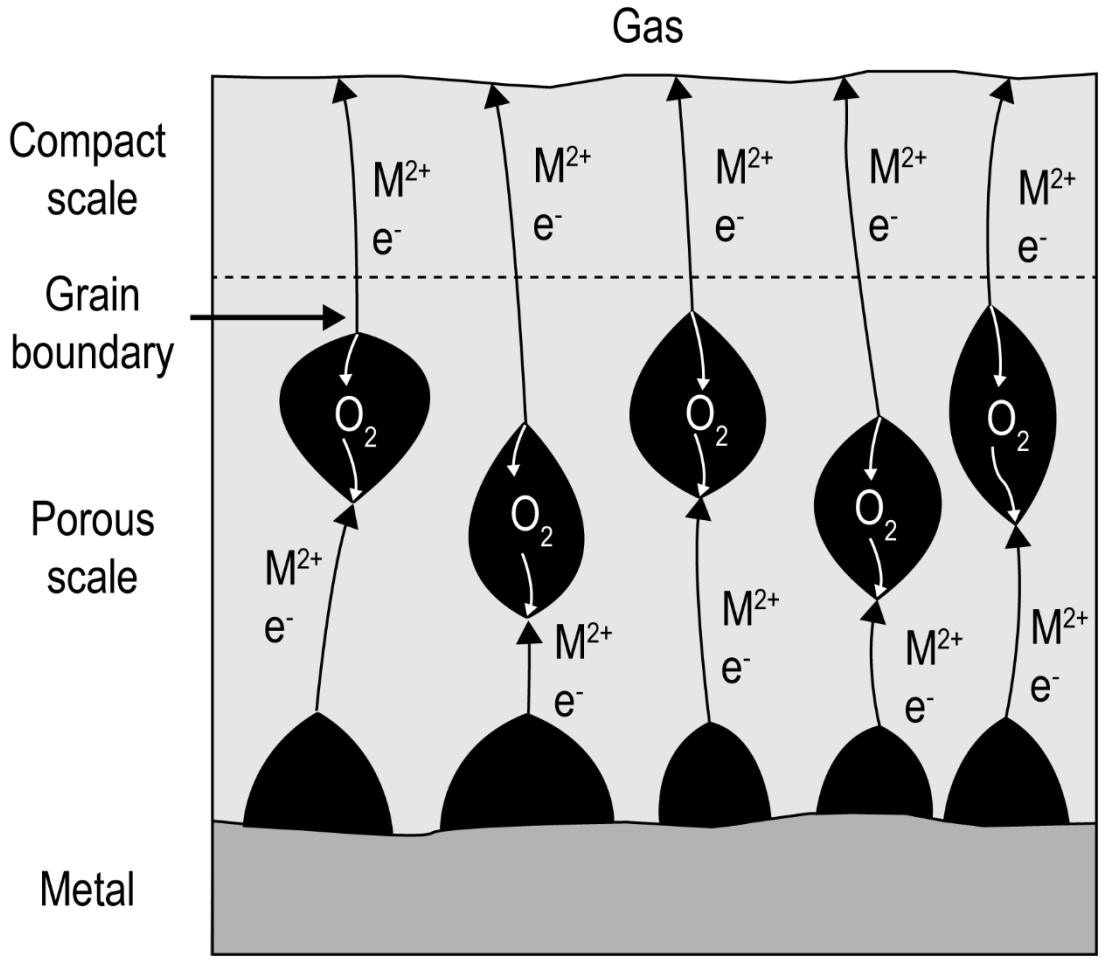

Figure 4.19. Formation of porous zone from metal-scale separation where the scale decomposes more readily at the grain boundaries. Image and caption adapted from [93].

4.2 Notes on microstructural evolution from shorter dwell times

The bulk of this chapter has been using the 25 h specimen since the shorter dwell times show similar features to this specimen. The 1 h specimen does not form any scale and its SAED patterns show strong reflections in the positions where they would be forbidden in α-Ti as discussed for the 25 h specimen. This suggests the formation of an α-Ti solid solution and an ordered phase with nitrogen and perhaps some oxygen ordering every other interstitial layer. At 9 h, a few grains appear whose SAED shows only a twinned δ-TiN with no additional reflections that would suggest a two-phase region (Figure 4.12). However, when obtaining SAED from the region of the substrate closest to the δ-TiN grains, the additional reflections corresponding to ε-Ti_2N can be seen (Figure 4.20). This suggests the presence of an ordering similar to ε-Ti_2N in the upper regions of the substrate, but not further into the metal grain. Additionally, this specimen also shows an orientation relationship between the hcp Ti and fcc TiN grains.

Given this evolution, it is possible that δ-TiN grains form first and the continued inward N diffusion from the TiN regions allows for the formation of ε-Ti_2N underneath while the N from the environment continues to supply nitrogen for the δ-TiN growth. Since the δ-TiN scale is thinner than the inner two-phase region in the 25 h, it is possible that δ-TiN reaches a critical thickness and continues to supply N to the two-phase region, resulting in a thin continuous δ-TiN outer scale at the 25 h dwell time. It is also noteworthy that voids are seen between the metal substrate and the δ-TiN grains at the 9 h despite the small size of these grains and their being discontinuous at this stage. This suggests that the transformation of hcp Ti to fcc TiN is a major factor in formation of voids in this system.

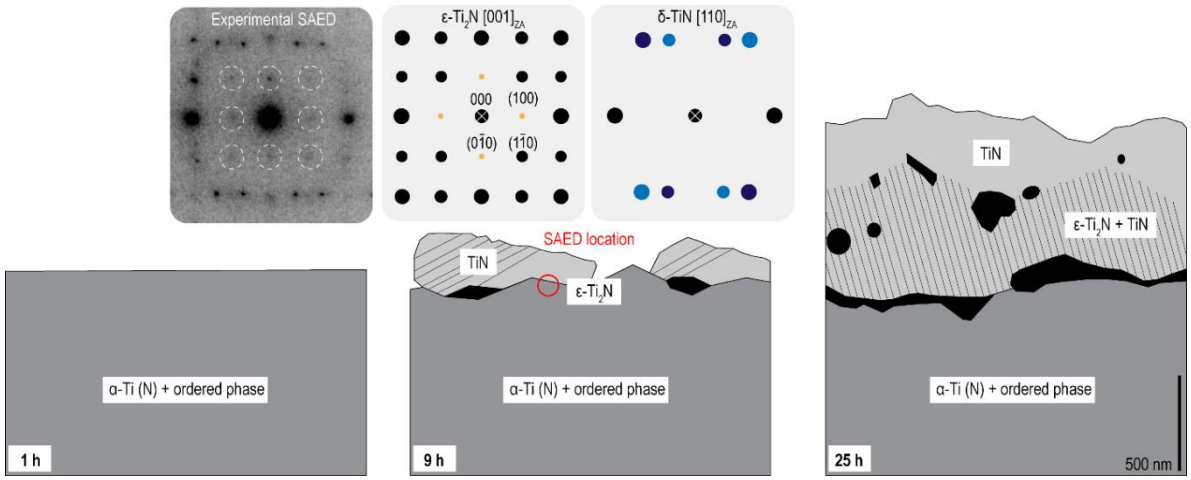

Figure 4.20. Schematic with proposed phase identification on the microstructures from 1, 9, and 25 h exposures to 800°C in parallel flow gettered Ar. Experimental SAED for the region between the outer scale and substrate in the 9 h is shown above next to relevant simulated diffraction patterns.

4.3 Conclusion

These results highlight the importance of considering nitrogen in the study of oxidation of titanium since early low partial pressure of oxygen studies rely on argon-based environments like the ones used in this research project. The major findings of these titanium studies with fast-cooled specimens exposed to parallel flow gettered Ar are:

- Specimens formed two scales with porosity along the metal-scale interface and in the inner-outer layer scale interface (Figure 4.21). The metal substrate shows evidence of α-Ti (N) solid solution formation well into the substrate from surface XRD as well as a possible hcp phase with nitrogen ordering every other interstitial layer similar to α" (staged Ti_2O). An inner layer is composed of a two-phase region with fcc rocksalt δ-TiN and a coherently-strained tetragonal ε-Ti_2N. The outermost layer is composed of twinned δ-TiN with a [110] twin axis and {111} twin plane.
- There is a strong orientation relationship between the metal substrate and the nitride scales growing above as evidenced by the electron diffraction patterns from the α-Ti

$[\bar{1}2\bar{1}0]$ and δ-TiN [110] zone axes. The hcp to fcc transformation in this system likely contains intermediate structures such as the coherently-strained tetragonal ε-Ti_2N seen in the two-phase region and by the possibility of long ordering or stacking faults in δ-TiN resulting in electron diffraction reminiscent of a 9R ordering.

- Voids are a salient feature of these specimens and are likely to be the result of a complex mechanism where dislocations, volume expansion, asymmetrical fluxes, and grain boundaries all play a role. Given the size, ubiquity, and morphology of the voids in this specimen, it is proposed that dislocations and an outward Ti flux are required to explain the void growth mechanism, but further work is needed to clarify this process.

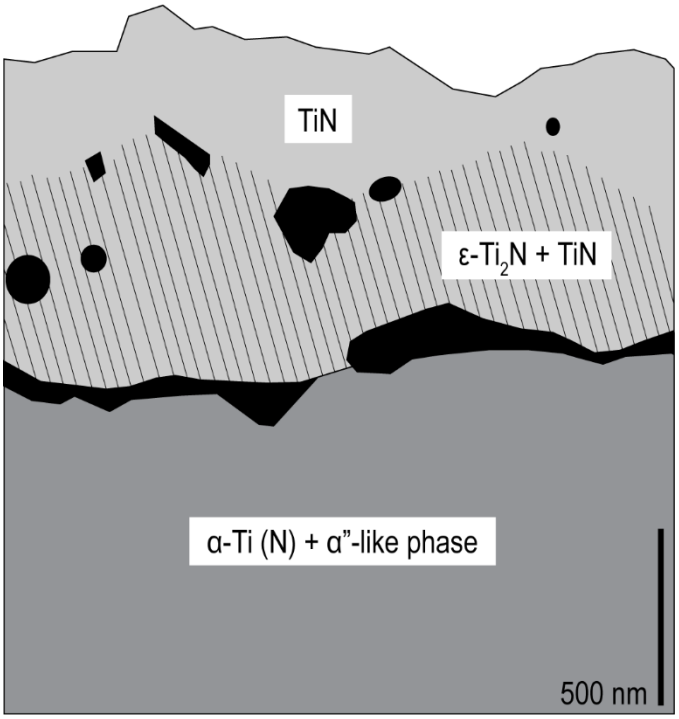

Figure 4.21. Summary of proposed phase identification for 25 h specimen exposed to gettered Ar in a parallel flow at 800°C.

4.4 Appendix discussing additional 25 h specimen for Chapter 4

Two specimens were generated using the same experimental conditions explained before and a 25 h dwell time at 800°C (Figure 4.22). Despite using the same parameters, one of these specimens formed an outermost O-rich phase that could be a Magnéli phase based on the evidence available. This once again shows the high sensitivity of titanium despite many similarities between the two specimens. In addition to variability in microstructures when changing experimental parameters, there is also some variability when using the exact same conditions. The rest of this analogue specimen shares features such as a two-phase region (ε-Ti_2N and δ-TiN) in the inner layer with tweed-like features and a thin twinned TiN layer above this. Pores are also located in similar locations and show comparable morphologies although this specimen shows more pronounced V-shapes in the voids at the metal-scale interface. This section will discuss the differences and similarities between these two specimens.

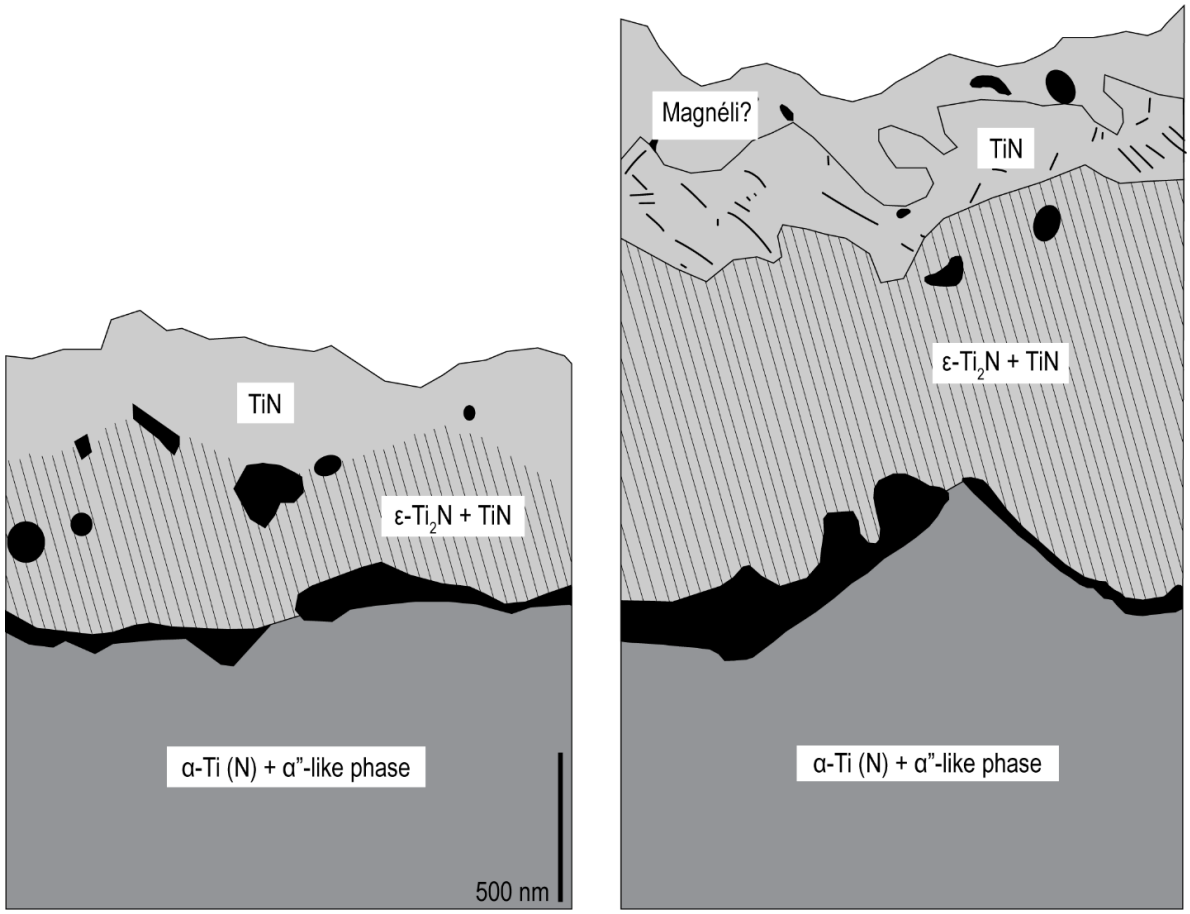

Figure 4.22. Schematic of two resulting microstructures from exposing Ti to gettered Ar with a parallel flow at 800°C for 25 h and fast-cooling at the end of the dwell time. Layers are labeled with the proposed phase identification. This chapter focused on the specimen on the left side and this appendix discusses the specimen on the right-hand side.

As seen in the elemental maps, the outermost layer shows an O signal significantly higher than its N signal (Figure 4.23). There is, as in the previous 25 h specimen, a slight O concentration around the voids at the metal-scale interface. The oxygen content remains below 10 at% O as before in the OL, IL, and substrate regions, while the outermost scale (OO) shows ~60 at% O content with N < 10 at%.

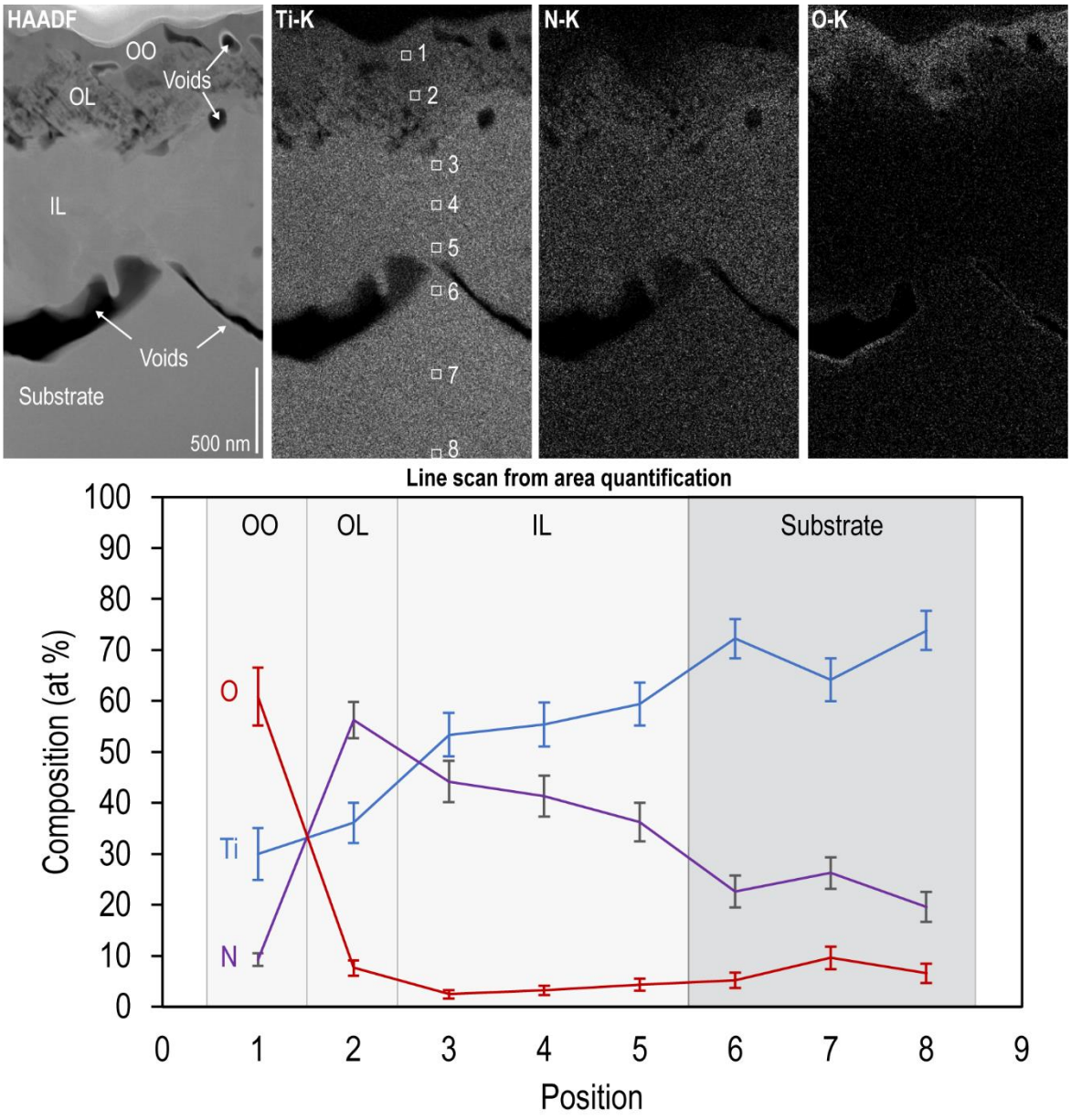

Figure 4.23. Cross-sectional micrographs from STEM HAADF and corresponding STEM EDX elemental maps for 25 h specimen with outermost O-rich layer (OO). Areas used for quantification are shown in the Ti-K elemental map and its values were used to construct the line scan below. O values reach ~60 at% O in the outermost layer (OO) while N values are highest within the OL and IL regions and decrease going into the substrate.

Comparing the line scans from both of these specimens, the general trends remain in the OL, IL, and substrate regions albeit with slightly different values for Ti, N, and O (Figure 4.24). The largest difference is in the nitrogen content in the metal substrate immediately

underneath the inner layer, where the first 25 h specimen has 36 at% N and 2 at% O and the analogue 25 h specimen has a lower N content of 22 at% N and a slightly higher 5 at% O. The low oxygen content in both specimens might provide supporting evidence for the hypothesis that nitride layers act as oxygen diffusion barriers preventing inward O diffusion into the metal substrate. This is perhaps a bit surprising given the significant porosity in these scales which could act as diffusion channels and where elemental maps suggest a concentration of oxygen. The analogous specimen exposed to counter flow gettered Ar, which will be discussed in the following chapter (see Figure 5.22), maintains the trend of a higher N content than O content within the substrate despite no scale formation.

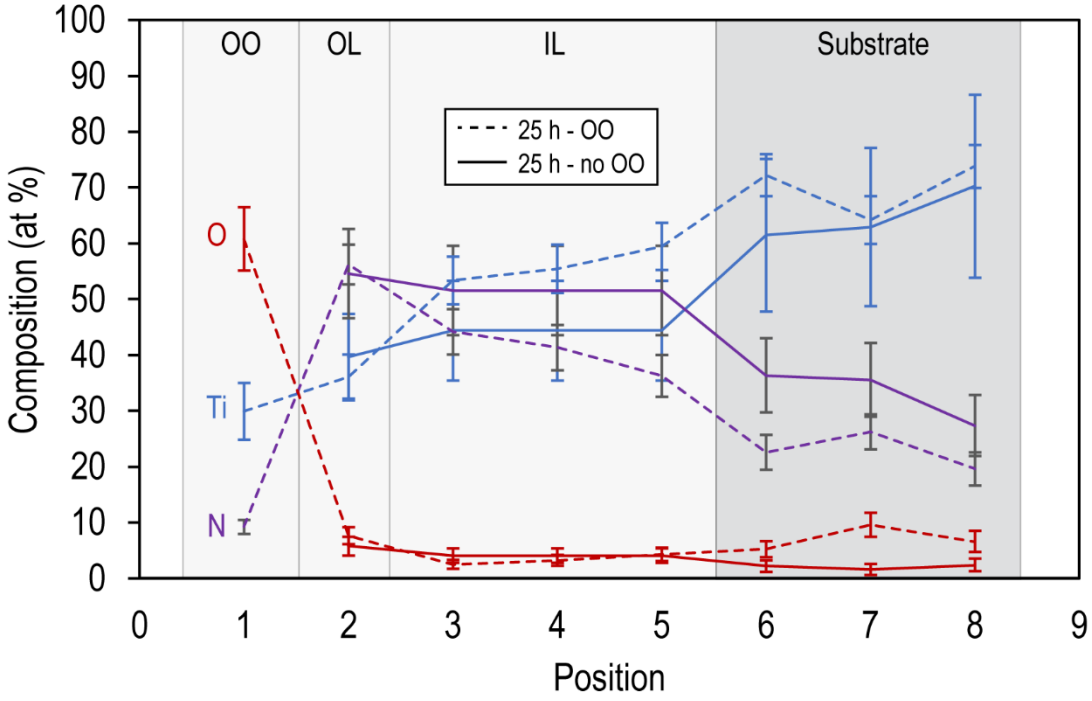

Figure 4.24. Comparison of the line scans for the two 25 h specimens where the dashed lines are for the specimen with O-rich layer (OO) and solid lines are for the specimen with only nitride formation. With the exception of the OO region, the Ti, N, and O plots show comparable trends in both specimens in the OL, IL and substrate regions.

From electron diffraction of the different layers, the same features from the previous 25 h specimen can be observed. Electron diffraction from the inner layer shows a two-phase

region with ε-Ti_2N and twinned δ-TiN once again as shown from the experimental SAED from this specimen's IL region (Figure 4.25).

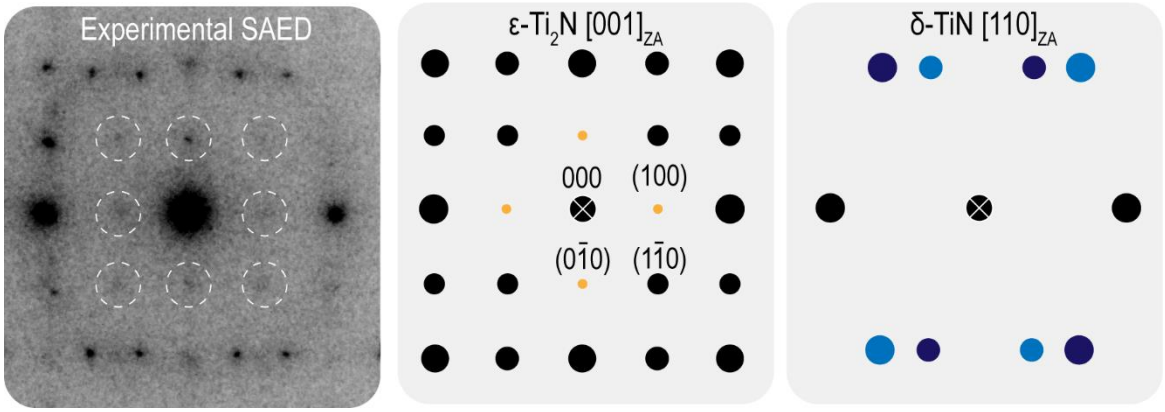

Figure 4.25. Experimental SAED from the tweed-like IL region in this specimen can also be explained with the presence of both nitrides, ε-Ti_2N and a twinned rocksalt δ-TiN as shown by the simulated SAED patterns. In δ-TiN simulation, black reflections are the same in both orientations whereas the dark blue and light blue denote the original and twinned reflections.

Since the OO and OL regions were difficult to discern during SAED acquisition, the available pattern for this region unfortunately samples both of these layers. This pattern (Figure 4.26) shows the same twinned rocksalt pattern from the previous 25 h. However, additional spots (encircled in red) can be observed towards the bottom right corner of the image. These spots can correspond to a rocksalt structure (α-TiO or δ-TiN) or a Magnéli phase such as Ti_3O_5 or Ti_4O_7. The simulated patterns for these phases match the positions of the additional spots from the experimental pattern and their main difference is in their intensities. TiO shows even intensities while Magnéli phases have varying expected intensities. This cannot be used reliably to distinguish between these phases from the given experimental pattern.

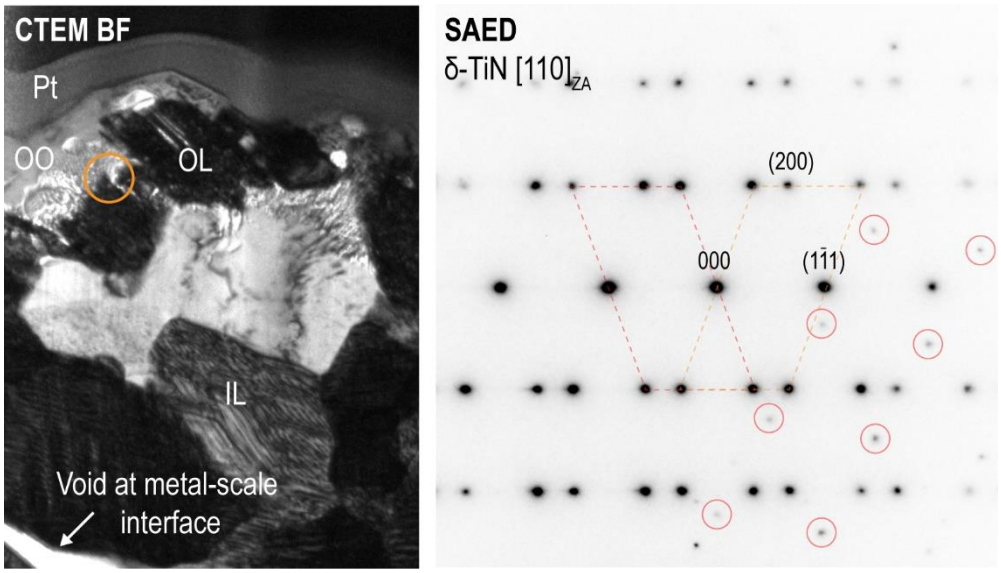

Figure 4.26. CTEM BF image of the specimen's cross-section showing where the experimental SAED was taken. SAED shows twinned rocksalt pattern as before and additional reflections circled in red that show a pattern that most closely matches rocksalt.

Acquiring Raman spectra afterwards allows for a quick comparison between these two specimens since the specimen with an outer oxide shows peaks around 103 cm^{-1} and 150 cm^{-1}, and faint ones near 200 cm^{-1}, 300 cm^{-1} and 478 cm^{-1} while the initial 25 h specimen shows no significant peaks. The spectrum from the analogue 25 h specimen is most similar to simulated Magnéli Raman spectra [139] and does not match the Raman spectra expected for rocksalt TiN [146] nor TiO phases [171] suggesting that this phase is either a Magnéli phase or a structure similar to it.

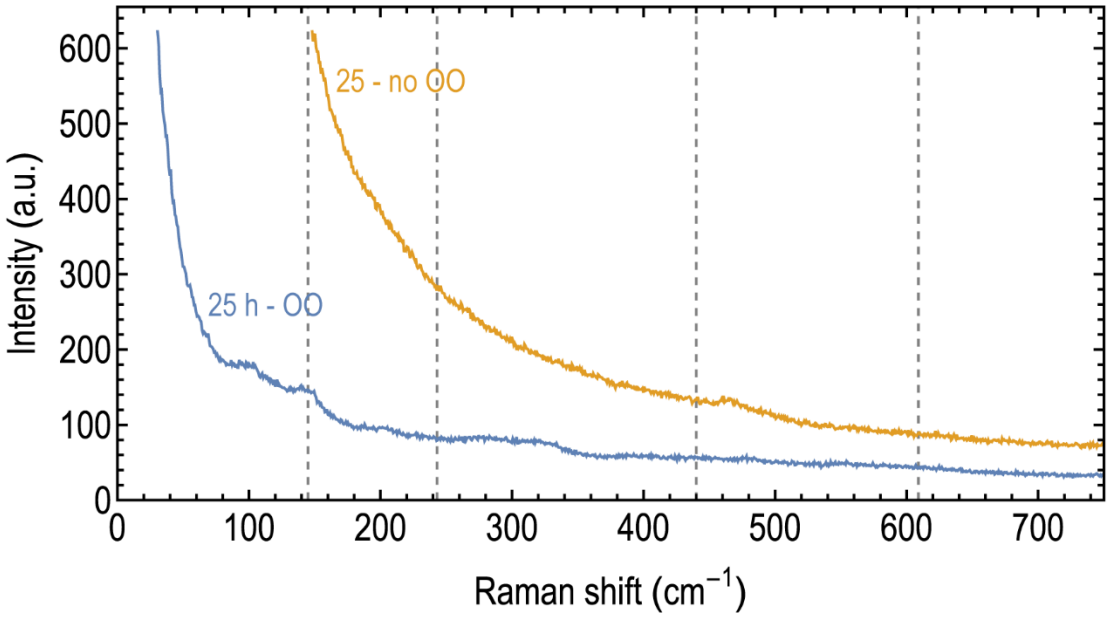

Figure 4.27. Raman spectra comparison of both 25 h specimens where the specimen with no OO (yellow line) shows no significant peaks and the one with OO (blue line) shows peaks around 103 cm^{-1} and 150 cm^{-1}, and faint ones near 200 cm^{-1}, 300 cm^{-1} and 478 cm^{-1}. Dashed gray lines show the expected positions for rutile Raman modes.

The XRD pattern from this specimen shows several additional peaks to the 25 h specimen with only nitrides (Figure 4.28). Checking for the presence of the TiO and Magnéli phases, there are peaks that could match these phases but not all peaks for a Magnéli Ti_4O_7 phase are visible. Spark plasma sintering of TiN reveals the formation of Ti_4O_7 in both vacuum and nitrogen flow environments [172]. It is possible that some regions of this specimen form Magnéli phases but that these form with a preferred orientation that does not show all of the expected peaks from a pure Magnéli phase.

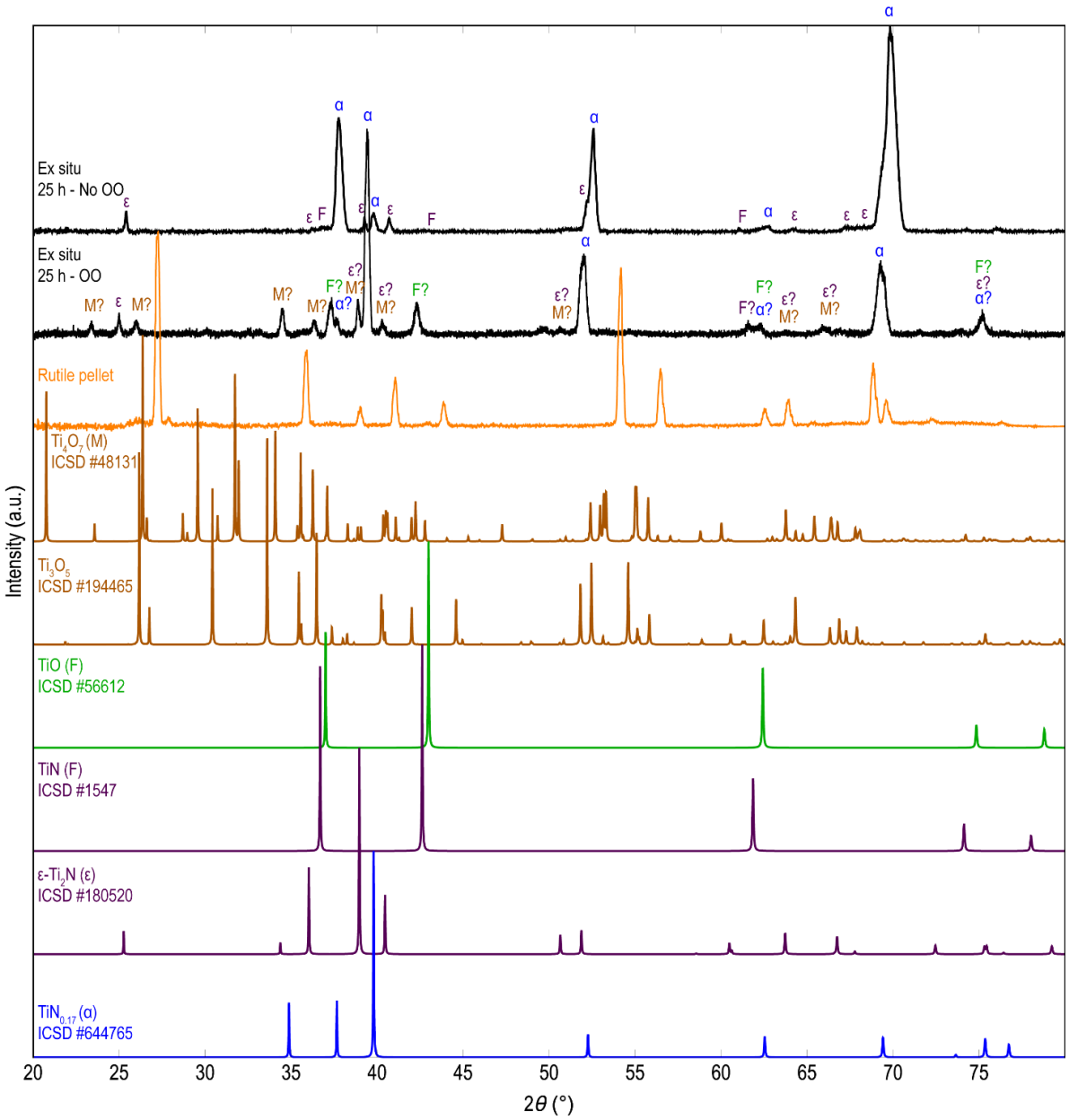

Figure 4.28. Experimental XRD patterns for both 25 h specimens (black) compared to reference spectra from rutile pellet and ICSD phases (color-coded based on type of phase). The analogue 25 h specimen with the OO layer shows additional peaks that can correspond to some of the peaks expected from a Magnéli Ti_4O_7 and may show fcc peaks based on TiO and/or TiN.

In summary, the 25 h specimen with an OO scale shares the features of the thin δ-TiN scale and innermost two-phase region (ε-Ti_2N and δ-TiN) with the nitride-only 25 h specimen. The OO scale could be either a Magnéli Ti_4O_7, a rocksalt α-TiO, or perhaps a mixture of both. An intriguing question is why an O-rich scale forms in one specimen but not

the other given the use of the same experimental conditions. One possible scenario is that the nitrides-only 25 h specimen did form an oxide scale initially, but this dissolved into the layers underneath. This would result in a higher oxygen content in the substrate of the nitrides-only specimen than its OO-containing counterpart, which is not the case from comparing the line scans from STEM EDX (Figure 4.24). An alternative scenario is that there were subtle changes in the temperature during cooling that resulted in conditions that favored oxide formation. However, the nitride scales remain the same in the inner regions and the oxide layer is thin. This provides supporting evidence for the nitrogen effect of reducing oxidation, although the mechanism for this remains unclear.

5 hcp Titanium under Counter Flow Gettered Argon at 800°C (Slow-Cooled) in Tube Furnace

As evidenced in Chapter 4, the nitrogen content in the gettered argon gas used for these experiments is sufficient to generate nitrides and can supersede the formation of titanium oxides. This further complicates the understanding of titanium oxidation since even minute nitrogen contents from low interstitial environments like gettered Ar can significantly impact the phases formed and their growth mechanisms. This chapter will use the same gettered argon gas but with an opposite gas flow direction and furnace-cooling in contrast to the fast-cooling used in the previous chapter (named **"slow-cooled in counter flow Ar"** in Chapter 3). The results show the importance of further developing the community's understanding of the ternary titanium-nitrogen-oxygen system.

These slow-cooled specimens form layered structures with significant and varying degrees of porosity throughout the scales. The scales in these specimens are much thicker than those from the fast-cooled specimens, suggesting that significant phase transformations occur during cooling in this set of experiments. In contrast to the previous chapter, these specimens form oxides, nitrides, and oxynitrides. The phases formed in these layers are lower oxides (Ti_2O_3 corundum), Magnéli phases (Ti_3O_5 and Ti_4O_7), rutile, as well as titanium nitrides and rocksalt oxynitride phases. As in the previous chapter, there is evidence of interstitial ordering in the metal. There, however, is additional ordering in the interfacial layer developed in the 9 h and 25 h specimen. This interfacial layer is likely a combination of various phases with varying interstitial orderings of nitrogen and oxygen.

An inner layer is formed in both 9 h and 25 h specimens which is identified as a rocksalt structure that is likely an oxynitride or a combination of varying compositions of TiN and

TiO, which all have the same rocksalt structure. This rocksalt shows an orientation relationship with the hcp substrate underneath it and also shows evidence of long period stacking ordering (LPSO) structures from electron diffraction patterns. The phase identification for the developed scales and discussions of their growth mechanisms will be described in this chapter. Areas of further exploration will also be proposed.

5.1 Results and discussion

The furnace-cooled specimens showed the formation of layered structures with significant porosity in outer oxide scales of rutile in the 9 h and 25 h and nanopores in inner layers of an fcc titanium oxynitride in these two specimens. The 1 h specimen, in contrast, does not show any evidence of nitride or oxynitride formation and, instead, forms a two-layer scale of lower oxides Ti_2O_3 corundum and Magnéli phases. Notably, this short dwell time specimen does not form rutile as is expected and seen in the longer dwell times. The microstructures and phase identifications of the 1, 9, and 25 h dwell specimens are summarized in Figure 5.1. This section will discuss their characterization for phase identification, orientation relationships between the substrate and scale, and the formation of the different types of pores.

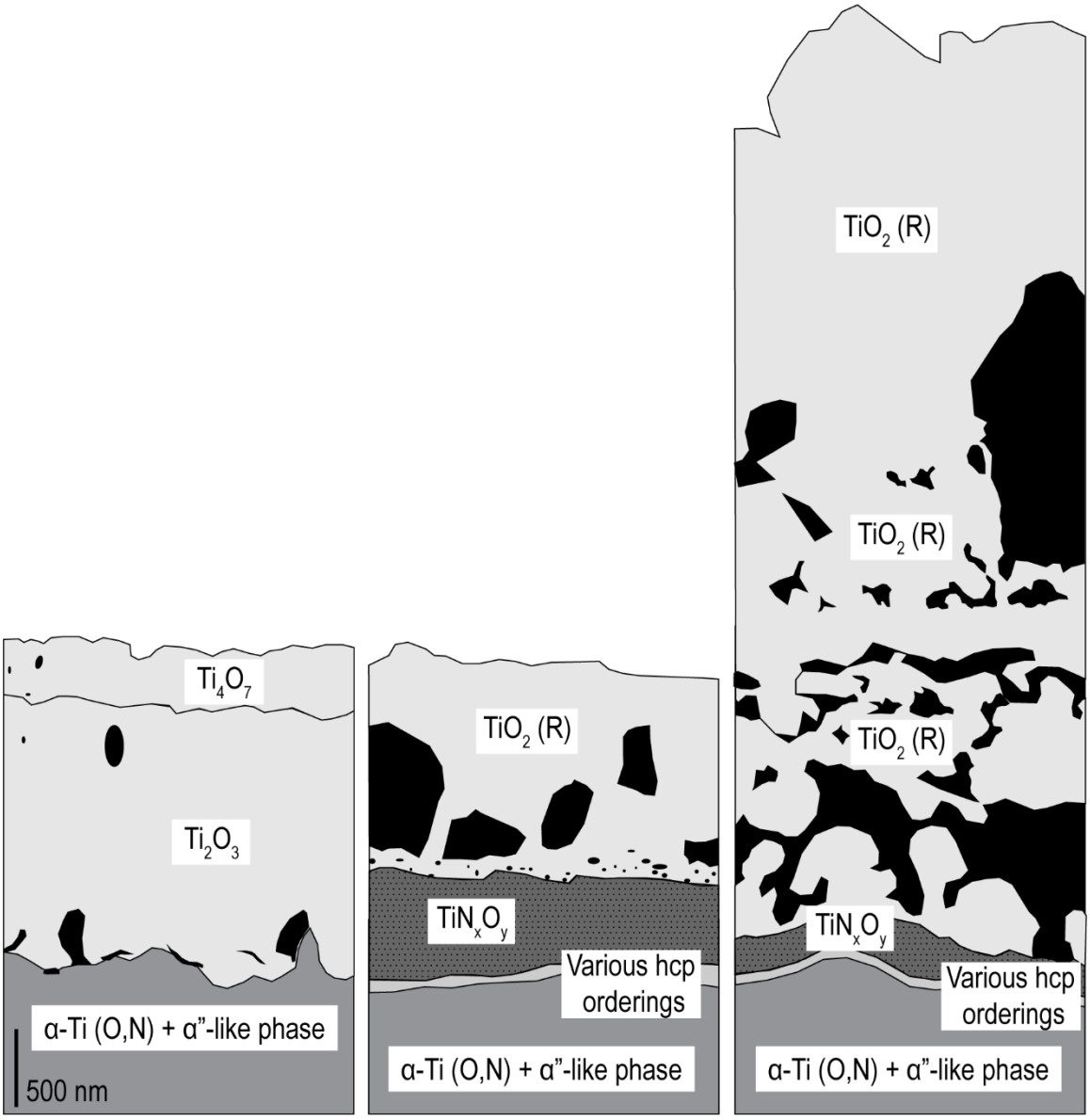

Figure 5.1. Summary of microstructures and proposed phase identification for slow-cooled specimens exposed to gettered Ar in a counter flow at 800°C for 1, 9, and 25 h.

5.1.1 Phase identification

The surface morphology of these specimens shows voids between the surface grains, and the eventual formation of significantly faceted grains (Figure 5.2). In the 1 specimen, the surface shows strand-like phases (~120 nm thick) that coarsen into grains in the 9 h and 25 h specimens and many small voids (~70-200 nm) throughout the surface. While some facets

can be seen in the 9 h grains (~500 nm - 2 μm, with most grains < 1 μm), they are clearer and more pronounced in the 25 h specimen, where grains are on average between 1.5 and 2 μm. The voids in the 9 h specimen are all close to 100 nm in size and grow to 200-500 nm in the 25 h specimen. Void size generally increases with increasing dwell time, while the number of voids visible on the surface decreases.

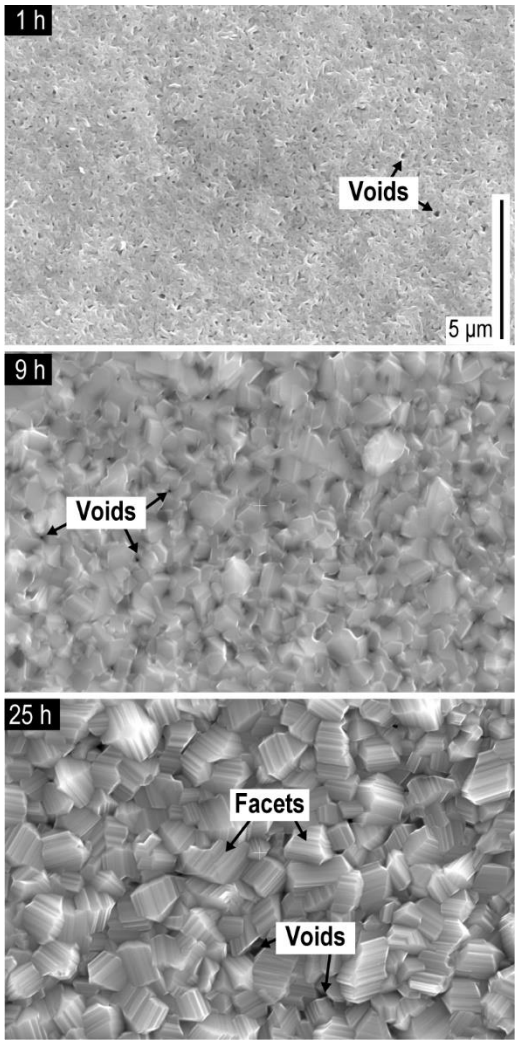

Figure 5.2. Top-view SE SEM micrographs of Ti oxidized ex situ at 800°C in counter flow gettered Ar for 1 h, 9 h, and 25 h slow-cooled after dwell time.

The cross-sections of the specimens reveal the formation of scales composed of at least two layers (Figure 5.3). The 1 h specimen shows a two-layer structure with equiaxed grains (~150-200 nm) in the outer oxide (OO) and columnar grains (~1.5 μm long and 250

nm wide) in the inner oxide (IO). There is some porosity (~200 nm) within the inner oxide as well as close to the metal-scale interface (~50-150 nm). At 9 h, the overall scale is surprisingly of a similar thickness (1.8-2.1 μm) to the 1 h specimen (1.7-2 μm) albeit with an entirely different microstructure. There are three layers developed in this scale with a significant porosity in the outer oxide in between grains (~180-700 nm) and near the OO-IL interface (~30-60 nm). There are also small voids (~10-50 nm) throughout the layer labelled 'IL' for 'inner layer'. At 25 h, the overall scale thickness increases significantly (5.3-6 μm) and the outer oxide has grown into larger grains (~2.7 μm in length). There is an inner oxide region in this specimen with smaller, almost equiaxed grains (~350-650 nm) that are separated by large voids and where the specimen seems to be spalling from its inner region near the metal substrate. Above the metal substrate there are two thin scales labelled 'IFL' for interfacial layer (~80 nm thick) and 'IL' (~180 nm thick). The grains above the 'IL' correspond to the inner oxide region as these grains are the same composition and phase as the ones in the spalling region (confirmed by STEM EDX and electron diffraction patterns).

From the elemental maps (Figure 5.3), the scale from the 1 h specimen shows a significant oxygen content in its outer and inner oxide layers and no significant nitrogen concentration anywhere in the specimen. In the 9 h, a significant nitrogen content can be seen in the 'IL' and 'IFL' region. While the 'IL' region (~450-520 nm) shows some oxygen signal from the elemental maps, there is an oxygen-deficient region immediately underneath in the 'IFL' region (~60-120 nm). In the 25 h specimen, similar trends are seen to the 9 h specimen with the outer oxide from the 9 h converting into an outer and inner oxide region in the 25 h, and the 'IL' and 'IFL' regions becoming thinner (~180 nm and ~80 nm respectively) than in

the 9 h. As in the 9 h specimen, the ‘IFL’ region is also oxygen-deficient compared to its ‘IL’ region.

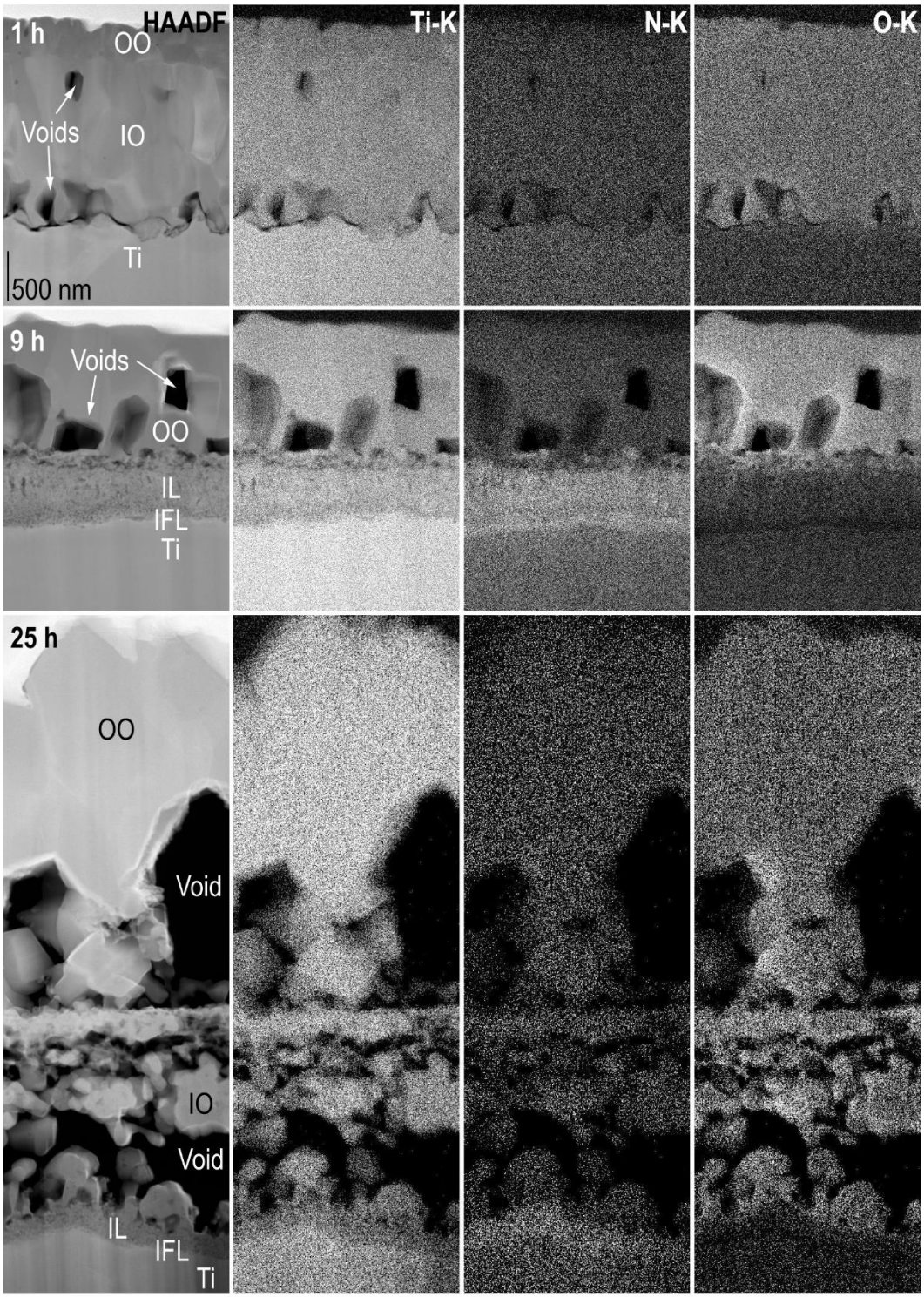

Figure 5.3. STEM HAADF cross-sectional micrographs and corresponding STEM EDX elemental maps for Ti foil exposed at 800°C in counter flow gettered Ar for (top row) 1 h, (middle row) 9 h, and (bottom row) 25 h showing Ti, N, and O signal. Features and scales are labelled in the HAADF images where OO is “outer oxide”, IO is “inner oxide”, IL is “inner layer”, and IFL is “interfacial layer”.

Looking at the line scans for each individual dwell time, the compositions from the STEM EDX quantification provide additional information about the phases possibly forming and the relative concentrations of nitrogen and oxygen throughout the specimen. In the 1 h specimen (Figure 5.4), the outer oxide shows a slightly larger oxygen composition than its inner oxide. The metal substrate shows significant contents of both nitrogen and oxygen of approximately 22 at% N and 24 at% O at 500 nm from the metal-scale interface. For nitrogen, this value is above the expected saturation composition from the Ti-N phase diagrams and oxygen is below its expected solubility limit of 33 at% O. Since α-Ti has large solubility limits expected for oxygen and nitrogen, it is possible that the hcp matrix can also dissolve large amounts of both nitrogen and oxygen. It is also possible that the incorporation of nitrogen could boost the overall solubility for both interstitials as has been proposed from the increased solubility of hydrogen in hcp Ti from nitrogen or oxygen incorporation [173].

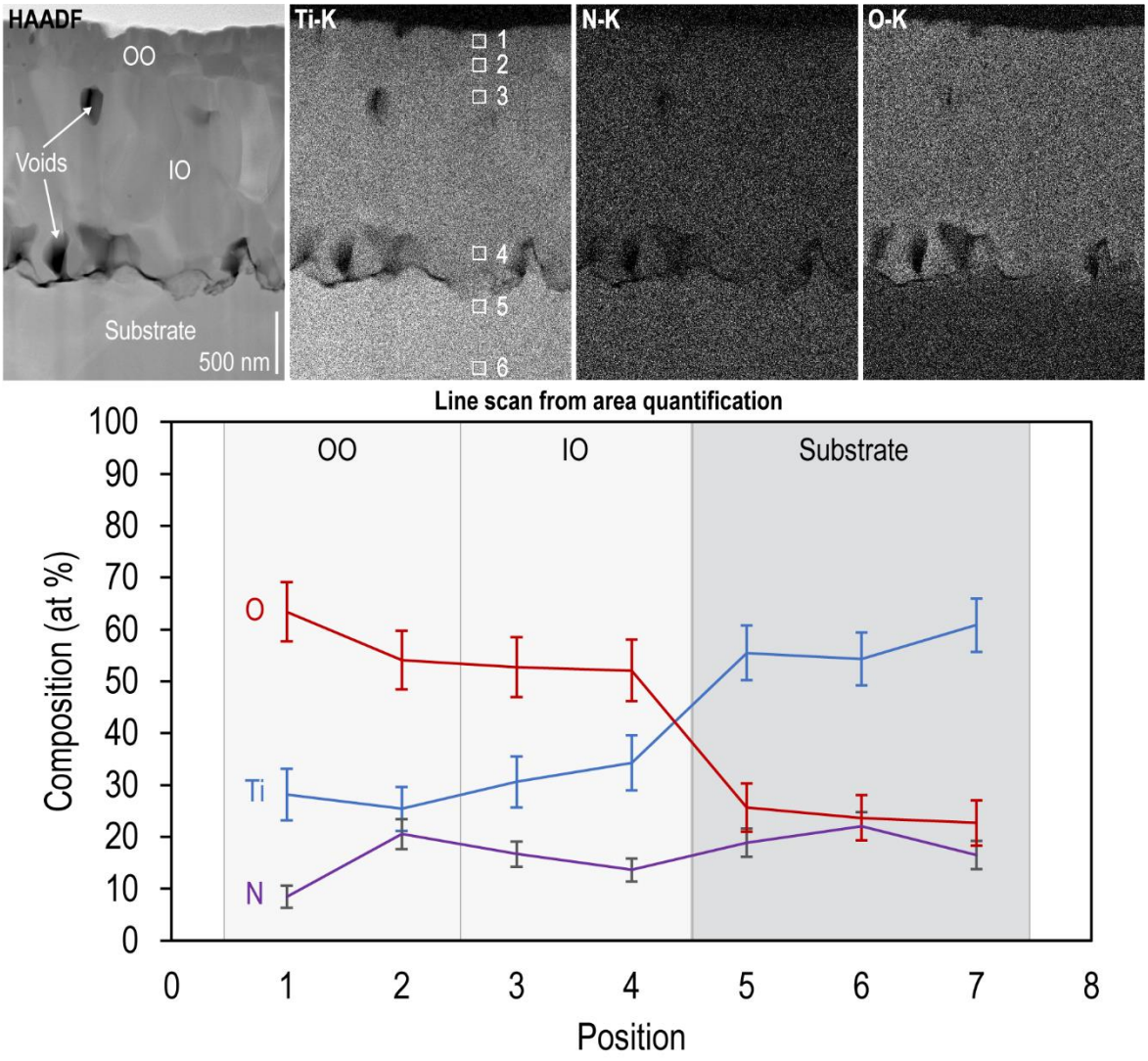

Figure 5.4. Cross-sectional micrograph for 1 h specimen from STEM HAADF and corresponding STEM EDX elemental maps. Areas used for quantification are shown in the Ti-K elemental map and its values were used to construct the line scan below. Oxygen content is highest in the OO layer and higher than the nitrogen content in the IO layer and substrate.

The line scan from the 9 h specimen shows the difference between the developed layers more clearly than just by viewing the elemental maps (Figure 5.5). In the outer oxide region, the oxygen content is shown around the 60 at% range and drops to below 20 at% O in the IL and further below 10 at% O in the IFL regions. In the metal substrate the nitrogen content (23 at% N) is higher than the oxygen content (18 at% O) at 500 nm from the metal-scale interface, which is the opposite of the 1 h specimen. The nitrogen content stays

consistent near 50 at% N in both the IL and IFL layers, a composition suggesting TiN formation.

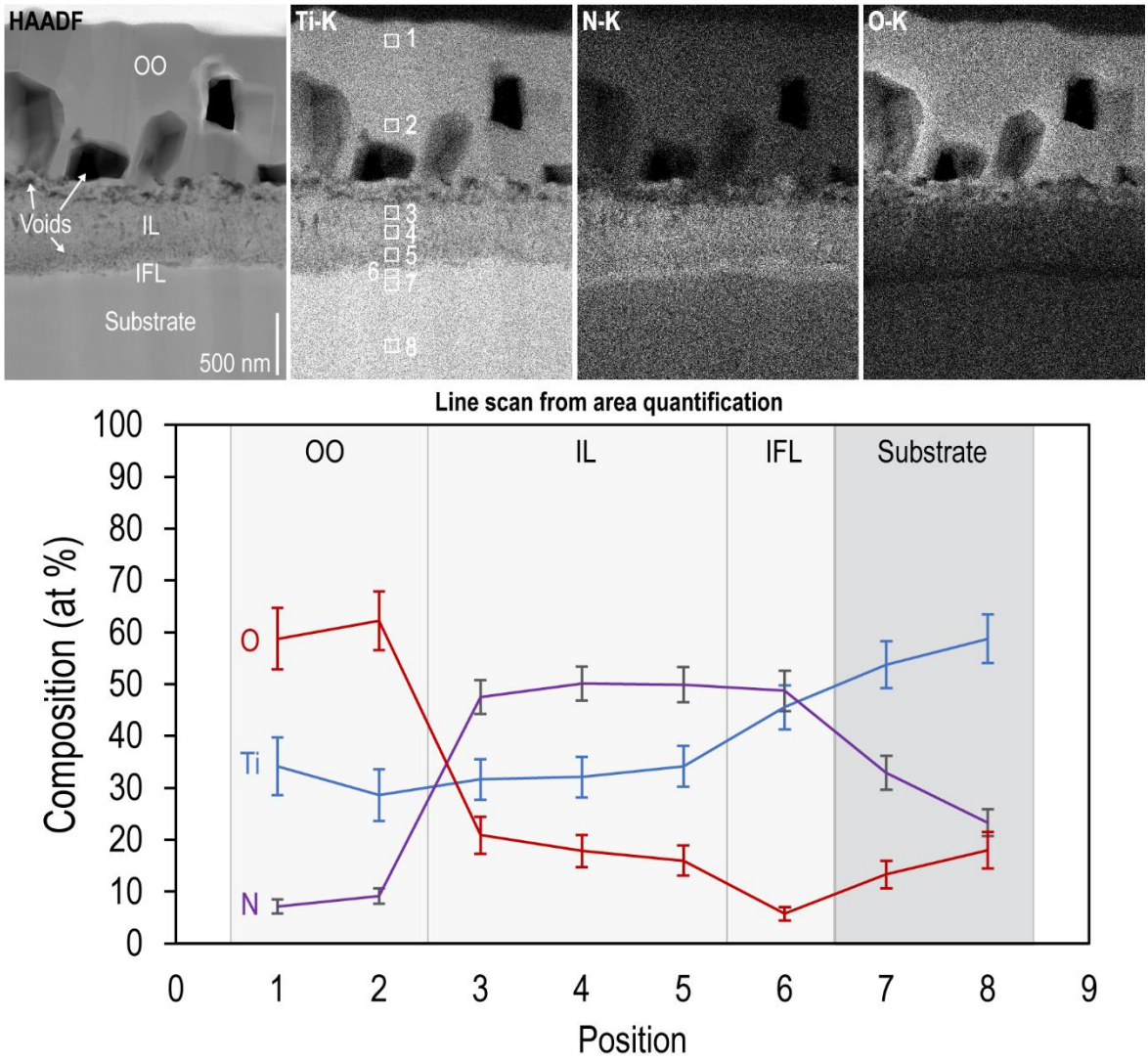

Figure 5.5. Cross-sectional micrograph for 9 h specimen from STEM HAADF and corresponding STEM EDX elemental maps. Areas used for quantification are shown in the Ti-K elemental map and its values were used to construct the line scan below. Oxygen content is highest in the OO layer and reduces to values lower than the nitrogen content in the IL layer. In the IFL layer, the oxygen content further reduces below 10 at% and increases again in the substrate. Nitrogen content is highest in the IL, IFL, and substrate regions.

Finally, the 25 h specimen shows high oxygen contents throughout most of the scale with the exception of IL and IFL layers immediately above the metal substrate and underneath the inner oxide grains (Figure 5.6). The oxygen content varies from ~50-63 at%

throughout the outer and inner oxide layers with negligible nitrogen contents (3 at% N is the highest value with 0 at% being the lowest). The IL region shows a composition of 42 at% N and 25 at% O while the IFL has 39 at% N and 4 at% O. These compositions suggest the formation of a titanium nitride δ-TiN in the IFL and an oxynitride in the IL region. It is important to remember that TiN and Ti oxynitrides have the same rocksalt structure, and that there are a wide range of compositions that may form due to different vacancy and interstitial orderings. Even the lower value of 39 at% N in the IFL is within the expected composition of a rocksalt TiN phase. In this specimen, the oxygen is higher than the nitrogen in the metal substrate, coinciding with the trend initially seen in the 1 h specimen. An elemental map zooming in on this interfacial region confirms this trend with 6 at% N and 18 at% O contents in the substrate (Figure 5.7).

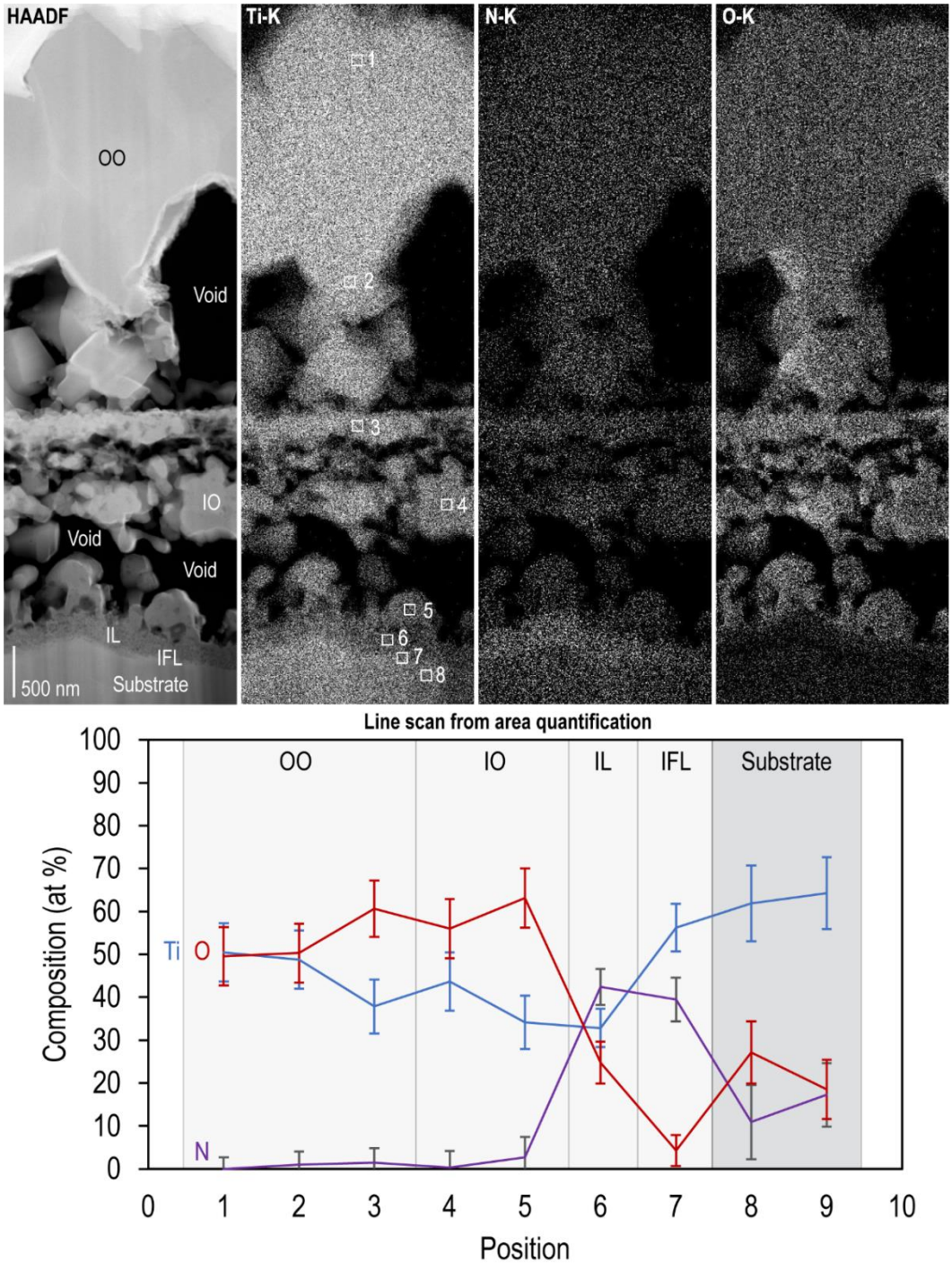

Figure 5.6. Cross-sectional micrograph for 25 h specimen from STEM HAADF and corresponding STEM EDX elemental maps. Areas used for quantification are shown in the Ti-K elemental map and its values were used to construct the line scan below. Oxygen is highest in the OO and IO layers where nitrogen content is negligible. Nitrogen content is highest in the IL and IFL layers. Oxygen content is higher than nitrogen in the substrate near the interface but is comparable to nitrogen 500 nm into the substrate.

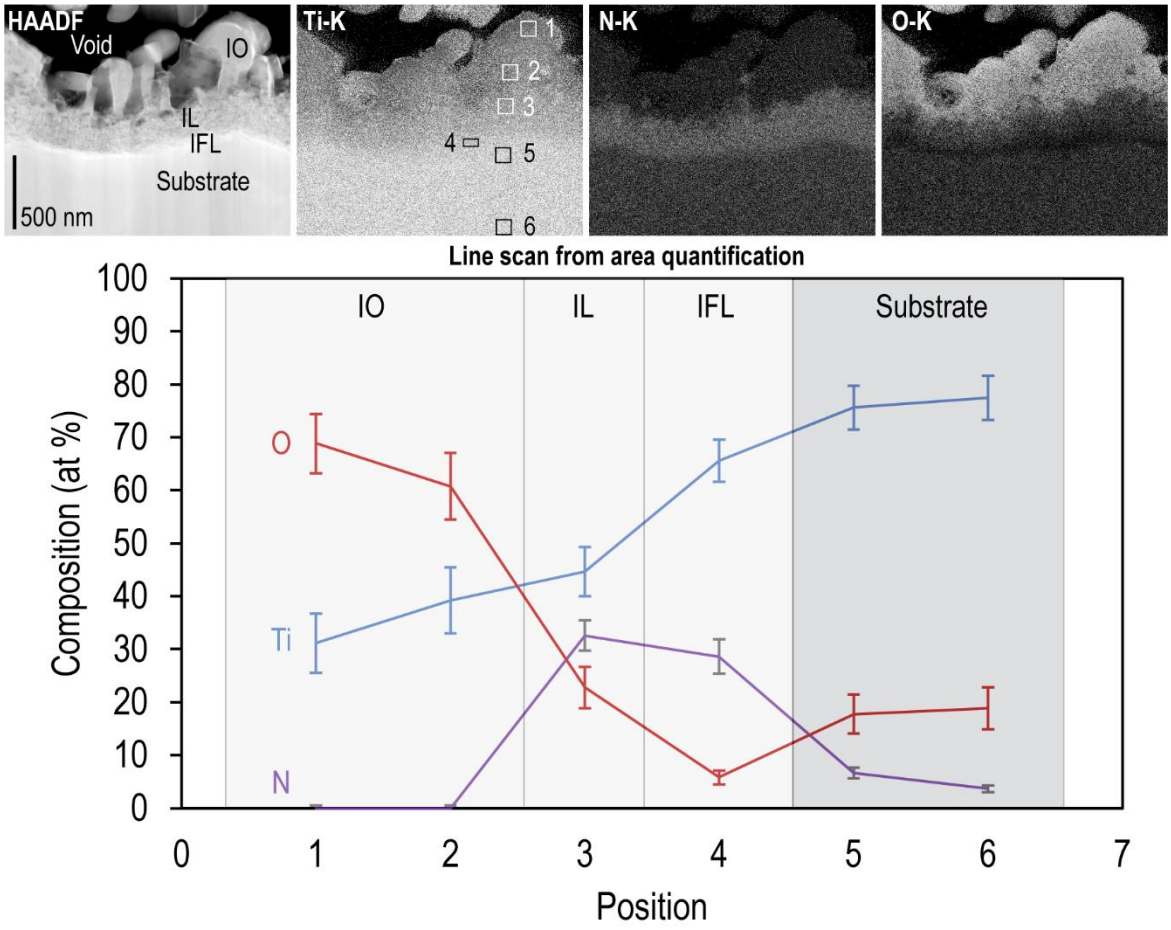

Figure 5.7. Cross-sectional micrograph for a smaller are of the 25 h specimen from STEM HAADF and corresponding STEM EDX elemental maps. Areas used for quantification are shown in the Ti-K elemental map and its values were used to construct the line scan below. Oxygen content is highest in the IO layer identified as rutile with negligible N content. N content is highest in the IL and IFL layers. Oxygen content is higher than nitrogen in the substrate, but this trend is sustained into the substrate in contrast to the lower magnification elemental map of this specimen.

Focusing on the interstitial contents in the 1-25 h specimens, the 1 h and 25 h specimens seem to showcase oxygen and nitrogen contents that would be consistent with expected saturation at the metal surface. However, it is important to note that the 9 h specimen shows more nitrogen than oxygen content despite the scales immediately forming above the substrate being the same layers as those in the 25 h. Additionally, while these N and O contents might make sense in terms of approaching the solubility limits of hcp Ti, using the same reaction gas (gettered Ar) and fast-cooling shows a significantly higher nitrogen

content (~30 at%) than oxygen (~8 at%). If we assume that slow-cooling enables more interstitial dissolution due to a longer time at high temperatures, we would expect both nitrogen and oxygen to have high contents. This is the case in the 1 h specimen, but not in the 9 or 25 h where nitrogen or oxygen contents, respectively, are around or below 10 at% (well below the solubility limit of either).

Acquiring XRD patterns from the surface of these specimens, the prevalent formation of rutile is evident in the 9 h and 25 h specimens with the presence of most rutile peaks and its $[110]_R$ peak being the most intense in the patterns (Figure 5.8). These two specimens show peaks that are predominantly rutile with a few α-Ti peaks. As in the previous chapter, some of these peaks are shifted in α-Ti from the incorporation of interstitials in the metal substrate. Rutile peaks can also be seen shifted, presumably from some residual strain. The 1 h specimen shows many peaks that do not coincide with rutile nor α-Ti. These are instead attributable to the formation of lower oxides, in particular of corundum which is in the inner oxide, and Magnéli phases likely located in the outer oxide.

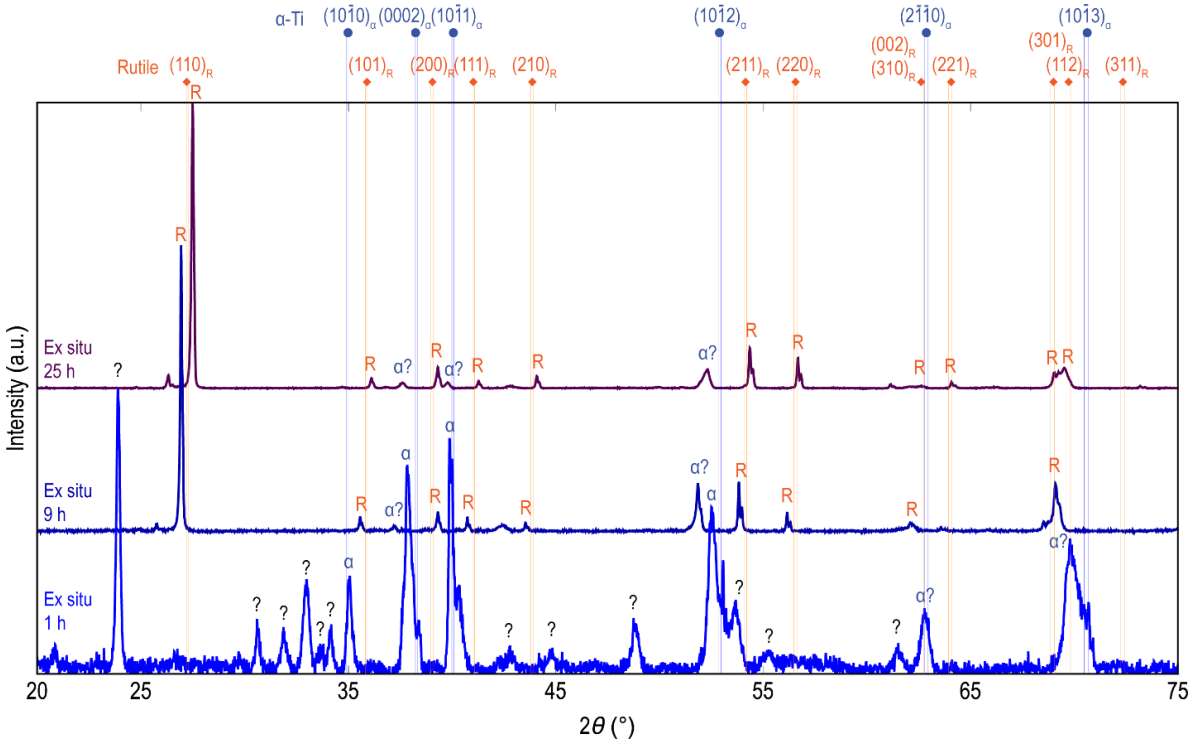

Figure 5.8. XRD patterns from the surface of Ti specimens exposed to counter flow gettered Ar at 800°C for 1 h, 9 h, and 25 h where α corresponds to α-Ti solid solution peaks and R to rutile peaks. Question marks are placed above peaks that do not match either α-Ti or rutile.

The 1 h specimen shows clear peaks that correspond to the Ti_2O_3 phase in its corundum structure and of Magnéli phases, Ti_3O_5 and Ti_4O_7, with more peaks corresponding to the latter than the former (Figure 5.9).

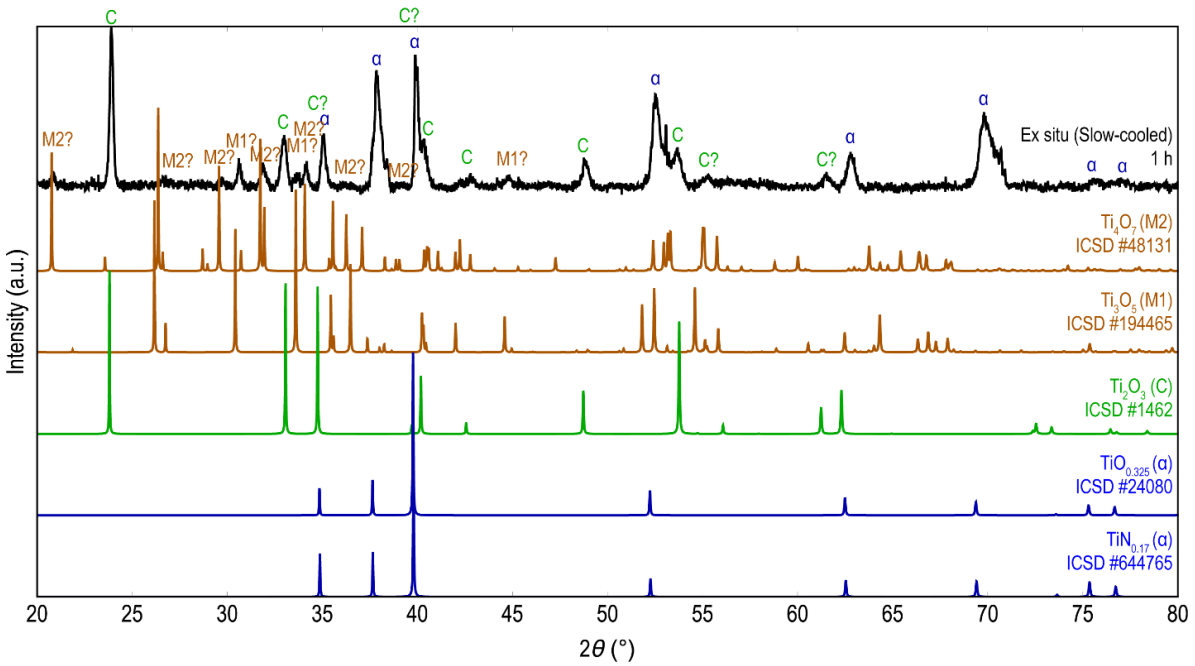

Figure 5.9. Comparison of experimental pattern from 1 h specimen to possible solid solution titanium, Ti_2O_3 corundum and two Magnéli phases from ICSD showing that this specimen shows the presence of both corundum and Magnéli phases. α denotes α-Ti peaks, C to Ti_2O_3 corundum, and M1 and M2 to Magnéli phases Ti_3O_5 and Ti_4O_7.

The elemental maps and XRD patterns from the three dwell times provide important clues of which phases may be present. Electron diffraction was used to identify which phase formed in which layers and any orientation relationship between these. The combined information from these characterization techniques provides a baseline for thinking about the microstructural evolution of these specimens.

5.1.1.1 Outer and inner oxides in the 1 h specimen

Using electron diffraction, the presence of Ti_2O_3 in its corundum crystal structure is confirmed in the columnar inner oxide grains (Figure 5.10). The outer oxide grains were too small for selected area diffraction and there were not enough grains to acquire a ring diffraction pattern. Based on the XRD pattern, it is likely that these are where the Magnéli phases are formed. While the Magnéli phases have slightly higher oxygen contents than

corundum (62.5 at% for Ti_3O_5 vs corundum's 60 at% O), this difference would not be visible in the elemental maps and the small difference would not be detectable with EDX. It makes sense that there is no significant change in the oxygen signal from STEM EDX between the inner and outer oxide given the presence of these lower oxides. Curiously, there is no evidence that suggests any rutile formation in this specimen since there is no rutile signal from XRD nor Raman spectroscopy.

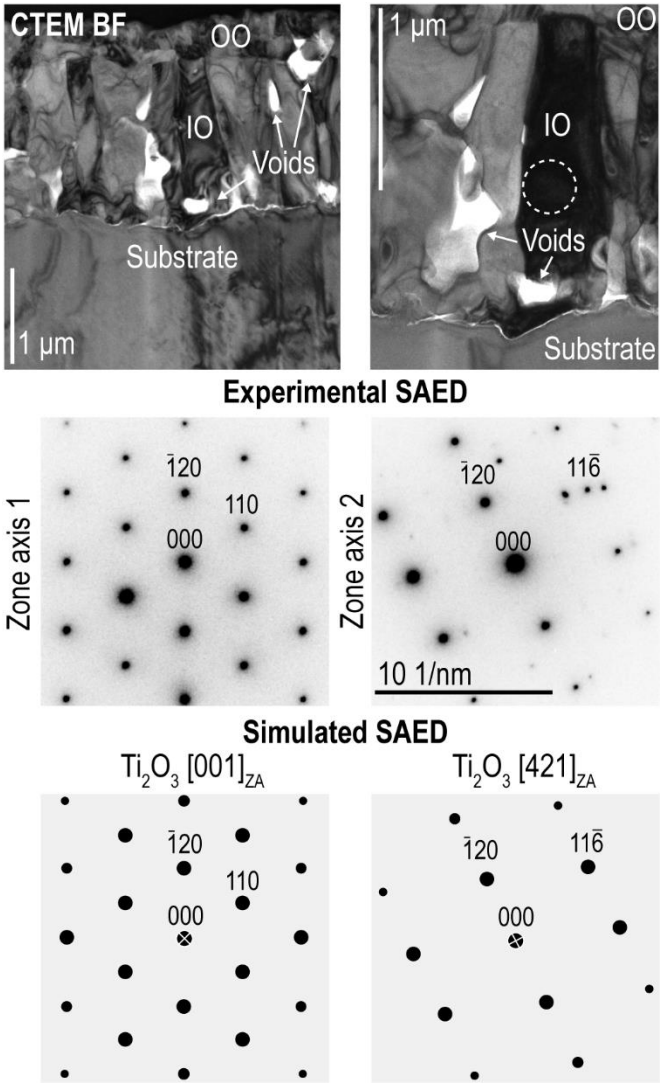

Figure 5.10. Cross-sectional micrograph showing area of interest for inner oxide SAED acquisition in 1 h specimen. Experimental SAED and their matching simulated SAED from Ti_2O_3 corundum are shown.

5.1.1.2 Inner layer in the 9 h and 25 h specimens

For the 9 h and 25 h, the inner and interfacial layers show similar electron diffraction patterns and structures and are assumed to be the same phase, albeit with different microstructures. Since the 9 h specimen has thicker layers than the 25 h specimens, these will be used to identify the phases developed in these layers. Based on the elemental maps from before, the inner layer shows high contents of nitrogen and oxygen, while the interfacial layer shows significantly more nitrogen than oxygen suggesting the formation of an oxynitride and a nitride respectively.

Electron diffraction from the inner layer of the 9 h unequivocally shows an fcc crystal structure (Figure 5.11). This fcc structure matches that of a rocksalt phase whose pattern can match TiO, TiN, or TiN_xO_y. For simplicity, the TiN phase was used for simulating the SAED patterns, but these three phases show the same patterns with only slight changes in interatomic distances. Given the EDX information, however, this phase is likely a rocksalt Ti oxynitride although its composition cannot be defined from STEM EDX alone. (A similar phase will form in experiments in UHP Ar in Chapter 6 of this thesis where EELS will be used to further explore this oxynitride phase and the presence of N and O will be further confirmed.) The SAED along the TiN [111] zone axis shows faint additional reflections near $\frac{1}{2}(20\bar{2})$ reflections. These reflections (circled in red in Figure 5.11) could arise from different vacancy or interstitial orderings, of which there are many given the TiN-TiO solid solution space. It is also important to note that, in contrast to the previous chapter's twinned TiN, the rocksalt phase in this inner layer does not show visible evidence of twinning. However, evidence of twinning will be found in the rocksalt phase of the 25 h specimen.

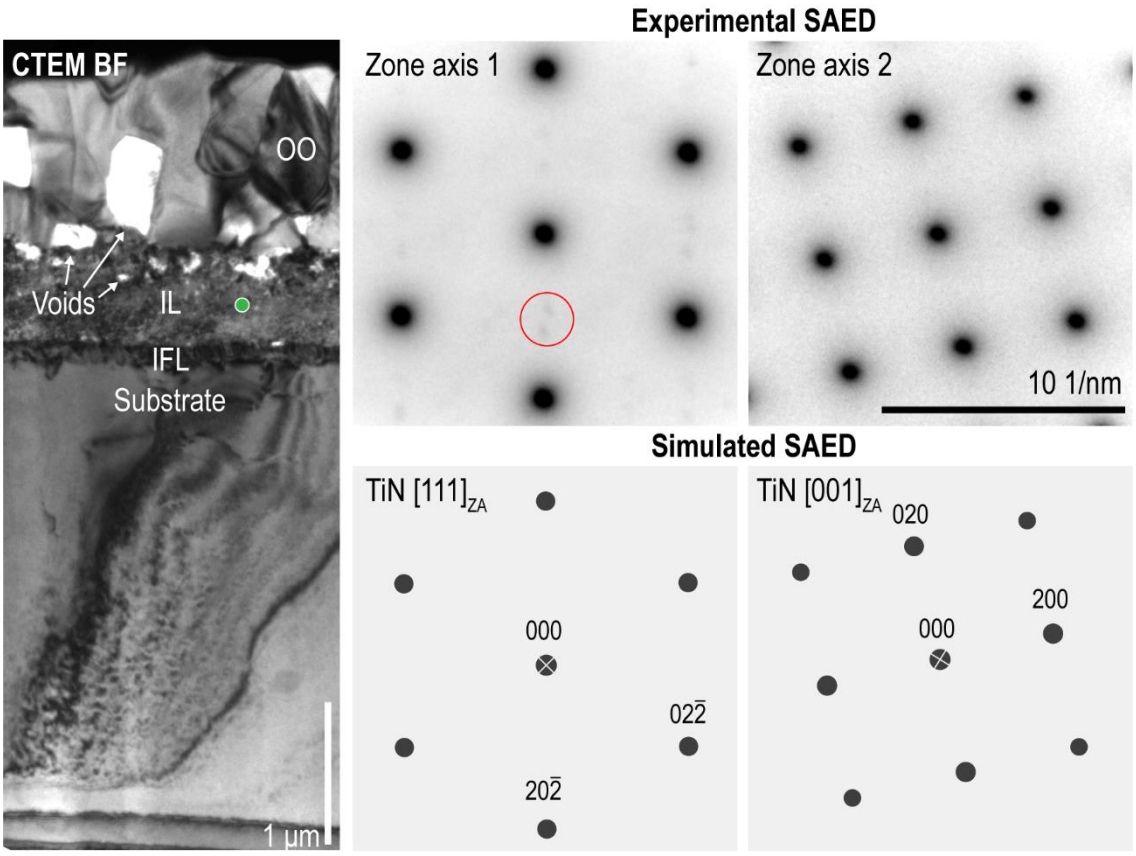

Figure 5.11. CTEM BF micrograph of the cross-section for the 9 h specimen showing a layered structure and the region where the aperture was for electron diffraction acquisition (green circle in IL). SAED from the IL region and their matching simulated SAED from TiN are shown. Additional reflections in the TiN $[111]_{ZA}$ pattern are shown circled in red.

A Ti-N-O partial ternary phase diagram calculated by Dupressoire et al. [77] using ThermoCalc's TCTI1 database proposes a large composition space for fcc Ti oxynitride (Figure 5.12). This diagram, although at 650°C rather than this research's 800°C, suggests a wide solubility for both nitrogen and oxygen in an fcc oxynitride phase they labelled $Ti(N_yO_{1-y})_{1\pm x}$. From the Ti-N and Ti-O binaries discussed in the Background chapter, the solubility of TiN and rocksalt TiO is expected to increase with increasing temperatures. The compositions acquired from the inner layer of the slow-cooled specimens for 1 and 25 h are labelled with circles in Figure 5.12 where they are clearly outside of the $Ti(N_yO_{1-y})_{1\pm x}$ composition space proposed at 650°C. Based on the binary phase diagrams, a larger

composition space would be expected at 800°C for both TiN and TiO which suggests a larger composition space for the rocksalt oxynitride phase would also be expected at higher temperatures.

It is generally agreed upon that titanium oxynitrides in the rocksalt phase can have a wide range of nitrogen and oxygen compositions, as well as vacancy orderings [69–73]. The δ-TiN rocksalt phase, for reference, is thought to be stable between 37.5 to 53 at% N and have vacancy orderings in the N sublattice [169,174]. The high-temperature TiO (γ-TiO), which has the pure rocksalt structure rather than the monoclinic low-temperature TiO (α-TiO), has a composition range of 40 to 55.3 at% O and vacancy orderings in the Ti and O sublattices [4]. Even stoichiometric TiO contains 15% disordered vacancies in the Ti and O sites [175] which supports the idea that oxynitrides would also be able to accommodate large amounts of vacancies.

Oxygen can incorporate into the anion sublattice of TiN to generate N-rich rocksalt oxynitrides. Alternatively, N can occupy vacant O sites from TiO. In Ti rocksalt oxynitrides $TiN_{1-x}O_x$, $x < 0.6$ seems to favor the NaCl structure while the monoclinic structure of α-TiO is more stable at $x > 0.6$ [176]. This suggests that N-rich oxynitrides would be closer to a "pure" rocksalt structure rather than a monoclinic rocksalt structure. From the compositions of this phase from EDX and the electron diffraction pattern, this N-rich oxynitride would be closer to a "pure" rocksalt structure as well. Oxynitride phases in the fcc rocksalt structure are expected to have a wide solubility for nitrogen and oxygen contents as can be seen in the ternary Ti-N-O phase diagram at 650°C [77] in Figure 5.12.

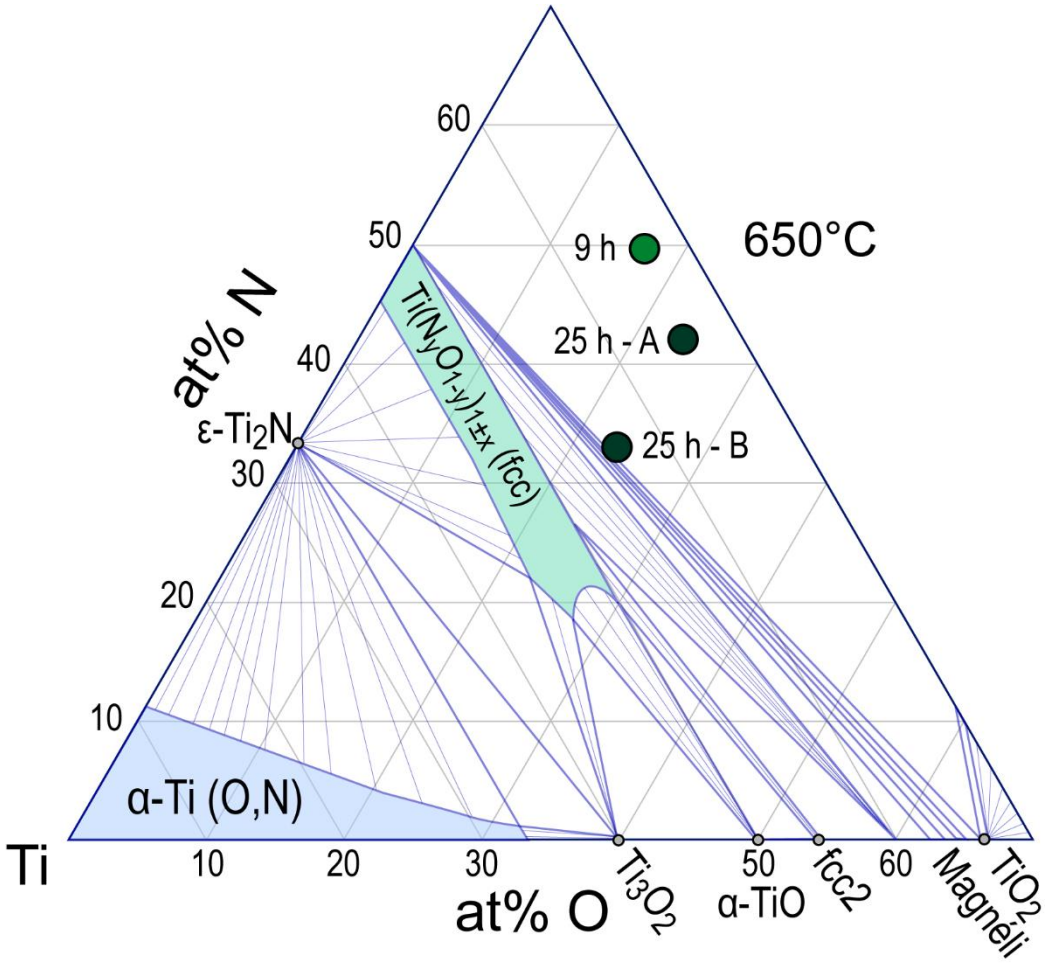

Figure 5.12. Partial ternary Ti-N-O phase diagram at 650°C showing wide solubility of N and O in α-Ti and rocksalt oxynitride phases. Adapted from Dupressoire et al.'s [77] diagram calculated using ThermoCalc and the TCTI1 database.

While the inner layer could be referred to as an oxynitride layer due to its rocksalt structure from electron diffraction and the presence of nitrogen and oxygen from STEM EDX elemental maps, there is a possibility that there are various phases present in this region. The wide range of solubility and the concentration gradient of oxygen throughout the layer suggests that this region could include combinations of compositions along the TiN-TiO solid solution. The electron diffraction pattern does not suggest more than one phase present, but TiN, TiO, and any concentrations between them would present nominally the same crystal structure.

Looking at the nitrogen and oxygen signal from this inner layer in the elemental map of the 9 h specimen (Figure 5.13) shows N-rich and O-rich regions which could seem reminiscent of spinodal decomposition. Spinodal decomposition has been reported in a TiAlN rocksalt-based systems where $Ti_{1-x}Al_xN$ transforms into coherent AlN and TiN phases [177]. From the available evidence, it is difficult to ascertain which phases are present and in what fractions, but two things are certain: (1) any phase present in the inner layer has a rocksalt crystal structure, and (2) there is both nitrogen and oxygen in the entire region. From the initial elemental map show of this specimen, the region is overall more N-rich than O-rich. Additionally, nitrogen content remains fairly constant while oxygen shows a slight concentration gradient with oxygen decreasing towards the IFL layer. Based on the composition of the inner layer, it is likely that TiN is the predominant phase, or that the oxynitride formed has more N than O content.

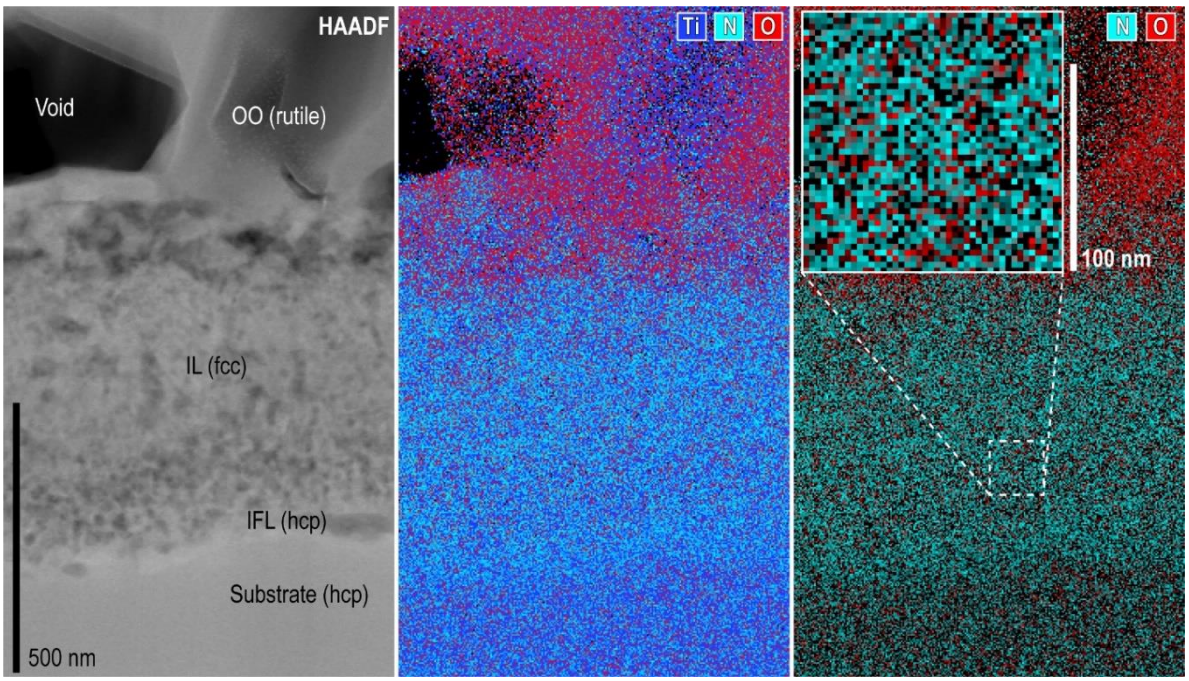

Figure 5.13. HAADF image of 9 h specimen accompanied by color-coded elemental maps for Ti (dark blue), N (light blue), and O (red) in the middle and only N and O on the rightmost image. An inset showing a higher magnification for the IL region shows regions of N and O enrichment.

5.1.1.3 Interfacial layer in the 9 h and 25 h specimen

From the elemental maps of the 9 h specimen (Figure 5.5), the 50 at% N content in the interfacial layer suggests that TiN could be forming in this region. Electron diffraction shows, instead, an hcp-based crystal structure with additional reflections that suggest various orderings (Figure 5.14). The top row of this figure shows the SAED pattern with a row of additional reflections labelled ‘a’, ‘b’, and ‘c’. These were used to generate dark field images which suggest the presence of more than one phase throughout the interfacial layer. The bottom row of this figure shows a SAED from the same zone axis of α-Ti with only the ‘b’ additional reflection (labelled ‘d’) from an analogue 9 h specimen. This interfacial layer shows a lamellar structure similar to the top row specimen, but with seemingly more solid brightness in the lamellar regions. This layer could still be from more than one ordering as suggested by the equivalent of the ‘d’ spot on the left of the 000 transmitted beam. This reflection is actually two spots that are close to each other, which means that the dark field image is likely sampling two different spots rather than a single one.

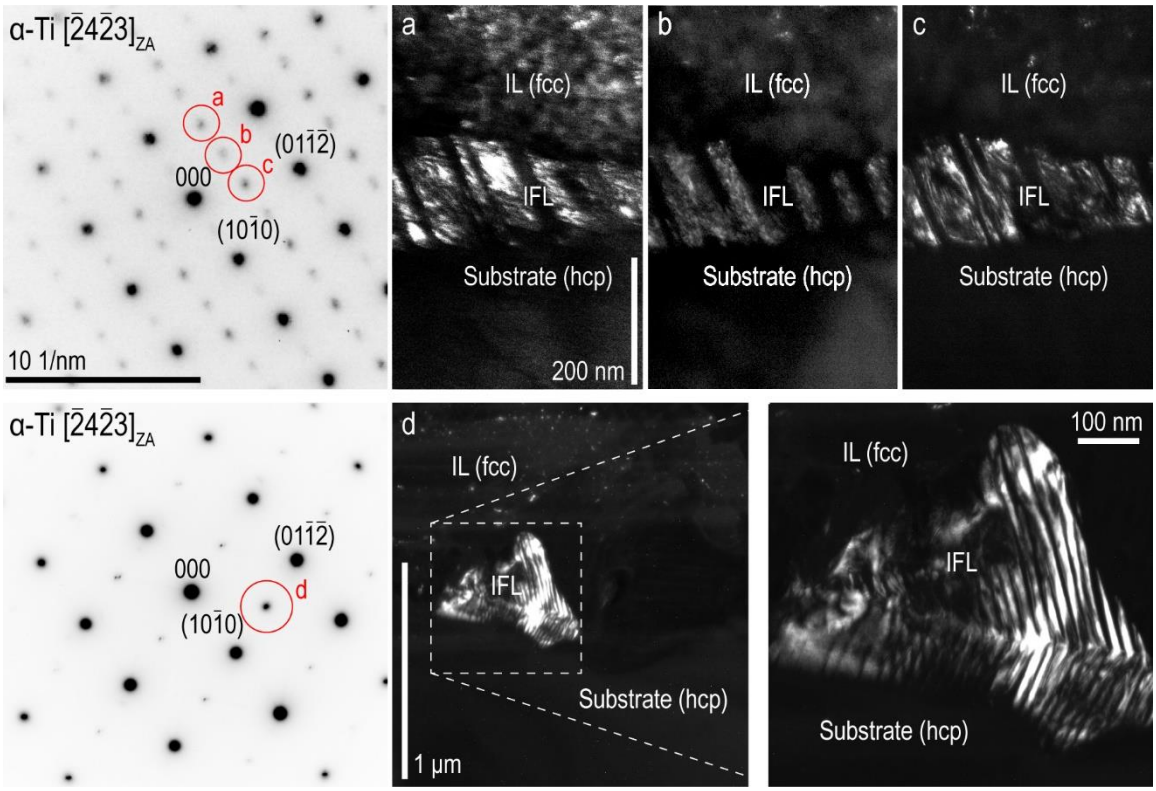

Figure 5.14. Experimental SAED patterns from the IFL region of two Ti specimens exposed to gettered Ar at 800°C for 9 h. Spots are labelled to denote which were used to generate the CTEM dark field images shown on the right.

While hcp-based oxides have been reported in literature [37], the addition of nitrogen could drastically change the preferred orderings of oxygen in the hcp lattice. In the Ti-N system, ordered nitrogen phases are not included in the phase diagrams and studies suggest nitrogen occupies interstitial sites in a random distribution (i.e. solid solution only) [63,68,174]. Preliminary studies from the Van der Ven group at UCSB suggest that no hcp-based orderings of nitrogen and oxygen in hcp titanium are energetically favorable. It could be possible that the orderings seen in this specimen are metastable hcp orderings of nitrogen that have not been thoroughly explored.

Although previous studies have suggested nitride layers act as an oxygen diffusion barrier [77,78,105–108], the nitrogen-rich IFL in this work suggests the formation of various phases and does not seem to be as effective a barrier as a solid, continuous ε-Ti_2N or TiN

scale given the oxygen contents in the metal substrate underneath. Additionally, the orderings are not explained along different zone axes solely with ε-Ti_2N or α" (staged Ti_2O) phases. This further implies that there are one or more orderings occurring, which are potentially from both nitrogen and oxygen occupying octahedral sites, with more nitrogen atoms than oxygen.

5.1.1.4 Ordering in metal substrate

Similar to the previous chapter's specimens, electron diffraction from the metal substrate shows solid spots where pure α-Ti would have forbidden reflections. These reflections are forbidden and can show up as double diffraction spots in α-Ti, its solid solution, and the DFT-calculated α-Ti_2O. The staged Ti_2O (α") phase shows these forbidden spots as allowed and with intensities comparable to the rest of the reflections. SAED patterns along two different zone axes are, once again, a closest match to this α" phase (Figure 5.15). This suggests that nitrogen and oxygen that dissolve into the metal could be ordering every other interstitial layer, thus breaking the symmetry in the hcp Ti lattice and allowing for these reflections.

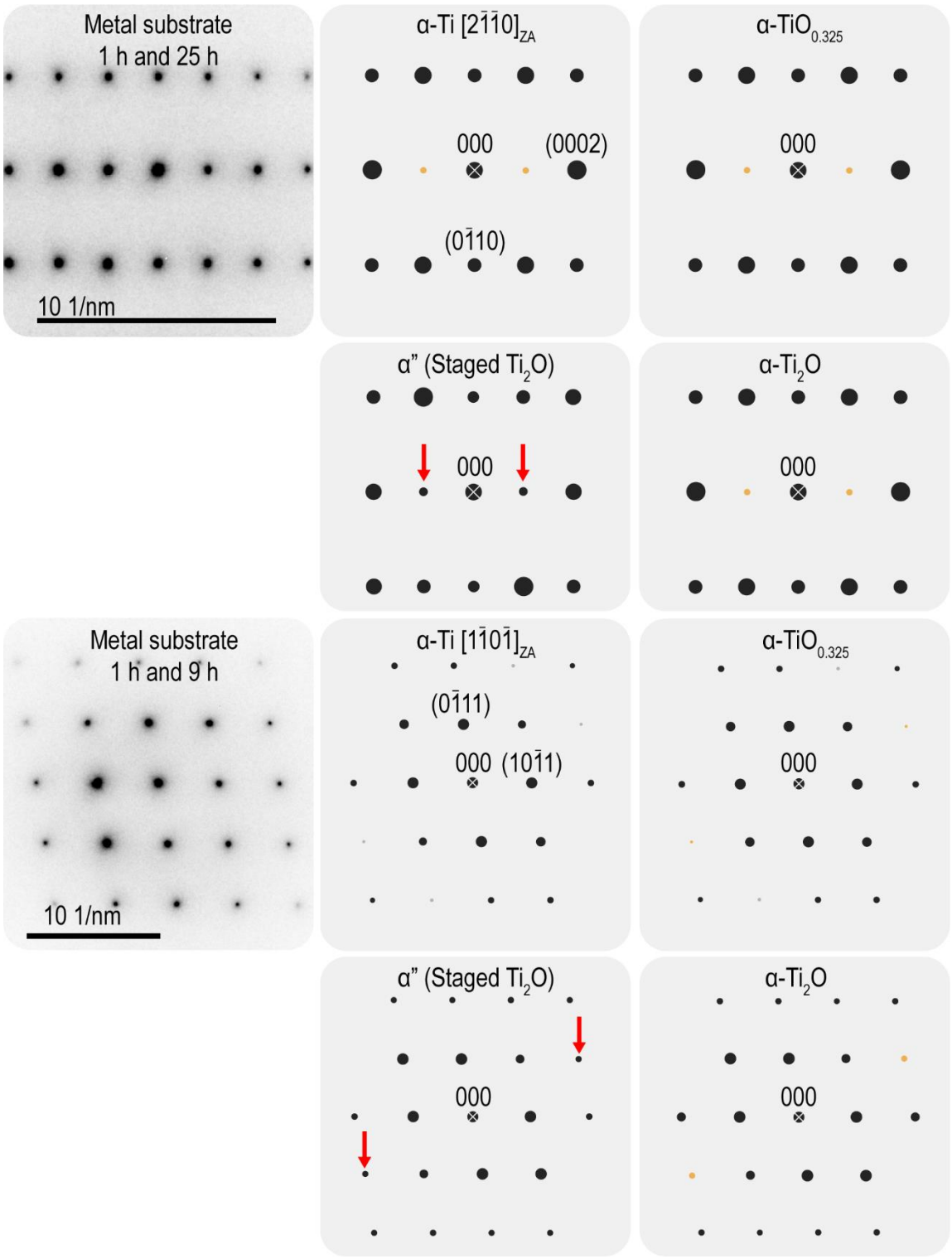

Figure 5.15. SAED from the metal substrates of all three dwell times (1, 9, and 25 h) are shown and compared to the solid solution and Ti_2O phases based on α-Ti. The experimental patterns are a closest match to the α" (staged Ti_2O) phase. Yellow circles denote double diffraction spots.

5.1.2 Orientation relationship and possible growth mechanisms

Like in Chapter 4, the hcp Ti substrate and fcc rocksalt phases show a strong orientation relationship as evidenced by electron diffraction from the 25 h specimen (Figure 5.16). In the 25 h, the inner layer shows the same fcc rocksalt structure from the 9 h specimen and is also believed to be a Ti oxynitride phase. The additional reflections along the $(0002)_{\alpha}$ direction in the substrate + scale patterns can be explained from overlaying the fcc inner layer diffraction pattern on the substrate pattern.

The figure below shows electron diffraction patterns from the same three layers along different positions in the specimen (illustrated by white circles in the STEM BF image). While the diffraction patterns for the substrate and inner layer are the same orientation and crystal structure, there are slight variations in ordering as evidenced by additional reflections in the substrate + scale pattern, and in the inner layer. The substrate + scale pattern from the top row does not have additional reflections in the red circle, while the bottom row does show faint reflections here. This pattern is reminiscent of the pattern found in the previous chapter for tweed-like regions with additional reflections in patterns similar to ε-Ti_2N.

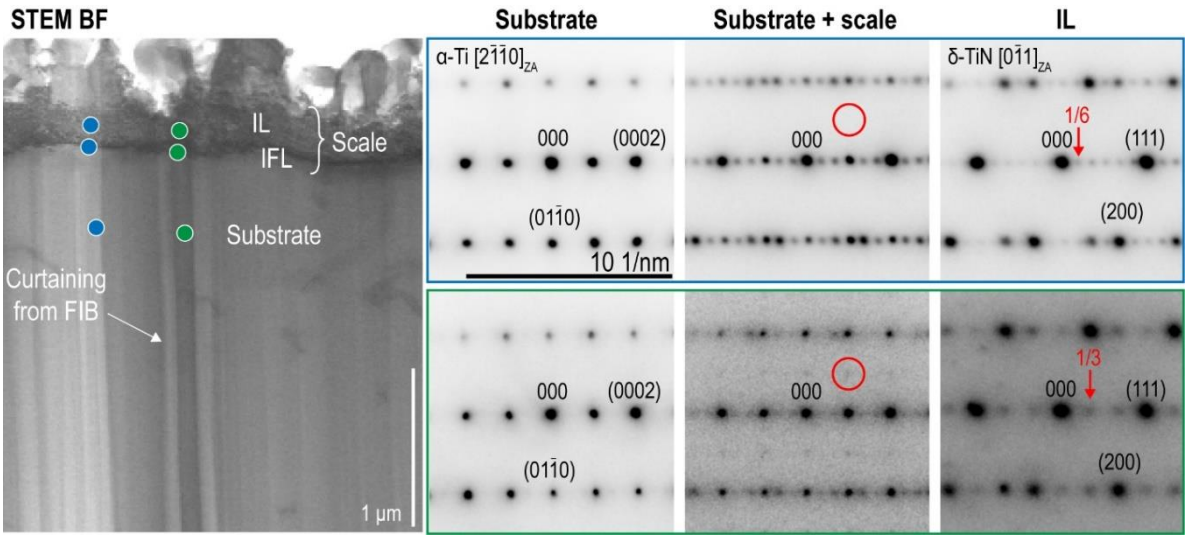

Figure 5.16. Cross-sectional STEM BF micrograph for 25 h specimen showing areas of interest from the substrate into the IL layer. The substrate and IL show an orientation relationship between the α-Ti (hcp) and δ-TiN (fcc) phases. The bottom row shows an additional reflection in the substrate + scale region that does not correspond to either α-Ti nor δ-TiN. The top row shows no such additional reflection. The additional reflections in this region along the (0002) row correspond to the spots from IL identified as δ-TiN. The IL shows additional reflections at 1/6 (111) in the top row and 1/3 (111) in the bottom row suggesting that there are different orderings occurring throughout the specimen in the same layers.

In the inner layer, the top and bottom row patterns both show additional reflections to a twinned fcc pattern (the strongest reflections) with the top showing additional spots at $\frac{1}{6}(111)$ and the bottom at $\frac{1}{3}(111)$.

From the indices of the SAED patterns, the relevant orientations of the hcp and fcc crystal structures can be matched to each other (Figure 5.17). Looking down the $[2\bar{1}\bar{1}0]$ direction in hcp titanium and the $[0\bar{1}1]$ direction for an fcc oxynitride, the changes of ABAB stacking in hcp to ACBA stacking for fcc can be clearly appreciated. As before, the {0001} hcp planes correspond to the {111} fcc planes. While δ-TiN was used for the SAED simulations and crystal structure model, oxygen atoms and vacancies have been added to showcase possible variations from the ideal δ-TiN phase.

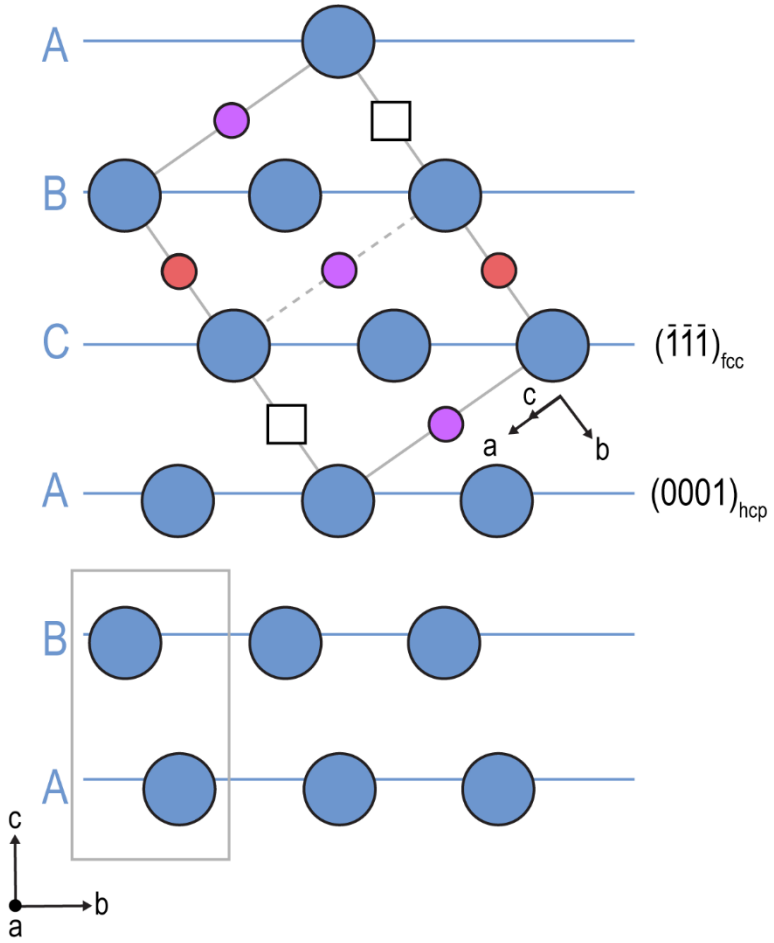

Figure 5.17. Schematic showing the orientation relationship between the hcp Ti substrate (ABAB stacking) looking down the $[2\bar{1}\bar{1}0]$ direction and the rocksalt TiN_xO_y outer layer (ACBA stacking) along the $[0\bar{1}1]$ direction. Vacancies (squares), oxygen atoms (pink) and nitrogen atoms (purple) are shown in the rocksalt structure as this is likely an oxynitride. The {0001} planes from hcp correspond to the {111} planes from fcc stacking. Blue atoms are Ti and unit cells are delineated in gray.

Regarding the additional reflections observed in the fcc oxynitride phase, these same orderings have been observed during in situ heating experiments of hcp Ti phases from a Nb-22Ti-16Si-3Al-3Cr (at %) alloy [86]. In Ma et al.'s work, hcp Ti was found to convert to fcc Ti by a growth ledge mechanism with two intermediate structures referred to in their work as PC_1 and PC_2 for 'periodic contrast'. These two orderings were proposed to have similarities with the long period stacking ordering (LPSO) structures of R phases, namely 18R for PC_1 and 9R for PC_2. While they checked for oxygen content to rule out the formation of any titanium oxides, there was no explicit mention of any possible nitrogen content in these

phases. The specimens discussed in this chapter, however, undoubtedly have significant nitrogen contents that lead to the identification of the inner layer as an oxynitride (or certainly a combination along the TiN-TiO solid solution space). In contrast, Ma et al.'s work identifies this fcc phase as purely titanium. The specimens discussed in this chapter show these same orderings and raise the possibility of nitrogen playing a role in the transformation of hcp titanium to fcc – whether to fcc titanium or any of the rocksalt monoxide, nitride, or oxynitride phases. The diffraction patterns from this work (white background with black spots) and Ma et al.'s work [86] (black background with yellow spots) are compared in Figure 5.18.

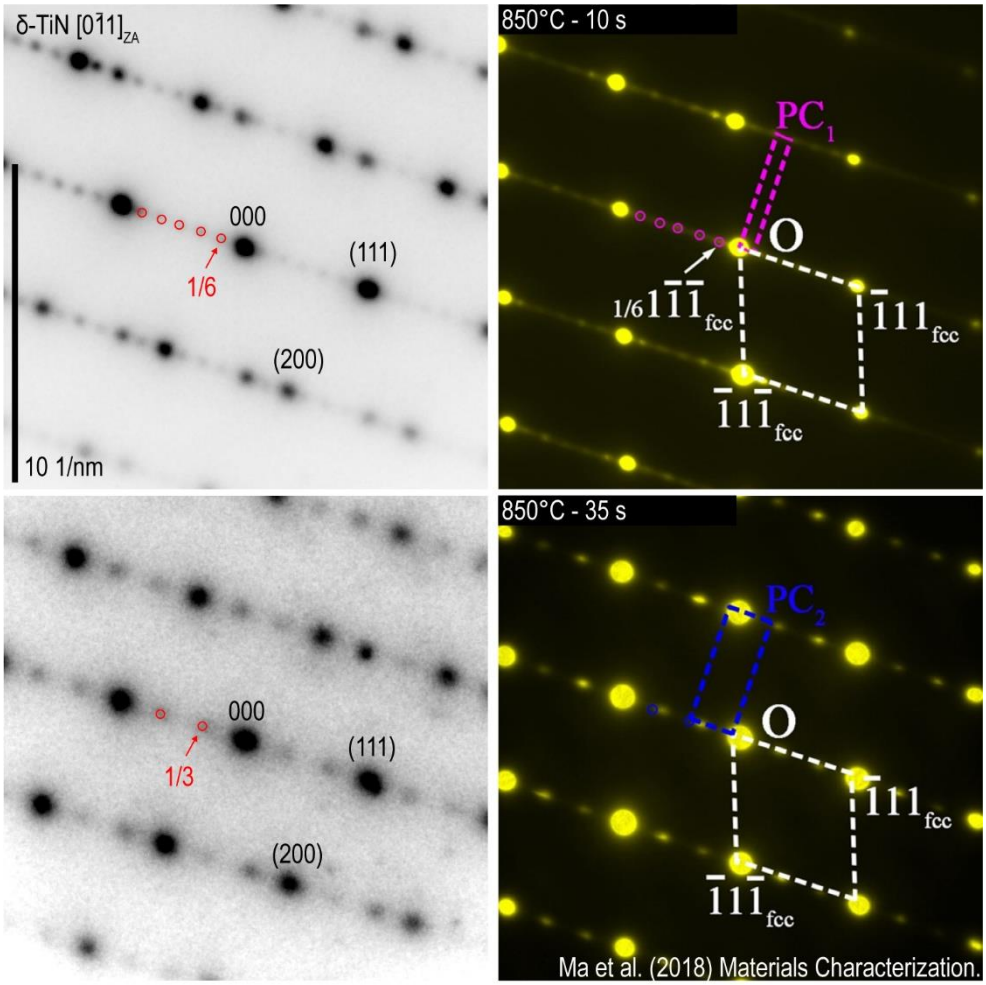

Figure 5.18. (Left) Experimental SAED patterns from the IL region of the 25 h specimen compared to the fcc patterns with periodic structures from Ma et al..'s work [86]. There are two periodic contrasts (PC) shown with spots at $\frac{1}{6}(111)$ for PC_1 and $\frac{1}{3}(111)$ for PC_2. These orderings are similar to 18R and 9R respectively.

A schematic showing the crystal structure changes from hcp to the LPSO structures to fcc is shown in Figure 5.19 with some nitrogen atoms interspersed in the first three phases, and all nitrogen atoms shown in the fcc illustrated as a rocksalt TiN. As in the previous chapter, these changes in structure could arise from stacking faults or dislocations that change the stacking order of the BCBC hcp to CAB in fcc, or similar stackings. The stacking layers labelled with a ' symbol represent those that have a different height compared to the initial hcp crystal structure.

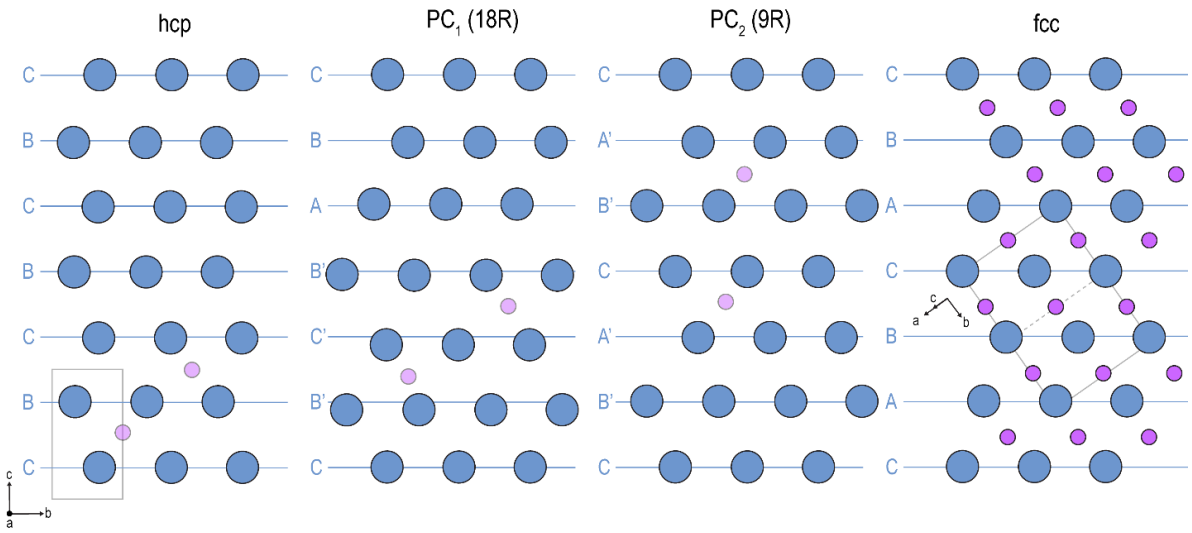

Figure 5.19. Side-view of crystal structures for the hcp to fcc transformation in hcp titanium showing two intermediate structures, PC_1 and PC_2. Figure created based on Ma et al.'s proposed structures for the intermediate phases from atomic configurations observed [86]. The ' next to the stacking letters denote a different height from the equivalent hcp stacking. Nitrogen atoms are shown in the fcc structure, but both oxygen and nitrogen could be ordering in different ways in the intermediate structure and as an oxynitride in the fcc given the experimental conditions for this chapter. Potential nitrogen atom positions in the hcp and intermediate structures are shown with semi-transparent purple atoms.

A different orientation relationship can also be seen between the hcp substrate and the fcc inner scale from the 9 h specimen (Figure 5.20). The IFL SAED pattern is the same that was used for dark field imaging earlier in this chapter (Figure 5.14). The substrate shows an hcp crystal structure which shows various hcp-based orderings from the SAED pattern of the IFL (additional reflections marked by red arrows in Figure 5.20). The reflections at $\frac{1}{2}(10\bar{1}0)_\alpha$ can be attributed to double diffraction, but those in the red arrows are likely to arise from interstitial orderings of which nitrogen is assumed to be the main component from STEM EDX. The inner layer identified as rocksalt immediately above the IFL shows common reflections with hcp when overlaying the substrate and inner layer SAED patterns. This suggests that the 9 h specimen also shows an orientation relationship between the substrate's hcp and the oxynitride's fcc in the inner layer.

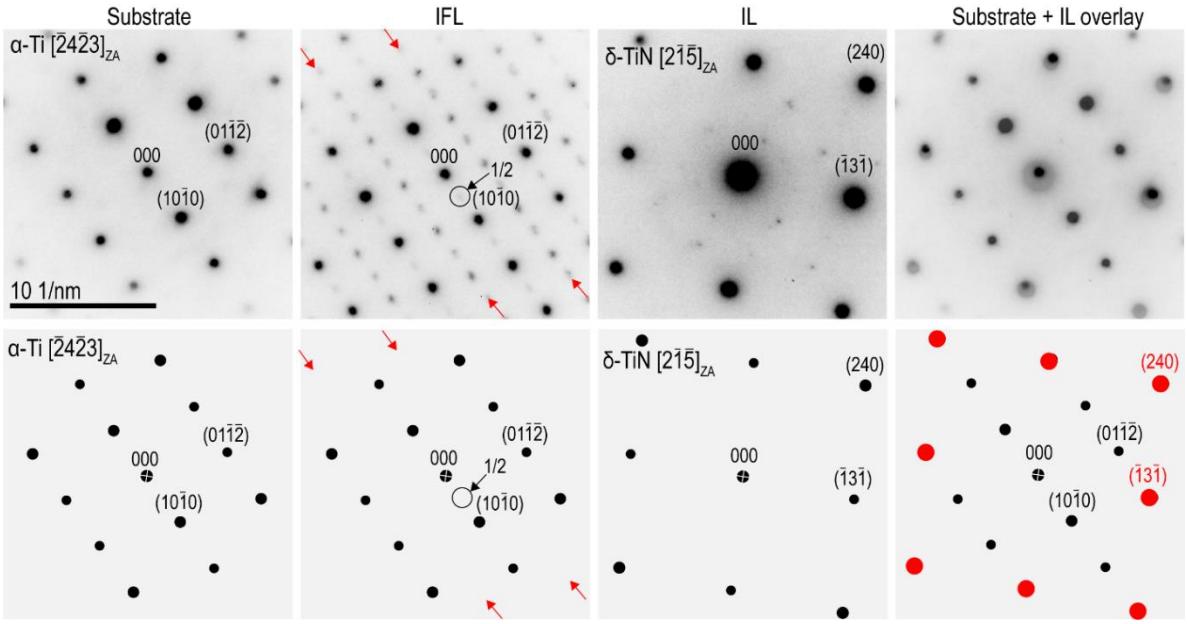

Figure 5.20. (Top) Experimental SAED from the substrate, interfacial layer (IFL) and inner layer (IL) of the 9 specimen. (Bottom) Simulated SAED pattern that corresponds to the experimental pattern above. The overlay of the substrate and inner layer show an orientation relationship between the hcp substrate and the fcc inner layer (likely an oxynitride). The IFL pattern shows additional reflections (red arrows) that are not explainable with a single phase of hcp-based oxides. The IL pattern shows additional reflections randomly dispersed that suggest disordered imperfections.

5.1.3 Void formation and growth mechanisms

While voids are visible in all three dwell times, the 9 h specimen provides a good case study for a few different morphologies of pores. The largest voids are located in the outer oxide composed of rutile, while the oxynitride inner layer shows nanoporosity throughout it with a few larger voids where there has been some void coalescence. SEM images from the FIB session where a lamella was obtained are shown in Figure 5.21 to showcase that the porosity in this specimen is not an artefact from specimen preparation. Since the fast-cooled specimens from Chapter 4 also show voids, these voids are not thought to form during cooling either. The TEM images shown in the same figure reveal that the large voids and nanopores can be seen as complete gaps or partial ones. This suggests that

the voids of the outer oxide extend through the scale in an elongated form and that the voids seen in the lamella are only a small cross-section of the entire voids.

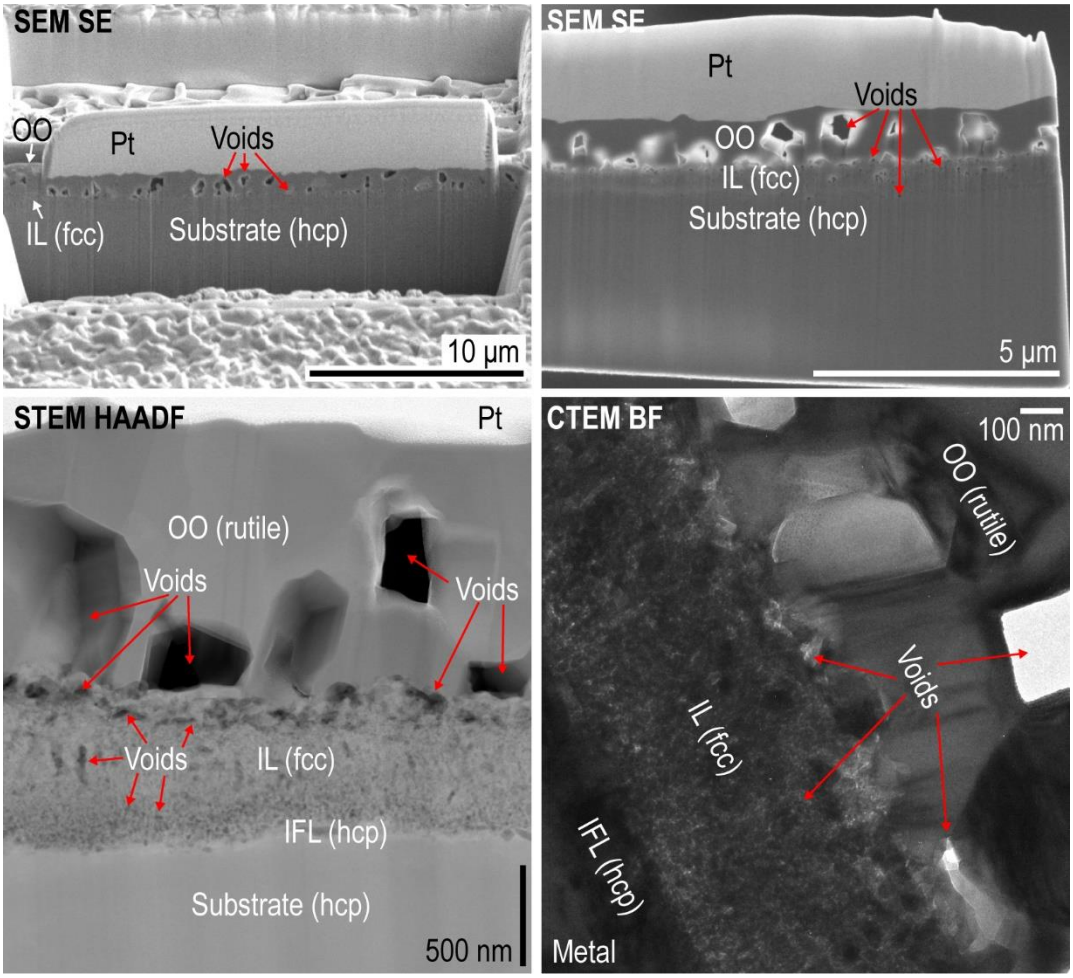

Figure 5.21. Cross-sections for the 9 h specimen showing its distinct layers and various void morphologies (highlighted with red arrows) within. (Top row) SEM SE micrographs showing images of the 9 h specimen during FIB lamella preparation (left) with the stage tilted at 52° after cutting the trenches, and (right) after thinning the lamella attached to a copper grid. (Bottom row) (left) HAADF and (right) CTEM BF images of the cross-sections where the voids can be seen in black in HAADF and white in CTEM BF. Large full and partial voids can be seen within the outer oxide (OO) rutile scale with some smaller voids near its interface with the inner layer (IL). The IL region has many nanopores throughout the layer. The interfacial layer (IFL) and metal substrate do not show any voids.

When thinking of this Ti-N-O system, the nitrogen and oxygen are presumed to diffuse through interstitial sites in the hcp Ti lattice. While the Ti lattice is known to expand from interstitial incorporation, it is difficult to think of large voids forming from interstitial

diffusion only. This section will seek an explanation for the void mechanism by analyzing the volume expansion from hcp Ti to various N and O-containing phases, as well as the known diffusivities for Ti, N, and O in relevant phases.

The volume expansion from hcp Ti to various nitride, oxynitride, and oxide phases is shown in Table 5.1. The smallest volume expansion occurs when transforming from hcp Ti to an fcc Ti oxynitride (4.8%), followed by the rocksalt δ-TiN (7.8%). Transforming from hcp Ti to any of the remaining oxide phases identified in this set of specimens results in volume expansions > 48%, with rutile showing a huge 77.6% expansion. Qualitatively, this seems to scale with the relative dimensions of the pores in the 9 h specimen. The smallest pores are in the oxynitride layer and the outer oxide contains the largest pores in the specimen within this layer.

Table 5.1. Normalized volumes and volume expansion in % relative to the initial volume of α-Ti for relevant Ti nitride, oxynitride, and oxide phases in that order. The volumes used are based on the ICSD reference phases detailed in Chapter 2.

Phase	**Vol/Ti atom**	**Volume expansion (%)**
α-Ti	17.66	0
ε-Ti_2N	18.97	7.4
δ-TiN	19.04	7.8
fcc TiN_xO_y	18.50	4.8
α-TiO	18.58	22.3
Ti_2O_3 (corundum)	26.13	48.0
Ti_4O_7	29.13	65.0
TiO_2 (rutile)	31.37	77.6

Analyzing the voids from a volume expansion perspective, it can seem odd that the 1 h specimen shows such small voids within its corundum layer given the expected 48% expansion from hcp Ti and the fact that there is no intermediate layer between these two phases. For the longer dwell times, a nanoporous oxynitride layer with the largest voids within the rutile scale could make qualitative sense given that the relative changes in void size follow the relative changes in volume expansion for the oxynitride and rutile phases. These expansion values rely on the assumption that the hcp Ti is converting into each phase. Given that furnace studies only allow for the observation of the initial and final microstructures, there is no certainty as to which scale develops first and how these may change during cooling. The in situ experiments in Chapter 6 will provide some information regarding phase presence during the dwell time. Importantly, in situ experiments will also show porosity in similar locations and dimensions to those discussed here. However, fast-cooled specimens from furnace studies do suggest initial nitride formation since no oxide nor oxynitride phases were found in those scales.

When measuring the areas of these voids, the increase of void size from the small inner layer voids to the large outer oxide voids is substantially larger than the 77.6% volume increase expected from α-Ti to TiO_2 (rutile). This indicates that the void formation is arising from more than just volume expansion from the transformation of one phase to another.

When treating a Ti specimen to the same gas, flow direction, temperature, and 25 h dwell time, fast-cooling results in a specimen with no significant scale formation (Figure 5.22). The surface images of this specimen show two main features: (1) preferred phase formation along the grain boundaries, and (2) clear dislocation ledges with dispersed particles along the surface. While the cross-section shows no scale, it does show a wavy

interface that could be explained by the ledges found in the entire specimen's surface. Since the lamella was taken from within a grain, the reaction product of the grain boundaries is not seen here. Two different line scans were acquired from spot STEM EDX along the substrate. While EDX is qualitative, the line scans sometimes show a higher interstitial content at the bottom of the substrate than at the interface where the gas would be interacting with the metal. This is contrary to what would be expected of a concentration gradient in the substrate after exposing it to an oxidizing and/or nitriding environment. This raises the possibility that, under certain conditions, the interstitials could be diffusing outward from the substrate and contributing to phase transformations in the scales this way. If true, the nitrogen and oxygen supply from the gas environment would suggest inward interstitial diffusion with some outward diffusion coming from the metal substrate. While this further complicates the understanding of this mechanism, it is not an impossible scenario given that the metal substrate essentially acts as an almost-infinite reservoir to nitrogen and oxygen.[7]

[7] As an attempt to simplify experimental studies, a titanium foil was oxidized in a 20%O_2-Ar environment at 800°C for 27 h. The goal was to saturate the metal substrate and remove the scale to use the saturated substrate in oxidation studies. This would allow for experimental observations of oxidation with only oxide formation and growth with no simultaneous oxygen dissolution in the metal. This foil oxidized entirely into rutile layers. A second attempt in a 10%O_2-Ar gas for 30 min left enough metal to analyze, but the substrate was nowhere near saturation despite it being a thin 50 μm foil.

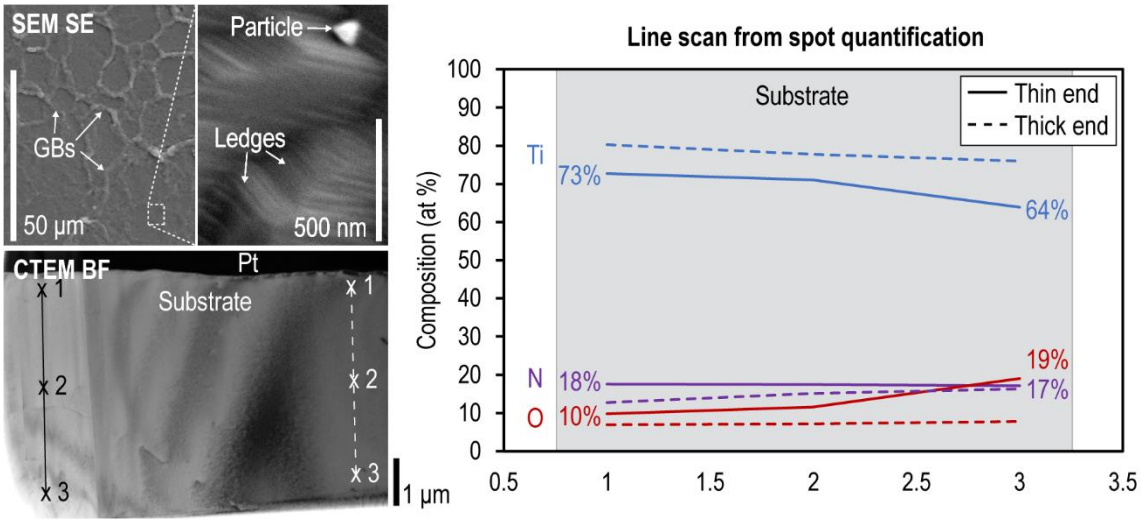

Figure 5.22. Data from a Ti specimen exposed to counter flow gettered Ar at 800°C for 25 h and fast-cooled. The SEM SE images of the surface show preferred growth along grain boundaries and the formation of ledges within the grains. Small (< 50 nm) particles can also be seen within the grains. The CTEM BF image of the cross-sections shows no scale formation but a slightly wavy interface. Line scans constructed from spot EDX measurements show increasing nitrogen or oxygen content into the metal substrate depending on which side (thin end on left or thick end on right side of lamella) is measured. No error bars are included in this line scan due to these measurements being acquired from three single spots rather than an elemental map. This was acquired in a Tecnai T20e TEM before the Talos with elemental map capacity was acquired at UCSB.

The diffusivities for Ti, N, and O through the relevant phases are shown in Table 4.3 when values could be found in literature with N and O reported mostly as inward diffusion. It is important to recall that reported diffusivities can show a wide range of values given the changes in the titanium purity (again related to the large affinity to and solubility of nitrogen and oxygen). It is also important to remember that diffusing species in titanium will have different values along the c-axis and a-axis in its hcp crystal structure and in its tetragonal structure when converted to rutile. In hcp, the current literature suggests that self-diffusion of titanium is slower than the oxygen diffusion in the α-Ti phase. If one assumes outward Ti diffusion influencing void formation, the Ti diffusion would have to be larger than the inward N or O diffusion. In rutile, literature suggests that outward Ti diffusion along the c-axis is faster than O diffusion [178,179]. This larger Ti outward diffusion would make sense

in partly explaining the void formation in the outer oxide composed of rutile grains (although perhaps not their dimensions).

Table 5.2. Diffusivities of Ti, N and O through α-Ti and relevant nitride and oxide phases at 800°C.

Diffusing element	**In phase**	**D at 800°C (m^2/s)**	**Reference**
Ti	α-Ti[8]	2.5×10^{-18}	[180]
Ti	TiO_2 (R)	6×10^{-18}	[179]
N	α-Ti	1.4×10^{-16}	[36]
N	(α-Ti)	3.4×10^{-15}	[115]
N	ε-Ti_2N	1.4×10^{-14}	[115]
N	δ-TiN	1.6×10^{-16}	[115]
N	TiO_2 (R)	-	-
O	α-Ti	1.2×10^{-15}	[35]
O	δ-TiN	-	-
O	TiO_2 (R)	1.2×10^{-19}	[178]

In an oxidation of TiN study at 700-850°C at oxygen pressures between 12.4 and 400 Torr (~0.016 – 0.53 atm), the possibility of outward nitrogen diffusion is introduced and thought to be the reason behind pressure dependence of the oxidation response [117]. This

[8] Diffusivity value is for a high-purity titanium. Low-purity titanium has diffusivity of 6.8×10^{-18} m^2/s, which is slower but within the same order of magnitude.

outward nitrogen diffusion was specified to occur through the inner rutile layer, but it is unclear whether there was evidence of outward nitrogen elsewhere.

Finally, the nanoporosity in the inner layer could be explained partly by the defects present in the rocksalt phase(s) of the region. If there are enough vacancies in either or both sublattices, there could be vacancy condensation that generates small voids throughout this layer. There does not seem to be any correlation between whether the region is N-rich or O-rich and the presence and size of voids nearby.

5.1.4 Microstructural evolution

As can be appreciated from these specimens, the interactions between nitrogen and oxygen with hcp titanium are complex even in low partial pressure environments with minute interstitial contents and while remaining below the β transus temperature. While the microstructural evolution is more complicated in this set of specimens than those of Chapter 4, these results provide important lessons and spark promising areas of future research.

Given the results from Chapter 4 and this chapter, a possible microstructural evolution is that a nitride scale forms first. As nitrogen and oxygen adsorb onto the metal surface, they begin to dissolve into the substrate. Since N solubility is smaller than O, it is possible that the metal saturates in nitrogen first despite its lower diffusivity than O at 800°C. Nitride formation would be the favored initial reaction as was seen in the scales of the fast-cooled specimens of Chapter 4. With continued oxygen ingress from the gettered Ar, the fcc TiN can convert to a range of oxynitrides while the outer part of this scale oxidizes to rutile. Throughout this process, continued outward Ti diffusion could provide enough titanium for continued reactions at the surface and explain some of the void formation from vacancy coalescence.

Assuming inward N and O diffusion, one can imagine a scenario where the TiN or oxynitride layer reaches a critical thickness at which rutile begins to form above it. Once the outer rutile scale is established, the nitrogen from the gas can no longer diffuse inward through the rutile scale and the nitrogen supply would be restricted to the nitrogen present in the nitride or oxynitride layer and in the metal substrate. The nitrogen from this scale could continue diffusing inward into the metal substrate. This would result in a decreasing thickness of the nitride/oxynitride layer, which is supported by the evidence seen in the cross-sections of the 9 h and 25 h specimens (Figure 5.3). This could explain why earlier studies [117] reported an outward N diffusion through the rutile layer. Since rutile can only account for ~3 at% N incorporation via implantation [181], most (if not all) nitrogen will be rejected from this phase. Rather than triggering an outward N diffusion through the rutile towards the free surface, the dense rutile scale could act as a diffusion barrier to any inward nitrogen diffusion through the rutile and into the layers underneath it. If nitrogen from the established nitride/oxynitride layers diffuses inward, the metal substrate would show a higher N content over time, which is the opposite of what the line scans from the metal substrate suggest (Figure 5.23). From the line scans, the oxygen content in the metal substrate near the metal-scale interface increases from 9 h to 25 h while the nitrogen content decreases. However, it could be possible that the nitrogen and oxygen have dissolved further into the metal substrate as well.

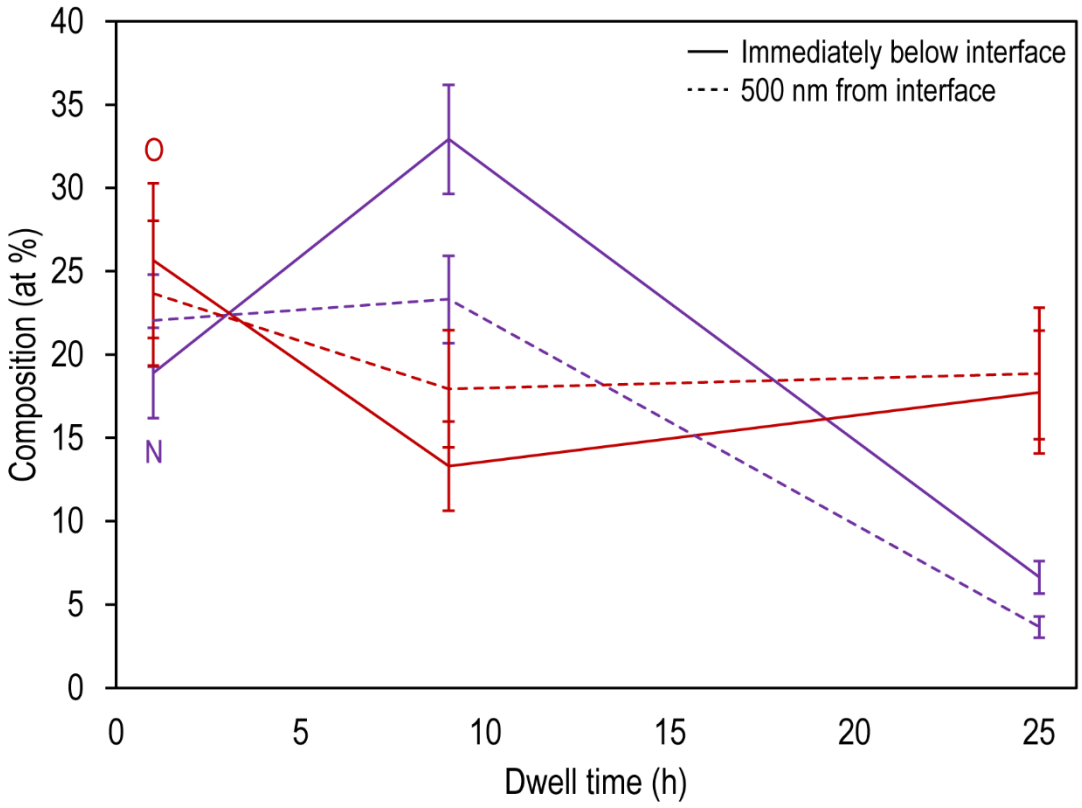

Figure 5.23. Interstitial content in the metal substrate for the 1-25 h specimens immediately below the surface (solid line) and 500 nm below the interface (dashed line). Extracted from the line scans shown earlier in the chapter. The 25 h specimen uses the values from the zoomed-in map.

While this scenario explains the 9 h and 25 h microstructures, it does not immediately explain the 1 h specimen where there is no nitride, oxynitride, nor rutile in the final microstructure. Assuming nitride formation first, the nitrogen would have had to dissolve entirely back into the metal substrate. One possible scenario to explain the 1 h microstructure would be that the nitride formed to a thickness where the inner surface reached a partial pressure low enough to allow for the formation of lower oxides. At this point, the nitrogen could have dissolved back into the substrate and the inward O ingress and outward Ti diffusion allowed for the formation of the Ti_2O_3 corundum and Magnéli phases. However, it is curious that there is no evidence for rutile since it is the most favorable reaction from thermodynamic considerations. To this end, it is also possible that rutile formed first and

reduced by dissolving some of its oxygen into the metal substrate and subsequently form the outer and inner oxide scales composed of lower oxides.

Despite incongruences in the literature regarding the thermodynamics of the Ti-N-O system, the predominance diagram (Figure 5.24) and Ellingham diagrams for Ti-N and Ti-O detailed in Chapter 2 suggest that rutile (TiO_2) formation would be favored even in the gettered argon environment used in these studies. However, the 1 h specimen shows no rutile formation and forms two lower oxides, Ti_2O_3 corundum and Magnéli phases. In the longer dwell times, rutile is found in the outermost layer with an oxynitride and ordered hcp-based layers underneath it.

The predominance diagram (Figure 5.24) suggests that the fcc oxynitride phase would necessitate extremely low partial pressures of oxygen ($< 10^{-30}$ atm O_2) and ambient to low partial pressures of nitrogen ($> 10^{-20}$ atm N_2) to form. Three different pathways are shown in this diagram to envision the expected layered structures given different partial pressures of oxygen vs nitrogen. In this gettered Ar, the larger N content and resulting microstructures would suggest the closest pathway to describe the reactions seen would be the top line marked as p (N_2) > p (O_2). Notably, there are missing phases in all three microstructures discussed in this chapter. None of the specimens show evidence of Ti_2N although there is evidence of hcp-based nitrogen orderings in its stead. In the 1 h specimen, there are no nitrides nor rutile, and the longer dwell times do not show any Ti_2O_3 or Magnéli layers. While there might be some differences in the expected phases at 800°C, the discrepancies could also be explained by the non-equilibrium conditions from heat-treating titanium and then slow-cooling it in the furnace's hot zone.

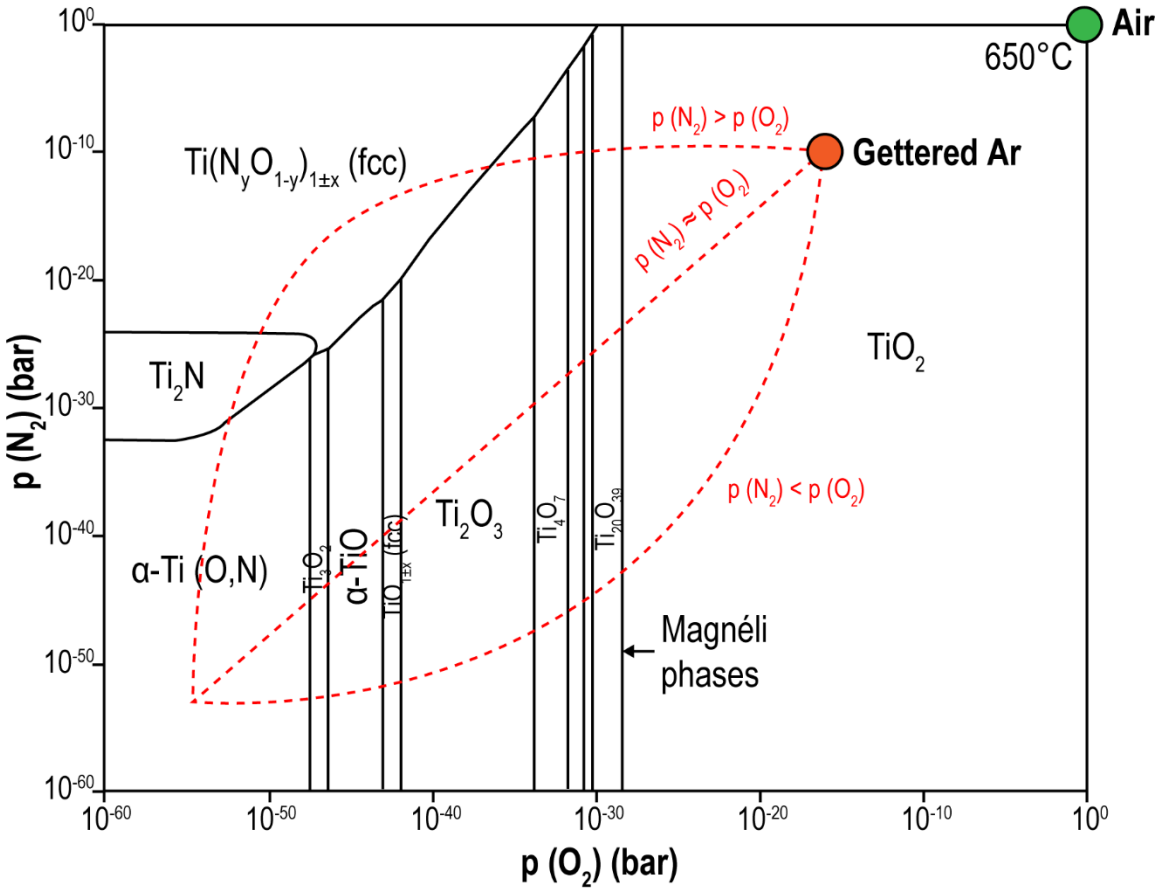

Figure 5.24. Predominance diagram showing which phases would be favored to form under various partial pressures of nitrogen and oxygen. Circles show the positions for relevant partial pressures for air (green circle) and gettered Ar used in this chapter (orange circle). Adapted from Dupressoire et al..'s [77] diagram calculated using ThermoCalc and the TCTI1 database.

5.2 Questions for further exploration

A set of questions that remain from these slow-cooled gettered Ar results are listed below. While some were discussed throughout the chapter, current thoughts and proposed work for solving them are summarized here.

- **Why do no nitrides, oxynitrides, nor rutile form in the 1 h dwell?**

  Given the use of the same gas environment, it is still possible that a nitride formed first and phase transformations during cooling enabled its dissolution into the metal substrate. Some N content is seen from STEM EDX in the lower oxides, but there is

not enough literature on N solubility in these phases to ascertain whether the composition given makes sense. Unfortunately, Raman spectroscopy (which will be used for in situ work in the following two chapters) does not allow for the detection of nitrides, oxynitrides, and many of the lower Ti oxides. An alternative in situ technique, such as in situ TEM using a holder with atmospheric control, would be beneficial to observe the phase transformations as they occur during dwell and subsequently during cooling. Special precautions should be taken to avoid any potential contamination of the titanium metal whether from the environment used or any of the materials that would be in contact with it during the experiment. (Carbon membranes, for instance, could readily change the Ti metal purity and therefore change the interstitial content and reactions being analyzed.)

- **Why do lower oxides not form during the longer dwell times of 9 h and 25 h?** From thermodynamic considerations, rutile formation is expected even in a gettered Ar environment and is present in the 9 h and 25 h specimens as the outermost scale. It is more unusual in titanium studies that any oxide other than rutile forms, which is the case of Ti_2O_3 and Magnéli phases in the 1 h specimens. Lower oxides could have formed from initial rutile formation and subsequent inward O diffusion from the rutile scale into the metal substrate until it transformed into these two lower oxides. If the rutile grew thick enough, the partial pressure at its inner surface would be lower and could allow for the formation of lower Ti phases. If these partial pressures allow for nitride formation first, the larger question would be why there is no nitride evidence in this specimen.

- **Why is the scale thickness for the 1 h and 9 h comparable?**

  The phase transformations during cooling complicate the interpretation of the final microstructures in this chapter. The expectation would be for scale thickness to increase with increasing dwell time since a longer dwell at high temperature allows for increased exposure of the Ti surface to the nitrogen and oxygen in the gas. At the end of the dwell time, the simplest scenario to imagine would be that nitrogen and oxygen only diffused into the metal substrate and all other phase transformations occur during cooling. This would imply that the initial conditions at the onset of cooling would be different in the 1 h and 9 h specimens since their interstitial content would not be the same. One possible scenario to explain the comparable thickness in these two dwell times would be that the initial nitride formed reached that thickness and further transformations relied on transforming that single scale. Is is unclear why the longer dwell times would have N-containing phases, but not be present in the 1 h dwell.

- **Why are nitrogen-containing phases always located close to the substrate?**

  From the predominance diagram at the gettered Ar partial pressures, the layer order seen in the 9 h and 25 h specimens make sense from a thermodynamics standpoint. Computational studies also suggest that N may diffuse further than O into the hcp Ti metal on its basal planes [182]. Due to its electronic structure, N begins diffusing into hcp Ti without reaching saturation at the surface first as O does. This would result in higher N than O contents into the metal.

- **When and how does porosity form in the oxynitride and rutile scales?**

  As discussed before, there is no single factor that can neatly explain the formation

and growth of voids throughout the specimens. Inert marker studies are often used to determine the relative flux directions of the elements involved in a reaction. In the case of titanium, its high reactivity makes it difficult to find an inert marker. An alternative method would be to use nitrogen and oxygen ions (e.g. ^{18}O and ^{17}N) to analyze their location after exposure. The number of steps required to incorporate both ions would require special care to avoid any contamination that could drastically change the final microstructures.

5.3 Conclusion

These results provide further evidence for why titanium oxidation has been studied for so long without the community reaching a clear agreement on a mechanism. Despite being treated in the same environment and using the same initial Ti metal, the microstructures and phases generated in Chapter 4 and Chapter 5 are vastly different. When fast-cooling, only nitride formation is appreciated, but slow-cooling enables the formation of oxynitrides, lower oxides, and rutile with significant porosity found throughout. The main results from the slow-cooled gettered Ar experiments are:

- Specimens formed layered structures in all three dwell times with varying degrees of porosity. In contrast to Chapter 4's fast-cooled specimens, nitrides are not the only phases to form in this set of specimens. The phases identified in these specimens are:
    - Substrate (1-25 h): **α-Ti with N/O ordering** likely in every other interstitial layer
    - IO (1 h): **Ti_2O_3** in a corundum crystal structure
    - OO (1 h): **Magnéli phase(s)** likely Ti_3O_5 and/or Ti_4O_7

    - IFL (9-25 h): **hcp-based N-rich ordered phases**
    - IL (9-25 h): **rocksalt Ti oxynitride** or TiN-TiO solid solutions
    - IO and OO (9-25 h): **rutile** (TiO_2)

- There is a strong orientation relationship between the hcp titanium substrate and the fcc rocksalt oxynitride phase(s) of the inner layer. The evidence provided for this came from electron diffraction patterns along the $[2\bar{1}\bar{1}0]_\alpha$ and $[110]_\delta$ zone axes. The $\{111\}$ planes of the fcc phase stack on top of the $\{0001\}$ planes of the hcp substrate.
- The inner layer of the 9 h and 25 h specimens shows the formation of an fcc rocksalt phase with a variety of compositions and orderings. Two long period stacking ordered (LPSO) structures are of particular interest and were identified through electron diffraction. These structures are comparable to intermediate structures proposed to form between the hcp and fcc Ti transformation. However, this region is N-rich and suggests that nitrogen could play an important role in promoting these orderings. This inner layer also shows varying concentrations of nitrogen and oxygen which could indicate ordering or spinodal decomposition along the TiN-TiO solid solution or TiN_xO_y composition range.
- Voids are ubiquitous in all three dwell times and show varying sizes and morphologies. The largest voids are found between rutile grains in the outer oxide scale and nanoporosity is found in the oxynitride region of the inner layer. The void formation and growth mechanism remains unclear, but is likely to grow along with the scales as will be demonstrated in the in situ experiments in Chapter 7. A combination of asymmetrical fluxes, volume expansions from phase transformations, and other factors are needed to explain the extent of porosity in these specimens.

6 hcp Titanium in UHP Ar at 800°C in Heating Stage under Raman Spectroscopy

This chapter will discuss titanium specimens treated in a gas environment with more nitrogen than oxygen (same as the preceding chapters), but with contents within the same order of magnitude (N_2:O_2 ratio = 5 as opposed to 10,000 for Chapters 4-5). The specimens discussed in this chapter were generated using the in situ heating stage setup under a Raman spectrometer as detailed in Chapter 3. The titanium specimens in this chapter were exposed to ultra-high purity (UHP) argon (Ar) gas (1 ppm O_2, 5 ppm N_2)[9] at 800°C for 5, 30, and 130 min dwells and cooled within the heating stage after shutting it off. An additional specimen that was held at 800°C for 4 h and cooled at 10°C/min will also be discussed.

The Ti specimens exposed to UHP Ar result in layered structures that show porosity in the inner oxynitride and outer rutile scales even after a short 5 min exposure. Due to the comparable nitrogen and oxygen contents, the phases formed include fcc rocksalt oxynitride (TiN_xO_y) with varying compositions, and rutile (TiO_2) in the outermost layer, as well as Magnéli phases (namely Ti_3O_5 and Ti_4O_7). As before, electron diffraction suggests ordering within the hcp Ti substrate similar to α" (staged Ti_2O) and X-ray diffraction shows shifts in the α-Ti peaks that indicate the formation of a solid solution with c-axis values larger than "pure" Ti.

The use of a heating stage allowed for acquisition of Raman spectra during the heating, dwell at 800°C, and cooling stages of the exposure. During in situ acquisition, rutile was

[9] The reason for the difference in gas environments was the location of the Raman system for the in situ experiments in a separate laboratory wherein a gettering furnace for Ar was not available. The highest purity Ar available from the gas supplier was used.

determined to form during the 800°C dwell, ruling out the possibility of rutile formation during cooling hypothesized from the resulting microstructures of previous furnace studies.

The microstructures of all specimens discussed in this chapter are reminiscent of those of the 9 h specimen from Chapter 5 which had an inner fcc oxynitride layer with an orientation relationship to the underlying hcp Ti substrate and an outer rutile scale with large voids. In contrast to this earlier 9 h specimen, the orientation relationship in this set of specimens will remain and extend to the rutile scale above the fcc oxynitride layer.

The phase identification for the developed scales and discussions of their microstructural evolution will be discussed in this chapter based on the Raman and post-experiment characterization results.

6.1 Results and discussion

The specimens exposed to UHP Ar form 2-3 scales depending on the dwell time (Figure 6.1). In general, their microstructure can be described as being composed of an hcp substrate, a nitride or N-rich TiN_xO_y scale (in the 5 min), a nanoporous TiN_xO_y scale (in the 30 and 130 min), and an outer rutile scale with large voids within (in all three dwell times). The slow-cooled 4 h dwell specimen will also share this microstructure and is most comparable to the 130 min specimen as it will have two TiN_xO_y regions with different compositions.

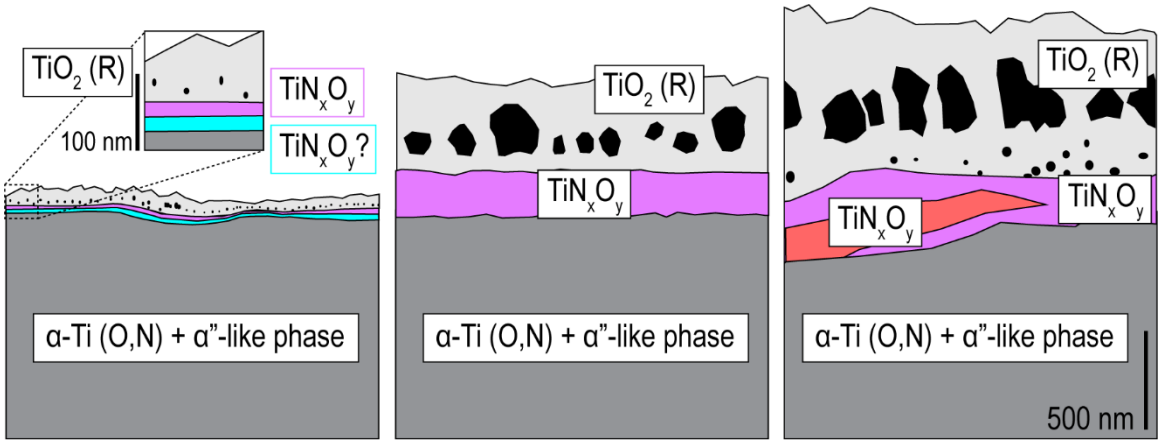

Figure 6.1. Schematic for Ti specimens exposed to UHP Ar at 800°C for (left) 5 min, (middle) 30 min, and (right) 130 min summarizing the proposed phase identification.

6.1.1 Phase identification

The surfaces of these in situ specimens (Figure 6.2) show fairly equiaxed and faceted grains that grow over time. At 5 minutes, the surface shows patches of continuous oxide as well as small sub-micron (55-175 nm) globular regions throughout the specimen. At 30 minutes, the grains have grown (~300 nm) to cover the surface and show faceted features. These grains grow to 400-600 nm after a 130 min dwell and show some small voids where there are gaps between the faceted grains.

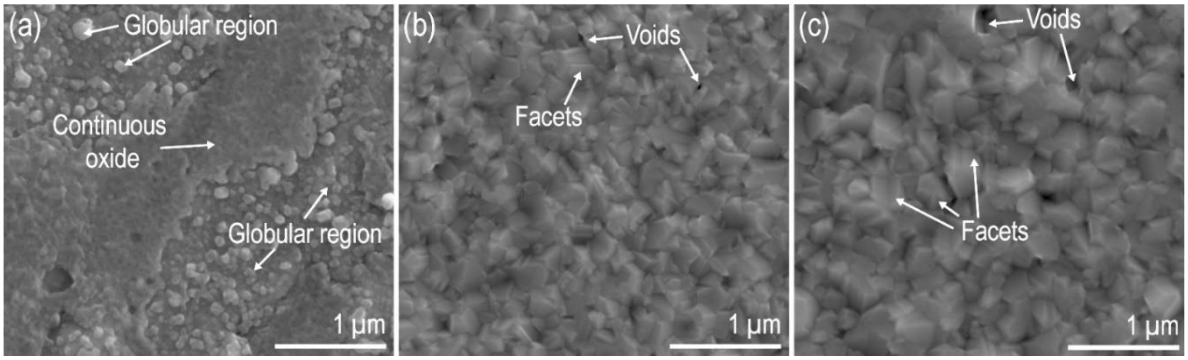

Figure 6.2. Top-view SEM SE micrographs from Ti foil oxidized under UHP Ar at 800°C for (a) 5 min, (b) 30 min, and (c) 130 min.

The cross-sections of these specimens reveal layered structures with significant porosity in the outer oxide scale which is always composed of rutile in this series of

experiments (Figure 6.3). One thing that is immediately apparent is that the outer oxide (~55 nm thick) and the voids (~20 nm) within this layer are visible even after a short 5 minute dwell at 800°C in UHP Ar. This suggests that both oxide and porosity formation happen early in the oxidation process. Furthermore, this same 5 min specimen shows a thin layer (40 nm) underneath the rutile scale. Upon closer inspection of the elemental maps, it is likely that this layer is two distinct scales (~20 nm each) since the oxygen signal shows the top of this region to be O-rich (labelled 'IL') and the bottom, O-lean (labelled 'IFL'). The nitrogen signal seems fairly even in these two scales. This could suggest that there is a titanium nitride above the metal substrate and a layer containing both nitrogen and oxygen (likely an oxynitride) above the nitride and beneath the porous rutile. While this region is too thin for EELS analysis, EELS measurements done for the 30 min specimen will reveal the presence of N and O throughout the specimen in these scales.

The voids within the outer oxide scale are always within this layer and not at the interface with the scale beneath. This suggests that there is both outward Ti and inward O diffusion within this scale and that asymmetrical fluxes of these can contribute to either void formation or void growth. In all three specimens a thin rutile layer can be identified underneath the large voids in the outer oxide. This region, along with the outer oxide voids, increases over time from ~15 nm to 220 nm size. It is possible that this region reaches a critical thickness above which the voids for the rutile layer are localized and may serve as a transition region of sorts above the oxygen and nitrogen-containing layer ('IL') underneath.

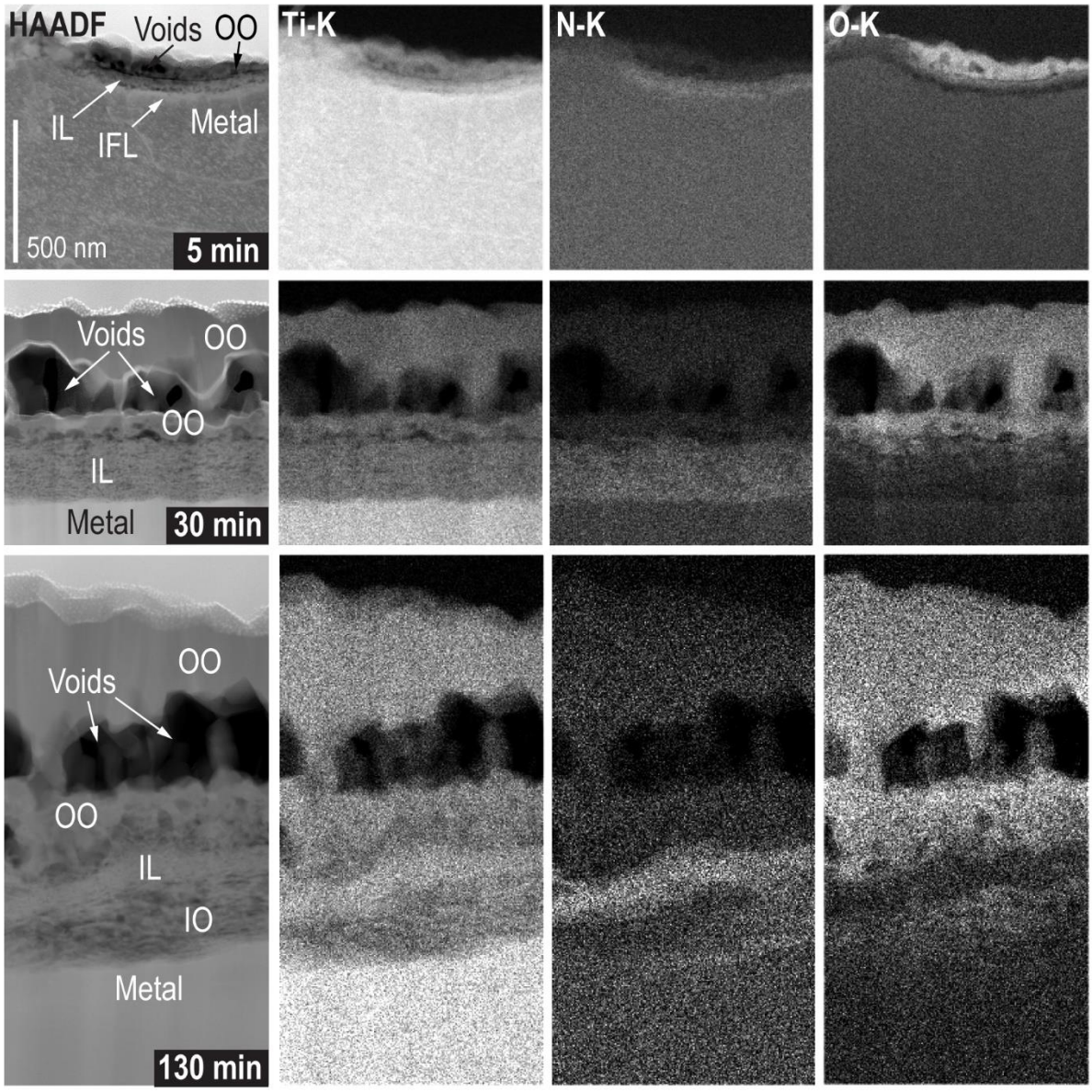

Figure 6.3. (Column 1) STEM HAADF cross-sectional micrographs and corresponding STEM EDX elemental maps for Ti foil oxidized in situ at 800°C in UHP Ar for (top row) 5 min, (middle row) 30 min, and (bottom row) 130 min showing (column 2) Ti, (column 3) N, and (column 4) O signal. OO stands for outer oxide, IL is inner layer, IFL is interfacial layer, and IO is inner oxynitride.

At 30 minutes, the outer oxide grains (350 nm) and the voids (80-200 nm) within this layer grow, compared to the 5 min specimen. In contrast to the 5 min specimen, there is a single scale underneath the outer oxide (~200 nm) that shows both nitrogen and oxygen signal in the STEM EDX elemental maps. Although it does not suggest two distinct scales as in the previous specimen, it does show a concentration gradient throughout this layer – most

evident in the oxygen signal showing a higher O concentration towards the top of this inner layer. This layer additionally shows nanoporosity (4-8 nm voids) throughout.

At 130 minutes, the outer oxide (650 nm) and its voids (~150-300 nm) have grown even larger and the thin region underneath the voids is also thicker (~220 nm) than in previous specimens. Interestingly, the continuity of the oxygen and nitrogen-bearing layer from the 30 min specimen is lost and there are now interspersed N-rich ('IL') and O-rich ('IO') regions rather than continuous layers or clear gradients of interstitial contents. While some literature argues that titanium nitride acts as an oxygen diffusion barrier in various Ti alloys [78,106,109], this specimen shows a higher oxygen content in the 'IO' region than in its 'IL' region above. Since the inner layer with more N than O is thickest and most distinguishable in the 30 min specimen, this specimen was used to further analyze this phase and its chemical composition using EELS.

Using STEM EDX area scans in the Velox software, line scans were generated for qualitative comparisons of the nitrogen and oxygen content throughout these microstructures (Figure 6.4). The scales are labeled in the background of each line scan to indicate the position for which each composition corresponds. Since EDX is unreliable for quantification of light elements (particularly in the Ti system where there are significant peak overlaps with N and O), these compositions should not be exclusively relied on for phase identification purposes but are useful to understand the possible diffusion of these interstitials throughout the scales. One important thing to note is that oxygen content is always larger than the nitrogen content in the metal substrate immediately underneath the developed scales with compositions oscillating around 23 at% O and around 10 at% N which would suggest that

these could be solubility limits for these interstitials in hcp Ti when both elements are present.

In general, the three dwell times show similar microstructures with an outer rutile layer, an inner oxynitride, and a metal substrate in all three specimens and an additional interfacial layer in the 5 min and an inner oxynitride in the 130 min specimen. Looking at the compositions for the different scales, the inner layer shows more nitrogen (34-37 at% N) than oxygen (25-31 at% O) in the 30 and 130 min with the 5 min showing more oxygen (34 at% O) than nitrogen (23 at%). These composition ranges could make sense for an fcc oxynitride with a rocksalt structure where half of the atoms are titanium and the remaining half are distributed between oxygen and nitrogen in different ratios. The interfacial layer (IFL) of the 5 min specimen shows ~25 at% N and 13 at% O, which while having more nitrogen than oxygen has enough oxygen to likely be an oxynitride rather than a nitride phase. The 'IO' region has a composition of 7-15 at% N and ~40 at% O. Similar to the IFL from the 5 min specimen, there is enough of both interstitials to likely form an oxynitride phase rather than a "pure" oxide.

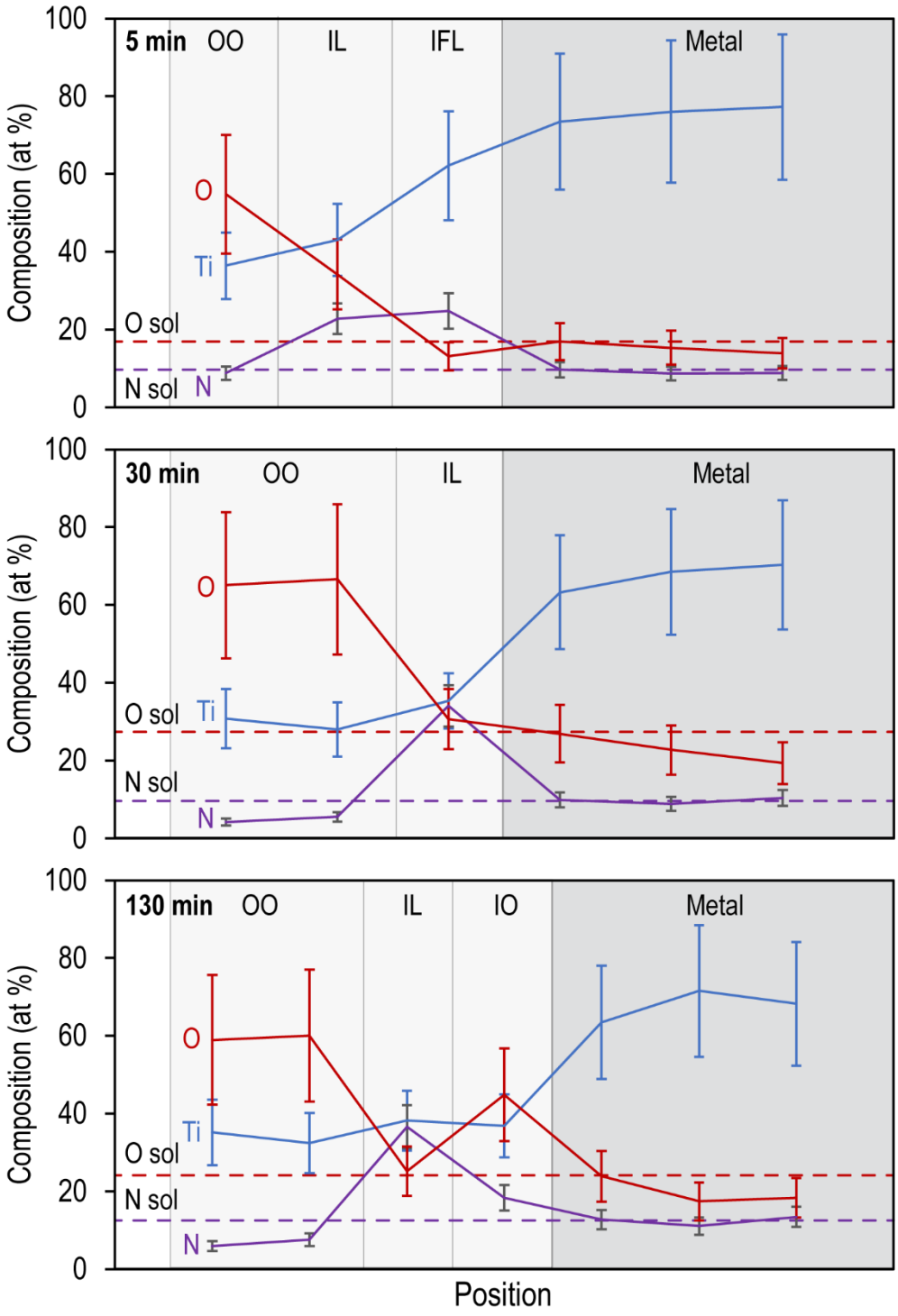

Figure 6.4. Line scans constructed from STEM EDX area scans in the different layers of Ti oxidized in situ at 800°C for 5, 30, and 130 min. Dashed lines indicate interstitial content at the metal surface underneath the scales. Names for scales indicated are the same as those used in the elemental maps (Figure 6.3). X-axis does not correspond to real distances and only represents the layers and areas measured.

The slow-cooled specimen that was held at 800°C for 4 h shows a similar microstructure to the 30 and 130 min specimens (Figure 6.5). From STEM EDX, the metal substrate has significantly more oxygen (~20 at% O) than nitrogen (0.5 – 3 at% N) up to 250 nm below the metal-scale interface which aligns with the trends shown in the 5-130 min specimens. Above the substrate, there are an IO and an IL region which appear indistinguishable from each other in the HAADF image but show distinct nitrogen and oxygen concentrations from their elemental maps. The IO region shows significantly more oxygen (~40 at% O) than nitrogen (8 – 15 at% N) whereas the opposite is true for the IL region albeit with more comparable nitrogen (27 – 34 at% N) and oxygen (19 – 28 at% N) contents. Given the similarity to the 9 h specimen from Chapter 5 and their compositions from EDX, these regions could both be oxynitrides with varying compositions and will be discussed in more detail later in this chapter.

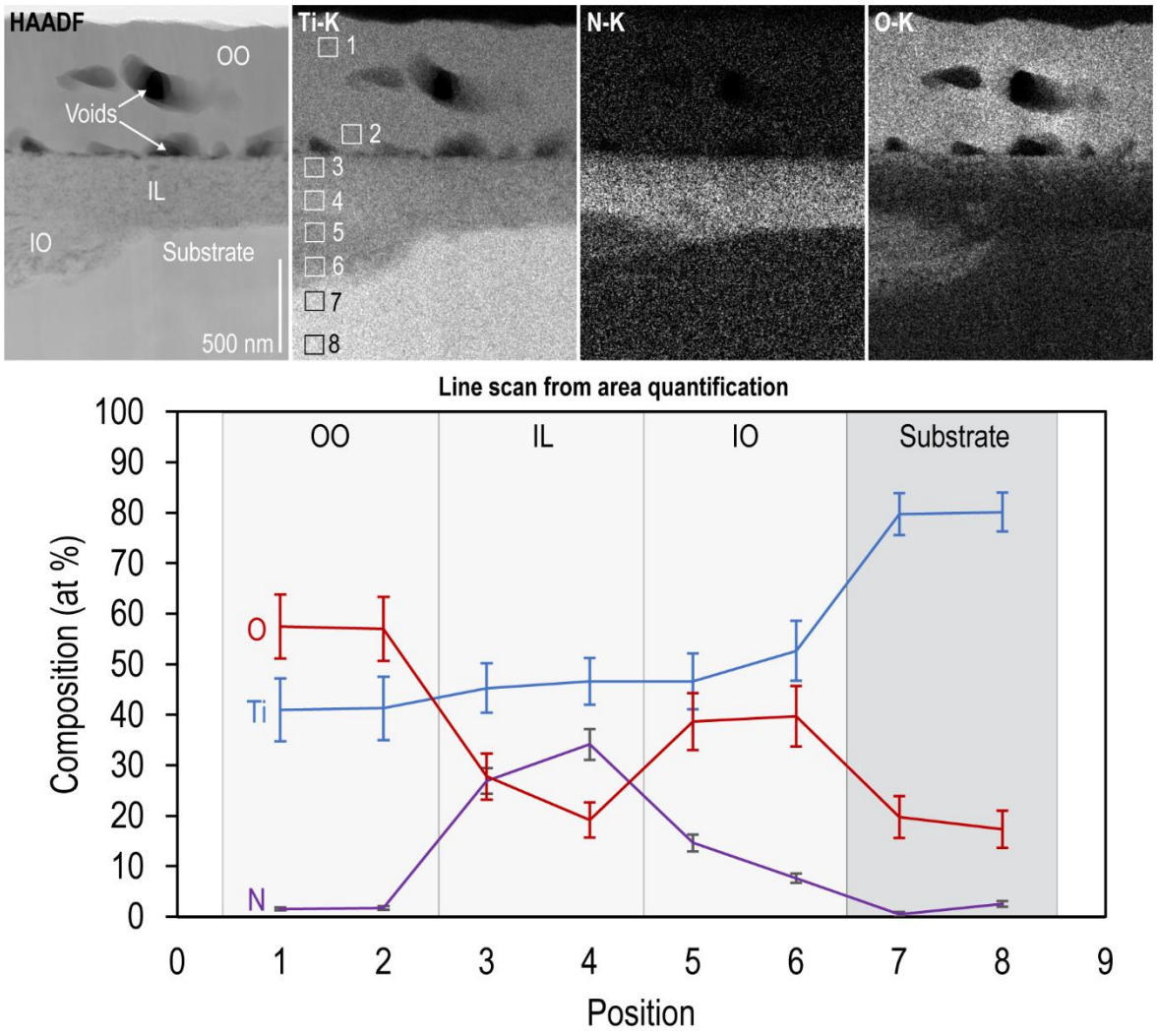

Figure 6.5. Cross-sectional micrograph for slow-cooled 4 h specimen from STEM HAADF and corresponding STEM EDX elemental maps. Areas used for quantification are shown in the Ti-K elemental map and its values were used to construct the line scan below. Oxygen content is highest in the OO layer and higher than the nitrogen content in the IO layer and substrate. Nitrogen content is highest in the IL layer, decreases in the IO layer, and is minimal in the substrate and OO layer.

X-ray diffraction patterns from the surface of these three specimens show the main $(110)_R$ peak with increasing intensity as dwell time increases suggesting a growing rutile scale over time (Figure 6.6). In contrast to the ex situ specimens described earlier in this chapter, all in situ specimens show rutile peaks. It is important to note that rutile peaks appear even in the short 5 min dwell time. Despite the short dwell time, the increase in oxygen content from gettered Ar (ex situ tube furnace studies from Chapters 4-5) to UHP Ar

(in situ heating stage studies in this chapter) enables the faster formation of rutile. The 5 min specimen shows a small additional peak to the right of the $(110)_R$ peak and shows peak splitting in the $(0002)_\alpha$, $(10\bar{1}1)_\alpha$, $(10\bar{1}2)_\alpha$, and $(2\bar{1}\bar{1}0)_\alpha$. Peak splitting usually denotes a loss of symmetry in the crystal structure and could indicate a phase transformation occurring from the hcp Ti to a lower symmetry phase in the metal substrate. While the additional peak to the right of $(110)_R$ is not expected in rutile, it is also seen in the rutile pellet XRD pattern obtained for reference so it is likely still related to the rutile phase. All three specimens show a shift in the basal and pyramidal planes that correspond to a c parameter of 4.77 Å (the expected c parameter for a $TiO_{0.325}$ solid solution and Ti_2O), 4.78 and 4.80 Å. These lattice changes correspond to a 2.0, 2.2 and 2.4% increase over hcp Ti respectively. This is consistent with an expected increase in the c lattice of the metal with oxygen incorporation congruent with hcp Ti nearing (or at) oxygen saturation. These α-Ti peaks also show significant peak broadening, particularly in the 5 min specimen, which could be attributed to a high number of defects within the substrate such as dislocations and stacking faults. (Some dislocations are visible in the lamella's substrate region for the 5 min specimen in Figure 6.3 whereas they are less frequent in the 30 and 130 min specimens.)

The 'a' parameters based on the rutile phase calculated from these XRD patterns are 4.61, 4.62, and 4.63 Å (-0.1, 0.1 and 0.2% change from rutile) showing minimal change in the lattice of the oxide scale. The small changes could arise from thermal changes during the experimental procedure. These XRD patterns also show an additional peak to the left of $(210)_R$ that could be consistent with an fcc rocksalt phase which will be further explored in the "Inner rocksalt layers (IL and IO)" section later in this chapter.

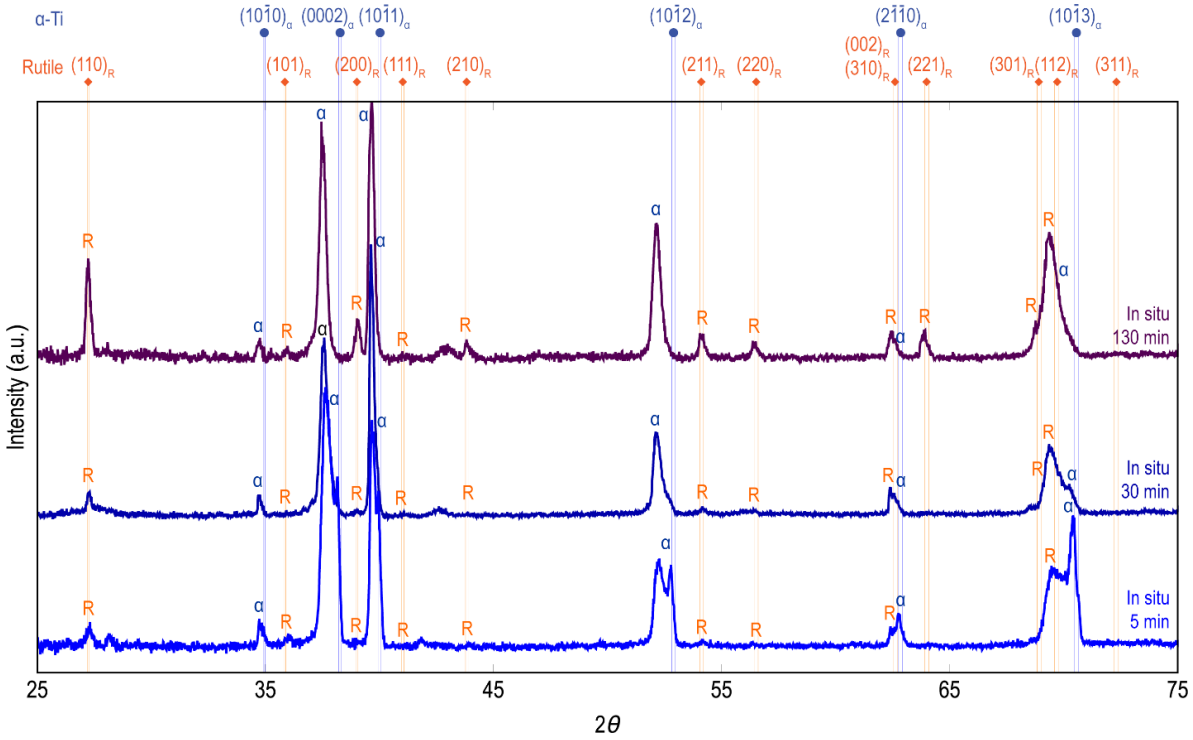

Figure 6.6. XRD patterns from surface of Ti specimens oxidized in situ in UHP Ar at 800°C for 5 min, 30 min, and 130 min. The peaks are labelled α for α-Ti and R for rutile. Reference lines in blue and orange show the expected positions for α-Ti and rutile respectively. The $[110]_R$ peak increases over time and α-Ti peaks show significant shifts to lower 2θ angles in the (0002), $(10\bar{1}1)$, and $(10\bar{1}2)$ peaks.

6.1.1.1 Outer oxide (OO) layer

From XRD, STEM EDX, and Raman spectra, the outer oxide is readily identified as rutile in all three specimens. However, electron diffraction shows the possibility of Magnéli formation due to the presence of additional reflections than those expected from the rutile phase. As described in Chapter 2, Magnéli phases (Ti_nO_{2n-1}) can be thought of as sheared rutile structures where the compositions can vary with values between $n = 3$ and $n = 9$.

Electron diffraction patterns along two different zone axes in the slow-cooled specimen show main reflections that can be matched to rutile and additional reflections that are not explainable by a single phase (Figure 6.7). The first zone axis along rutile's $[11\bar{1}]$

direction shows additional reflections at roughly $\frac{1}{3}$, $\frac{1}{2}$, and $\frac{2}{3}$ (101) which are located in the row highlighted by red arrows. While these reflections are seen at the same locations throughout the pattern, their intensities vary and do not follow a consistent pattern. For the $[010]_{ZA}$, additional spots can be seen to the immediate left and right of the main reflections as well as for the faint reflections (i.e. $(\bar{1}00)$) that are expected from rutile. These extra reflections suggest the presence of defects in the rutile scale. An additional electron diffraction pattern will be used to explore whether these can be attributed to Magnéli phases.

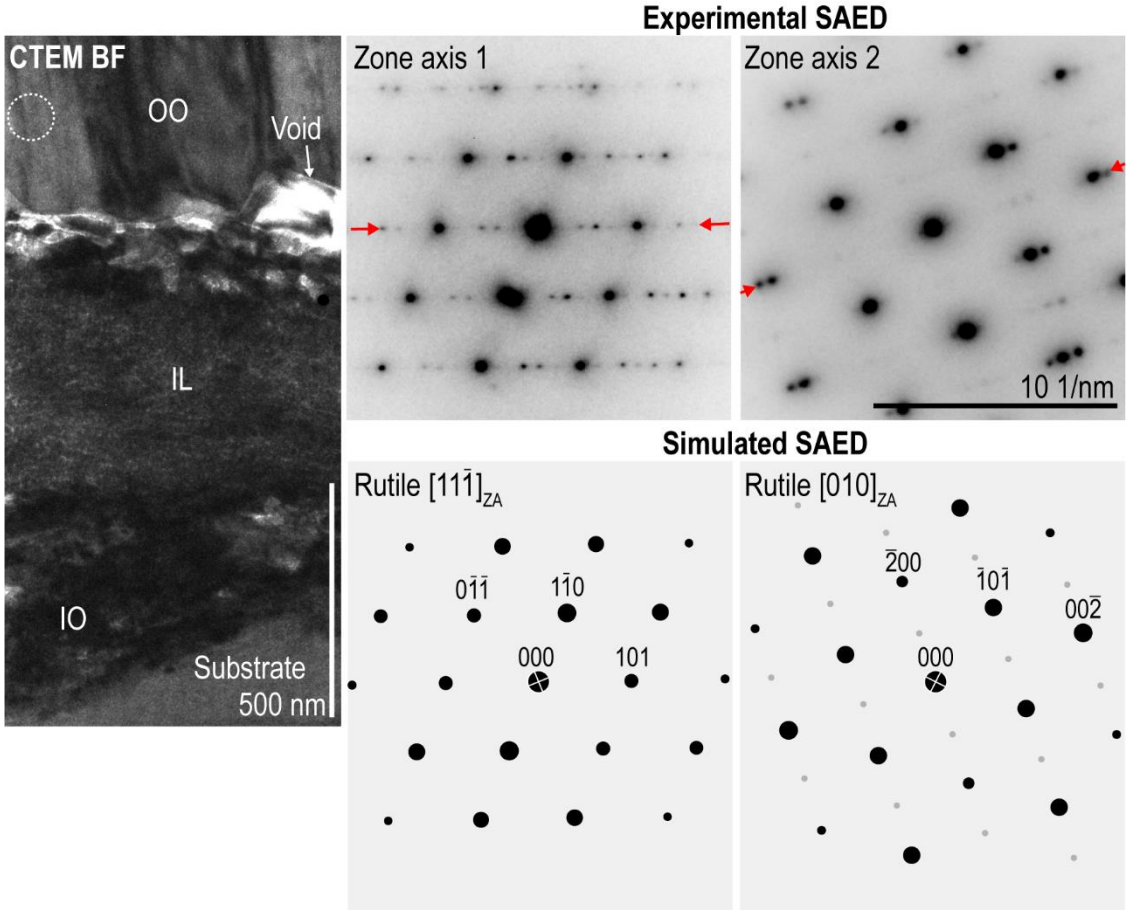

Figure 6.7. Cross-sectional CTEM BF micrograph showing area of interest for outer oxide SAED acquisition in slow-cooled 4 h specimen. Experimental SAED and their matching simulated SAED from rutile TiO_2 are shown.

An additional pattern with an $[0\bar{1}1]$ zone axis shows rows of faint additional reflections with alternating intensities (signaled in Figure 6.8 with red arrows). An interesting

feature of these additional reflections is the appearance of various vertically-stacked spots which give the appearance of streaking. Simulated patterns for rutile (TiO_2), the hcp α-Ti phase, and two Magnéli phases (Ti_3O_5 and Ti_4O_7) are shown next to the experimental diffraction pattern. From indexing the experimental spots to the Magnéli phases, the closest matches were to Ti_3O_5 $[102]_{ZA}$ and Ti_4O_7 $[77\bar{1}]_{ZA}$. Notably Ti_4O_7 shows no additional reflections, but the Ti_3O_5 simulation does. The row of additional reflections also shows alternating intensities, with the faintest reflection in the middle as in the experimental pattern. However, the rows for the main reflections are at a different interatomic distance and show different intensities from the experimental pattern. Upon closer inspection, the main spots from the experimental pattern also seem to have overlapped faint spots above them. Using both the Ti_3O_5 and the Ti_4O_7 patterns would most closely explain all of the features seen in the experimental pattern from the rutile scale. Since there is a wide number of Magnéli phases, it is possible that a range of them can form in different regions (e.g. a few layers of rutile, a few layers of Ti_3O_5, etc.) and appear as additional reflections in electron diffraction. Since there is no significant evidence of the Magnéli phases in the XRD patterns (they show significantly more peaks than rutile does in XRD), it is possible that Magnéli phases form in relatively small amounts.

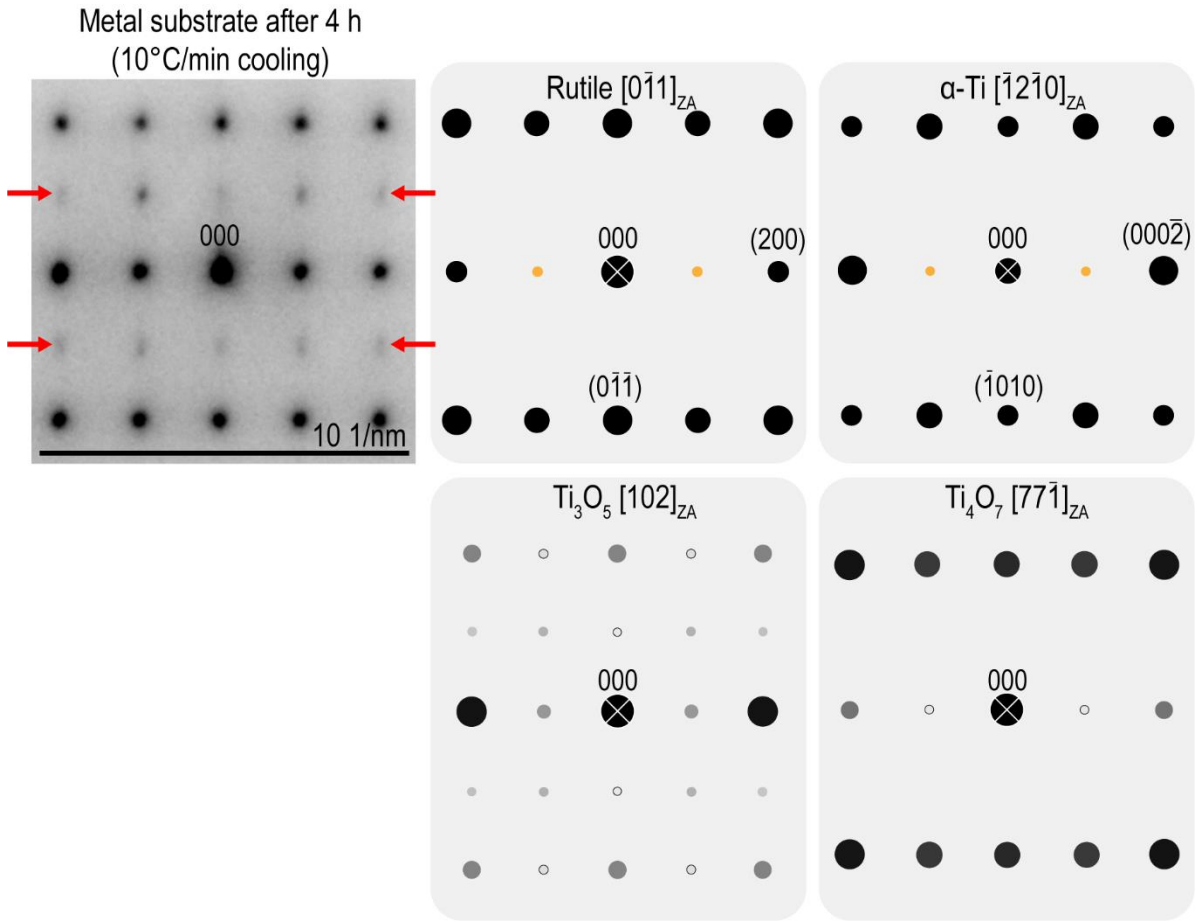

Figure 6.8. SAED from the outer oxide of the slow-cooled 4 h specimen is shown with additional reflections not expected in rutile. Simulated SAED patterns for the relevant orientations are shown for rutile, α-Ti, and two Magnéli phases, Ti_3O_5 and Ti_4O_7. Yellow circles denote double diffraction spots.

The crystal structures of the rutile and Magnéli phases along the orientations used for their simulated electron diffraction patterns are shown in Figure 6.9. The rutile and Ti_4O_7 show similar structures while the Ti_3O_5 shows an entirely different configuration of Ti and O atoms when looking along its [102] direction. While it could be possible for Ti and O atoms to shift from the rutile to the Ti_3O_5 configuration, there might be other orientations or Magnéli phases that could also explain these additional reflections.

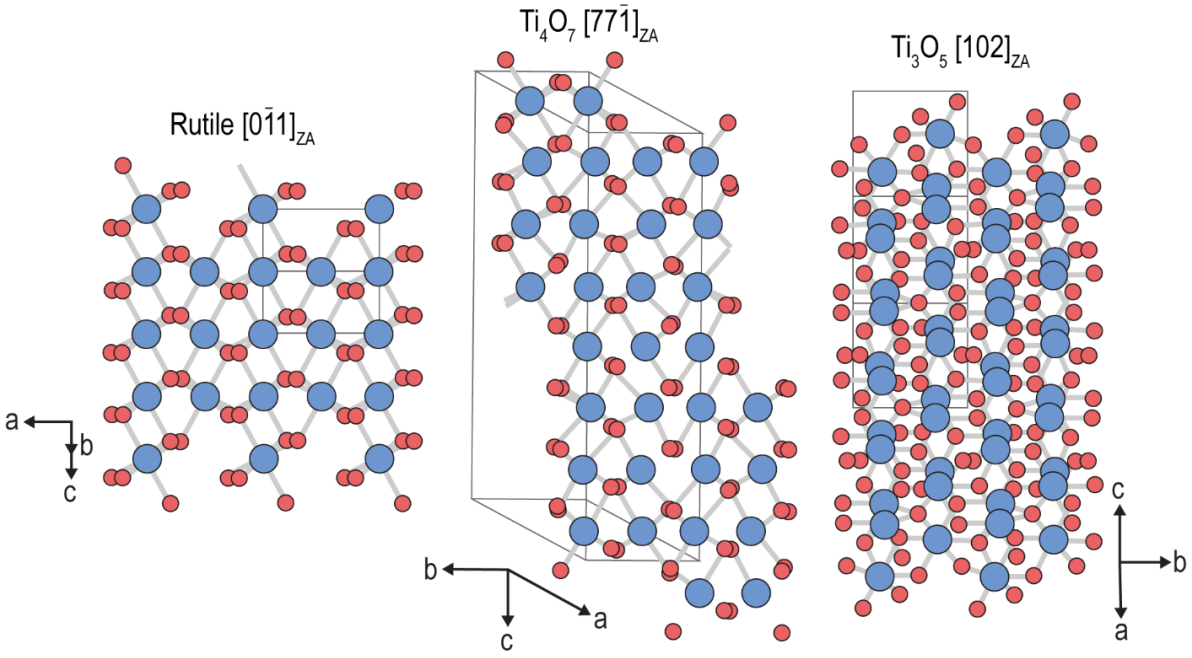

Figure 6.9. Crystal structures for the rutile and Magnéli phases that were used for the simulated SAED patterns. The rutile and Ti_4O_7 orientations are comparable while the Ti_3O_5 structure shows titanium and oxygen atoms in distinct positions that would not match the experimental pattern from Figure 6.8.

6.1.1.2 Inner rocksalt layers (IL and IO)

To explore the phase identification of the rocksalt phase containing N and O from the elemental maps, several characterization techniques were used including electron diffraction, XRD, and ELNES fingerprinting using EELS. To begin, the analysis will focus on the 'IL' region and the discussion on the 'IO' region from the 130 min and slow-cooled specimens will build on this analysis.

Electron diffraction from the 'IL' region unmistakably shows a NaCl-type (or fcc rocksalt) crystal structure (Figure 6.10). This rocksalt structure is clearly seen in the $[001]_{ZA}$ for rocksalt TiN and in the $[\bar{1}12]_{ZA}$ where there are a few faint additional reflections. As before, the TiN phase was used as a reference, but the inner layer contains both oxygen and nitrogen and is likely an oxynitride. Given the wide solubility range of Ti oxynitrides, a

possible explanation for any additional reflections would be ordering of vacancies or interstitials in the rocksalt phase even if only in small regions rather than throughout the entire layer.

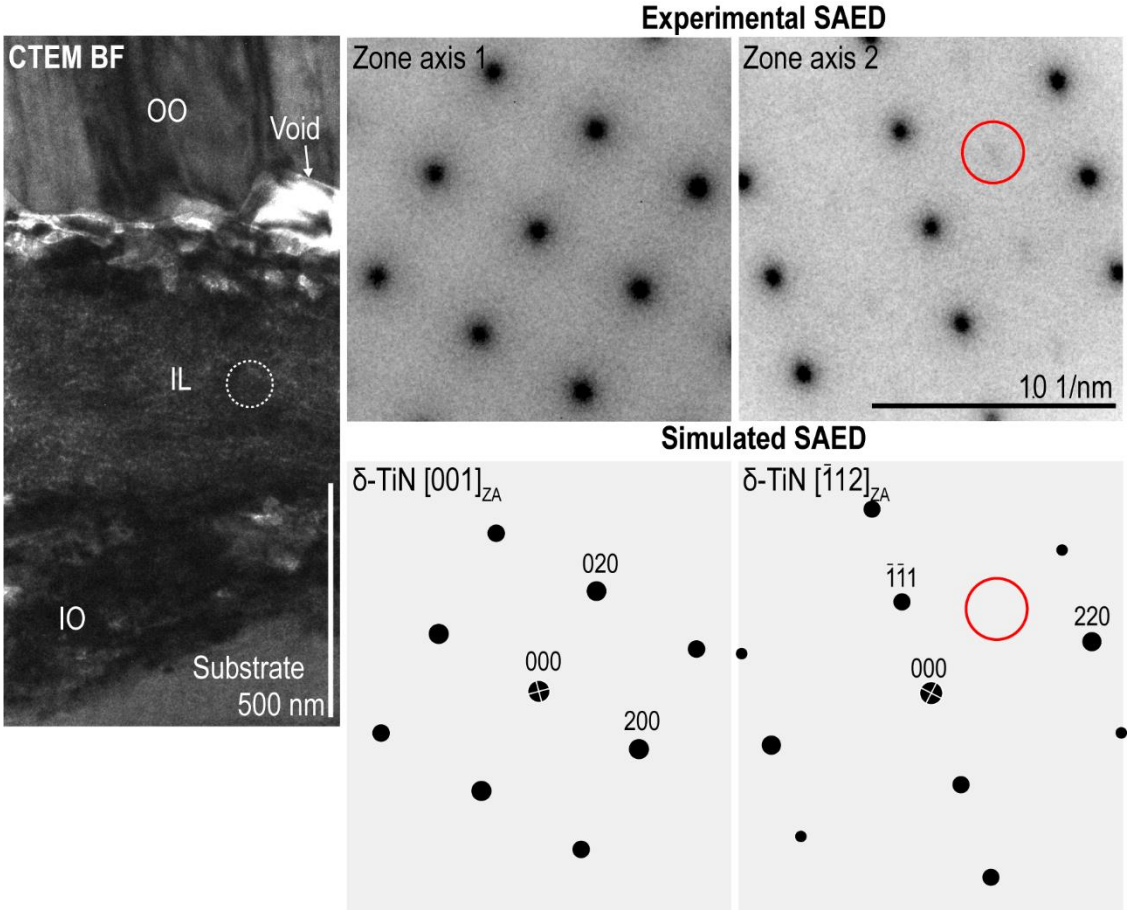

Figure 6.10. CTEM BF micrograph of the cross-section for the slow-cooled 4 h specimen showing a layered structure and the region where the aperture was for electron diffraction acquisition (dashed white circle within IL region). SAED from the IL region and their matching simulated SAED from TiN are shown. Additional reflections in the TiN $[\bar{1}12]_{ZA}$ pattern are shown circled in red.

Using these electron diffraction patterns, the interplanar spacings can be measured and compared to those of fcc Ti and relevant rocksalt phases (Table 6.1). The interplanar spacings were measured for (111) and (200) and are shown to be larger than those expected from rocksalt TiO or TiN, as well as those from the reference fcc oxynitride phase.

Table 6.1. Interplanar spacings for (111) and (200) for relevant rocksalt phases and from experimental SAED of the inner layer from the slow-cooled specimen.

Phase	**ICSD Reference No.**	**$d_{(111)}$ (Å)**	**$d_{(200)}$ (Å)**
fcc Ti	[80]	2.40397	2.0819
TiO	56612 or [56]	2.42735	2.10215
Rocksalt TiN_xO_y	426340 or [73]	2.42414	2.09936
TiN	1547 or [67]	2.44739	2.11950
In situ Ti – 4 h	This work	2.47524	2.12539

When looking at the XRD patterns from the surface, the peaks expected from rocksalt are not visible or very small. The 130 min pattern which has the highest rocksalt peaks will be used to compare to the rocksalt phases. Simulated XRD patterns zooming in on the region with (111) and (200) reflections for α-TiO and three Ti rocksalt phases are shown next to the experimental 130 min pattern in Figure 6.11. The monoclinic α-TiO was included since this phase has been reported to form in the temperature ranges used for these experiments, but none of the characterization of the inner layer provides evidence for this phase. In the XRD comparison figure, the (111) peak for the rocksalt phase can be seen as a small shoulder to the larger (0002) basal α-Ti peak around $2\theta = 37°$. However, the (200) peak near $2\theta = 43°$ is distinguishable despite its small intensity. When compared to the rocksalt TiO, TiN, and TiN_xO_y (namely $Ti_{0.7}N_{0.33}O_{0.67}$), the (200) peak from the experimental patterns lies somewhere between the TiO and TiN phases, suggesting that it is still a rocksalt phase but its lattice parameter is somewhere between these two "pure" phases.

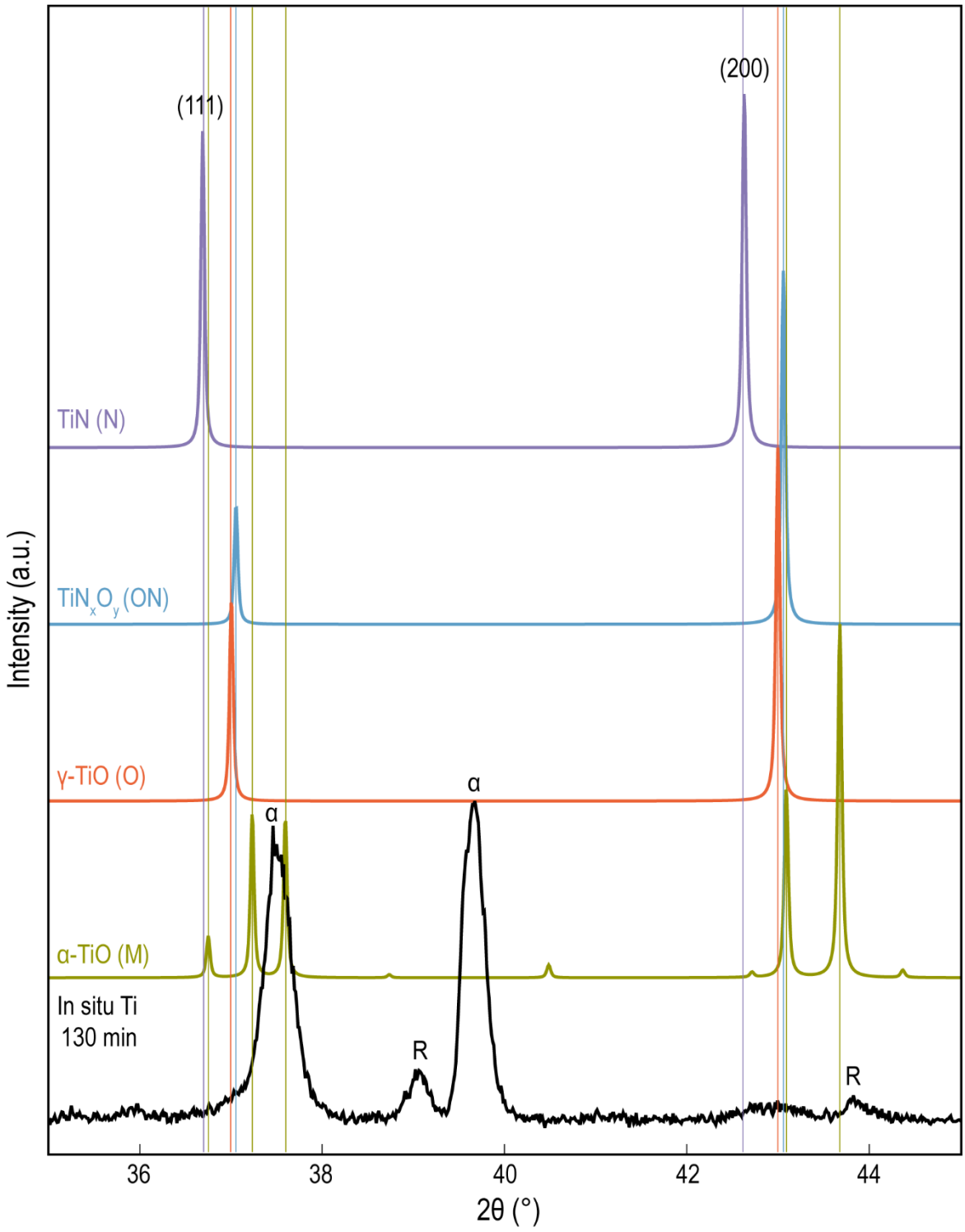

Figure 6.11. Simulated XRD patterns for select Ti rocksalt structures and monoclinic low-temperature α-TiO compared to the experimental XRD for the 130 min Ti specimen. Colored guidelines correspond to the simulated XRD patterns of the ICSD reference phases. The low peak near 43° is situated between the expected positions of a rocksalt TiN and TiO.

Due to the issues quantifying interstitials in EDX, EELS was used to confirm the presence of nitrogen and oxygen throughout the various specimen layers and to attempt quantification of the interstitial content in the 'IL' region. ELNES and core loss spectra of the Ti-$L_{2,3}$, N-K, and O-K edges were obtained for this purpose. The fine structure changes for these three elements across the 30 min specimen are shown in Figure 6.12. Nitrogen presence is confirmed in the unidentified 'IL' region exclusively, with no noticeable N-K edge in the rutile scale nor in the metal substrate.

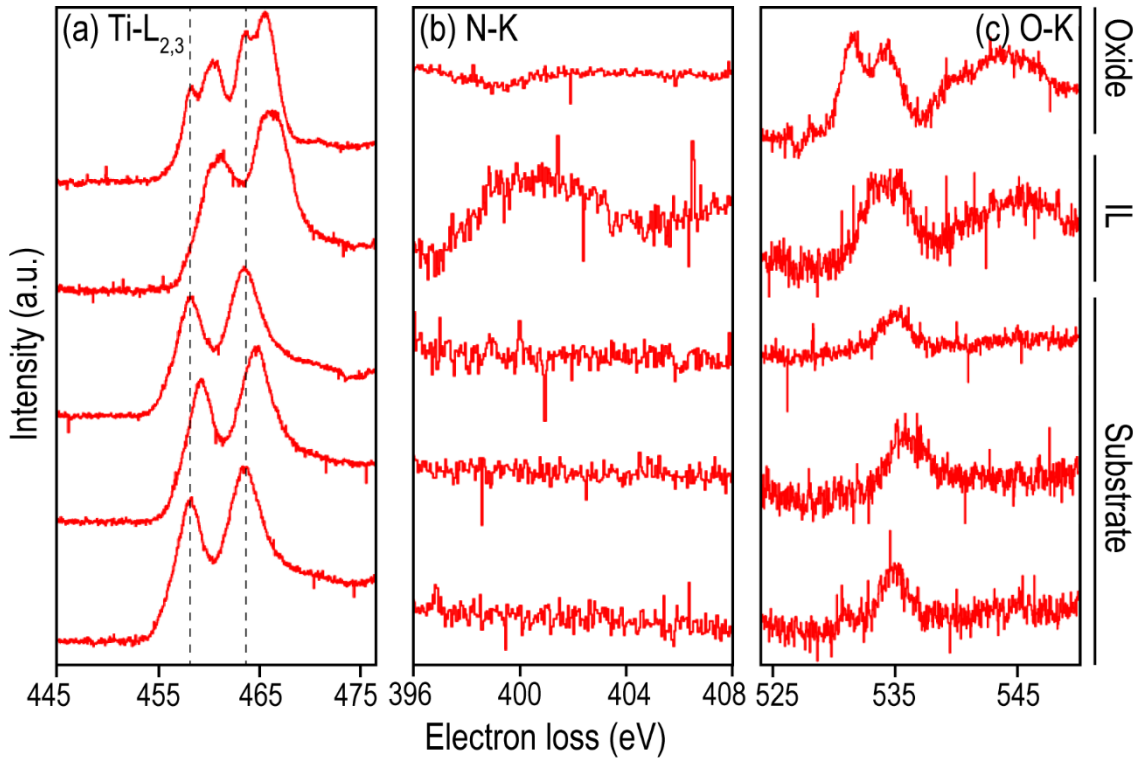

Figure 6.12. A magnified view of the ELNES (a) Ti-$L_{2,3}$, (b) N-K, and (c) O-K spectra showing the changes in fine structures throughout the developed layers in the titanium specimen oxidized for 30 minutes in UHP Ar at 800°C and cooled by furnace shut-off. The microstructure is shown in Figure 6.3. An N-K edge is visible only in the IL while O-K edges are seen in the substrate, IL, and oxide layers. The Ti-L edges are split into four peaks at the oxide only due to its +4 oxidation state in rutile. There are only two Ti-L peaks in the substrate and IL regions.

Notably, oxygen is present throughout the specimen given O-K edges are seen in the oxide, IL, and substrate regions, but nitrogen is only present in the IL. The split in the Ti-$L_{2,3}$ peaks in the outer oxide region is indicative of the Ti^{4+} charge when titanium is in rutile

(although these four peaks can also be seen in Magnéli phases [183]). Since the Ti-L peak splitting is missing in the IL region and because there is both nitrogen and oxygen present, this further supports the phase identification of this region as an oxynitride. The 2 peaks from Ti-L edges in the IL region represent a Ti^{2+} valence state seen for cubic TiO [183] and in Ti oxynitride [78]. Their energy loss in the IL region is higher compared to the Ti-L edges from the metallic substrate, which is consistent with previous observations and calculations [183]. Since previous XRD and SAED data has shown an fcc phase, it is most probable that this is an fcc rocksalt Ti oxynitride.

Quantification of this region using the Hartree-Slater model gives a composition of 16.4 at% N, 50.8 at% O, balance Ti. It is important to note that this same region gives a composition of 34 at% N, 31 at% O, balance Ti using STEM EDX. This composition approaches an equiatomic one as suggested by Tkachuk et al. [79] with decreasing pO_2 in the partial pressure ranges of 0.00001-0.01 Pa in 2-step oxynitriding studies of Ti alloys. Given the vast discrepancy between the compositions obtained from EELS and STEM EDX, these values should not be relied upon as a dependable chemical composition. However, the cumulative evidence supports the phase identification of fcc rocksalt Ti oxynitride phases of varying compositions in the 'IL' regions of the specimens shown in this chapter.

For the slow-cooled specimen, ELNES measurements were also attempted, but the specimen was not thin enough for proper spectra acquisition. Despite this, ELNES from the same energy regions in the 'IO' layer found underneath the 'IL' layer in the 130 min and slow-cooled specimen also shows a clear N-K edge around 400 eV. This confirms nitrogen presence in this region (even if there is more nitrogen than oxygen) and suggests that both the 'IL' and 'IO' regions are oxynitrides but with 'IL' having N > O contents and 'IO' having O

> N compositions. Since they are indistinguishable in HAADF imaging, it is likely that they are both the same fcc crystal structure albeit with different chemical compositions. Furthermore, the presence of 'IO' underneath 'IL' suggests that oxygen can continue to diffuse from the surface through the porous oxynitride layer.

6.1.1.3 Interstitial ordering in metal substrate

Electron diffraction patterns from the 30 min and slow-cooled specimen are shown here to compare the same orientation (Figure 6.13). In both experimental patterns, the (0001) reflections are strong which is a closest match to the α" (staged Ti_2O) phase. This phase is labelled 'α"-like phase' in the schematic at the beginning of this chapter (Figure 6.1).

Since ELNES shows no significant N-K edge peak, it is probable that the interstitial ordering seen in electron diffraction arises mainly from oxygen atoms rather than from a mixture of nitrogen and oxygen atoms. Given the non-equilibrium conditions of the experimental setup, this ordering could also be local and short-range and probably does not represent the bulk of the metal substrate, which from XRD is likely to be a solid solution phase of α-Ti (O,N) or α-Ti (O).

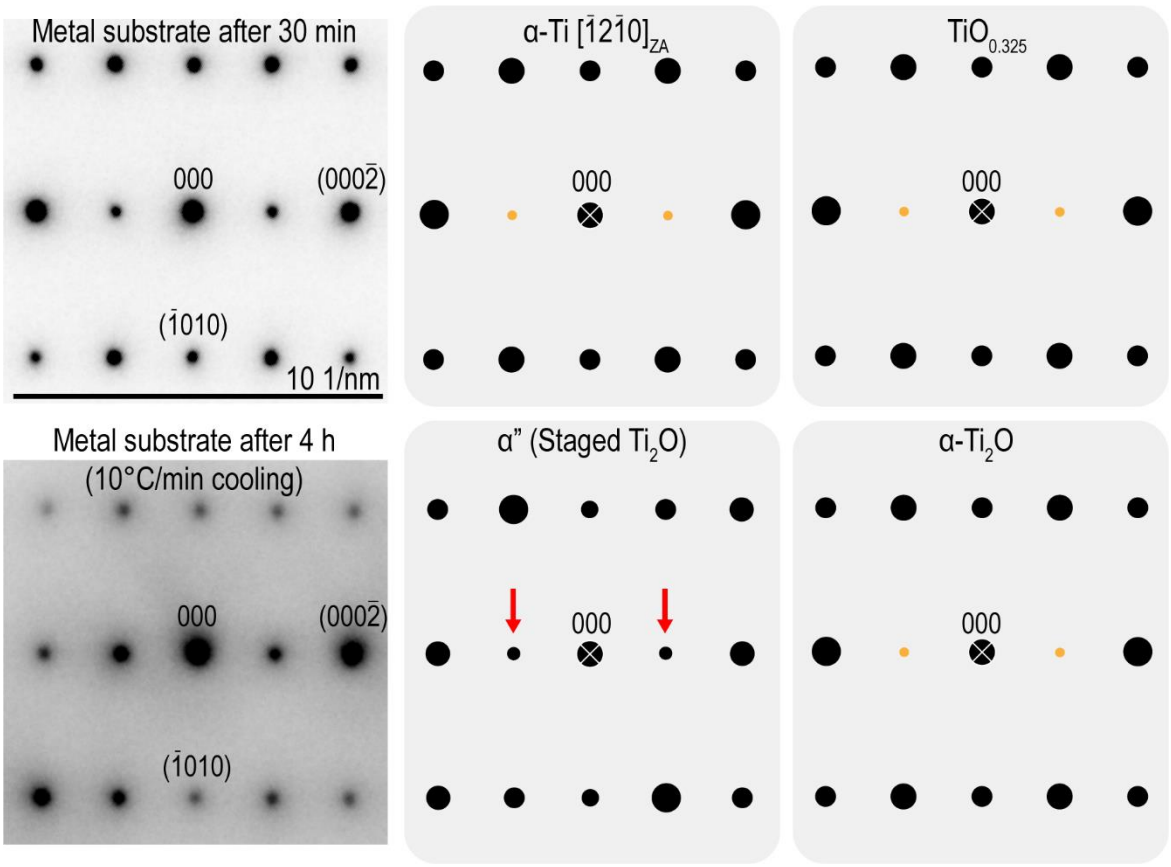

Figure 6.13. SAED from the metal substrate of the 30 min specimen and the slow-cooled 4 h specimen are shown and compared to the hcp-based α-Ti, solid solution and Ti_2O phases based on α-Ti. The experimental patterns are a closest match to the α" (staged Ti_2O) phase. Yellow circles denote double diffraction spots.

The slow-cooled 4 h specimen provided strong evidence of oxygen ordering throughout the metal substrate (Figure 6.14). SAED patterns obtained from the metal grain beneath the scale show the presence of different superlattice spots depending on the distance from the metal-scale interface. The main reflections in these patterns are corresponding to a [$\bar{1}$10] or [$\bar{1}$100] zone axis from hcp titanium. The schematic drawn highlights the three types of superlattice reflections, described by Yamaguchi [40] as a [110] zone axis, whose presence correspond to different concentrations of oxygen present in each hcp-based suboxide phase. All superlattice reflection types are seen furthest from the interface and only

Type I remains near the interface, suggesting ordering corresponding to different oxygen compositions.

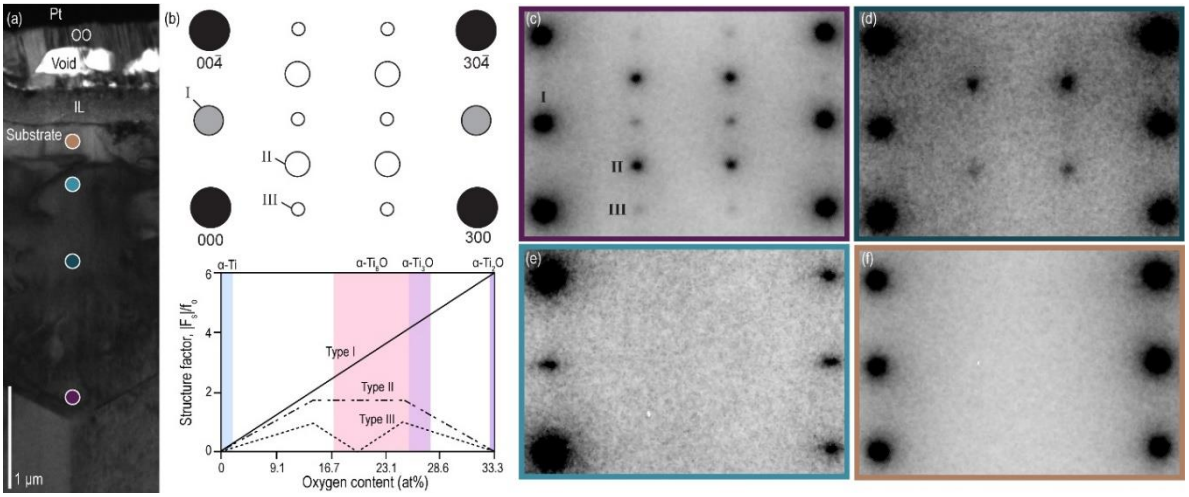

Figure 6.14. (a) Bright field TEM image of the cross-section of titanium oxidized for 4 h in argon (1 ppm O_2, 5 ppm N_2) and cooled at 10°C/min. (b) Schematic of the types of superlattice reflections expected in hcp Ti with various oxygen contents based on Yamaguchi's diffraction work along the [$\bar{1}$100] zone axis [40]. Shaded colored areas represent oxygen solubility ranges from the metastable Ti-O phase diagram [5] at 200K where all orderings can form. (c-f) Selected area diffraction patterns from (c) to the titanium substrate region immediately below the scale-metal interface to (f) the bottom of a titanium substrate grain.

Oxidation typically shows complex non-equilibrium structures so it could be possible that oxygen does not fully order to correspond to stoichiometric α-based suboxides. When comparing the ordering seen deepest into the metal to the hcp-based Ti suboxides from literature, only Ti_3O shows the three types of superlattice reflections (Figure 6.15). While this is a close match to the experimental SAED showing all superlattice reflection types, there is no suboxide that shows Type I and Type II reflections as in Figure 6.14d. The types of superlattice reflections seen in the experimental SAED pattern match the expectations for increasing oxygen contents towards the metal-scale interface where all superlattice types are visible in low oxygen contents and only Type I reflections are visible in high oxygen contents (corresponding to a staged Ti_2O structure). The ordering in the 130 min in situ

specimen showed Type I and II reflections (SAED not shown here but analogous to Figure 6.14d).

From the comparison to Yamaguchi's work and to simulated SAED from reference patterns, the metal substrate shows an ordering similar to Ti_3O furthest from the metal-scale interface. The next SAED (Figure 6.14d) does not have a match to the suboxides, and the two final SAED near the top of the substrate are closest to the α" (staged Ti_2O) phase where Type I reflections are solid (rather than double diffraction) and there are no Type II or Type III reflections. It is possible that the SAED from Figure 6.14d showing Type I and Type II reflections is a metastable suboxide phase or is a suboxide similar to Ti_6O but with some in-plane disorder that would shift the expected Type III reflections of Ti_6O to Type II.

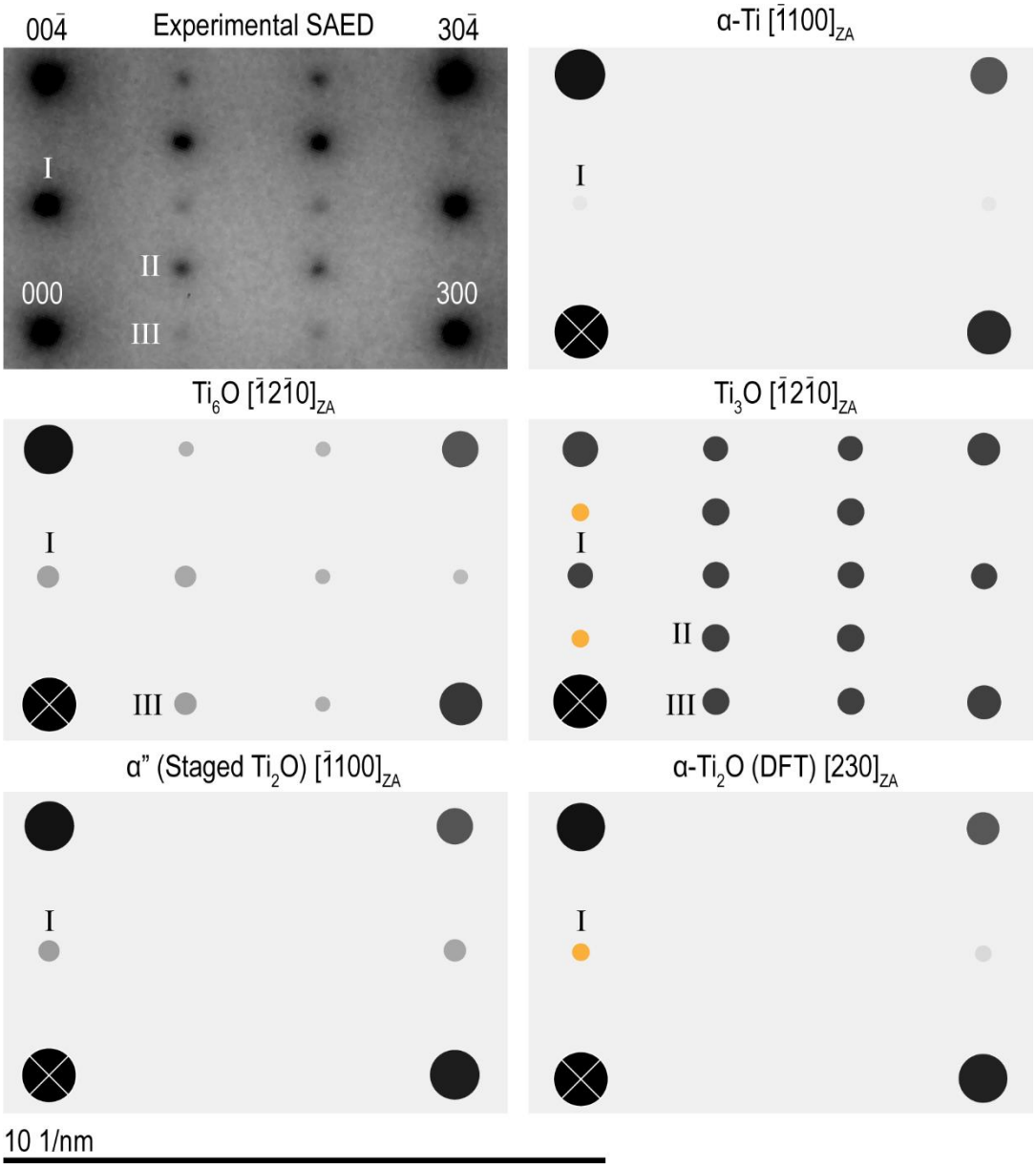

Figure 6.15. Experimental SAED from the slow-cooled specimen's metal substrate (Figure 6.14) compared to the equivalent directions of hcp Ti, Ti_6O, Ti_3O, α" (staged Ti_2O), and α-Ti2O from DFT work [5]. The crystal structures used are from ICSD and are denoted in Chapter 2. All suboxides show superlattice reflections Type I, while Type II appears in the Ti_3O and Type III appears in the Ti_6O and Ti_3O suboxides. Only Ti_3O shows all superlattice types which is closest to the experimental diffraction pattern. Yellow spots denote double diffraction.

Another interesting feature from this orientation of SAED patterns is the diffuse scattering of the Type I reflections that can be seen on diffraction patterns obtained from line defects in the substrate of Ti oxidized in situ for 30 min (Figure 6.16). This type of diffuse

scattering was also observed by Yamaguchi [40] with the streaking becoming more pronounced when increasing the temperature from which their specimens were quenched. This type of streaking along the reciprocal a* axis has been attributed to interstice lattice stacking faults [184] or antiphase boundaries [40,185]. As can be appreciated in Figure 6.16, the streaking does not correspond to interstitial contents since the SAED acquired closest to the scale (where higher interstitial contents would be expected) does not show streaking. The location of the orange SAED which shows the streaking is located on a linear defect within the substrate.

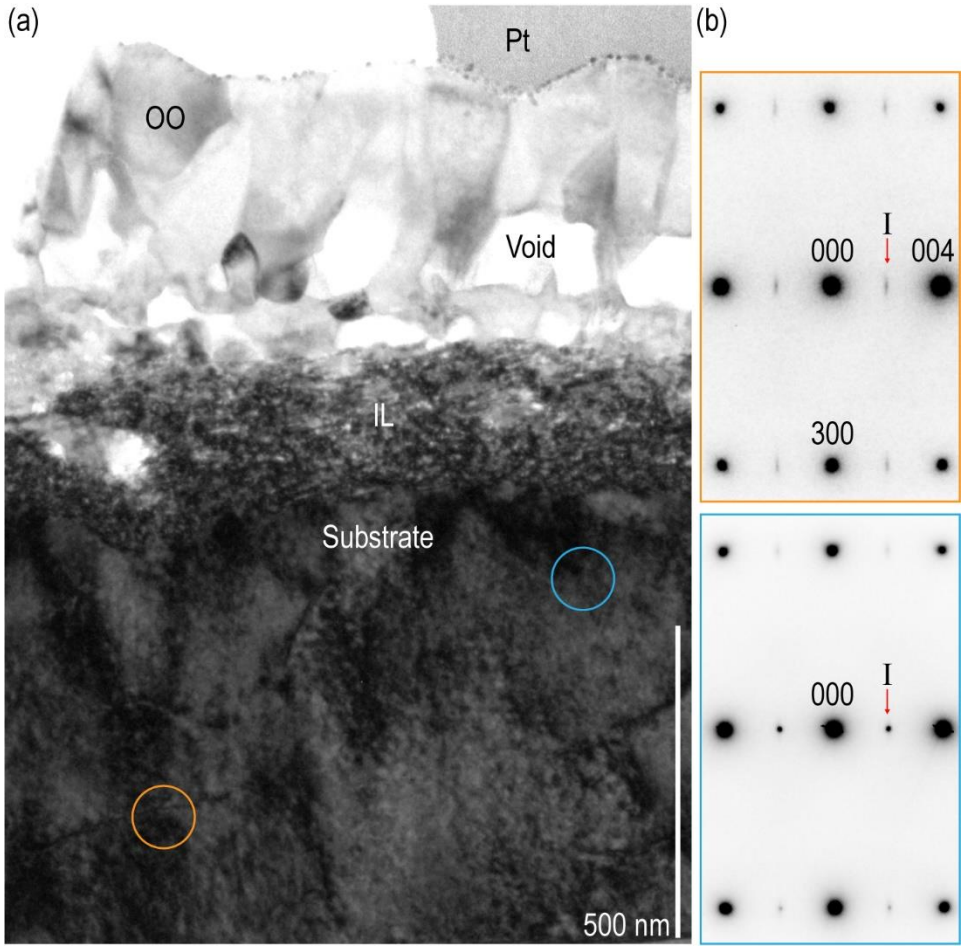

Figure 6.16. (a) CTEM BF cross-section of Ti oxidized in situ at 800°C in UHP Ar for 30 min. SAED patterns in (b) show α-Ti reflections for $[\bar{1}100]_{ZA}$. Notation used is based on solid solutions proposed by Yamaguchi [40] whose SAED is shown in Figure 6.14. Patterns show diffuse scattering when

sampling small areas of the substrate with line defects (orange circle – 100 nm aperture) which disappear when sampling a larger 500 nm area of the entire substrate.

6.1.2 Orientation relationship between hcp and the scales above

As in Chapters 4 and 5, the same orientation relationship can be seen between the hcp Ti substrate and the fcc rocksalt oxynitride phase of the inner layer. Interestingly, when acquiring an electron diffraction pattern from each region using the same stage tilt, an orientation relationship can also be extended into the outer rutile layer (Figure 6.17). The substrate and outer oxide SAED are the same ones shown previously in Figure 6.13 and Figure 6.8 respectively. The inner layer SAED is a bit unclear given the thickness of the lamella at the inner layer was not thin enough. The SAED from this fcc region shows streaking along the $(1\bar{1}\bar{1})$ spots where distinct additional reflections were attributed to long period stacking ordering structures in Chapter 5.

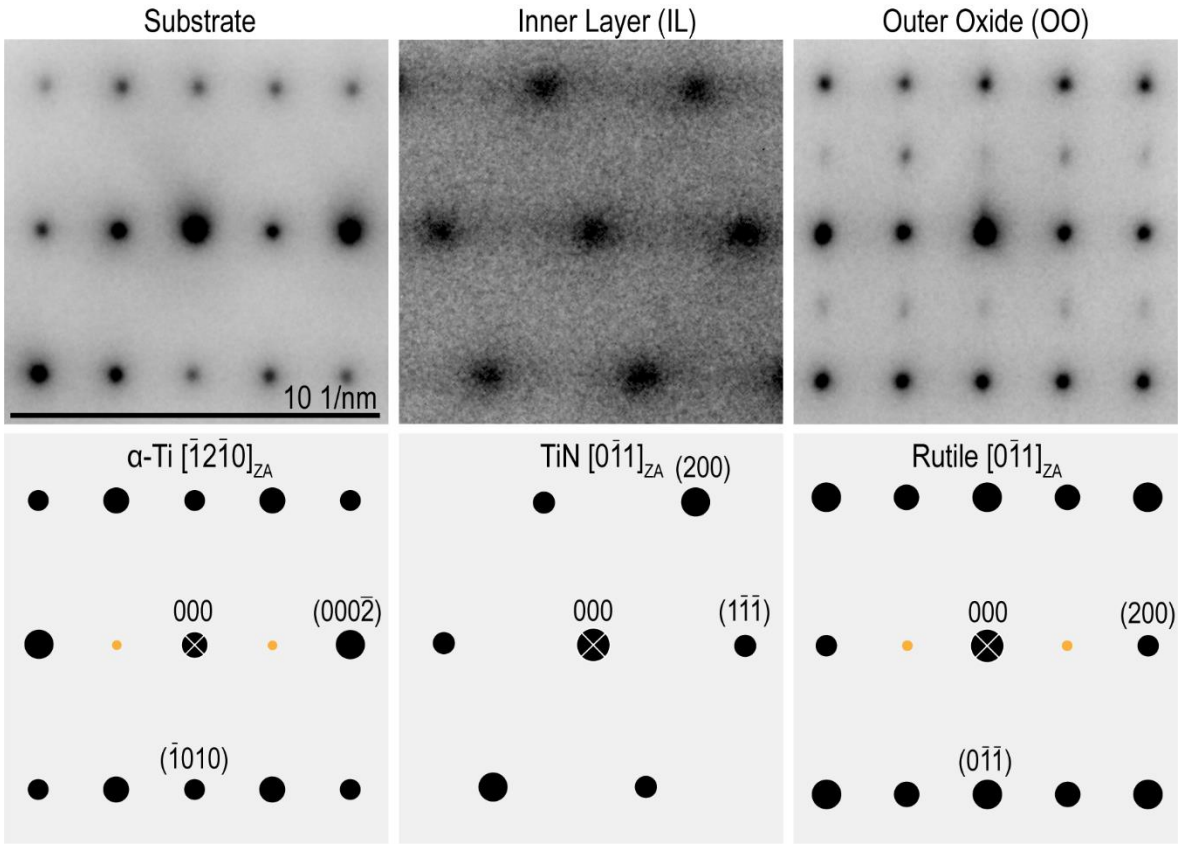

Figure 6.17. (Top) Experimental SAED patterns from metal substrate, inner layer, and outer layer regions of the slow-cooled 4 h specimen compared to (bottom) their respective simulated SAED patterns for α-Ti, rocksalt TiN, and rutile respectively.

The hcp Ti to fcc oxynitride orientation relationship is similar to that described in the previous two chapters. The crystal structures of these two is shown in Figure 6.18 looking at the hcp Ti unit cell down its $[\bar{1}2\bar{1}0]$ orientation and along the $[0\bar{1}1]$ orientation of the fcc oxynitride phase. A rutile unit cell is added above the fcc oxynitride crystal structure looking down its $[0\bar{1}1]$ direction. An orientation relationship of $[11\bar{2}0]_{\alpha} \parallel [1\bar{1}0]_{\gamma}$ has been reported previously in literature when transforming from hcp Ti to γ-TiAl with a c/a ratio of roughly 1.02 [186]. Rutile in particular, a tetragonal phase with a c/a ratio of ~0.64, can form as an epitaxial film on hcp titanium with the orientation relationships (010), [100] for rutile || (0001), $[1\bar{1}00]$, $[10\bar{1}0]$ and $[01\bar{1}0]$ for hcp Ti [187]. During in situ oxidation of titanium by high voltage electron microscopy, rutile grows epitaxially on the hcp titanium metal with the

orientation relationships of (0001) for hcp Ti || (010) for rutile TiO_2, which is the same as the one reported by Ievlev et al. [187], and an additional relationship of $(1\bar{2}10)$ hcp Ti || (001) rutile TiO_2 [188]. Orientation relationships between the hcp titanium and the tetragonal rutile phase have therefore been observed before when growing rutile on titanium. Having the fcc oxynitride phase in between the hcp Ti and the rutile does not seem to interrupt the orientation relationships than can arise between hcp Ti and rutile. From a different perspective, the rutile structure can be thought of as an hcp ordering of oxygen atoms. In this sense, the oxynitride to rutile phase transformation can be thought of as an 'fcc' O to 'hcp' O transformation analogous to the hcp Ti to fcc transformation explained in Chapters 4 and 5.

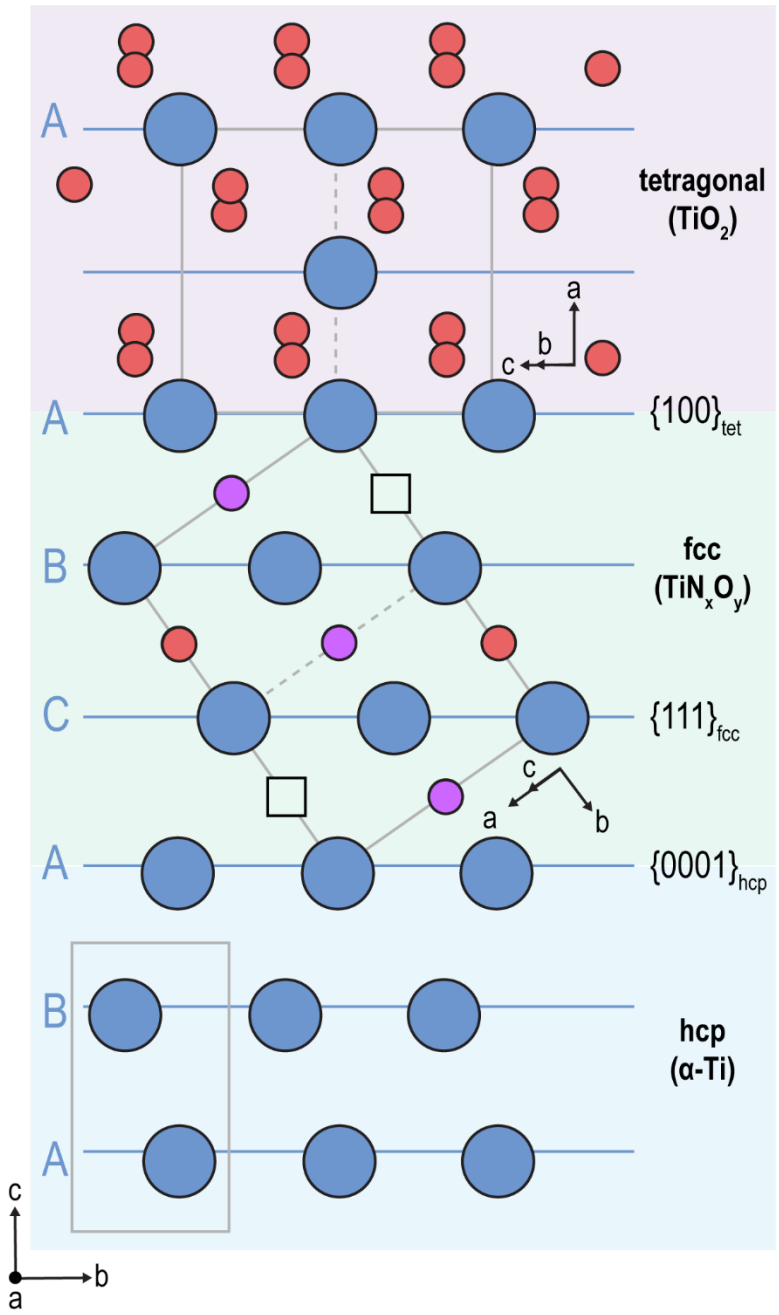

Figure 6.18. Schematic showing the orientation relationship between the hcp Ti substrate (ABA stacking) looking down the $[\bar{1}2\bar{1}0]$ direction, rocksalt TiN_xO_y inner layer (ACBA stacking) along the $[0\bar{1}1]$ direction, and the tetragonal rutile outer scale along the $[0\bar{1}1]$ direction. Vacancies (squares), oxygen atoms (pink) and nitrogen atoms (purple) are shown in the rocksalt structure as this is likely an oxynitride. The {0001} planes from hcp correspond to the {111} planes from fcc stacking. Blue atoms are Ti and unit cells are delineated in gray.

6.1.3 Raman spectral evolution

In contrast to previous chapters, the heating stage setup in this set of experiments allowed for acquisition of Raman spectra during the Ti exposure to UHP Ar at 800°C. Since all dwell times follow the same trends, the in situ spectra and corresponding optical images will only be shown for the 30 min specimen.

In the Raman spectral evolution (Figure 6.19), the background starts to increase during heating at 600°C and continues to increase over time during the dwell. As in the previous chapter, rutile peaks become apparent at temperature but take a longer time (~20 min) to be clearly distinguishable. This suggests that rutile forms at temperature even in the UHP Ar environment with lower interstitial contents. During cooling, the background and peak intensities decrease, and the final spectrum shows a significant background and a more intense E_g peak than an A_{1g} peak. While other Raman spectra of oxidized titanium show different E_g/A_{1g} ratios under different processing conditions [138], it is unclear what these represent. The intensity of E_g, for instance, is thought to correlate with increased crystallinity in the oxides [138].

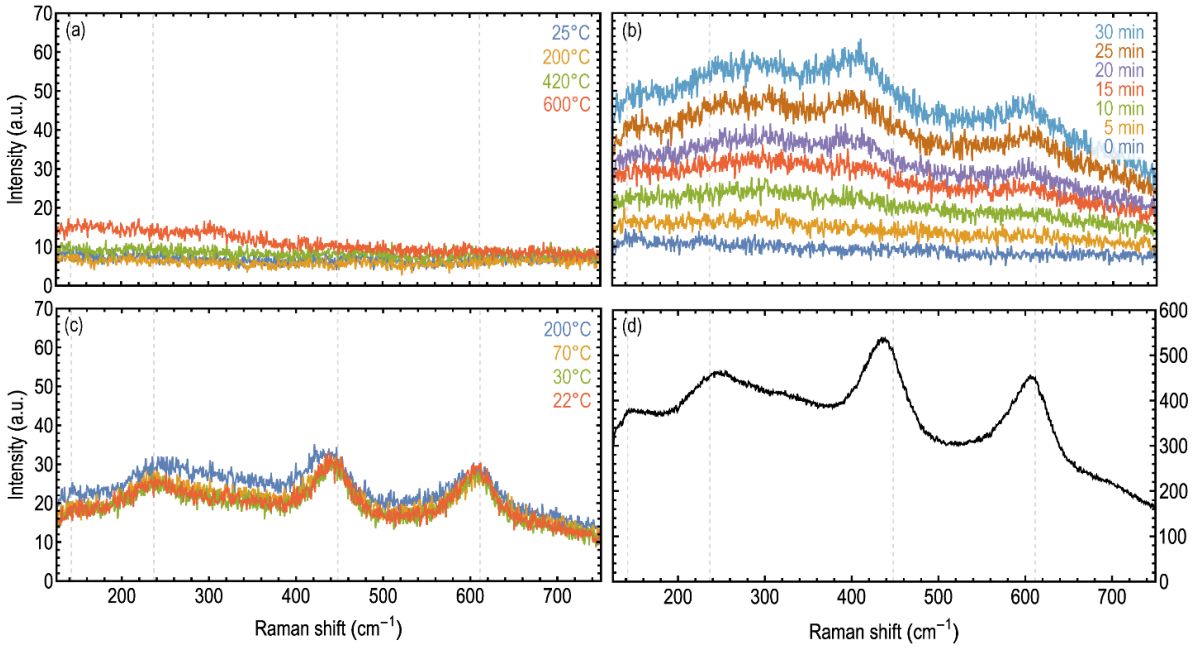

Figure 6.19. In situ Raman spectra for Ti foil oxidized in UHP Ar at 800°C for 30 min. Spectra shown indicate evolution during (a) heating, (b) dwell at temperature, and (c) cooling. The final spectrum outside of the heating stage is shown in (d). Dashed gray lines indicate the expected rutile Raman shifts from the reference pellet.

After removing the specimens from the heating stage, their final Raman spectra show a clear rutile pattern in the 30 and 130 min specimens which grow in intensity over time (Figure 6.20). The 5 min specimen shows small peaks indicative of rutile formation at 133, 232, 440, and 607 cm^{-1} and an additional peak at 342 cm^{-1}. When compared to the initial polished Ti foil, this peak does not appear in the initial metal either. Work on Raman spectra of rocksalt TiN shows broad peaks in the 310-350 cm^{-1} frequencies [145,146]. These are attributed to Ti peaks that arise due to the presence of nitrogen vacancies. This additional peak in the 5 min specimen could arise from sampling the thin oxynitride layers underneath the rutile scale.

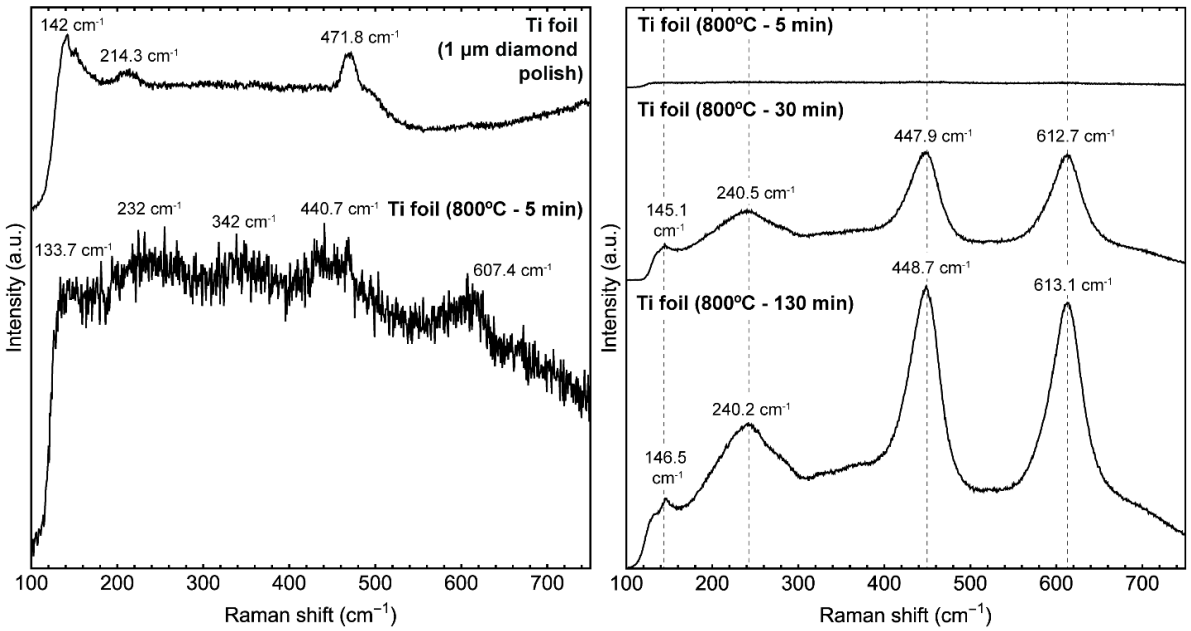

Figure 6.20. (Left) Raman spectra for polished Ti specimen pre-experiment and 5 min Ti specimen. The 5 min spectrum is expanded vertically to show the peaks. (Right) Raman for the 5, 30, and 130 min to scale showing a clear rutile spectrum in the 30 and 130 min. Dashed lines indicate the rutile Raman mode positions from the 130 min specimen.

During the in situ experiment, optical images of the surface were taken to observe coloration changes throughout the heating, dwell, and cooling stages (Figure 6.21). This specimen shows a variety of color changes on the surface throughout the experiment and never forms the stable gray surface characteristic of a thick rutile scale. During heating, some of the metal surface becomes dark blue at 650°C and a light blue in the same regions at 700°C. At temperature, grain boundaries start becoming distinguishable and the surface shows a combination of green, pink, purple, and gray that changes locations over time. Coloration does not change significantly during the cooling process compared to the end of the dwell stage.

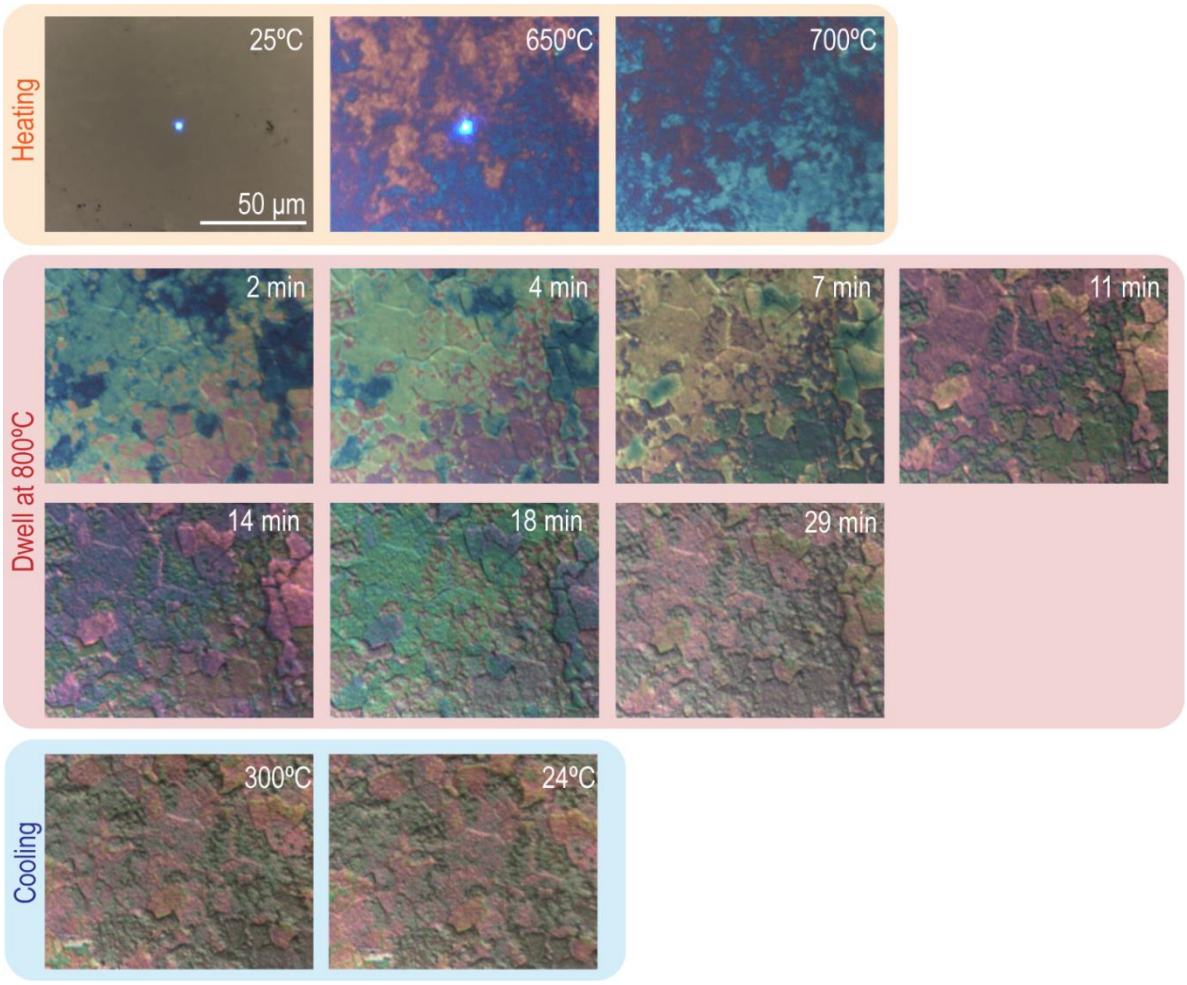

Figure 6.21. Optical micrographs of the surface showing coloration changes during the in situ oxidation experiment of a titanium foil oxidized in UHP Ar at 800°C for 30 min. The blue spot in the middle of the first two images is the 488 nm laser from the Raman spectrometer.

6.1.3.1 Interpretation of Raman mode shifts

Raman spectra are sensitive to stress changes because strains associated with tensile and compressive stresses are manifested through peak shifts to lower (redshift) and higher (blueshift) frequencies or "Raman shifts", respectively [189–193]. Previous Raman studies of rutile have reported changes in its Raman modes such as peak broadening, intensity, and Raman shift frequencies depending on temperature and stresses applied [138]. In rutile, the

molecular vibrations detected by Raman spectroscopy are dependent on oxygen atom movement around the central titanium atom as illustrated in Chapter 2.

The mode positions of the three dwell times at the end of the in situ experiments are shown and compared to those from the reference rutile pellet in Table 6.2. While the 5 min has too low a signal to properly identify the peaks, the 30 and 130 min specimens show the second order, E_g and A_{1g} modes from rutile. This spectra and the mode positions are similar to rutile Raman spectra from previous oxidation and electrochemical studies [135,136,138]. In contrast to electrochemical synthesis and previous studies of titania, only rutile bands are seen from the surface of in situ experiments.

Table 6.2. Rutile Raman spectrum mode frequencies for in situ specimens in UHP Ar compared to reference rutile pellet. Peaks that had too low of an intensity to be detected by the LabSpec 6 software have N/A written as their frequency.

Assigned mode	**5 min (cm^{-1})**	**30 min (cm^{-1})**	**130 min (cm^{-1})**	**Rutile pellet (cm^{-1})**
B_{1g}	N/A	N/A	141.9	141.9
Multi-phonon process	N/A	N/A	236.7	236.7
E_g	N/A	448.6	445.7	447.9
A_{1g}	N/A	609.8	611.3	611.3

All but the E_g modes from rutile remain in the expected Raman shifts (Figure 6.19). During dwell, the E_g mode is at lower frequencies than the reference rutile and shifts towards the higher expected value with decreasing temperature. Previous studies have observed redshift of E_g with increasing temperature [194] which has been attributed to non-stoichiometric changes in rutile [195]. The shifts in E_g could be attributed to thermal changes during the oxidation study, as well as the continued oxygen diffusion from rutile into the

substrate which would lead to non-stoichiometric rutile. This could also suggest oxygen deficiency and the formation of Magnéli phases as suggested from electron diffraction evidence.

6.1.3.2 Whisker formation in Ti oxidation

All three specimens and the slow-cooled one show regions with networks of nanowhiskers whose tips grow over time (Figure 6.22). At the 5 min dwell, the whiskers seem confined to regions where there are small parallel cracks from the initial titanium foil, but in longer dwell times the whiskers can be seen protruding from the facets of certain oxide grains. For phase identification, a few whiskers were extracted by scraping them off the surface with a razor and transferring them onto lacy carbon. From electron diffraction, these whiskers were identified as rutile. It is possible that these rutile whiskers form to relieve stress from the volume expansion of titanium transforming into rutile or from CTE mismatch during cooling. In Ni and Cu systems, oxide whiskers have been observed and are hypothesized to form using dislocations as nucleation points where ledges continue to be oxidized by adsorbed oxygen [196].

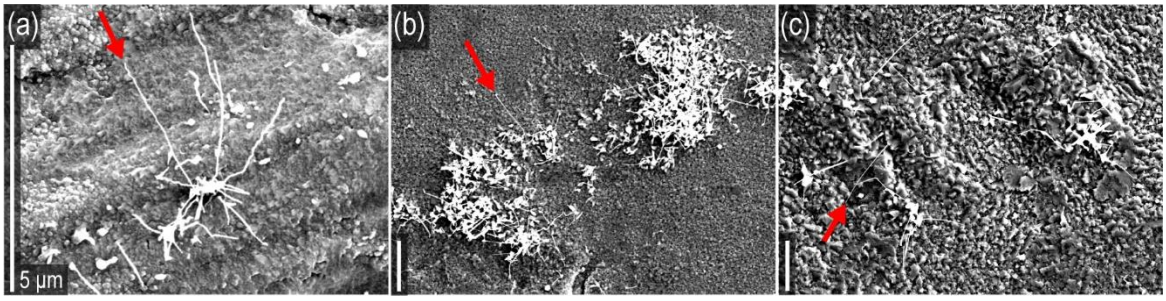

Figure 6.22. Top-view SE SEM images showing the surface oxides and clusters of nanowhiskers of Ti foil oxidized under UHP Ar at 800°C for (a) 5 min, (b) 30 min, and (c) 130 min. The scale bar represents 5 µm in all three scales. Note scale bar differences between (a) and (b-c).

Whiskers are defined as single crystals with aspect ratios of 20 to 1000 [197]. They were first observed and have been most widely studied in tin, but have been reported in other

metals with low melting temperatures [198,199]. It has been reported that whiskers in the Ti-O system form in low partial pressures of oxygen [200] or with the presence of water vapor [196,201]. Rose [202], for instance, reported whisker formation in titanium oxidation at 500° in low partial pressures of oxygen but provided no mechanism of formation or explanation for their presence.

In situ specimens exposed to UHP Ar in this chapter show evidence of oxide whisker formation. These whiskers were identified as rutile from electron diffraction. Using the SEM images as reference (Figure 6.22), the diameters of these whiskers vary from around 50 to 150 nm with lengths of 2.5 to 7.5 μm. In the shortest dwell time (5 min), the nanowhiskers have an aspect ratio of 50 which increases to 87.5 at the longest dwell time (130 min).

Although formation mechanisms and their driving forces remain a matter of debate, whiskers typically form as a means of stress relaxation in the presence of compressive stress regardless of this stress's origin [199]. In the case of titanium oxidation, surface oxidation is believed to play a role in whisker growth from pure Ti either from stress arising from CTE mismatch or due to oxidation reaction at the surface with preferential growth along particular rutile faces [203]. In contrast to tin, rutile nanowires were only formed in environments with low oxygen contents which is what was observed in these studies as well as in previous studies on titania nanowires [203,204]. The upcoming chapter for pure Ti in Ar-1%O_2 will show few (if any) nanowhiskers.

In some regions, nanowhiskers can be seen extending from a corner of a faceted rutile grain. Since grain boundary triple points are high energy sites, whiskers can nucleate in these regions and could explain why whiskers in these oxidation studies seem to be extending from

particular rutile grains. Additionally, oxide grain boundaries may act as continual sources of dislocation where nucleation events would be favored [196].

6.1.4 Void formation and growth

The extent and morphology of the voids formed in these microstructures can be appreciated in the bright-field image of the 30 min specimen's cross-section in Figure 6.23. As in the 9 h specimen from Chapter 5, the voids are largest in the outer oxide scale and nanoporosity is seen throughout the inner layer in what appears to be a lamellar arrangement. These nanovoids are 2-3 nm and can be seen coalescing to lengths of 15-20 nm connecting at least two of these voids. Since the phase identification of the inner and outer layer is the same as in Chapter 5, the reader is referred to the void section in that chapter for information on the relevant volume expansions and diffusivities.

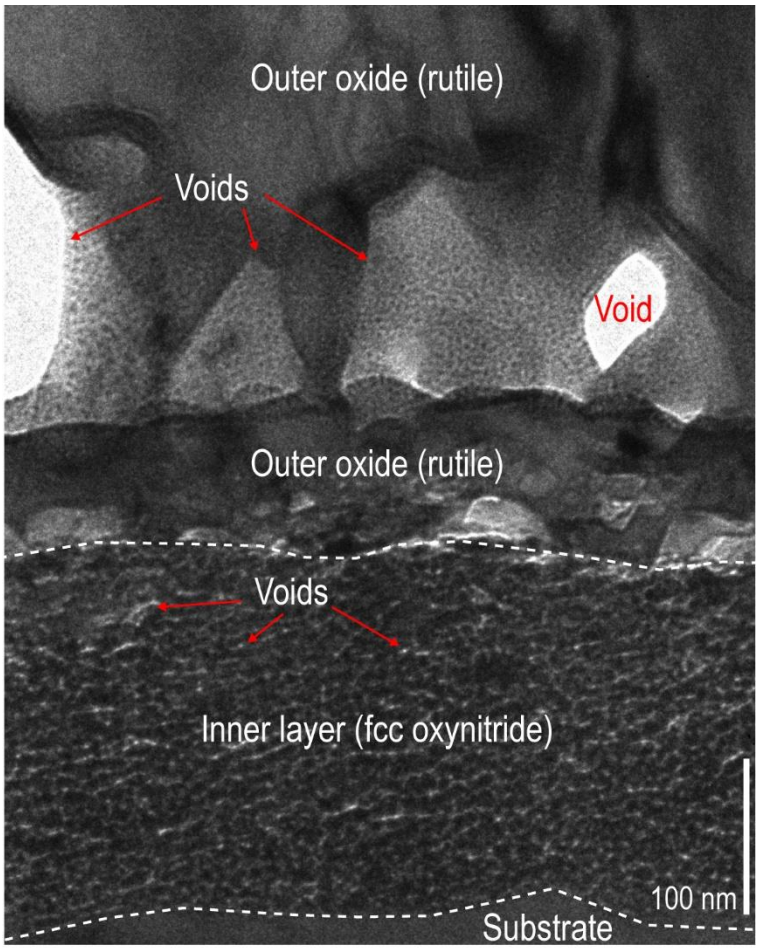

Figure 6.23. CTEM BF micrograph of the cross-section from the 30 min UHP Ar specimen highlighting voids with red arrows and font in the outer oxide (rutile) layer and the inner layer composed of fcc oxynitride. The specimen layers are delineated with white dashed lines to easily identify them. Voids are largest in the outer oxide layer and are small (< 10 nm) but ubiquitous throughout the inner oxynitride layer.

As before, the relative sizes of the voids in the oxynitride and rutile layers scale in the same trend as their volume expansions (~5% to oxynitride and ~77% to rutile). However, from a volume expansion perspective, TiN (used as an approximate for the oxynitride phase) would expand 64% when converting to rutile. The voids in the oxynitride layer grow from 2-3 nm to 80-160 nm in the rutile layer. This represents a 96-99% increase in void size which is larger than the volume expansion alone. While the mechanism cannot be explained by a

single factor, it is likely that volume expansion, asymmetrical fluxes, and grain boundary diffusion play a role in the formation and growth of these voids.

One important lesson regarding void formation from this set of experiments is the fact that voids can be found in the same locations and morphologies even in the short 5 min dwell specimen. This suggests that the void formation is inherent to the reaction between titanium and the interstitials in the gas and is not an artefact from cooling or other experimental factors. Attempted Ti-rutile diffusion couple studies also showed porosity in the Ti and rutile substrates which provides further evidence that void formation is inherent to this materials system.

6.1.5 Microstructural evolution

One possible mechanism for the microstructural evolution of these in situ specimens is illustrated in Figure 6.24. The hcp titanium contains minimal impurities before exposure. At temperature, the nitrogen and oxygen from the environment dissolve simultaneously into the metal substrate forming a solid solution α-Ti (N,O) or α-Ti (O) since evidence suggests minimal nitrogen content in the substrate. Given the partial pressures of N and O, an oxynitride layer begins forming and starts to grow. (Alternatively, a nitride could form first upon nitrogen saturation in the metal but immediately convert into an oxynitride.) With continued exposure to the UHP Ar, the outer portion of the oxynitride layer oxidizes and transforms into a rutile oxide. This rutile oxide continues growing from outward Ti diffusion from underneath it and continued O ingress from the gas. Meanwhile, oxygen continues to diffuse inward from the rutile into the oxynitride and from the oxynitride into the metal substrate.

Nitrogen from the oxynitride likely also continues to diffuse inward but might do so further into the scale given that the nitrogen compositions near the interface remain low in all of the specimens from this chapter. Although N content may be low or negligible in the metal, it is crucial for the formation of the initial nitride or oxynitride layers.

It is important to remember that the metal substrate essentially acts as infinite reservoir or sink due to hcp Ti's high nitrogen and oxygen solubilities. This allows for continued inward diffusion despite scale formation. For long dwell times ($t > 130$ min), the continued inward O diffusion from the rutile (and potentially gas diffusing through the rutile scale) forms an oxynitride layer underneath the original oxynitride layer that shows a composition with more oxygen and nitrogen.

The steps of this microstructural evolution can be summarized as those shown in the schematic of Figure 6.24:

(a) Initial hcp Ti

(b) Dissolution of N and O into hcp Ti (or formation of a solid solution) + onset of TiN_xO_y formation

(c) Growth of TiN_xO_y scale(s)

(d) Growth of rutile scale

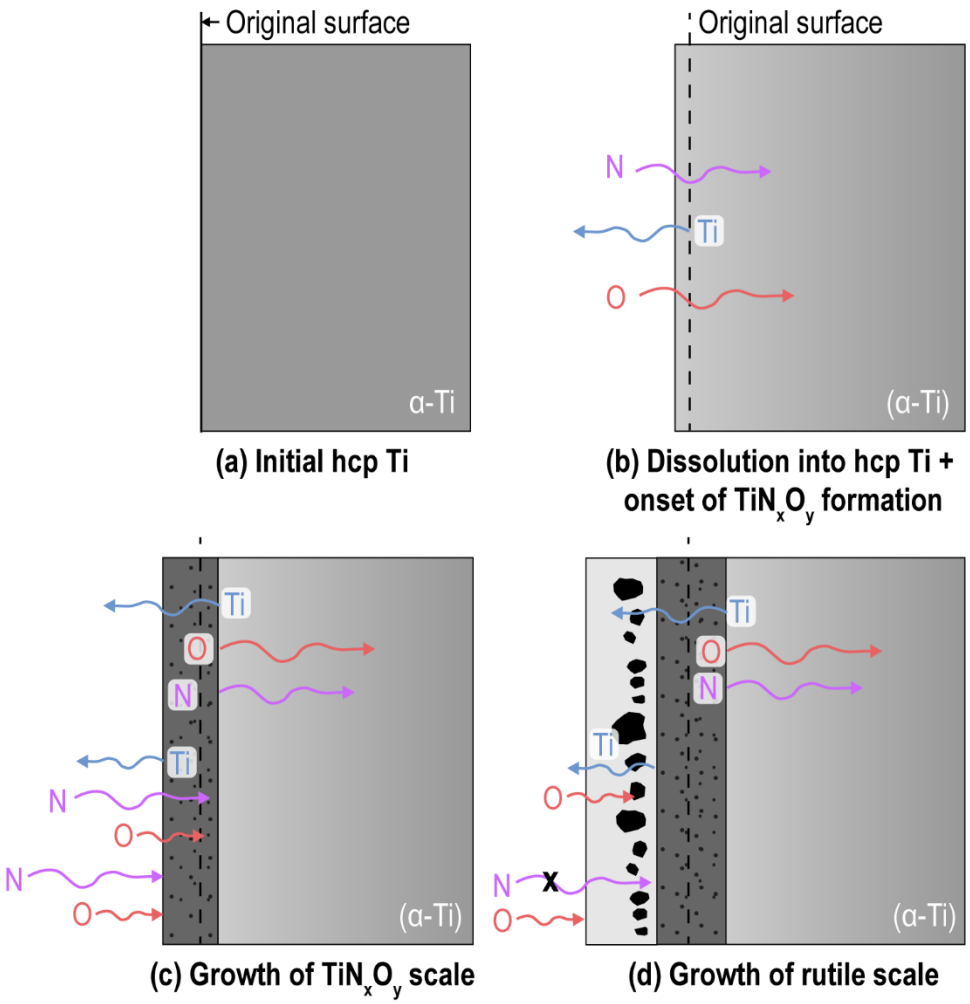

Figure 6.24. Steps in the evolution of the oxynitride and rutile scales in titanium under UHP Ar showing associated fluxes for Ti (blue), oxygen (red), and nitrogen (purple). The flux arrows are scaled relative to each other based on the fluxes reported in literature (Table 5.2). For fluxes to contribute to void formation, the outward Ti flux would have to be larger than the inward interstitial fluxes which is not what is shown from these values but could still be the case in this system.

The partial pressure of nitrogen (pN_2) required to form TiN from Ti metal is > 10^{-24} atm while the partial pressure of oxygen (pO_2) needed to form rutile is > 10^{-36} atm (Table 6.3). Both of these values are well below the partial pressures used in the experiments in this chapter.

Table 6.3. Partial pressures and equilibrium standard Gibbs free energies required for formation of Ti oxides and nitrides at 800°C from Ellingham diagram [205].

Reaction	**ΔG (kJ/mol)**	**log pO_2**
$Ti + O_2 \rightarrow TiO_2$	-750	-36
$6Ti + 5O_2 \rightarrow 2Ti_3O_5$	-793	-38
$4Ti + 3O_2 \rightarrow 2Ti_2O_3$	-817	-39
$2Ti + O_2 \rightarrow 2TiO$	-870	-42
$2Ti + N_2 \rightarrow 2TiN$	-261 [206]	-24

Despite the increase in partial pressures for both nitrogen and oxygen from the gettered Ar in the previous chapter, the predominance diagram predicts the formation of the same layered structure when p (N_2) > p (O_2) as shown in Figure 6.25. As before, the Ti_2N nitride phase is missing from the specimens and Magnéli phases are not present in layers underneath the rutile scale (although there are likely Magnéli phases within the outer rutile layer).

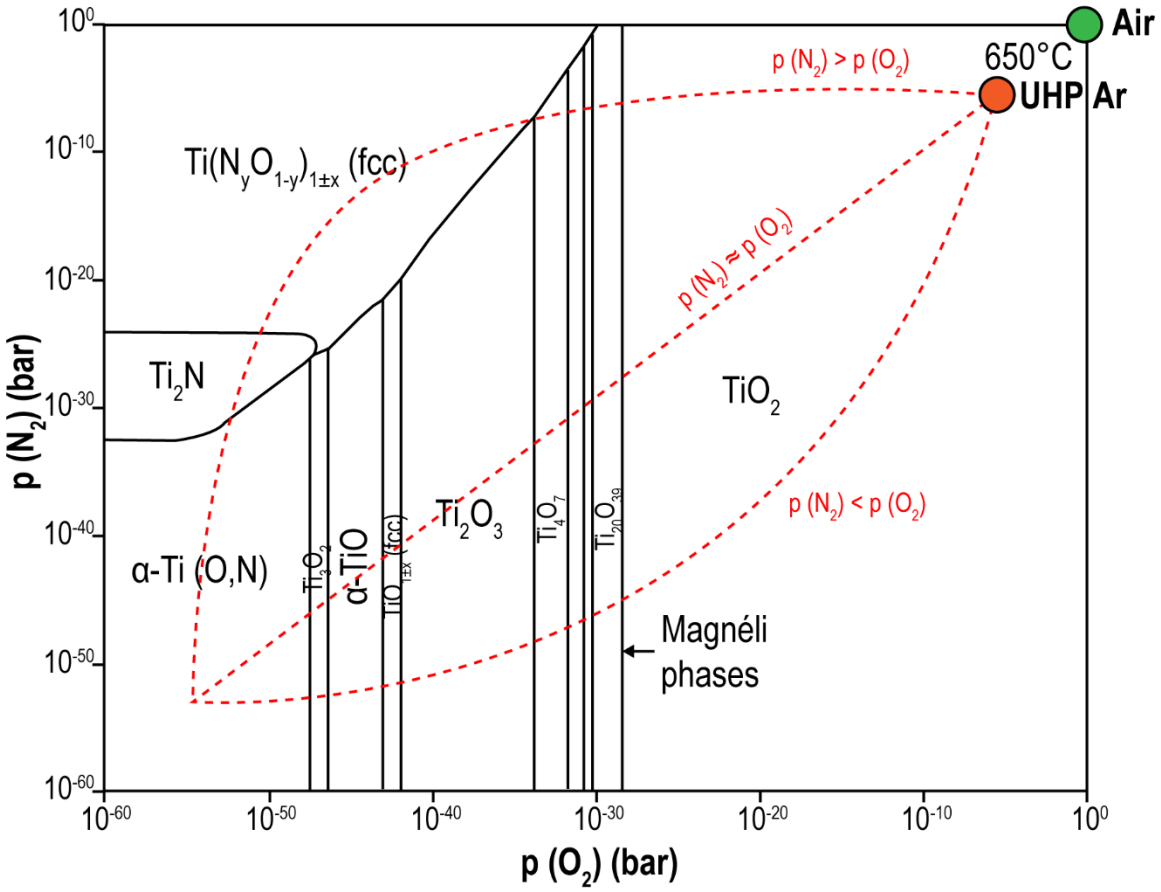

Figure 6.25. Predominance diagram showing which phases would be favored to form under various partial pressures of nitrogen and oxygen. Circles show the positions for relevant partial pressures for air (green circle) and UHP Ar used in this chapter (orange circle). Adapted from Dupressoire et al.'s [77] diagram calculated using ThermoCalc and the TCTI1 database.

6.1.6 Comparison to gettered Ar specimens

While it would make sense to attribute microstructural changes to changes in the partial pressures of the environments, similar microstructures were generated in the gettered Ar when slow-cooling (i.e. 9 h specimen from Chapter 5) compared to the microstructures of the in situ specimens (e.g. 30 min specimen from this chapter). Oxidizing Ti alloys that had previously been nitrided suggests that oxynitride formation is favored in partial pressures of oxygen below 1 Pa at which point rutile forms with no evidence of oxynitride formation [79].

The results in this chapter show the formation of both oxynitride and rutile in the UHP Ar with 1 ppm O_2 and 5 ppm N_2.

Chapter 4 showed only nitride formation under gettered Ar, but slow-cooling by furnace shut-off in the same gettered Ar (Chapter 5) enabled the formation of oxynitride and rutile scales. From thermodynamic considerations, the gettered Ar and UHP Ar can both form the oxynitride and rutile layered scales as long as the partial pressure of nitrogen is higher than the partial pressure of oxygen in the environment. It is possible that the changes from slow-cooling are therefore attributed to local changes in the partial pressures of the layers developed during the dwell times that can occur during the cooling stage.

6.2 Conclusion

Experimental studies of pure titanium exposed to a UHP Ar ($N_2 > O_2$ ratio) environment for various dwell times enabled the observation of Ti reactions with nitrogen and oxygen at 800°C. These specimens formed layered structures with oxynitride and rutile scales with porosity throughout the various layers. Answering the research questions guiding these studies, the following summarizes the findings from this set of Ti specimens exposed to UHP Ar:

- These specimens exposed to UHP Ar and cooled in the heating stage formed layered structures with large voids in the outermost scale and nanoporosity in the inner layer. The phases identified in these specimens are:
    - Substrate (5-130 min): **α-Ti with N/O ordering (but mostly O)** likely in every other interstitial layer

- Substrate (slow-cooled 1 h dwell): **Ordered α-Ti** showing a range of superlattice Type I, II, and III reflections throughout the substrate indicative of oxygen ordering
- IFL (5 min): **N-rich Ti oxynitride or a Ti nitride (Ti_2N or TiN)** (Scale was too thin for extensive analysis)
- IO (130 min): **rocksalt Ti oxynitride** (likely low N content)
- IL: **rocksalt Ti oxynitride** (likely low O content)
- OO: **rutile** (TiO_2)

- The comparable interstitial contents in the gas environment suggest competitive fluxes between N and O which allow for the initial formation of a thin nitride layer. This gets quickly oxidized and converted to an oxynitride layer. From continued outward Ti and inward O diffusion, a rutile scale forms on the outermost layer. The oxynitride (N > O) scale grows over time but becomes interspersed with another oxynitride (with O > N) underneath it at the longest dwell time suggesting that oxynitride is not an effective oxygen diffusion barrier as titanium nitride has been postulated to be.
- There is a strong orientation relationship between the hcp titanium substrate, the fcc rocksalt oxynitride phase(s) of the inner layer, and the tetragonal rutile phase of the outer oxide. The evidence provided for this came from electron diffraction patterns along the $[1\bar{2}10]_{hcp}$, $[0\bar{1}1]_{fcc}$, and $[0\bar{1}1]_{tet}$ zone axes. The {111} planes of the fcc phase stack on top of the {0001} planes of the hcp substrate, while the {100} planes of rutile stack on top of the fcc ones.

- Utilizing Raman spectroscopy during the heating, dwell, and cooling stages confirmed the formation of rutile during early stages of the dwell and its growth over time given its increase in peak intensity. This disproved the initial hypothesis that rutile might be forming during cooling from observations of preliminary ex situ furnace studies. The specimen that showed no scale formation from these initial furnace studies likely formed rutile that dissolved back into the metal substrate at some point in the experiment.
- Porosity is observed as nanopores (<10 nm) in the oxynitride scale and as large voids within the outer rutile scale during in situ studies. These voids may evolve partially due to volume expansions when transforming from metal into rocksalt (TiN or TiN_xO_y) or rutile phases, from asymmetrical fluxes, or from metal-scale separation, but their mechanism of formation remains unknown.

7 hcp Titanium in 1%O_2-Ar at 800°C in Tube Furnace and in Heating Stage under Raman Spectroscopy

This chapter will cover titanium oxidation in a 1%O_2-Ar gas mixture using both ex situ and in situ methodologies. With a 1% oxygen content in the flowing gas, the 5 ppm nitrogen content in the argon of the mixture is much smaller than the oxygen present in the gas (O_2:N_2 = 2000). By increasing the O_2:N_2 ratio, this gas environment decreases the likelihood of forming any nitride or oxynitride phases as the specimens that were discussed in Chapters 4-6. Like titanium oxidation in air, all scales formed in 1%O_2-Ar discussed in this chapter will be composed of rutile, forming various layers, and with blistering occurring in some cases. This chapter will discuss the phase stability and microstructural evolution for pure titanium oxidized using the ex situ and in situ configurations in an 1%O_2-Ar environment.

7.1 Results

Since the same gas will be used in two different experimental setups, this chapter will show the results from ex situ tube furnace studies and then from in situ heating stage studies. The information from these two sets of experiments will be consolidated in the Discussion section.

For both setups, the resulting microstructures form three or more layers of rutile with dense outer layers and some porosity in the innermost layer or at the rutile-rutile interfaces. There is no evidence of other oxides, oxynitrides, or nitrides throughout any of the specimens. As before, the metal substrate will show evidence of solid solution α-Ti(O) formation and electron diffraction will show an α”-like ordering in the substrate. A schematic

summarizing the microstructures and phase identification for each specimen is shown in Figure 7.1.

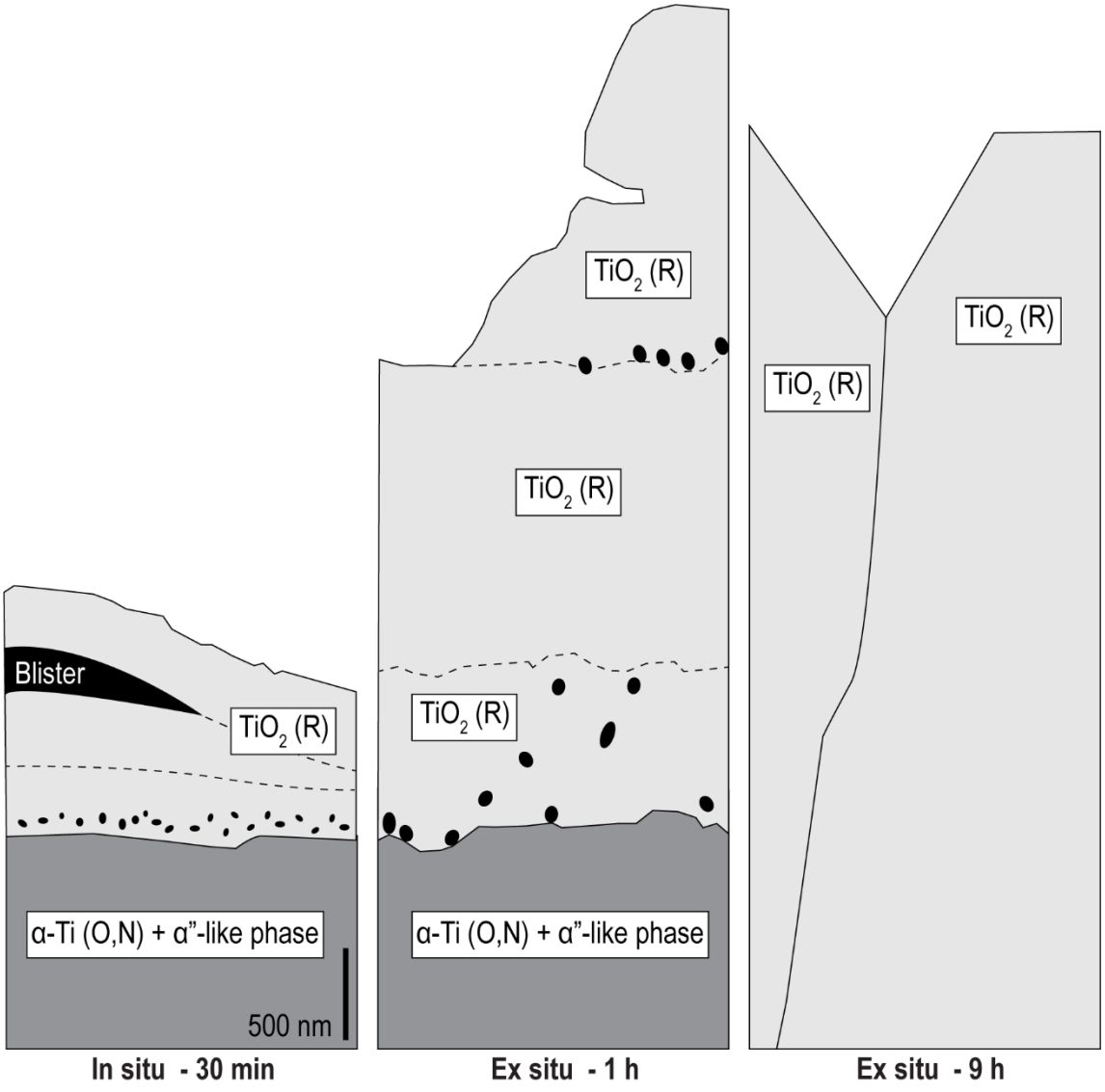

Figure 7.1. Microstructures and proposed phase identification for the in situ and ex situ Ti specimens exposed to 1%O_2-Ar mixtures at 800°C.

7.1.1 Ex situ oxidation studies

Tube furnace oxidation studies were performed using an 1%O_2-Ar gas environment and dwell times of 1 and 9 h at 800°C. These specimens were fast-cooled to preserve a microstructure closest to the at-temperature reaction. Although changes during the oxidation

process cannot be observed during ex situ studies (such as coloration changes and oxide evolution from in situ studies), the resulting microstructures and oxidized surfaces help provide information towards understanding the oxidation behavior of pure titanium in this 1%O_2-Ar environment.

SEM images from the oxidized surfaces (Figure 7.2) show slightly different morphologies between the 1 and 9 h specimens. The 1 h specimen shows large 3-8 μm oxide grains that seem to be growing in many different preferential orientations. Many of these grains look triangular-shaped. In some of the surface area there are tubular regions 80-300 μm in length which show a different morphology to the rest of the surface oxide. These regions have whisker-like oxides (~400 nm thick) with large (2-6 μm) faceted oxide crystals. A trench into the specimen shows porosity between and within oxide layers. The 9 h specimen shows significant spallation (most evidenced in the specimen's corner) that suggests the formation of at least 4 oxide scales. The center of the specimen shows large 1-10 μm oxide crystals with many well-defined facets within each grain. While the cross-section from TEM will only feature rutile grains, the trench from the FIB process shows that voids also form within the oxide scale of the 9 h specimen in layers beneath the outer oxide scale, although it is unclear at this length scale whether the voids are delineating oxide layers or forming within a specific rutile layer.

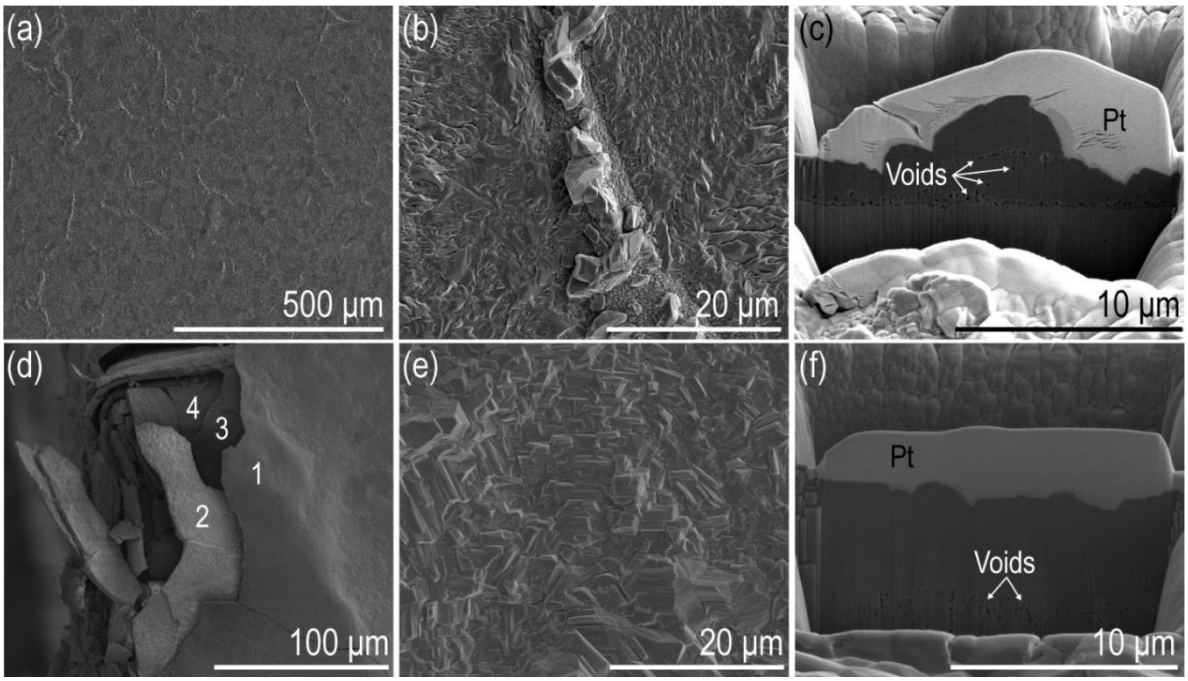

Figure 7.2. SEM SE micrographs for ex situ Ti oxidized in 1%O_2-Ar at 800°C for (a-c) 1 h and (d-f) 9 h. (d) shows the spallation of various scales with the numbering designating the potential number of oxide layers.

The cross-section from the 1 h (Figure 7.3a-d) specimen shows the formation of at least two distinct scales above the metal substrate. There is an inner porous oxide layer, a dense middle oxide layer, and a large grain on top that suggests the possible formation of a third oxide layer. From the elemental maps, oxygen concentration is even throughout the scales and there is a concentration of oxygen at the top of the metal substrate, suggesting inward oxygen diffusion into the metal.

In the 9 h specimen (Figure 7.3e-f), the oxide scale is too thick for the metal-oxide interface to be accessed via FIB cross-sectioning and thus only rutile is shown. The rutile in this specimen shows large columnar grains with defects distributed throughout the oxide grains. The elemental map of this oxide shows no significant concentration variations of oxygen nor nitrogen. This suggests that the grains shown are all the same phase (which was

confirmed by XRD and RS). Titanium intensity changes from the elemental map are likely attributed to crystallographic orientation.

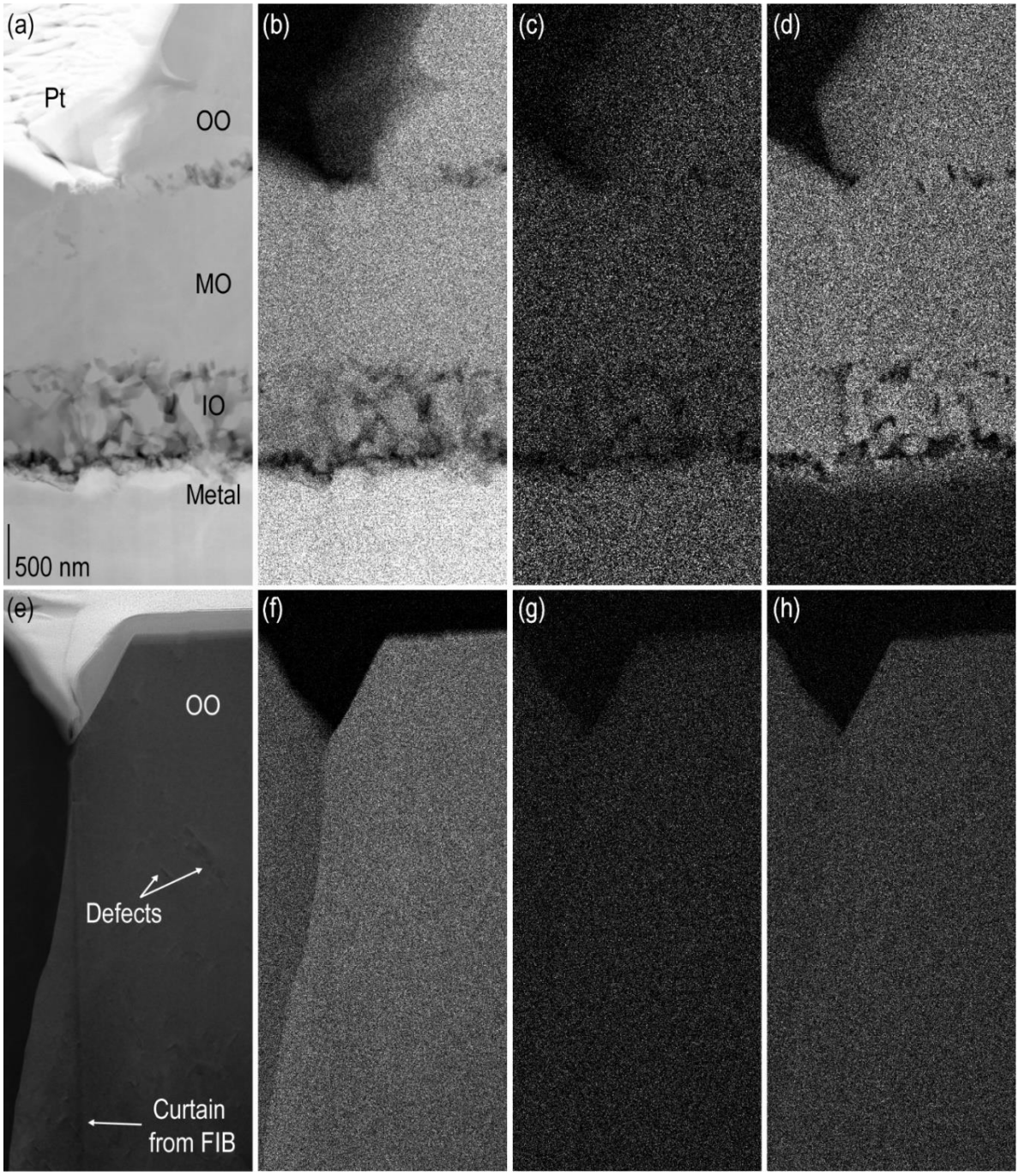

Figure 7.3. (a) STEM HAADF cross-section of the oxidized titanium specimens from ex situ studies in 1%O_2-Ar at 800°C for 1 h and (e) 9 h and the corresponding elemental maps for (b, f) Ti, (c, g) N, and (d, h) O. OO, MO, and IO stand for “outer oxide”, “middle oxide” and “inner oxide” respectively.

When using area quantification from the elemental maps of the 1 h specimen, the oxygen content remains fairly even throughout the oxide scales (Figure 7.4). The substrate shows a composition of 26 at% O and 15 at% N, suggesting that there is still significant nitrogen content despite the larger oxygen content throughout the specimen and the lack of nitride phases.

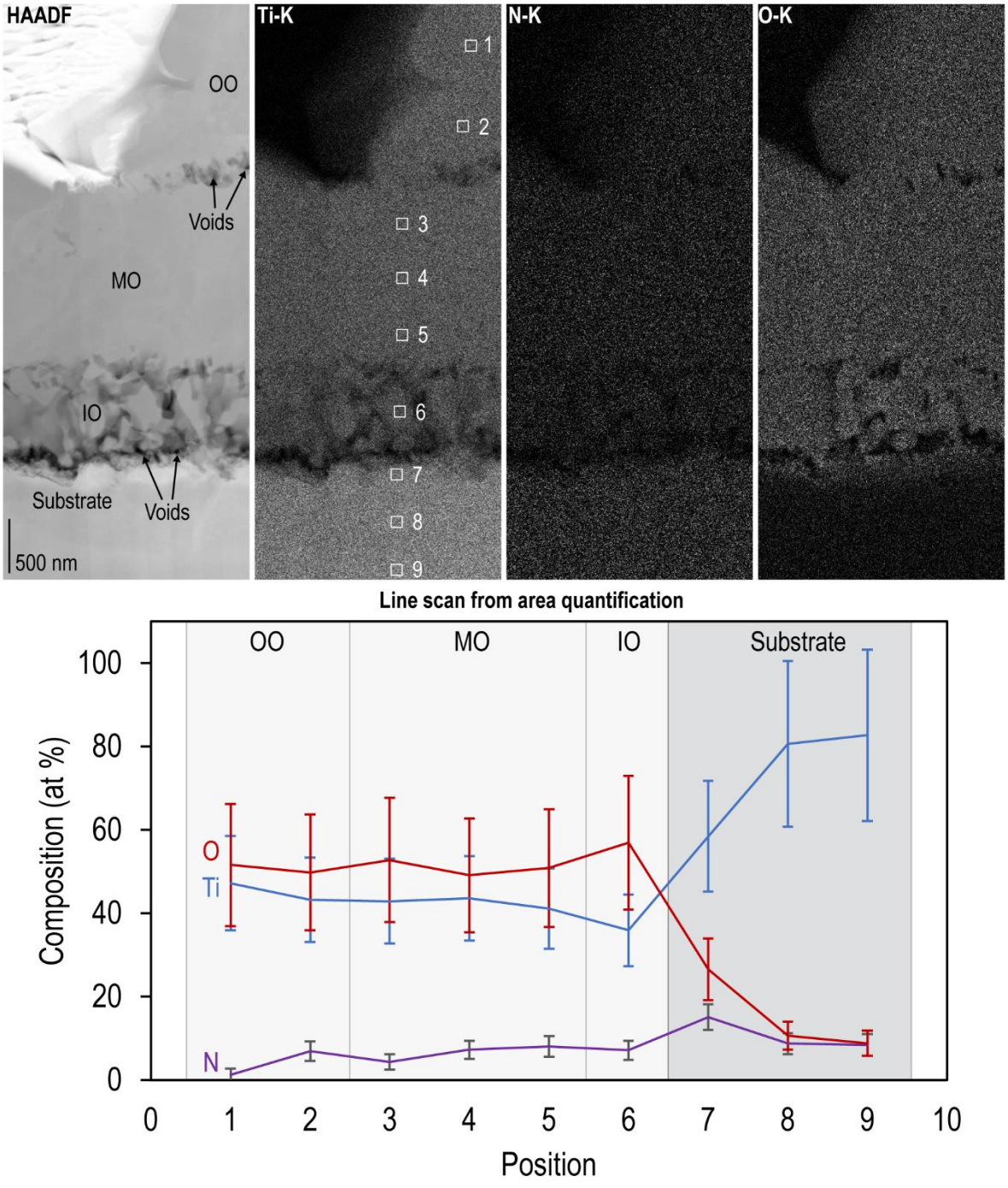

Figure 7.4. Cross-sectional micrograph for ex situ 1 h specimen from STEM HAADF and corresponding STEM EDX elemental maps. Areas used for quantification are shown in the Ti-K elemental map and its values were used to construct the line scan below. Oxygen content is highest in the oxide scales and higher than the nitrogen content in the substrate. Nitrogen content is highest near the metal-scale interface and decreases when moving further into the substrate.

XRD from the surface (Figure 7.5) of the ex situ oxidation studies shows intense (110) rutile peaks in both specimens oxidized for 1 and 9 h. Peaks from hcp Ti can be seen in the 1 h specimen but not the 9 h where oxide layers are much thicker and the metal is not reached from the surface measurement. The (0002) basal plane, $(10\bar{1}0)$ prismatic plane, and $(10\bar{1}1)$ pyramidal plane peaks from hcp Ti in the 1 h specimen show shifts to the left that suggest lattice expansion due to the incorporation of interstitials. The shift in the basal plane corresponds to a 4.78 Å c axis which corresponds to a 2.2% expansion compared to the hcp Ti. This matches the expected c axis of a solid solution $TiO_{0.325}$ (ICSD #24080), which is a solid solution α-Ti structure.

In the 9 h ex situ specimen, the rutile a lattice parameter is 4.60 Å (0.3% contraction with respect to the original lattice) and the titanium c lattice parameter is 4.77 Å, a 1.8% expansion. This c-axis of the oxidized titanium is closest to that of $TiO_{0.325}$. None of the rutile peaks in either specimen shows significant shifts that would suggest lattice parameter changes in the oxide. Any rutile expansion or contraction can be attributed to stress changes from the oxidation process.

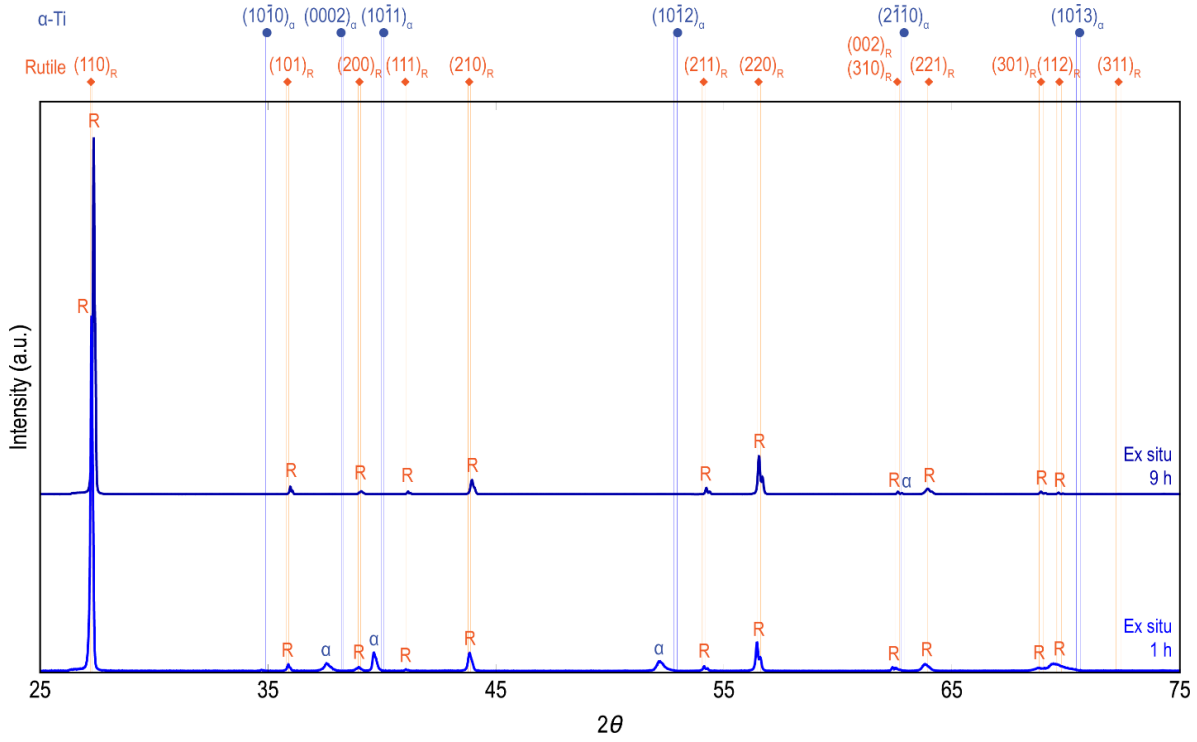

Figure 7.5. XRD patterns comparing ex situ spectra. α denotes α-Ti peaks and R denotes rutile peaks. Both experimental patterns are dominated by rutile peaks. The $(0002)_\alpha$ and $(10\bar{1}1)_\alpha$ peaks in the 1 h specimen are shifted to the left of the expected α-Ti peaks due to the incorporation of interstitials in the metal substrate. No significant α-Ti peaks are seen in the 9 h specimen.

The three oxide layers in the 1 h specimen are identified as rutile from all characterization techniques. When looking at these regions with electron diffraction, the patterns are indexed as rutile and do not show additional reflections that would suggest Magnéli phase formation. As an example, the SAED patterns and their matching simulated patterns from rutile are shown in Figure 7.6.

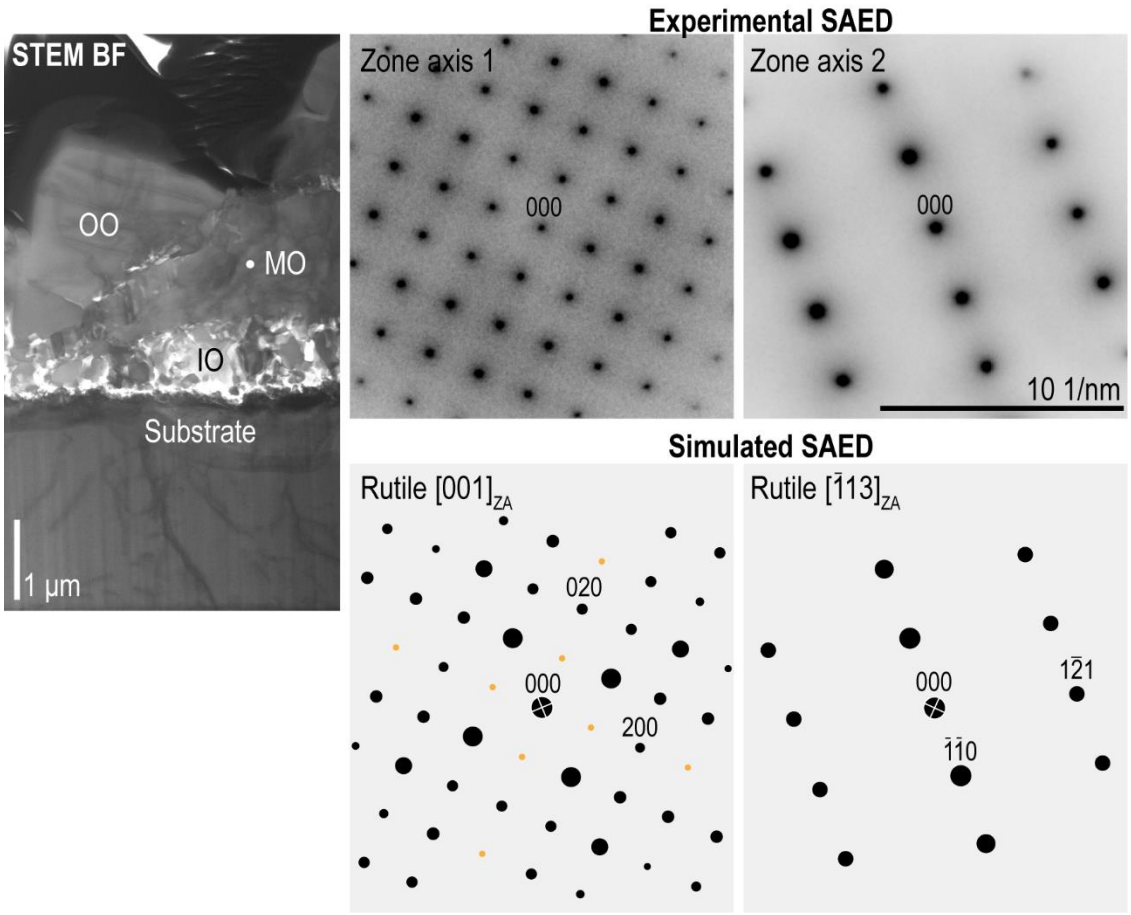

Figure 7.6. STEM BF micrograph of the cross-section for ex situ 1 h Ti specimen showing a layered structure and the region where the aperture was for electron diffraction acquisition (white circle within MO region). SAED from the MO region and their matching simulated SAED from rutile (TiO_2) are shown. There are no additional reflections that would suggest Magnéli phase formation.

Similar to the SAED patterns from previous chapters, SAED obtained from the metal substrate in this specimen (Figure 7.7) suggests the formation of α" (staged Ti_2O) since (0001) reflections are intense and not forbidden as in hcp Ti and the rest of the hcp-based suboxides or solid solution $TiO_{0.325}$ phase.

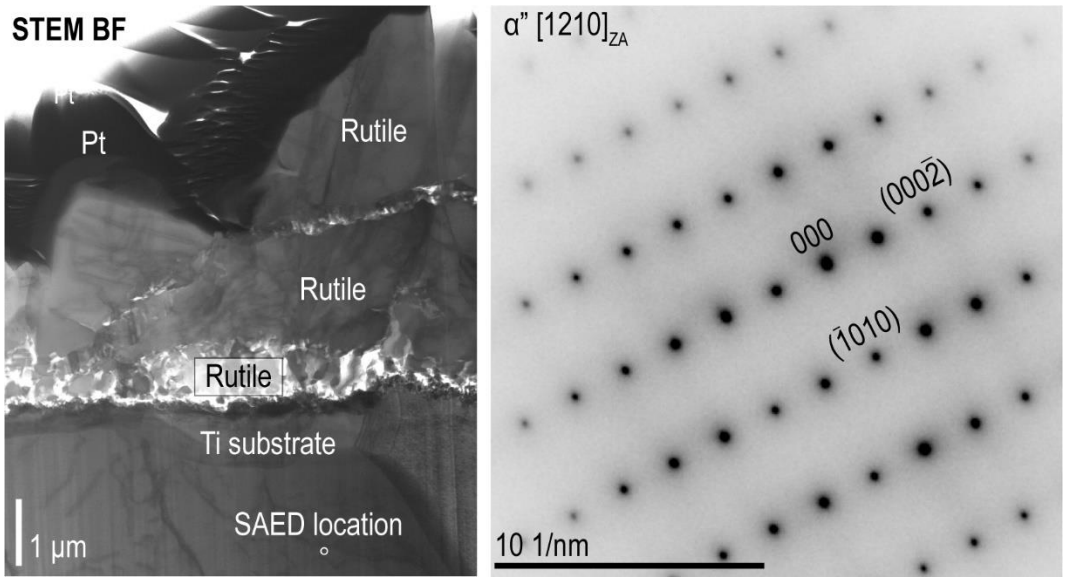

Figure 7.7. STEM BF micrograph of oxidized Ti (ex situ – 1 h) showing a SAED pattern obtained from the metal substrate that suggests the formation of α" (staged Ti_2O).

In contrast to previous chapters, the ex situ specimens only form rutile scales. Moving on to in situ studies, the microstructures will also consist of various rutile scale with small amounts of porosity throughout.

7.1.2 In situ Raman oxidation studies

Using the methodology for in situ oxidation studies described in Chapter 3, a 50 µm-thick titanium foil was heated at 80°C/min, oxidized for 30 min at 800°C and cooled by furnace shut-off (approximate cooling rate of the heating stage's temperature is 125°C/min). Once cooled, the specimens were characterized as detailed in Chapter 3.

The surface of this in situ specimen shows light gray and dark gray regions in the SEM SE image but uniform elemental contrast from the corresponding BSE image (Figure 7.8). This suggests that the contrast stems from surface topography rather than from different phases forming on the surface. The light gray regions show the initial formation of small dagger-shaped and elongated blade-shaped whiskers (similar to those in Chapter 6). The

bases of these are 60-180 nm with 260-400 nm lengths. Most of the whiskers are dagger or triangle-shaped as seen in the inset of Figure 7.8a. Short parallel cracks can be seen in the BSE image and are ~400 nm in length. Underneath these features, the oxide grains are small (100-200 nm) and equiaxed.

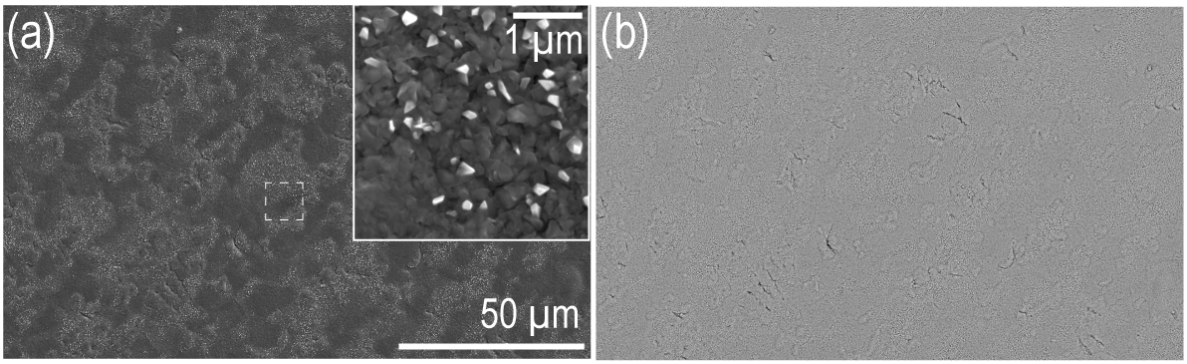

Figure 7.8. SEM micrographs of the oxidized surface for Ti oxidized in situ in 1%O_2-Ar at 800°C for 30 min. (a) SE image showing light and dark regions with the inset image showing the magnified light region with short oxide whiskers. (b) BSE for the same region as (a) showing an even elemental contrast and some cracks.

The elemental maps (Figure 7.9) reveal the oxygen concentration is uniform throughout the oxide scales (as expected since rutile is the predominant phase) and shows minimal signal in the metal substrate. Nitrogen appears in a slight concentration in the metal substrate near the metal-oxide interface, but that could be ascribed to nitrogen in solid solution in the titanium rather than the presence of a nitride or oxynitride phase. There are no noticeable concentrations of any of the elements near the tip of the delamination crack at the edge of the blister.

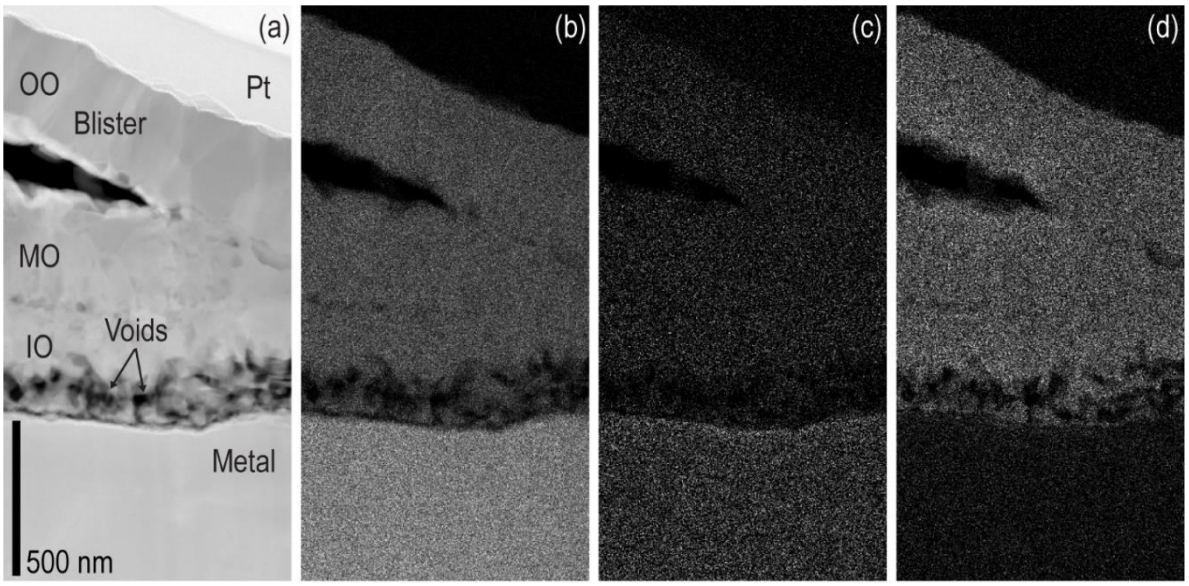

Figure 7.9. (a) STEM HAADF cross-sectional micrograph and corresponding STEM EDX elemental maps for Ti foil oxidized in situ at 800°C for 30 min in 1%O_2-Ar showing (b) Ti, (c) N, and (d) O signal. OO stands for outer oxide, MO is middle oxide, and IO is inner oxide.

Line scans from these elemental maps (Figure 7.10) show similar trends to those from the ex situ 1 h specimen. The highest oxygen content is seen in all oxide scales and remains fairly even around the 66 at% O value. As before, the oxygen content is higher than the nitrogen content within the substrate with a composition nearest the metal-scale interface of 22 at% O and 8 at% N.

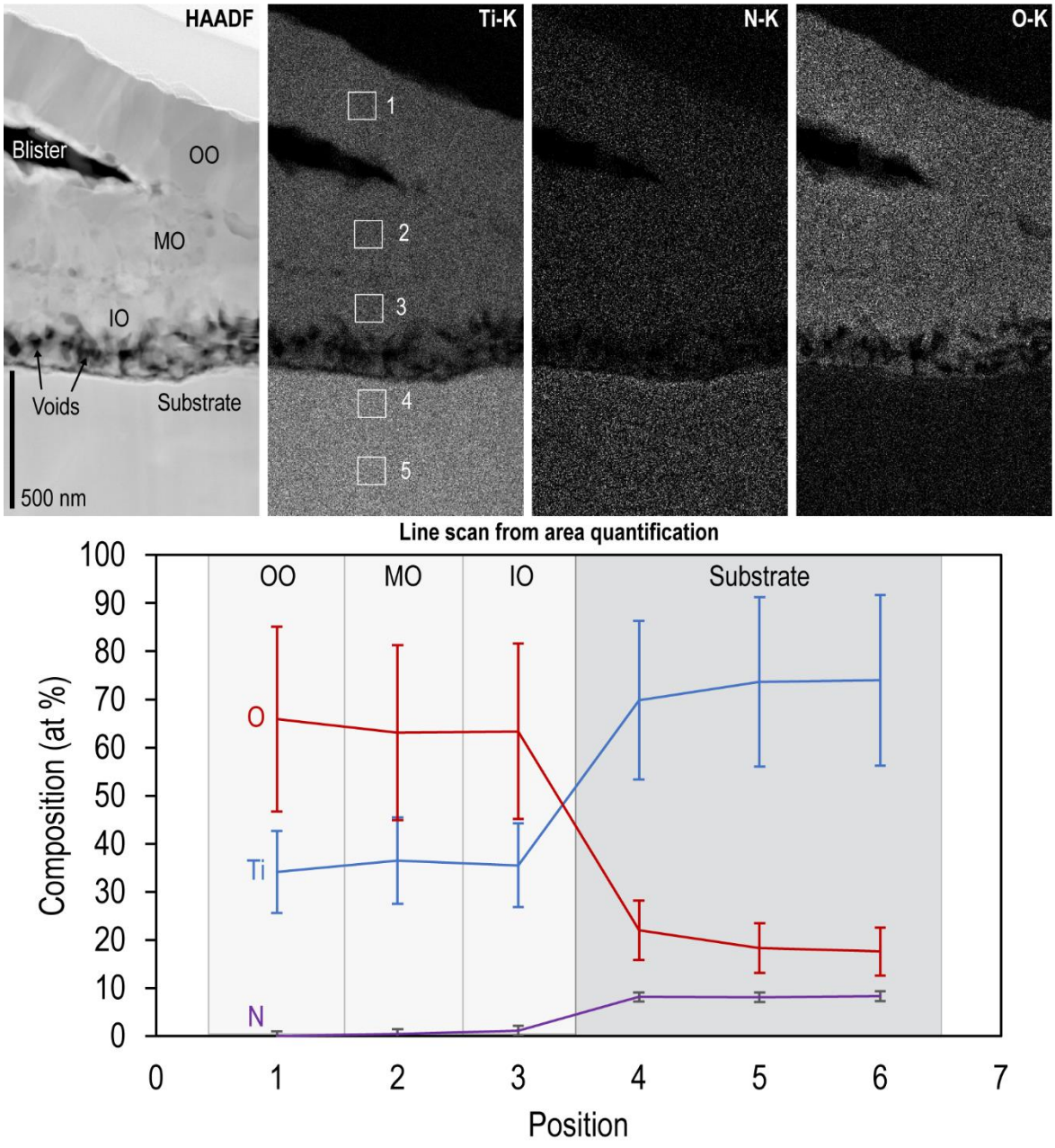

Figure 7.10. Cross-sectional micrograph for in situ 30 min specimen from STEM HAADF and corresponding STEM EDX elemental maps. Areas used for quantification are shown in the Ti-K elemental map and its values were used to construct the line scan below. Oxygen content is highest in the oxide scales and higher than the nitrogen content in the substrate. Nitrogen content is highest within the substrate but remains below 10 at% N.

X-ray diffraction patterns from the oxidized surface show peaks that can all be attributed to either hcp titanium or rutile (Figure 7.11). All peaks are normalized to the highest peak within each spectrum. In the oxidized specimen, most rutile peaks are observed

(except for a small (311) peak). The (110) rutile peak is the most intense oxide peak in the experimental pattern, almost as intense as the two highest titanium peaks. All hcp Ti peaks are still detected in the experimental pattern, although some of the Ti peaks are shifted to 2θ values lower than those of the reference titanium foil. The largest peak shifts are observed in the (0002) basal plane, $(10\bar{1}0)$ prismatic plane, and $(10\bar{1}1)$ pyramidal plane. The shift in the basal plane indicates a c lattice parameter of 4.78 Å which corresponds to a 2.2% expansion compared to the hcp Ti, which matches the expected c axis of a solid solution $TiO_{0.325}$ and is smaller than the expected c axis of α" or staged Ti_2O (4.83 Å). From the (110) rutile peak, the a lattice parameter is 4.62 Å which indicates a 0.1% expansion from the initial a-axis in the tetragonal rutile suggesting that there is no significant change in the lattice parameter of the rutile scale.

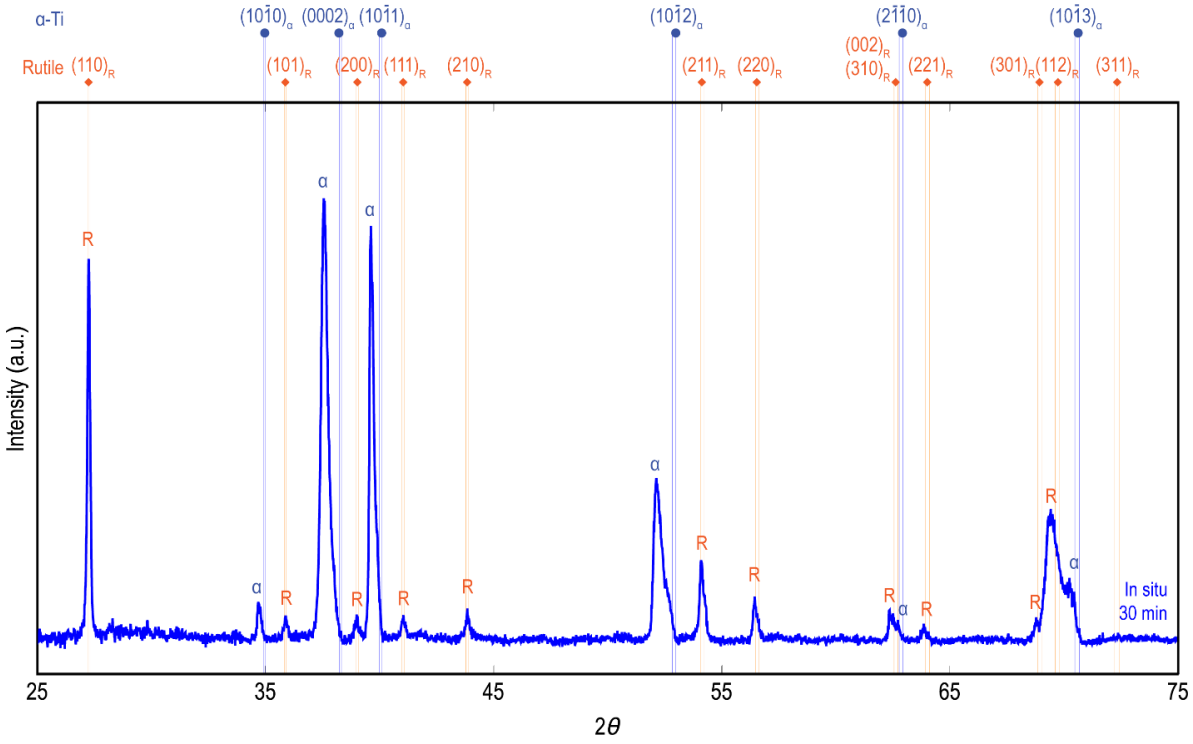

Figure 7.11. XRD pattern for Ti oxidized in situ for 30 min at 800°C in 1%O_2-Ar. α denotes α-Ti peaks and R denotes rutile peaks. The $(0002)_\alpha$, $(10\bar{1}1)_\alpha$, and $(10\bar{1}2)_\alpha$ peaks in the in situ specimen are shifted to the left of the expected α-Ti peaks due to the incorporation of interstitials in the metal substrate. The (110) rutile peak is significant and denotes rutile scale formation along with the other rutile peaks seen in the experimental pattern.

Comparing the XRD patterns from this in situ specimen to those in the ex situ 1 h, the α-Ti peak shifts suggest the formation of a solid solution $TiO_{0.325}$ as can be seen in Figure 7.12. From the 2θ of the (0002) basal plane in the oxidized specimen of the in situ experiment (as well as the 1 h ex situ specimen), the c lattice parameter is 4.78 Å which corresponds to a 2.2% expansion from the original c-axis. This is consistent with the c lattice expected from a solid solution $TiO_{0.325}$ phase. Other suboxides are included for comparison in the figure below.

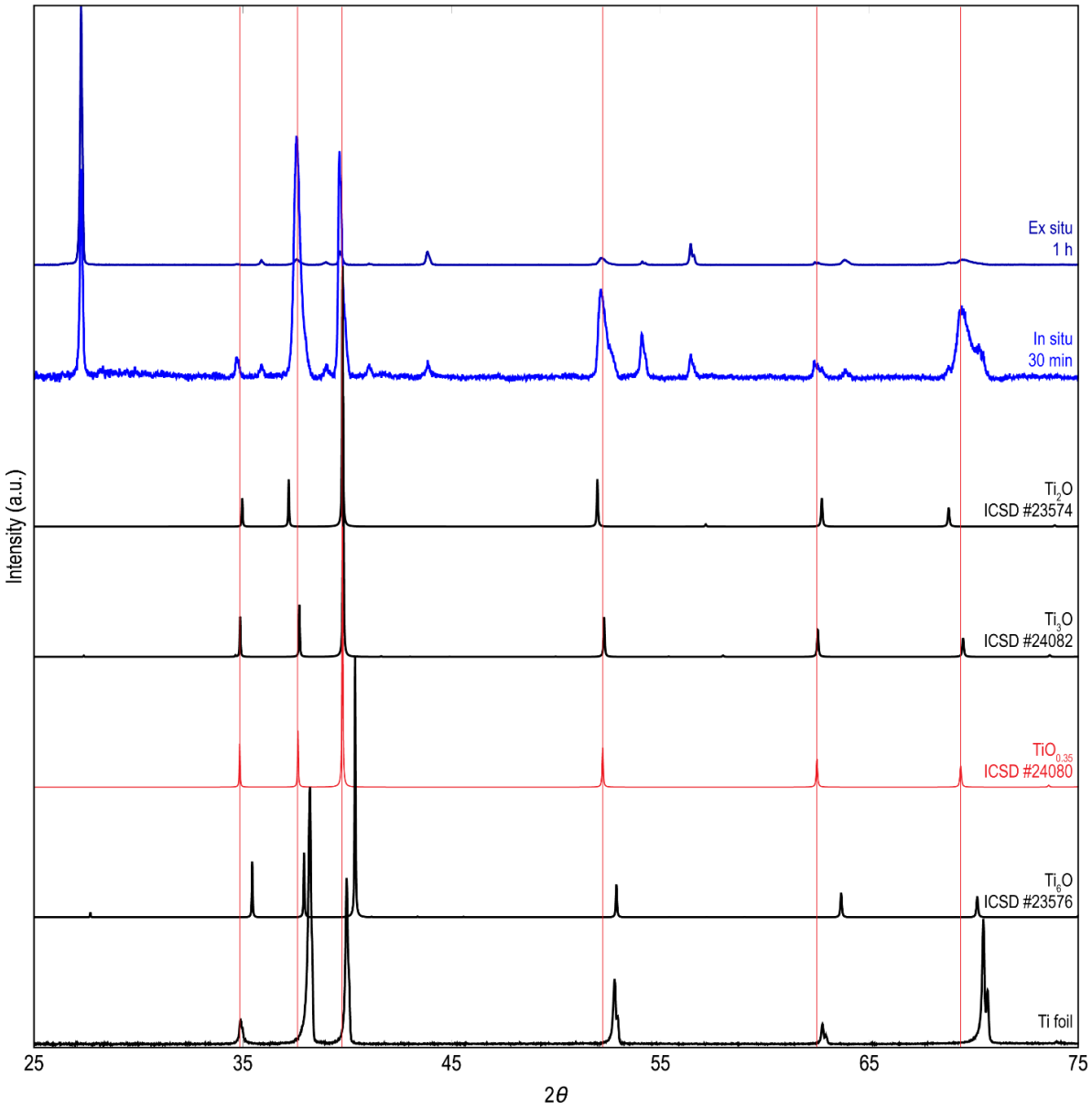

Figure 7.12. Comparison of experimental XRD patterns from specimens where the metal substrate is visible in TEM cross-sections (Figure 7.3a for ex situ 1 h and Figure 7.9 for in situ 30 min) to titanium foil and simulated XRD patterns for hcp-based suboxides. The red lines are extended from the expected peaks of a solid solution $TiO_{0.325}$ which are closest to the positions of the experimental peaks seen in the ex situ 1 h and in situ 30 min specimen. This suggests that there is a solid solution throughout the metal substrate due to the incorporation of interstitials into the hcp lattice during exposure to the oxidizing environment.

Since the elemental contrast from HAADF and STEM EDX mapping of the metal substrate looks even throughout the lamella, electron diffraction patterns were obtained to look for evidence of interstitial ordering within the titanium (Figure 7.13). Notably, there are

no superlattice reflections that could be associated with α-Ti_6O, α-Ti_3O, or α-Ti_2O. However, these are indexed as α" (staged Ti_2O) (ICSD#23574 or [52]) due to the intense reflections seen throughout the diffraction patterns, which are absent in α-Ti and the solid solution $TiO_{0.325}$ but present in α". This suggests that the structure of Ti_2O is that of oxygen interstitials occupying every other interstitial layer rather than every layer as was proposed by first-principles calculations [5].

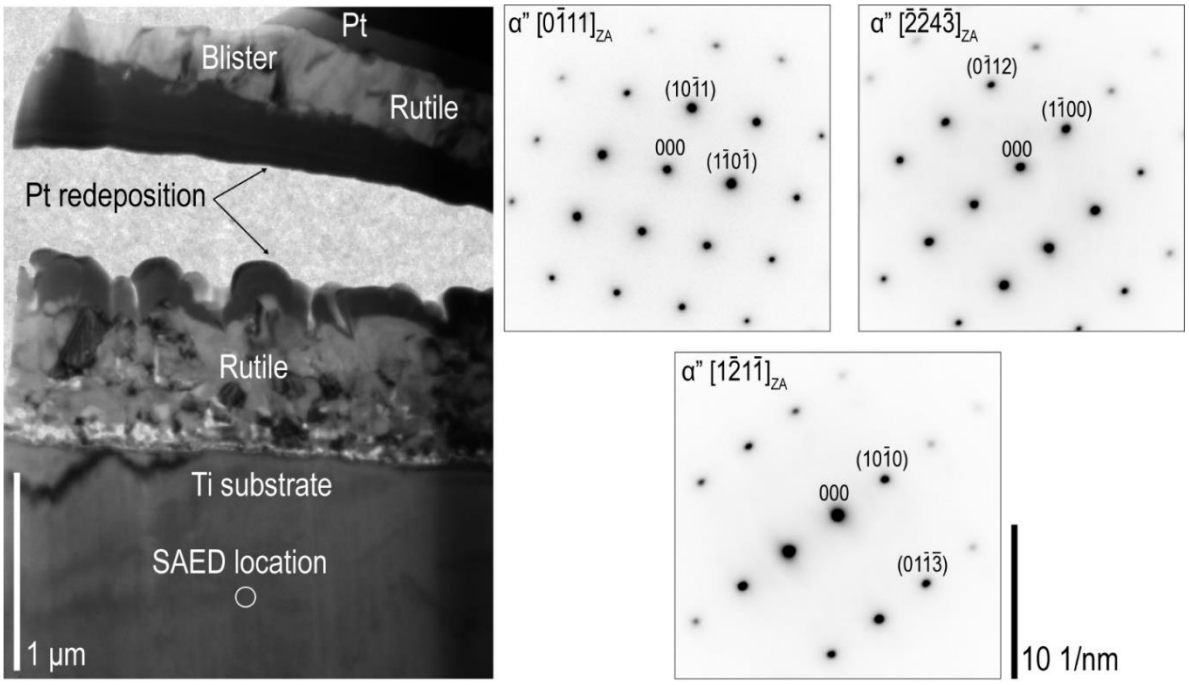

Figure 7.13. CTEM BF micrograph of oxidized Ti (in situ – 30 min) cross-section and SAED patterns from the metal substrate in three different orientations corresponding to different zone axes of α" (staged Ti_2O).

The Raman spectral evolution during this same experiment is shown in Figure 7.14 and only shows Rutile modes which appear during the dwell. The Raman spectrum shows no significant signal during the heating period even as it approached 790°C. At 800°C, no peaks are seen initially (lowest blue line in graph), but the background increases over time and the disorder, the E_g, and A_{1g} bands of rutile start to become visible in small intensities relative to the background at 5 min into the dwell. These peaks become more pronounced over time

although they remain the same at the 10 and 15 min time points. The four bands associated with rutile are visible at the end of the dwell (although B_{1g} is difficult to see because it is very small). The background and intensities of these peaks decrease slightly over time during the cooling period. At the end of the oxidation process, when the Raman spectra is taken outside the heating stage, the four bands (B_{1g}, disorder, E_g, and A_{1g}) are well-defined and some of the background intensity remains as is visible around the 100 cm^{-1} Raman shift. Notably the B_{1g} peak from the post-oxidation spectrum is more pronounced than in the dwell because this spectrum was obtained outside the heating stage and thus obtained from a different region. In this specimen, B_{1g} peaks are most intense when acquiring spectra from areas with blisters.

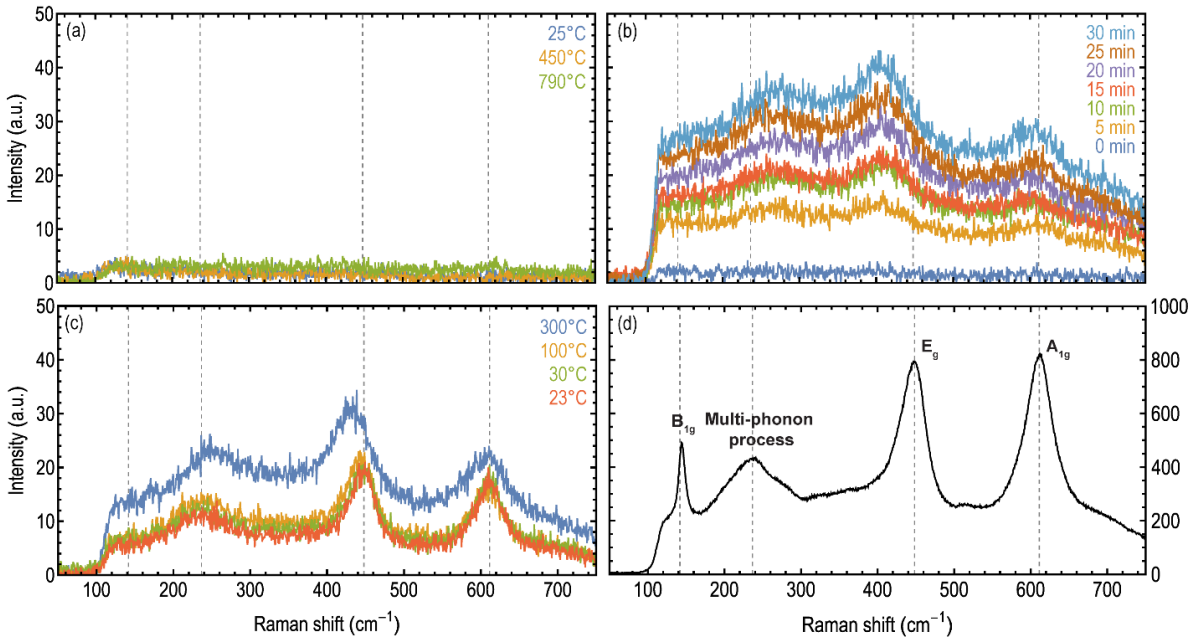

Figure 7.14. In situ Raman spectra for Ti foil oxidized in 1%O_2-Ar at 800°C for 30 min. Spectra shown indicate evolution during (a) heating, (b) dwell at temperature, and (c) cooling. The final spectrum outside of the heating stage is shown in (d) with rutile Raman modes labelled.

The frequencies for the Raman modes of the 30 min and reference rutile pellet are listed in Table 7.1. These values are within 2 cm^{-1} for all modes, a variation that could stem from slightly different oxygen content or stress states.

Table 7.1. Rutile Raman spectrum mode frequencies for in situ specimen in 1%O_2-Ar compared to literature values.

Assigned mode	**30 min (cm^{-1})**	**Rutile pellet (cm^{-1})**
B_{1g}	142.7	141.9
Multi-phonon process	234.4	236.7
E_g	447.9	447.9
A_{1g}	609.1	611.3

The positions of the disorder, E_g, and A_{1g} rutile Raman modes are plotted over the dwell time in Figure 7.15. (B_{1g} is not included since it is very small and difficult to detect so the Raman shift range investigated excludes this mode.) The E_g peak during the dwell appears at a lower Raman shift (redshift) than that of the reference polycrystalline rutile. The disorder peak appears at higher frequencies (blueshift) during dwell and shifts to the expected frequency at room temperature. A_{1g} does not show significant shifts throughout the experiment. Once the experiment is over, all rutile Raman modes are found in the expected Raman shifts from the polycrystalline rutile.

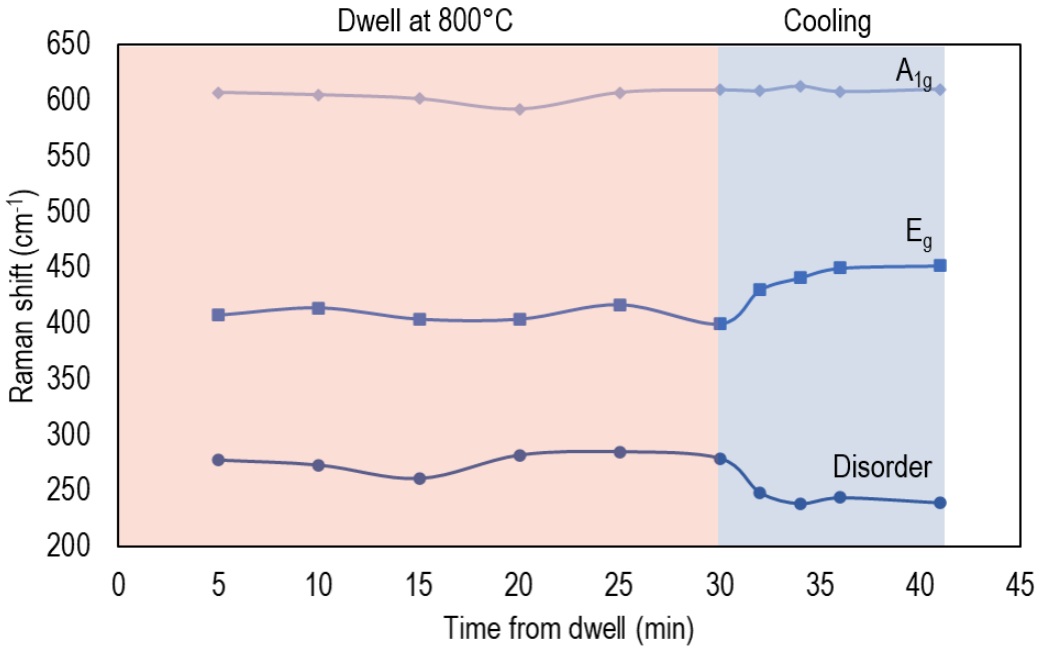

Figure 7.15. Raman shift changes on the multi-phonon process (or 2nd order), E_g, and A_{1g} modes for rutile during dwell at 800°C and cooling to room temperature.

During the in situ oxidation studies, the optical microscope attached to the Raman instrument allowed for observation of surface color changes that might be associated with the evolution of oxide films (Figure 7.16). These are most significant during the heating period and at the beginning of the dwell at 800°C. The surface of the titanium foil begins with a gray metallic color at room temperature. Dark spherical features correspond to small voids and texture from the initial titanium foil. At ~500°C, some regions become darker and form two different regions that are clearly distinguishable. At 600°C, most of the surface becomes a dark pink color with some dark blue regions. The light regions seem to remain light while the dark regions transform to the pink and blue as temperature increases. Over the next 50°C increment, most of the surface becomes a light blue and then transforms into a light blue-green color. At 700°C, the surface looks mostly gray but with undertones of pink and green in different regions. During the dwell, these pink and green undertones become more visible

and begin to transform into a gray color over time at 800°C. Most of the surface becomes gray near the mid-point of the dwell, which is likely to be associated with a rutile scale.

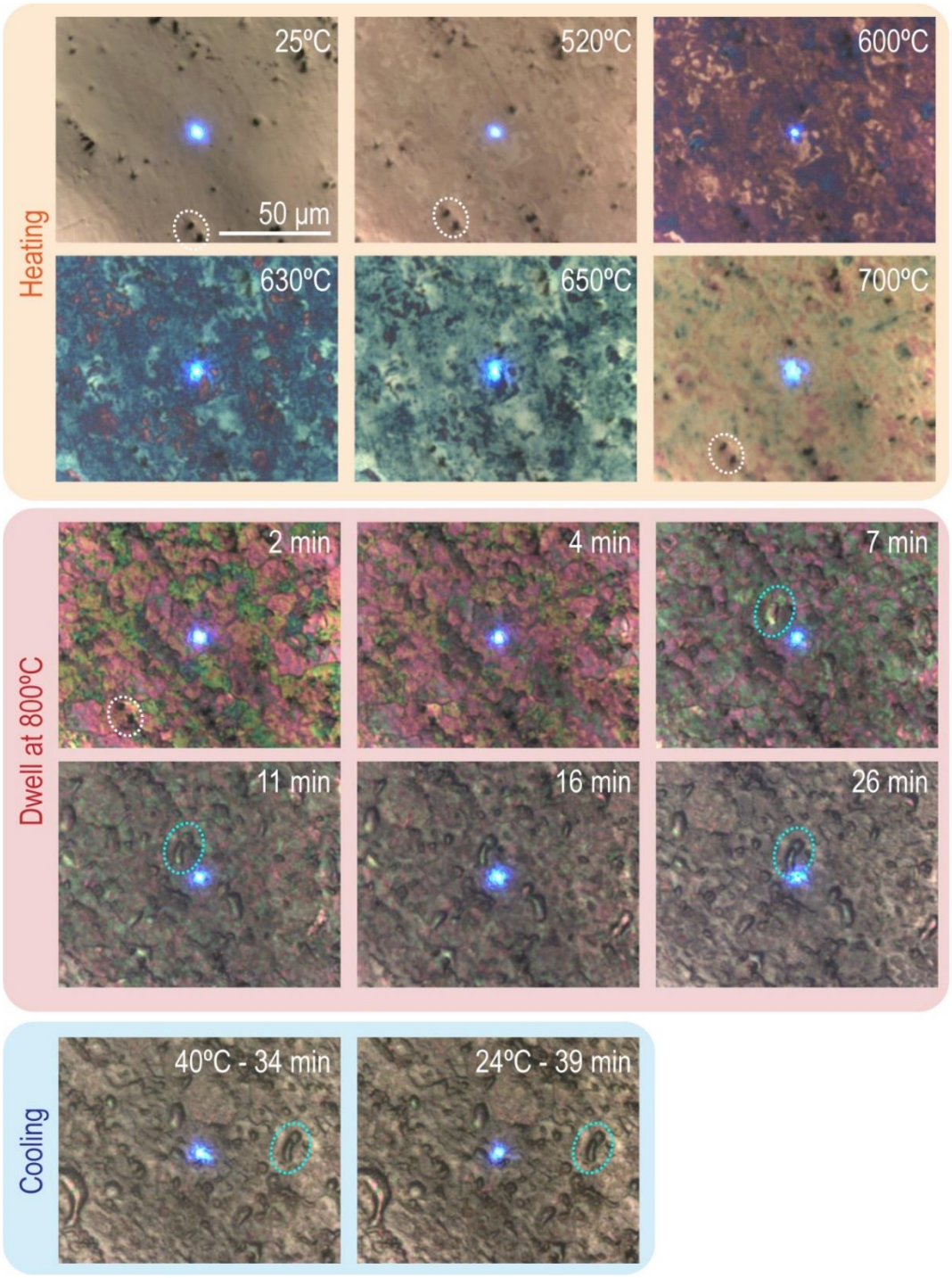

Figure 7.16. Optical micrographs of the surface showing coloration changes during the in situ oxidation experiment of a titanium foil oxidized in 1%O_2-Ar at 800°C for 30 min. The blue spot in the middle is the 488 nm laser from the Raman spectrometer. Two voids are highlighted with white dashed circles during heating and dwell to use as references for how the specimen moves during the experiment. A reference blister is highlighted in light blue dashed circles starting at the 7 min mark of the dwell stage.

Interestingly, evidence of blisters can be seen starting in the 7 minute mark of the dwell stage (immediately above and to the right of the laser beam) and become more pronounced over time, but do not seem to grow in length. Two voids are highlighted in the figure to use as reference to identify how the specimen moved during oxidation. Since the specimen was not attached to the heating stage or constricted in any way, movement is expected from the associated thermal expansion and contraction of the specimen during heating and cooling respectively. At the end of the experiment, the surface is gray throughout (consistent with a continuous, dense rutile scale) and shows several blisters of varying sizes.

The oxidized surface shows blisters that are visible in different areas of the specimen (Figure 7.17). These blisters are straight-sided with a few short branches with a width of 8-10 μm and lengths of ~70 μm for the longest blister shown in this figure. Additional smaller blister-like features are visible on top of some of the large blisters.

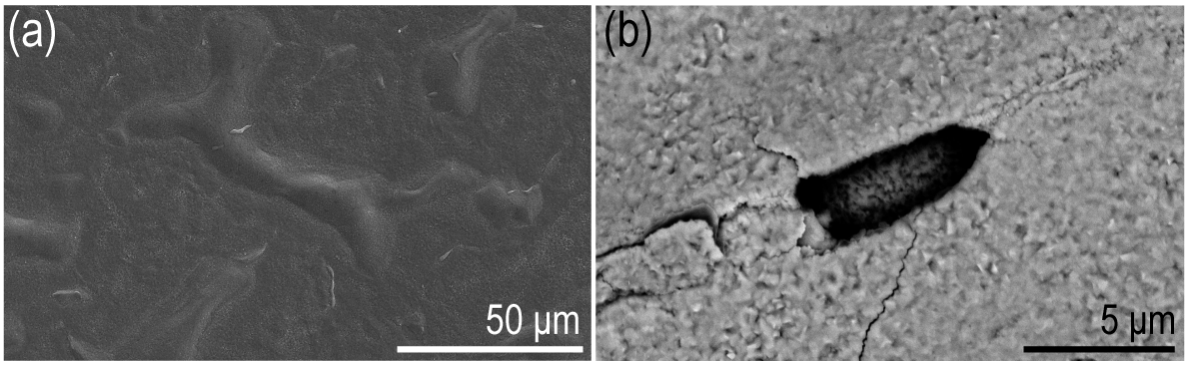

Figure 7.17. (a) SEM SE micrograph showing a few blisters for the oxidized Ti foil specimen. (b) SEM BSE image showing spallation in one of the blisters. Another oxide layer is visible under the missing oxide.

A cross-section was obtained from the edge of one of the blisters to observe the microstructure of both the base and the blistered oxide regions (Figure 7.18 for FIB location and Figure 7.9 for STEM HAADF cross-section and elemental maps). The main features of the cross-section are the multiple oxide scales, a blister underneath the outer oxide scale, and

small (20-40 nm) voids in the oxide layer closest to the metal-scale interface. Regions of coalescing voids serve as demarcations between oxide layers.

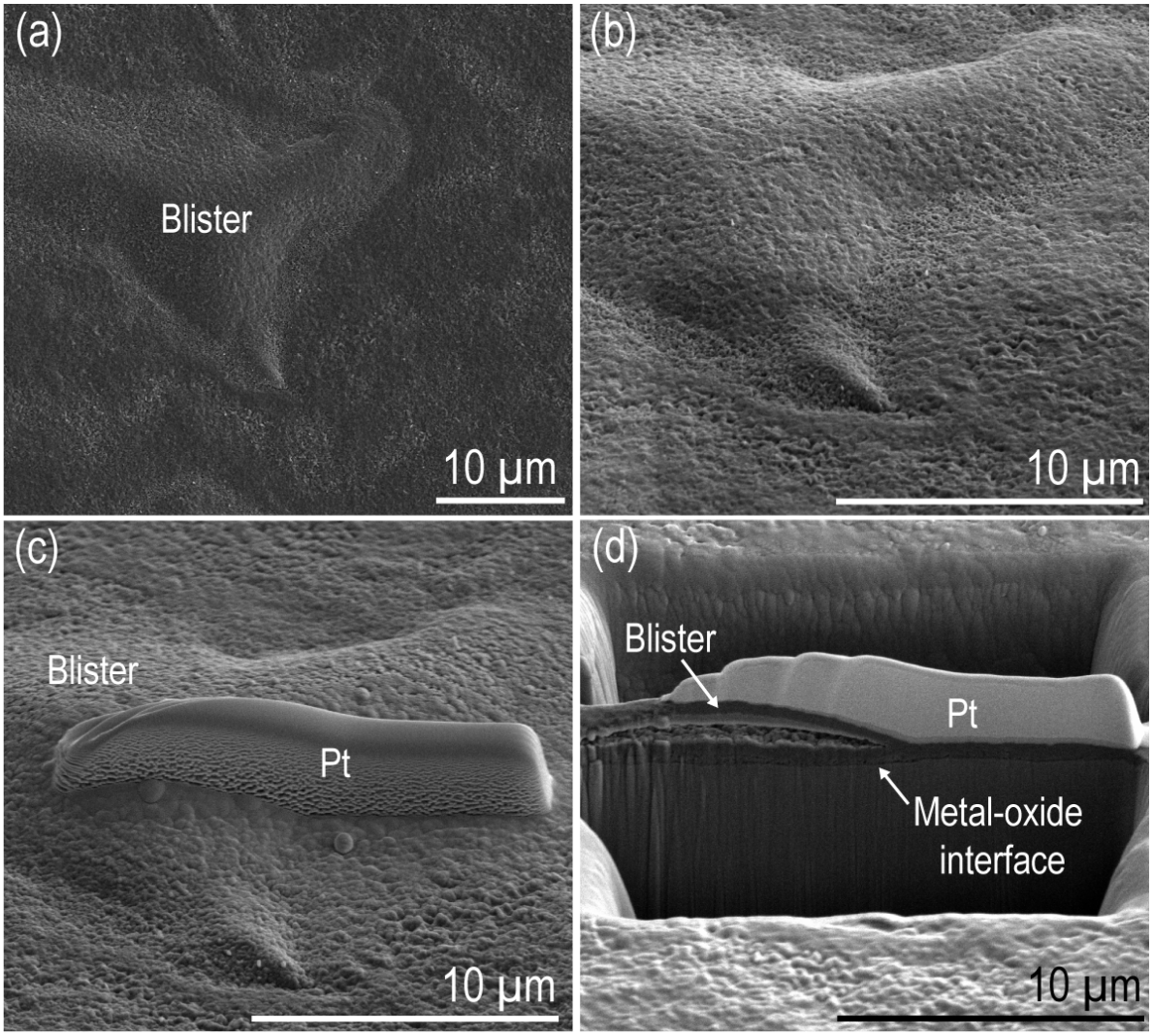

Figure 7.18. SEM micrographs of the oxidized surface of the in situ specimen showing (a) blister of interest from in-plane viewing, (b) blister viewed at 52° tilt, (c) Pt deposit, and (d) the trench showing the specimen's cross-section.

7.2 Discussion

7.2.1 Phase identification

All characterization of ex situ and in situ specimens supports the conclusion that the several oxide layers formed in the oxidized specimens are rutile, as is typically observed in

oxidation of titanium in air discussed in Chapter 2. There is potentially a concentration of nitrogen at the top of the metal substrate of the in situ specimen, but this area is too thin (~10 nm) to enable electron diffraction or to quantify interstitial content. While there is a minor probability of nitride formation, the evolution of multiple thick rutile layers suggests that oxide formation is the most favorable reaction.

Within the metal substrate in all in situ and in the 1 h ex situ specimens where the metal was visible, there was evidence of oxygen ordering within the hcp titanium in a structure similar to α". Electron diffraction showed no additional superlattice reflections that would suggest formation of other hcp-based suboxides like Ti_6O or Ti_3O. There was also evidence of the formation of a solid solution where titanium remains in an hcp crystal structure, but lattice parameters expand along the c axis to accommodate the oxygen incorporating into octahedral positions of the hcp lattice.

A summary of the features and phases seen in the in situ and ex situ oxidation specimens is shown in Table 7.2. In the shortest dwell, the metal shows evidence of oxygen incorporation as α" (staged Ti_2O) and no superlattice reflections indicative of other α-based suboxides. The ex situ specimen also provides diffraction evidence for oxygen incorporation as α" as in the in situ specimen. In these specimens, no evidence of nitrogen incorporation or nitride formation is seen.

Table 7.2. Summary of Ti oxidation study results at 800°C in 1%O_2-Ar environment.

Specimen name	Type	Dwell time	No. of oxide layers	Description of microstructure	Identified phases
M8030F	In situ	30 min	3-4	Shows clusters of whiskers on surface. Has dense outer oxide scales and a porous inner oxide.	α-Ti (O), α", rutile
TO11	Ex situ	1 h	2-3	Shows faceted oxide grains with ridges of larger oxide crystals. Dense outer oxide scale divided by small voids, and a porous inner oxide.	α-Ti (O), α", rutile
TO13	Ex situ	9 h	4	Only large columnar rutile grains were observed in TEM specimen, but voids are noticeable from trench and could delineate oxide layers.	α-Ti (O)[10], rutile

7.2.2 Microstructural evolution

An initial observation on the microstructural evolution of the in situ specimen was the coloration changes in the oxidized surface. Titanium oxides and nitrides are both known to

[10] This specimen might have also formed an hcp suboxide but the rutile scale was too thick for the XRD to measure into the metal substrate or for the metal substrate to be seen from FIB liftout (typically ~5 μm into the specimen from the surface).

exhibit different colors depending on the phase or thickness and is a technique commonly used in titanium jewelry and art. Unfortunately, there is no systematic study that can directly relate which phases these colors correspond to nor was there any distinguishable differences in the Raman spectra during these color changes. Furthermore, any titanium nitride below 50 at% N or oxide below 60 at% is not expected to have a strong Raman spectrum that could help identify the initial phases formed during oxidation. However, it is likely that the amount of oxygen in the 1%O_2-Ar environment allows for accelerated rutile formation.

Based on coloration and the environment used, the initial coloration changes could be associated with: (1) formation of solid solution or lower oxides for which there is no strong Raman signal, or (2) the formation of a rutile film thin enough to not generate a strong signal. Since rutile has strong scattering in Raman, it is more likely that these coloration changes are instead associated with the formation of phases other than rutile. Similar coloration changes were observed by Tkachuk et al. [79] in oxynitriding titanium, although their methodology consisted of nitriding with subsequent oxidation rather than heat treating in an environment with both interstitials reacting with titanium as in this work.

Based on the phase identification and literature on Ti oxidation, it is likely that outward Ti and inward O fluxes are the main diffusing species in this environment as illustrated in Figure 7.19. The fact that only rutile scales develop indicates that at the partial pressures of oxygen in the 1%O_2-Ar environment (pO_2 = 0.01 atm), oxide formation is the most favorable reaction. The likely oxidation mechanism for titanium in 1%O_2-Ar is:

1. Incorporation of oxygen into the metal as solid solution
2. Formation of α” (staged Ti_2O) as metal saturates

3. Immediate formation of rutile and subsequent oxide growth with outward Ti and inward O fluxes

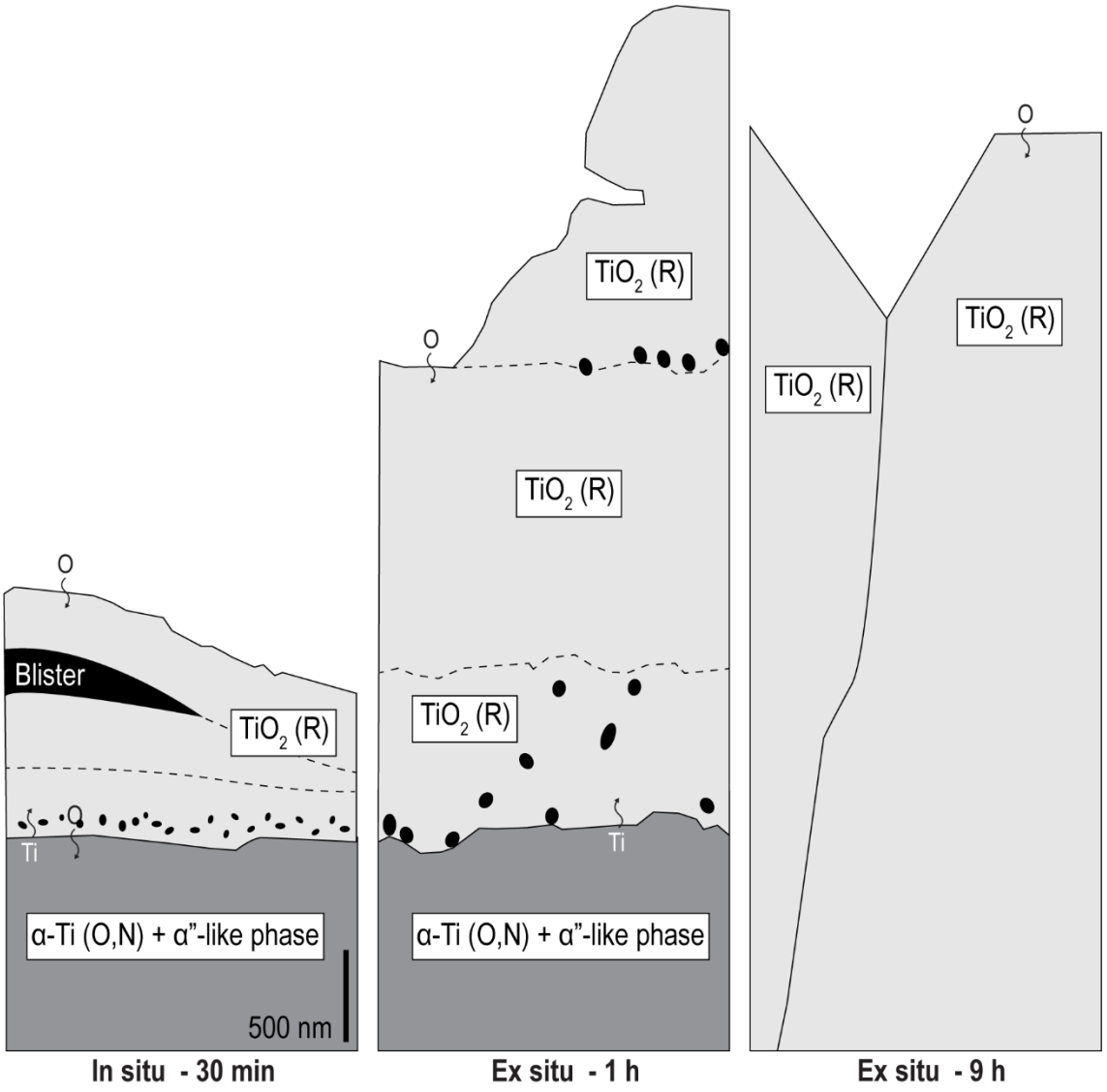

Figure 7.19. Schematic comparing the microstructures of the three specimens: in situ 30 min, ex situ 1 h, and ex situ 9 h. Dashed lines indicate possible layer delineations based on small voids. Solid lines indicate grain boundaries. Black regions indicate voids. Outward Ti and inward O fluxes are show throughout the specimens.

7.2.3 Thermal and growth stresses in specimen with buckling

An interesting feature of these specimens is the evidence of oxide stress evolution through the formation of whiskers, blisters, and spallation. Typically, blisters are seen at the

metal-oxide interface and are indicative of large compressive stresses in the scale. In the in situ specimen, blisters occur between the outermost oxide layer and the one beneath it rather than at the metal-oxide interface. Underneath the blister, oxide scales are all ~300 nm in thickness suggesting a stratification like those observed by Bertrand [207]. However, there is also significant porosity within the innermost oxide scale, which is not a feature typically observed in stratified oxide microstructures in titanium. The general microstructure of an outer compact scale and inner porous scale has also been observed in titanium oxidation [89], but those oxidation experiments as well as those by Bertrand [207] were performed at temperatures above the β transus where the transformation to β-Ti might play a role. The microstructures in this work show multiple layers with the innermost containing several small voids near the metal-oxide interface where the rest of the oxide scales are compact. To explore the origins of the blister formation, stresses were calculated based on information from the in situ specimen.

Assuming the conditions of a straight-sided buckling delamination of a thin film (i.e. the outermost rutile layer) in a thick substrate, the onset stress required to buckle said film is given by (Equation 10.10 from [208]):

$$\sigma_c = \frac{\pi^2}{12} E_1 \left(\frac{h}{b}\right)^2$$

where σ_c is the onset buckling stress, E_1 is the Young's modulus of the oxide, h is the thickness of the blister, and b is half the width of the debonded region. Assuming a 300 nm blister with b = 5 μm as seen in the in situ specimen cross-section, the necessary stress for buckling is 479 MPa.

Two common sources for stress during oxidation are thermal mismatch of the oxide and metal upon cooling and the volume expansion from the metal forming an oxide. Since

the PBR of forming rutile from titanium is 1.75, a high compressive stress is expected from volume expansion. Thermal stress from cooling was also calculated to compare it to the onset stress required for buckling.

Using LayerSlayer [209], a software tool that can calculate thermal stresses in multilayer systems, the thermal stress from cooling from 800°C to 25°C can be calculated using the material properties specified in Table 7.3. Assuming a 50 μm thick titanium foil with three ~300 nm rutile layers on top, the thermal mismatch stress is ~415 MPa throughout the rutile scales (Figure 7.20). This implies that thermal mismatch could be sufficient to cause the onset of buckling. However, since blisters form at the dwell temperature, this suggests that the growth stresses are much larger than the calculated thermal stress.

Table 7.3. Material properties for LayerSlayer calculations assuming a polycrystalline titanium substrate and polycrystalline rutile films on top.

Layer	Material	E (GPa)	ν	κ (W/m·K)	α ($\times 10^{-6}$)/K at 800°C
Metal	Ti	103	0.33	17	9.8
Oxide	Rutile	162	0.28	8.9	7.14

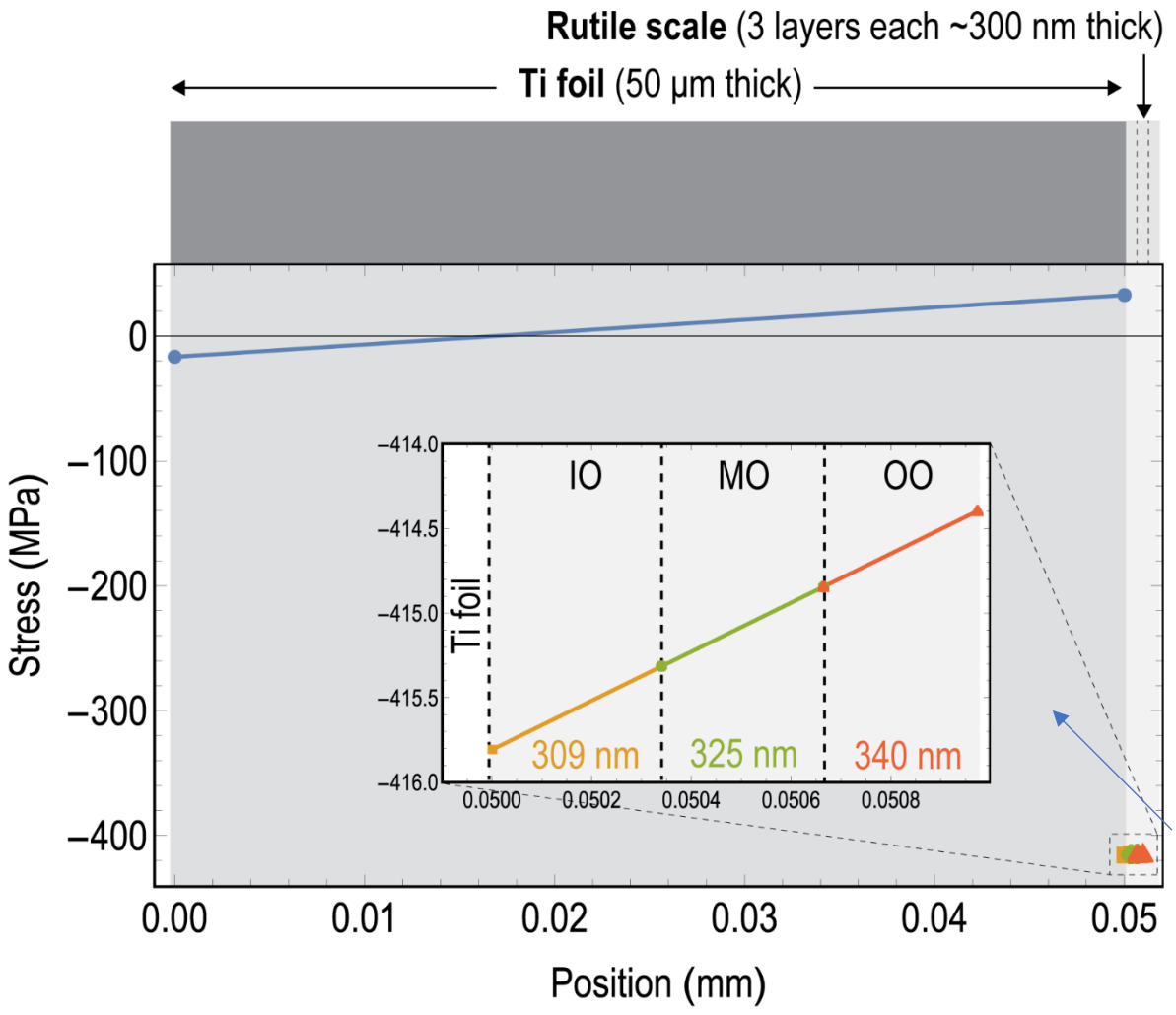

Figure 7.20. Stress states throughout a simulated titanium substrate assuming three rutile layers of ~300 nm thickness on top of a 50 μm thick titanium foil. Schematic of the Ti and rutile layers shown on top right aligns with the position (x-axis of the stress vs position plot). Inset shows magnified region for the stress within the rutile layers.

Using the blister height (δ = 1 μm) from this particular lamella, the stress in the unbuckled state (σ_o) can be calculated with (Equation 10.9 from [208]):

$$\frac{\delta}{h} = \sqrt{\frac{4}{3}\left(\frac{\sigma_o}{\sigma_c} - 1\right)}$$

resulting in a stress of ~4.5 GPa which would support that growth stresses from volume expansion are sufficiently large to onset buckling. Additionally, this large stress could also explain why there is more than one feature evident of stress relief such as the whiskers and

porosity. In oxides, whiskers are thought to alleviate the compressive stress of the oxide scale [196].

It is important to note that the growth stress alone is not sufficient for buckling to occur without the presence of a defect that can act as the initiation site for delamination. One possible scenario is that small voids formed from asymmetrical titanium and oxygen fluxes early in the oxidation process can either grow to accommodate the stress, or act as nucleation sites for delamination.

While voids are rather small in these specimens, their location within oxide scales suggests that metal and oxygen are both being transported through outward diffusion of titanium simultaneous and inward diffusion of oxygen. Assuming a divergence in flux:

$$\frac{\partial C_{TiO_2}}{\partial t} = -\frac{\partial J_{Ti}}{\partial x} = -\frac{1}{2}\frac{\partial J_O}{\partial t}$$

suggests that a large oxygen diffusion contribution is required for void formation. This large contribution could be explained by considering enhanced oxygen diffusivity though grain boundaries which for near-α Ti alloys has been reported to be 10^5 times faster than oxygen diffusivity through the Ti grains at 650°C [170]. Since these experiments were done at a higher temperature of 800°C, it is possible that oxygen diffusivity through the grain boundaries is even faster than previously reported values. This, in turn, could suggest that proximity to grain boundaries may have an impact on where blisters and whiskers form.

7.2.4 Proposed oxidation mechanism

To consolidate the results of the oxidation studies in 1%O_2-Ar into an oxidation mechanism, some of the salient observations from these experiments are:

- Specimens all form at least two oxide layers – all of which are unequivocally rutile.

- Blisters are formed at temperature (800°C) and are therefore not a result of cooling effects at the end of the oxidation experiment.
- While volume changes between metal and oxide could account for the development of growth stresses, blisters are found beneath the outer oxide and not at the metal-oxide interface where these volume changes would be most immediate.
- It had been suggested that recrystallization or sintering occurred at the outer scales to explain the dense and compact nature of them [89]. However, both processes are known to relieve stress rather than generate it and have been proposed to occur above 950°C. It could be that recrystallization occurs on the rutile scale (since the outer scale is compact) but does not fully alleviate the large compressive stress and begins to form whiskers to further alleviate this stress.
- Since voids are formed in between and within oxide scales, outward titanium and inward oxygen migration are likely. This suggests diffusion properties might govern the porosity formation through enhanced oxygen diffusion within grain boundaries.

From these results, a possible oxidation mechanism would follow these steps:

1. Oxygen and nitrogen in the atmosphere adsorb onto the metal surface. In the 1%O_2-Ar environment, no evidence of nitrogen is seen so it is likely that oxide formation is most thermodynamically and kinetically favorable in these conditions.
2. Oxygen dissociates and starts dissolving into the metal substrate. This process forms a solid solution in the bulk of the metal substrate and an α”-like phase near the metal-scale interface.
3. Once the metal surface is saturated, rutile nucleates and continues growing over time.

4. Due to the large volume expansion associated with the transformation from titanium to rutile, small voids form at the metal-oxide interface.
5. As rutile continues to grow, the voids both grow and move towards outer rutile layers as titanium diffuses outward and oxygen inward to form various rutile layers with varying degrees of porosity. It is possible that oxygen from the rutile also continues to diffuse into the metal during this process.
6. When the rutile layers reach a critical thickness, the growth stress is sufficient to buckle the outer rutile layer.
7. Upon cooling, there are additional thermal stresses associated with the CTE mismatch between metal and oxide, but these do not have as large an effect as the growth stresses.

7.2.5 Comparison to Ti oxidized in UHP Ar and gettered Ar

In Chapters 4-6, titanium specimens showed evidence of nitride and oxynitride formation from oxidation studies in gettered Ar and UHP Ar – both environments in which $O_2 < N_2$. By increasing this O_2:N_2 ratio in the 1%O_2-Ar, the formation of nitrogen-containing phases was suppressed and only rutile formation was observed in the developed scales. For a quick comparison, the scale thickness (including voids in the measurement) of the specimens discussed throughout the thesis is plotted in Figure 7.21. In general, scales grow over time and an increase in oxygen content in the gas corresponds to an increase in scale thickness.

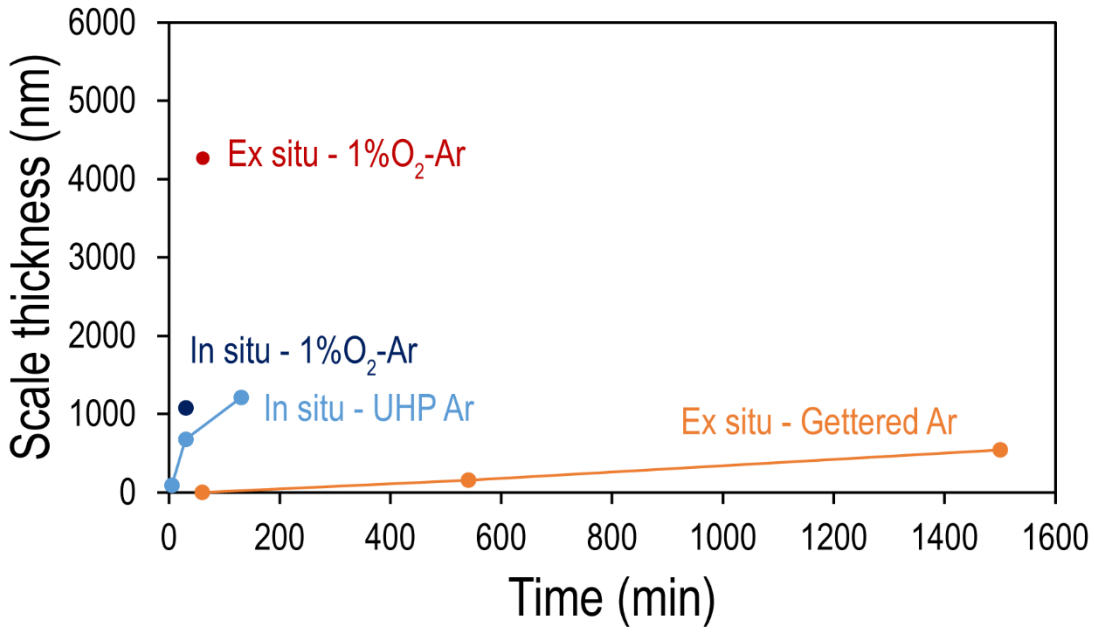

Figure 7.21. Comparison of scale thickness in Ti specimens oxidized ex situ and in situ using the various gas environments with different O_2:N_2 ratios. Light colors correspond to O_2<N_2 ratios (orange line – Chapter 4; light blue – Chapter 6) and dark colors to O_2>N_2 ratios (red and dark blue – this chapter).

Comparing the in situ 30 min specimens from each environment, in UHP Ar oxynitride is able to form while this is suppressed in 1%O_2-Ar where only rutile forms. Interestingly, the voids in the outer rutile scale are larger in the UHP Ar (~150 nm) than when using the 1%O_2-Ar (~35 nm), in which the outer rutile layers show the presence of blisters and delamination in certain regions of the oxidized surface instead of voids within the scale. In the 1%O_2-Ar specimen, the voids are found in the innermost rutile layer instead of in the outer layer.

If void formation relied solely on the asymmetrical flux of outward Ti vs inward N or O, the voids in the 1%O_2-Ar would be larger than in UHP Ar due to the increased availability of both interstitials. While asymmetrical flux might still be contributing to void formation and growth, this suggests that there are other factors that drive the formation of these pores in the oxide and nanopores in the oxynitride regions. One possibility is the volume change from

transforming from the metal into the different nitride, oxynitride and rutile phases leaving behind voids at the different stages of the oxidation process.

7.3 Conclusion

Ex situ and in situ oxidation experiments using 1%O_2-Ar showed the formation of multiple rutile layers that were dense in the outer layers and porous in the innermost layer immediately above the metal-scale interface. Evidence of stresses associated with the oxidation process were observed on the surface through the formation of emerging whiskers and the blistering between rutile scales in the in situ specimen, and in the spallation of multiple scales in the corners of the 9 h ex situ specimen.

Oxidation of titanium in this environment showed no suboxides, nitrides, or oxynitrides in the developed scales, although α" (staged Ti_2O) was observed within the metal substrate of the 1 h ex situ and 30 min in situ specimens. All specimens showed only the formation of rutile with stratified morphologies and varying degrees of porosity depending on the distance of the rutile layer from the metal-oxide interface.

8 Conclusions and outlook

When this project began, the initial goal was to develop a deeper understanding of the early stages of titanium oxidation. To achieve this, experiments were designed to develop layers of titanium suboxides by oxidizing titanium metal under low partial pressures of oxygen and identifying which phases formed and how. During this investigation, the influence of nitrogen became evident, even when gettering research-grade argon gas to reduce interstitial content in the reacting environment. This investigation thus shifted its focus to exploring the reactions of titanium metal with nitrogen and oxygen under environments with three different N_2:O_2 ratios. The gases used were gettered Ar (N_2:O_2 = 10,000), ultra-high purity Ar (N_2:O_2 = 5), and a 1%O_2-Ar mixtures (N_2:O_2 = 0.0005).

The primary goal of investigating titanium reactions under these different environments was to characterize which phases formed as scales and in the metal substrate to elucidate the reactions between the hcp α-titanium phase and nitrogen and oxygen from the reacting environments. Since nitrogen and oxygen are the main components of air where titanium is mainly used, it is important to understand the fundamental interactions of these interstitials with hcp titanium. A deeper understanding of these reactions can help better develop strategies for prevention of titanium embrittlement from nitrogen and oxygen ingress or by exploiting the formation of nitride, oxynitride, or oxides that might provide interesting properties for a variety of applications. The low partial pressures used in these studies allowed for exploration of nitride, oxynitride, and oxide formation in hcp titanium.

It was found that these environments allowed for the formation of ε-Ti_2N, TiN, fcc rocksalt Ti oxynitrides, Ti_2O_3 corundum, Magnéli phases, and rutile in the scales. From diffraction evidence, the substrate is mostly a solid solution α-Ti (N,O) although some

regions near the metal-scale interface show interstitial ordering similar to the α" (staged Ti_2O) phase. When slow-cooling in UHP Ar, various additional oxygen orderings can be appreciated that show Types I, II, and III of superlattice reflections along the $[\bar{1}100]_{ZA}$ in hcp Ti. Based on the guiding research questions for this work, the key findings from these experiments are:

1) **What phases form under gases with various N_2:O_2 ratios?**

    a. Gettered Ar (fast-cooled):

        i. Substrate: α-Ti (N,O) and α"-like (staged Ti_2O) phase

        ii. Scale: ε-Ti_2N-like phase and fcc TiN with a [110] twin axis and {111} twins

    b. Gettered Ar (slow-cooled):

        i. Substrate: α-Ti (N,O) and α"-like phase

        ii. Inner oxide (1 h): Ti_2O_3 (corundum)

        iii. Outer oxide (1 h): Magnéli phase(s) likely Ti_3O_5 and/or Ti_4O_7

        iv. Interfacial layer (9-25 h): hcp-based N-rich ordered phases (not ε-Ti_2N from electron diffraction)

        v. Inner layer (9 -25 h): fcc rocksalt TiN_xO_y

        vi. Inner oxide and outer oxide (9-25 h): TiO_2 (rutile)

    c. UHP Ar:

        i. Substrate: α-Ti (N,O) and α"-like phase; α-Ti with various oxygen orderings in slow-cooled specimen (similar to Ti_3O and α")

ii. Interfacial layer (5 min): N-rich fcc Ti oxynitride or a Ti nitride (Ti_2N or TiN) (Scale was too thin for extensive analysis)

iii. Inner oxynitride (130 min): fcc rocksalt Ti oxynitride (likely low N content)

iv. Inner layer: fcc rocksalt Ti oxynitride (likely low O content)

v. Outer oxide: TiO_2 (rutile); evidence of Magnéli phases in slow-cooled specimen

d. 1%O_2-Ar:

i. Substrate: α-Ti (O) and α”-like phase

ii. Scales: TiO_2 (rutile)

2) How do these phases form?

a. In the gettered Ar and UHP Ar environments, nitrogen and oxygen dissolve into the substrate and form a solid solution and interstitial ordering occurs in metal grains near the metal-scale interface. With increased interstitial content, the hcp Ti begins forming an fcc TiN or TiN_xO_y scale (depending on the reacting environment used). Upon further oxygen ingress, the outer portion of this scale converts into rutile and the nitrogen and oxygen from the inner fcc scale continues diffusing into the metal substrate. Partial dislocations likely play a role in the hcp Ti to fcc TiN/TiN_xO_y transformation. The fcc TiN/TiN_xO_y phases also show the formation of twins in some of the specimens. Notably, an orientation relationship can be appreciated between the hcp substrate and its fcc scales. The mechanism of void formation remains unclear but is possibly

explained by a combination of factors such as the volume expansion from hcp to fcc, asymmetrical fluxes, and enhanced diffusion at the grain boundaries.

b. In the 1%O_2-Ar environment, nitrogen and oxygen dissolve into the substrate forming a solid solution in the bulk and an α”-like phase near the metal-scale interface. The scales developed are multiple rutile layers with blistering occurring in the UHP Ar experiments where 50 μm thick Ti foils were used. This blistering occurs at temperature and can be attributed to growth stresses.

In summary, this thesis has shown the importance of considering the effect of nitrogen on titanium even when reacting in environments that would normally be considered inert. These experiments have shown the formation of nitride, oxynitride, and lower oxides, in addition to the rutile expected from typical titanium oxidation studies. Oxygen orderings were found in the metal substrate of a slow-cooled specimen, showing that oxygen ordering can occur when reacting titanium metal to UHP Ar. Additionally, interesting features such as twins in fcc phases, an hcp Ti-fcc orientation relationship, voids, and blisters were observed and mechanisms for their formation were proposed. Finally, in situ heating stage studies under Raman spectroscopy proved that rutile formation occurs at the exposure temperature rather than developing during cooling as had been suspected from initial tube furnace studies.

The work described in this thesis provides further evidence for the complexity of studying titanium oxidation or any titanium reactions with other interstitial elements. While specimens were carefully generated and analyzed, experimental limitations, such as quantifying interstitial elements or only being able to detect rutile in Raman, provide opportunities for further exploration of the results from this work. For instance, computational work on the Ti-N-O system could aid in determining the solubility limits of

the phases found in this thesis's specimens as well as the ordering of nitrogen and oxygen within the hcp and fcc phases discussed.

Future work would be beneficial to further understand the microstructural evolution and void formation mechanism in titanium exposed to nitrogen and oxygen. For microstructural evolution, in situ TEM studies in a heating stage could prove useful in observing any defect formation alongside phase evolution during exposure to an argon gas[11]. In the case of voids, it was shown that these are inherent to the system and that they appear in all reacting environments used. However, the sensitivity of titanium impedes the use of inert marker studies which could help elucidate the flux direction of the diffusing elements. As an alternative, oxygen and nitrogen isotopes could be used to in a two-step furnace experiment to track ion transport and whether either interstitial have migration paths through grain boundaries that could explain void formation.

One additional area of potential study is to expand this experimental framework to dilute Ti binary alloys to analyze the effect of alloying element additions on the phase stability and microstructural evolution that was established in this thesis. Preliminary work was done for Ti-2Al and Ti-2Nb specimens that suggested Al addition increased scale thickness and porosity while Nb addition resulted in thinner and more compact scales.

The analysis performed in these studies has contributed to the understanding of titanium reactions with nitrogen and oxygen at high temperatures and low partial pressures. The experimental approaches used can be applied towards studying further complex systems either in Ti-based alloys or in other systems such as complex concentrated alloys (CCAs).

[11] Exposure to vacuum would likely also generate a reaction despite its low interstitial content given the sensitivity of titanium.

9 References

[1] G. Lütjering, J.C. Williams, Titanium, Springer Science & Business Media, 2013.

[2] C. Leyens, M. Peters, Titanium and Titanium Alloys: Fundamentals and Applications, John Wiley & Sons, 2003.

[3] T.M. Group, Reducing the High Cost Of Titanium, (n.d.). https://www.aerodefensetech.com/component/content/article/adt/features/articles/35667 (accessed April 13, 2022).

[4] H. Okamoto, O-Ti (Oxygen-Titanium), J. Phase Equilib. Diffus. 32 (2011) 473. https://doi.org/10.1007/s11669-011-9935-5.

[5] N.S.H. Gunda, B. Puchala, A. Van der Ven, Resolving phase stability in the Ti-O binary with first-principles statistical mechanics methods, Phys. Rev. Materials. 2 (2018) 033604. https://doi.org/10.1103/PhysRevMaterials.2.033604.

[6] W. Lengauer, The titanium-nitrogen system: A study of phase reactions in the subnitride region by means of diffusion couples, Acta Metallurgica et Materialia. 39 (1991) 2985–2996. https://doi.org/10.1016/0956-7151(91)90031-U.

[7] I. Khidirov, Revision of the Ti-N phase diagram as probed by neutron diffraction, Russian Journal of Inorganic Chemistry. 56 (2011) 298–303.

[8] N.S.H. Gunda, A. Van der Ven, First-principles insights on phase stability of titanium interstitial alloys, Phys. Rev. Materials. 2 (2018) 083602. https://doi.org/10.1103/PhysRevMaterials.2.083602.

[9] H. Wriedt, J. Murray, The N-Ti (nitrogen-titanium) system, Bulletin of Alloy Phase Diagrams. 8 (1987) 378–388.

[10] H. Okamoto, C−Ti (Carbon-Titanium), JPED. 27 (2006) 306–307. https://doi.org/10.1361/154770306X109980.

[11] H. Conrad, Effect of interstitial solutes on the strength and ductility of titanium, Progress in Materials Science. 26 (1981) 123–403. https://doi.org/10.1016/0079-6425(81)90001-3.

[12] H. Ogden, R. Jaffee, The effects of carbon, oxygen, and nitrogen on the mechanical properties of titanium and titanium alloys, Battelle Memorial Inst. Titanium Metallurgical Lab., Columbus, Ohio, 1955.

[13] H. Okamoto, O-Ti (Oxygen-Titanium), Journal of Phase Equilibria and Diffusion. 32 (2011) 473–474. https://doi.org/10.1007/s11669-011-9935-5.

[14] G. Lütjering, J.C. Williams, Titanium, Springer, 2003.

[15] F.C. Campbell, Elements of Metallurgy and Engineering Alloys, ASM International, 2008.

[16] R.S. Uwanyuze, J.E. Kanyo, S.F. Myrick, S. Schafföner, A review on alpha case formation and modeling of mass transfer during investment casting of titanium alloys, Journal of Alloys and Compounds. 865 (2021) 158558. https://doi.org/10.1016/j.jallcom.2020.158558.

[17] X. Chamorro, N. Herrero-Dorca, P.P. Rodríguez, U. Andrés, Z. Azpilgain, α-Case formation in Ti-6Al-4V investment casting using ZrSiO4 and Al2O3 moulds, Journal of Materials Processing Technology. 243 (2017) 75–81. https://doi.org/10.1016/j.jmatprotec.2016.12.007.

[18] S.-Y. Sung, Y.-J. Kim, Influence of Al contents on alpha-case formation of Ti–xAl alloys, Journal of Alloys and Compounds. 415 (2006) 93–98. https://doi.org/10.1016/j.jallcom.2005.07.051.
[19] S.-Y. Sung, Y.-J. Kim, Alpha-case formation mechanism on titanium investment castings, Materials Science and Engineering: A. 405 (2005) 173–177. https://doi.org/10.1016/j.msea.2005.05.092.
[20] Y. Guilin, L. Nan, L. Yousheng, W. Yining, The effects of different types of investments on the alpha-case layer of titanium castings, The Journal of Prosthetic Dentistry. 97 (2007) 157–164. https://doi.org/10.1016/j.prosdent.2007.01.005.
[21] V. Deshmukh, R. Kadam, S.S. Joshi, Removal of alpha case on titanium alloy surfaces using chemical milling, Null. 21 (2017) 257–278. https://doi.org/10.1080/10910344.2017.1284558.
[22] M.J. Donachie, Titanium: a technical guide, ASM international, 2000.
[23] H. Nakajima, M. Koiwa, Diffusion in Titanium., ISIJ International. 31 (1991) 757–766. https://doi.org/10.2355/isijinternational.31.757.
[24] L. Scotti, A. Mottura, Interstitial diffusion of O, N, and C in α -Ti from first-principles: Analytical model and kinetic Monte Carlo simulations, The Journal of Chemical Physics. 144 (2016) 084701. https://doi.org/10.1063/1.4942030.
[25] H.H. Wu, D.R. Trinkle, Direct Diffusion through Interpenetrating Networks: Oxygen in Titanium, Physical Review Letters. 107 (2011). https://doi.org/10.1103/PhysRevLett.107.045504.
[26] W.P. Roe, H.R. Palmer, W.R. Opie, Diffusion of oxygen in alpha and beta titanium, Trans. ASM. 52 (1960) 191.
[27] C.J. Rosa, Oxygen diffusion in alpha and beta titanium in the temperature range of 932° to 1142°C, MT. 1 (1970) 2517–2522. https://doi.org/10.1007/BF03038377.
[28] L. Sokiryansky, D. Ignatov, A.Y. Shinyaev, Influence of polymorphic transformation in oxygen diffusion in titanium, PHYS METALS METALLOGR. 28 (1969) 103–108.
[29] M. Dechamps, R. Feldman, P. Lehr, High-Temperature Oxidation of Titanium Physical and Mathematical Models, Titanium and Titanium Alloys, Scientific and Technological Aspects,. 2 (1976) 1045–1056.
[30] D. David, A Study of the Diffusion of Oxygen in α-Titanium Oxidized in the Temperature Range 460°–700°C, Journal of The Electrochemical Society. 130 (1983) 1423. https://doi.org/10.1149/1.2119966.
[31] V. Repkin, G. Kurtukov, A. Kornilov, V. Bespalov, Metalloterm. Protessy v Khimii i Metallurgii, in: Russian Collection, Published Nauka Novosibirsk, 1971: pp. 320–330.
[32] V. Eremeev, Y.M. Ivanov, A. Panov, Diffusion of nitrogen in titanium and zirconium., Izv. Akad. Nauk SSSR, Metal., No. 4, 262-7 (July-Aug. 1969). (1969).
[33] R. Wasilewski, G. Kehl, Diffusion of nitrogen and oxygen in titanium, J. Inst. Metals. 83 (1954).
[34] A. Anttila, J. Räisänen, J. Keinonen, Diffusion of nitrogen in α-Ti, Appl. Phys. Lett. 42 (1983) 498–500. https://doi.org/10.1063/1.93981.
[35] F.L. Bregolin, M. Behar, F. Dyment, Diffusion study of 18O implanted into α-Ti using the nuclear resonance technique, Applied Physics A. 86 (2007) 481–484. https://doi.org/10.1007/s00339-006-3782-y.

[36] F.L. Bregolin, M. Behar, F. Dyment, Diffusion study of 15N implanted into α-Ti using the nuclear resonance technique, Appl. Phys. A. 90 (2008) 347–349. https://doi.org/10.1007/s00339-007-4280-6.
[37] J. Murray, H. Wriedt, The O- Ti (oxygen-titanium) system, Journal of Phase Equilibria. 8 (1987) 148–165.
[38] B.P. Burton, A. van de Walle, First principles phase diagram calculations for the octahedral-interstitial system αTiOX, 0≤X≤1/2, Calphad. 39 (2012) 97–103. https://doi.org/10.1016/j.calphad.2012.09.004.
[39] M. Cancarevic, M. Zinkevich, F. Aldinger, Thermodynamic description of the Ti–O system using the associate model for the liquid phase, Calphad. 31 (2007) 330–342. https://doi.org/10.1016/j.calphad.2007.01.009.
[40] S. Yamaguchi, Interstitial Order-Disorder Transformation in the Ti-O Solid Solution. I. Ordered Arrangement of Oxygen, J. Phys. Soc. Jpn. 27 (1969) 155–163. https://doi.org/10.1143/JPSJ.27.155.
[41] S. Amano, D. Bogdanovski, H. Yamane, M. Terauchi, R. Dronskowski, ε-TiO, a Novel Stable Polymorph of Titanium Monoxide, Angewandte Chemie International Edition. 55 (2016) 1652–1657. https://doi.org/10.1002/anie.201510479.
[42] F.C. Walsh, R.G.A. Wills, The continuing development of Magnéli phase titanium sub-oxides and Ebonex® electrodes, Electrochimica Acta. 55 (2010) 6342–6351. https://doi.org/10.1016/j.electacta.2010.05.011.
[43] J. Muscat, V. Swamy, N.M. Harrison, First-principles calculations of the phase stability of ${\mathrm{TiO}}_{2}$, Phys. Rev. B. 65 (2002) 224112. https://doi.org/10.1103/PhysRevB.65.224112.
[44] F. Labat, P. Baranek, C. Domain, C. Minot, C. Adamo, Density functional theory analysis of the structural and electronic properties of TiO2 rutile and anatase polytypes: Performances of different exchange-correlation functionals, J. Chem. Phys. 126 (2007) 154703. https://doi.org/10.1063/1.2717168.
[45] M.E. Arroyo-de Dompablo, A. Morales-García, M. Taravillo, DFT+U calculations of crystal lattice, electronic structure, and phase stability under pressure of TiO2 polymorphs, J. Chem. Phys. 135 (2011) 054503. https://doi.org/10.1063/1.3617244.
[46] Z. Hu, H. Metiu, Choice of U for DFT+U Calculations for Titanium Oxides, J. Phys. Chem. C. 115 (2011) 5841–5845. https://doi.org/10.1021/jp111350u.
[47] J. Moellmann, S. Ehrlich, R. Tonner, S. Grimme, A DFT-D study of structural and energetic properties of TiO2modifications, J. Phys.: Condens. Matter. 24 (2012) 424206. https://doi.org/10.1088/0953-8984/24/42/424206.
[48] M.T. Curnan, J.R. Kitchin, Investigating the Energetic Ordering of Stable and Metastable TiO2 Polymorphs Using DFT+U and Hybrid Functionals, J. Phys. Chem. C. 119 (2015) 21060–21071. https://doi.org/10.1021/acs.jpcc.5b05338.
[49] J. He, W. Zhou, X. Zhou, X. Zhong, X. Zhang, P. Wan, B. Zhu, W. Chen, The anatase phase of nanotopography titania plays an important role on osteoblast cell morphology and proliferation, J Mater Sci: Mater Med. 19 (2008) 3465–3472. https://doi.org/10.1007/s10856-008-3505-3.
[50] M. Uchida, H.-M. Kim, T. Kokubo, S. Fujibayashi, T. Nakamura, Structural dependence of apatite formation on titania gels in a simulated body fluid, Journal of Biomedical Materials Research Part A. 64A (2003) 164–170. https://doi.org/10.1002/jbm.a.10414.

[51] M. Sabeena, S. Murugesan, P. Anees, E. Mohandas, M. Vijayalakshmi, Crystal structure and bonding characteristics of transformation products of bcc β in Ti-Mo alloys, Journal of Alloys and Compounds. 705 (2017) 769–781. https://doi.org/10.1016/j.jallcom.2016.12.155.
[52] I.I. Kornilov, V.V. Vavilova, L.E. Fykin, R.P. Ozerov, S.P. Solowiev, V.P. Smirnov, Neutron diffraction investigation of ordered structures in the titanium-oxygen system, Metallurgical Transactions. 1 (1970) 2569–2571. https://doi.org/10.1007/BF03038386.
[53] B. Holmberg, Disorder and order in solid solutions of oxygen in a-titanium, Acta Chem. Scand. 16 (1962) 1245–1250.
[54] S. Andersson, The Crystal Structure of the So-Called Delta-Titanium Oxide and Its Structural Relation to the co-Phases of Some Binary Alloy Systems of Titanium, Acta Chem. Scand. 13 (1959).
[55] D. Watanabe, J.R. Castles, A. Jostsons, A.S. Malin, The ordered structure of TiO, Acta Cryst. 23 (1967) 307–313. https://doi.org/10.1107/S0365110X67002634.
[56] S. Bartkowski, M. Neumann, E.Z. Kurmaev, V.V. Fedorenko, S.N. Shamin, V.M. Cherkashenko, S.N. Nemnonov, A. Winiarski, D.C. Rubie, Electronic structure of titanium monoxide, Phys. Rev. B. 56 (1997) 10656–10667. https://doi.org/10.1103/PhysRevB.56.10656.
[57] C.E. Rice, W.R. Robinson, Structural changes in the solid solution (Ti1−xVx)2O3 as x varies from zero to one, Journal of Solid State Chemistry. 21 (1977) 145–154. https://doi.org/10.1016/0022-4596(77)90154-2.
[58] I.E. Grey, C. Li, I.C. Madsen, Phase Equilibria and Structural Studies on the Solid Solution MgTi2O5-Ti3O5, Journal of Solid State Chemistry. 113 (1994) 62–73. https://doi.org/10.1006/jssc.1994.1342.
[59] M. Marezio, P.D. Dernier, The crystal structure of Ti4O7, a member of the homologous series TinO2n−1, Journal of Solid State Chemistry. 3 (1971) 340–348. https://doi.org/10.1016/0022-4596(71)90069-7.
[60] T. Mashimo, R. Bagum, Y. Ogata, M. Tokuda, M. Okube, K. Sugiyama, Y. Kinemuchi, H. Isobe, A. Yoshiasa, Structure of Single-Crystal Rutile (TiO2) Prepared by High-Temperature Ultracentrifugation, Crystal Growth & Design. 17 (2017) 1460–1464. https://doi.org/10.1021/acs.cgd.6b01818.
[61] L. Jian, S. Gong-Bao, W. Mei-Li, Z. Bao-Shu, Study on phase relations, crystal structure and magnetic properties of Ti1-xCrxO2+/-delta system, ACTA PHYSICA SINICA. 56 (2007) 3379–3387.
[62] I. Djerdj, A.M. Tonejc, Structural investigations of nanocrystalline TiO2 samples, Journal of Alloys and Compounds. 413 (2006) 159–174. https://doi.org/10.1016/j.jallcom.2005.02.105.
[63] W. Lengauer, Properties of bulk δ-TiN1-x prepared by nitrogen diffusion into titanium metal, Journal of Alloys and Compounds. 186 (1992) 293–307. https://doi.org/10.1016/0925-8388(92)90016-3.
[64] I. Khidirov, Neutron diffraction determination of homogeneity ranges of ε-T2n1-y, and δ'-Ti2n2x phases by Rietveld full-profile analysis, Альтернативная Энергетика и Экология. (2010) 10–13.
[65] W. Lengauer, The crystal structure of η-Ti3N2−x: An additional new phase in the Ti-N system, Journal of the Less Common Metals. 125 (1986) 127–134. https://doi.org/10.1016/0022-5088(86)90087-1.

[66] W. Lengauer, P. Ettmayer, The crystal structure of a new phase in the titanium-nitrogen system, Journal of the Less Common Metals. 120 (1986) 153–159. https://doi.org/10.1016/0022-5088(86)90637-5.
[67] A.N. Christensen, The temperature factor parameters of some transition metal carbides and nitrides by single crystal x-ray and neutron diffraction., (1978).
[68] B. Holmberg, Structural studies on the titanium-nitrogen system, Acta Chem. Scand. 16 (1962) 1255–61.
[69] M. Radecka, E. Pamula, A. Trenczek-Zajac, K. Zakrzewska, A. Brudnik, E. Kusior, N.-T.H. Kim-Ngan, A.G. Balogh, Chemical composition, crystallographic structure and impedance spectroscopy of titanium oxynitride TiNxOy thin films, Solid State Ionics. 192 (2011) 693–698. https://doi.org/10.1016/j.ssi.2010.07.021.
[70] M.-H. Chan, F.-H. Lu, Preparation of titanium oxynitride thin films by reactive sputtering using air/Ar mixtures, Surface and Coatings Technology. 203 (2008) 614–618. https://doi.org/10.1016/j.surfcoat.2008.04.094.
[71] F. Vaz, P. Cerqueira, L. Rebouta, S.M.C. Nascimento, E. Alves, P. Goudeau, J.P. Rivière, K. Pischow, J. de Rijk, Structural, optical and mechanical properties of coloured TiNxOy thin films, Thin Solid Films. 447–448 (2004) 449–454. https://doi.org/10.1016/S0040-6090(03)01123-4.
[72] A. Rizzo, M.A. Signore, L. Mirenghi, T.D. Luccio, Synthesis and characterization of titanium and zirconium oxynitride coatings, Thin Solid Films. 517 (2009) 5956–5964. https://doi.org/10.1016/j.tsf.2009.03.131.
[73] S.G. Seo, C.-H. Park, H.-Y. Kim, W.H. Nam, M. Jeong, Y.-N. Choi, Y.S. Lim, W.-S. Seo, S.-J. Kim, J.Y. Lee, Y.S. Cho, Preparation and visible-light photocatalysis of hollow rock-salt TiO1−xNx nanoparticles, J. Mater. Chem. A. 1 (2013) 3639–3644. https://doi.org/10.1039/C3TA00936J.
[74] K. Rees, E. Lorusso, S. D. Cosham, A. N. Kulak, G. Hyett, Combining single source chemical vapour deposition precursors to explore the phase space of titanium oxynitride thin films, Dalton Transactions. 47 (2018) 10536–10543. https://doi.org/10.1039/C7DT04694D.
[75] G. Hyett, M.A. Green, I.P. Parkin, The Use of Combinatorial Chemical Vapor Deposition in the Synthesis of Ti3-δO4N with $0.06 < \delta < 0.25$: A Titanium Oxynitride Phase Isostructural to Anosovite, J. Am. Chem. Soc. 129 (2007) 15541–15548. https://doi.org/10.1021/ja073355s.
[76] C.D. Garner, S.C. Wallwork, The crystal structures of anhydrous nitrates and their complexes. Part III. Titanium(IV) nitrate, J. Chem. Soc. A. (1966) 1496–1500. https://doi.org/10.1039/J19660001496.
[77] C. Dupressoire, M. Descoins, A.V. Put, E. Epifano, D. Mangelinck, P. Emile, D. Monceau, The role of nitrogen in the oxidation behaviour of a Ti6242S alloy: a nanoscale investigation by atom probe tomography, Acta Materialia. 216 (2021) 117134. https://doi.org/10.1016/j.actamat.2021.117134.
[78] I. Abdallah, C. Dupressoire, L. Laffont, D. Monceau, A. Vande Put, STEM-EELS identification of TiOXNY, TiN, Ti2N and O, N dissolution in the Ti2642S alloy oxidized in synthetic air at 650 °C, Corrosion Science. 153 (2019) 191–199. https://doi.org/10.1016/j.corsci.2019.03.037.
[79] O. Tkachuk, I. Pohrelyuk, O. Yaskiv, Formation of Oxynitride Layers on Titanium Alloys, Materials Performance and Characterization. 6 (2017) 546–553.

[80] J. Chakraborty, K. Kumar, R. Ranjan, S.G. Chowdhury, S.R. Singh, Thickness-dependent fcc–hcp phase transformation in polycrystalline titanium thin films, Acta Materialia. 59 (2011) 2615–2623. https://doi.org/10.1016/j.actamat.2010.12.046.
[81] R. Traylor, R. Zhang, J. Kacher, J.O. Douglas, P.A.J. Bagot, A.M. Minor, Impurity and texture driven HCP-to-FCC transformations in Ti-X thin films during in situ TEM annealing and FIB milling, Acta Materialia. 184 (2020) 199–210. https://doi.org/10.1016/j.actamat.2019.11.047.
[82] P. Marcus, F. Jona, Identification of metastable phases: face-centred cubic Ti, Journal of Physics: Condensed Matter. 9 (1997) 6241.
[83] A.A. Saleh, V. Shutthanandan, R. Smith, Observation of ultrathin metastable fcc Ti films on Al (110) surfaces, Physical Review B. 49 (1994) 4908.
[84] A.F. Jankowski, M.A. Wall, Formation of face-centered cubic titanium on a Ni single crystal and in Ni/Ti multilayers, Journal of Materials Research. 9 (1994) 31–38.
[85] F.B. Kværndrup, F.B. Grumsen, S. Kadkhodazadeh, K.V. Dahl, M.A. Somers, T.L. Christiansen, Diffraction based identification of an elusive FCC phase in carbo-oxidized titanium, Materials Characterization. 180 (2021) 111435.
[86] X. Ma, X. Guo, M. Fu, Y. Qiao, In-situ TEM observation of hcp-Ti to fcc-Ti phase transformation in Nb-Ti-Si based alloys, Materials Characterization. 142 (2018) 332–339. https://doi.org/10.1016/j.matchar.2018.05.052.
[87] N.-S. Peighambardoust, F. Nasirpouri, Electropolishing behaviour of pure titanium in perchloric acid–methanol–ethylene glycol mixed solution, Transactions of the IMF. 92 (2014) 132–139. https://doi.org/10.1179/0020296713Z.000000000135.
[88] Howard, Stanley, Ellingham Diagrams, (n.d.).
[89] P. Kofstad, P.B. Anderson, O.J. Krudtaa, Oxidation of titanium in the temperature range 800–1200°C, Journal of the Less Common Metals. 3 (1961) 89–97. https://doi.org/10.1016/0022-5088(61)90001-7.
[90] J.E.L. Gomes, A.M. Huntz, Correlation between the oxidation mechanism of titanium under a pure oxygen atmosphere, morphology of the oxide scale, and diffusional phenomena, Oxid Met. 14 (1980) 249–261. https://doi.org/10.1007/BF00604567.
[91] G. Bertrand, K. Jarraya, J.M. Chaix, Morphology of oxide scales formed on titanium, Oxidation of Metals. 21 (1984) 1–19.
[92] P. Kofstad, High-temperature oxidation of titanium, Journal of the Less Common Metals. 12 (1967) 449–464. https://doi.org/10.1016/0022-5088(67)90017-3.
[93] N. Birks, G.H. Meier, F.S. Pettit, Introduction to the High Temperature Oxidation of Metals, 2nd ed., Cambridge University Press, 2006. https://doi.org/10.1017/CBO9781139163903.
[94] I. Vaquila, M.C.G. Passeggi, J. Ferrón, Temperature effects in the early stages of titanium oxidation, Applied Surface Science. 93 (1996) 247–253. https://doi.org/10.1016/0169-4332(95)00334-7.
[95] Y. Mizuno, A. Tanaka, Y. Takakuwa, F. Ishida, K. Takahiro, H. Tonda, K. Ishikawa, T. Takano, T. Ikeuchi, T. Okada, S. Yamaguchi, T. Homma, The surface characterization of the early stages of the oxidation of titanium, Materials at High Temperatures. 17 (2000) 13–21. https://doi.org/10.1179/mht.2000.004.
[96] A.E. Jenkins, An Investigation of the Reactions Between Titanium and Oxygen at High Temperature, PhD Thesis, University of Melbourne, Office of Research, 1953.

[97] A. Jenkins, A further study of the oxidation of titanium and its alloys at high temperatures, J. Inst. Metals. 84 (1955).
[98] P. Kofstad, High temperature oxidation of metals, 1966.
[99] J. Stringer, Some observations on the kinetics of oxidation of titanium at high temperatures, Journal of the Less Common Metals. 6 (1964) 207–213. https://doi.org/10.1016/0022-5088(64)90100-6.
[100] J. Stringer, The oxidation of titanium in oxygen at high temperatures, Acta Metallurgica. 8 (1960) 758–766. https://doi.org/10.1016/0001-6160(60)90170-X.
[101] J. Unnam, R.N. Shenoy, R.K. Clark, Oxidation of commercial purity titanium, Oxidation of Metals. 26 (1986) 231–252.
[102] K. Chou, P.-W. Chu, C.G. Levi, E.A. Marquis, Influence of a silicon-bearing film on the early stage oxidation of pure titanium, J Mater Sci. 52 (2017) 9884–9894. https://doi.org/10.1007/s10853-017-1143-1.
[103] P.K. Imbrie, D.C. Lagoudas, Morphological Evolution of TiO2 Scale Formed on Various 1D and 2D Geometries of Titanium, Oxidation of Metals. 55 (2001) 359–399. https://doi.org/10.1023/A:1010368412822.
[104] C. Oviedo, Oxidation kinetics of pure titanium at low pressures, J. Phys.: Condens. Matter. 5 (1993) A153–A154. https://doi.org/10.1088/0953-8984/5/33A/037.
[105] A.M. Chaze, C. Coddet, The role of nitrogen in the oxidation behaviour of titanium and some binary alloys, Journal of the Less Common Metals. 124 (1986) 73–84. https://doi.org/10.1016/0022-5088(86)90478-9.
[106] R.J. Hanrahan, D.P. Butt, The effects of nitrogen on the kinetics and mechanisms of oxidation of Titanium-Tantalum alloys, Oxidation of Metals. 48 (1997) 41–58. https://doi.org/10.1007/BF01675261.
[107] C. Dupressoire, A. Rouaix-Vande Put, P. Emile, C. Archambeau-Mirguet, R. Peraldi, D. Monceau, Effect of Nitrogen on the Kinetics of Oxide Scale Growth and of Oxygen Dissolution in the Ti6242S Titanium-Based Alloy, Oxid Met. 87 (2017) 343–353. https://doi.org/10.1007/s11085-017-9729-1.
[108] A. Kanjer, V. Optasanu, M.C. Marco de Lucas, O. Heintz, N. Geoffroy, M. François, P. Berger, T. Montesin, L. Lavisse, Improving the high temperature oxidation resistance of pure titanium by shot-peening treatments, Surface and Coatings Technology. 343 (2018) 93–100. https://doi.org/10.1016/j.surfcoat.2017.10.065.
[109] M. Göbel, V. a. C. Haanappel, M.F. Stroosnijder, On the Determination of Diffusion Coefficients of Oxygen in One-Phase Ti (α-Ti) and Two-Phase Ti–4Nb (α- and β-Ti) by Micro-Hardness Measurements, Oxidation of Metals. 55 (2001) 137–151. https://doi.org/10.1023/A:1010333410938.
[110] R.J. Hanrahan, D.P. Butt, Oxidation kinetics and mechanisms of Ti-Ta alloys, Oxid Met. 47 (1997) 317–353. https://doi.org/10.1007/BF01668517.
[111] J.L. Murray, The Ta- Ti (Tantalum-Titanium) system, Bulletin of Alloy Phase Diagrams. 2 (1981) 62–66.
[112] H.L. Du, A. Aljarany, P.K. Datta, J.S. Burnell-Gray, Oxidation behaviour of Ti–46.7Al–1.9W–0.5Si in air and Ar–20%O2 between 750 and 950°C, Corrosion Science. 47 (2005) 1706–1723. https://doi.org/10.1016/j.corsci.2004.08.014.
[113] A.M. Kamat, S.M. Copley, A.E. Segall, J.A. Todd, Laser-Sustained Plasma (LSP) Nitriding of Titanium: A Review, Coatings. 9 (2019) 283. https://doi.org/10.3390/coatings9050283.

[114] A. Zhecheva, W. Sha, S. Malinov, A. Long, Enhancing the microstructure and properties of titanium alloys through nitriding and other surface engineering methods, Surface and Coatings Technology. 200 (2005) 2192–2207. https://doi.org/10.1016/j.surfcoat.2004.07.115.
[115] E. Metin, O.T. Inal, Kinetics of layer growth and multiphase diffusion in ion- nitrided titanium, Metall Mater Trans A. 20 (1989) 1819–1832. https://doi.org/10.1007/BF02663213.
[116] S. Malinov, A. Zhecheva, W. Sha, Proc. 13th IFHTSE Congress, (2003).
[117] J. Desmaison, P. Lefort, M. Billy, Oxidation mechanism of titanium nitride in oxygen, Oxid Met. 13 (1979) 505–517. https://doi.org/10.1007/BF00812775.
[118] I. Milošv, H.-H. Strehblow, B. Navinšek, M. Metikoš-Huković, Electrochemical and thermal oxidation of TiN coatings studied by XPS, Surface and Interface Analysis. 23 (1995) 529–539. https://doi.org/10.1002/sia.740230713.
[119] H.-Y. Chen, F.-H. Lu, Oxidation behavior of titanium nitride films, Journal of Vacuum Science & Technology A. 23 (2005) 1006–1009. https://doi.org/10.1116/1.1914815.
[120] I.M. Robertson, C.M. Wayman, Tweed microstructures I. Characterization in β-NiAl, Philosophical Magazine A. 48 (1983) 421–442. https://doi.org/10.1080/01418618308234902.
[121] D.E. Laughlin, R. Sinclair, L.E. Tanner, Comments on “the early stages of the transformation in dilute alloys of titanium in nickel,” Scripta Metallurgica. 14 (1980) 373–376. https://doi.org/10.1016/0036-9748(80)90362-2.
[122] A.M. Bratkovsky, E.K.H. Salje, V. Heine, Overview of the origin of tweed texture, Phase Transitions. 52 (1994) 77–83. https://doi.org/10.1080/01411599408201201.
[123] A.M. Bratkovsky, E.K.H. Salje, S.C. Marais, V. Heine, Theory and computer simulation of tweed texture, Phase Transitions. 48 (1994) 1–13. https://doi.org/10.1080/01411599408200351.
[124] Y. Ustinovshikov, I. Igumnov, B. Pushkarev, The nature of the periodic microstructure in Fe–Ti alloys, Materials Science and Engineering: A. 259 (1999) 105–109. https://doi.org/10.1016/S0921-5093(98)00866-1.
[125] Y. Ni, A.G. Khachaturyan, From chessboard tweed to chessboard nanowire structure during pseudospinodal decomposition, Nature Mater. 8 (2009) 410–414. https://doi.org/10.1038/nmat2431.
[126] R.J. Rioja, D.E. LAughlin, The early stages of GP zone formation in naturally aged Ai-4 wt pct cu alloys, Metall Mater Trans A. 8 (1977) 1257–1261. https://doi.org/10.1007/BF02643840.
[127] L.A. Bendersky, W.J. Boettinger, A. Roytburd, Coherent precipitates in the b.c.c./orthorhombic two-phase field of the Ti□Al□Nb system, Acta Metallurgica et Materialia. 39 (1991) 1959–1969. https://doi.org/10.1016/0956-7151(91)90165-W.
[128] N. Resnina, S. Belyaev, A. Shelyakov, V. Rubanik, V. Rubanik, R. Konopleva, V. Chekanov, E. Ubyivovk, M. Krzhizhanovskaya, Pre-martensitic phenomena in Ti40.7Hf9.5Ni44.8Cu5 shape memory alloy, Intermetallics. 67 (2015) 69–74. https://doi.org/10.1016/j.intermet.2015.07.018.
[129] D. Wang, Y. Wang, Z. Zhang, X. Ren, Modeling Abnormal Strain States in Ferroelastic Systems: The Role of Point Defects, Phys. Rev. Lett. 105 (2010) 205702. https://doi.org/10.1103/PhysRevLett.105.205702.

[130] Y. Nii, T. Arima, H.Y. Kim, S. Miyazaki, Effect of randomness on ferroelastic transitions: Disorder-induced hysteresis loop rounding in Ti-Nb-O martensitic alloy, Phys. Rev. B. 82 (2010) 214104. https://doi.org/10.1103/PhysRevB.82.214104.
[131] M. Tahara, H.Y. Kim, T. Inamura, H. Hosoda, S. Miyazaki, Lattice modulation and superelasticity in oxygen-added β-Ti alloys, Acta Materialia. 59 (2011) 6208–6218. https://doi.org/10.1016/j.actamat.2011.06.015.
[132] M. Tahara, H.Y. Kim, T. Inamura, H. Hosoda, S. Miyazaki, Role of interstitial atoms in the microstructure and non-linear elastic deformation behavior of Ti–Nb alloy, Journal of Alloys and Compounds. 577 (2013) S404–S407. https://doi.org/10.1016/j.jallcom.2011.12.113.
[133] H.Y. Kim, L. Wei, S. Kobayashi, M. Tahara, S. Miyazaki, Nanodomain structure and its effect on abnormal thermal expansion behavior of a Ti–23Nb–2Zr–0.7Ta–1.2O alloy, Acta Materialia. 61 (2013) 4874–4886. https://doi.org/10.1016/j.actamat.2013.04.060.
[134] J. Fan, J. Li, Y. Zhang, H. Kou, J. Ghanbaja, W. Gan, L. Germain, C. Esling, The origin of striation in the metastable β phase of titanium alloys observed by transmission electron microscopy, J Appl Cryst. 50 (2017) 795–804. https://doi.org/10.1107/S1600576717004150.
[135] L.D. Arsov, C. Kormann, W. Plieth, Electrochemical synthesis and in situ Raman spectroscopy of thin films of titanium dioxide, Journal of Raman Spectroscopy. 22 (1991) 573–575. https://doi.org/10.1002/jrs.1250221006.
[136] W. Ma, Z. Lu, M. Zhang, Investigation of structural transformations in nanophase titanium dioxide by Raman spectroscopy, Appl Phys A. 66 (1998) 621–627. https://doi.org/10.1007/s003390050723.
[137] M. Cortes-Jacome, G. Ferrat-Torres, L.F. Ortiz, C. Angeles-Chavez, E. Lopez-Salinas, J. Escobar, M. Mosqueira, J. Toledo-Antonio, In situ thermo-Raman study of titanium oxide nanotubes, Catalysis Today. 126 (2007) 248–255.
[138] E.J. Ekoi, A. Gowen, R. Dorrepaal, D.P. Dowling, Characterisation of titanium oxide layers using Raman spectroscopy and optical profilometry: Influence of oxide properties, Results in Physics. 12 (2019) 1574–1585. https://doi.org/10.1016/j.rinp.2019.01.054.
[139] M. Watanabe, Raman spectroscopy of charge-ordered states in Magnéli titanium oxides, Physica Status Solidi c. 6 (2009) 260–263. https://doi.org/10.1002/pssc.200879898.
[140] J. Yan, G. Wu, N. Guan, L. Li, Z. Li, X. Cao, Understanding the effect of surface/bulk defects on the photocatalytic activity of TiO2: anatase versus rutile, Phys. Chem. Chem. Phys. 15 (2013) 10978–10988. https://doi.org/10.1039/C3CP50927C.
[141] Y. Zhang, C.X. Harris, P. Wallenmeyer, J. Murowchick, X. Chen, Asymmetric Lattice Vibrational Characteristics of Rutile TiO2 as Revealed by Laser Power Dependent Raman Spectroscopy, J. Phys. Chem. C. 117 (2013) 24015–24022. https://doi.org/10.1021/jp406948e.
[142] U. Balachandran, N.G. Eror, Raman spectra of titanium dioxide, Journal of Solid State Chemistry. 42 (1982) 276–282. https://doi.org/10.1016/0022-4596(82)90006-8.
[143] S. Xie, E. Iglesia, A.T. Bell, Effects of Temperature on the Raman Spectra and Dispersed Oxides, J. Phys. Chem. B. 105 (2001) 5144–5152. https://doi.org/10.1021/jp004434s.

[144] O. Frank, M. Zukalova, B. Laskova, J. Kürti, J. Koltai, L. Kavan, Raman spectra of titanium dioxide (anatase, rutile) with identified oxygen isotopes (16, 17, 18), Physical Chemistry Chemical Physics. 14 (2012) 14567–14572. https://doi.org/10.1039/C2CP42763J.
[145] C. Chen, N. Liang, W. Tse, I. Chen, J. Duh, Raman spectra of titanium nitride thin films, Chinese Journal of Physics. 32 (1994) 205–210.
[146] N.K. Ponon, D.J.R. Appleby, E. Arac, P.J. King, S. Ganti, K.S.K. Kwa, A. O'Neill, Effect of deposition conditions and post deposition anneal on reactively sputtered titanium nitride thin films, Thin Solid Films. 578 (2015) 31–37. https://doi.org/10.1016/j.tsf.2015.02.009.
[147] N.S.H. Gunda, A. Van der Ven, Understanding the interactions between interstitial and substitutional solutes in refractory alloys: The case of Ti-Al-O, Acta Materialia. 191 (2020) 149–157. https://doi.org/10.1016/j.actamat.2020.04.017.
[148] C.B. Carter, D.B. Williams, Transmission Electron Microscopy: Diffraction, Imaging, and Spectrometry, Springer, 2016.
[149] G.F. Vander Voort, Titanium Specimen Preparation, Advanced Materials & Processes. (2008) 25–27.
[150] K. Momma, F. Izumi, VESTA 3 for three-dimensional visualization of crystal, volumetric and morphology data, J Appl Cryst. 44 (2011) 1272–1276. https://doi.org/10.1107/S0021889811038970.
[151] T.P. Schreiber, A.M. Wims, A quantitative X-ray microanalysis thin film method using K-, L-, and M-lines, Ultramicroscopy. 6 (1981) 323–334. https://doi.org/10.1016/S0304-3991(81)80219-7.
[152] F.A. Grant, Properties of rutile (Titanium dioxide), National Bureau of Standards, Washington, D.C., 1959. https://www.osti.gov/biblio/4235222 (accessed September 23, 2021).
[153] J. Rumble, ed., CRC handbook of chemistry and physics (Online version), 102nd ed., CRC Press, London, England, 2021.
[154] M.I. Aroyo, J. Perez-Mato, D. Orobengoa, E. Tasci, G. de la Flor, A. Kirov, Crystallography online: Bilbao crystallographic server, Bulg. Chem. Commun. 43 (2011) 183–197.
[155] H. Cheng, M. Hon, Texture formation in titanium nitride films prepared by chemical vapor deposition, Journal of Applied Physics. 79 (1996) 8047–8053. https://doi.org/10.1063/1.362358.
[156] K. Han, G.C. Weatherly, Transmission electron microscopy investigation of twinning in titanium carbonitride, Philosophical Magazine Letters. 76 (1997) 247–258. https://doi.org/10.1080/095008397178995.
[157] S. Muto, S. Takeda, R. Oshima, F.E. Fujita, High-Resolution Electron Microscopy of the Tweed Microstructure in an Fe-Pd Alloy, Jpn. J. Appl. Phys. 27 (1988) L1387. https://doi.org/10.1143/JJAP.27.L1387.
[158] D. Sundararaman, A.L.E. Terrance, V. Seetharaman, V.S. Raghunathan, Electron Microscopy Study of Microstructural Changes in a Ti-1.6 at%N Alloy, Transactions of the Japan Institute of Metals. 24 (1983) 510–513. https://doi.org/10.2320/matertrans1960.24.510.
[159] J.-Y. Xu, Z.-Z. Shi, Z.-B. Zhang, H.-G. Huang, X.-F. Liu, Significant enhancement of high temperature oxidation resistance of pure titanium via minor addition of Nb and

Si, Corrosion Science. 166 (2020) 108430. https://doi.org/10.1016/j.corsci.2020.108430.
[160] C.R. Houska, B.L. Averbach, M. Cohen, The cobalt transformation, Acta Metallurgica. 8 (1960) 81–87. https://doi.org/10.1016/0001-6160(60)90088-2.
[161] H. Fujita, S. Ueda, Stacking faults and f.c.c. (γ) → h.c.p. (ϵ) transformation in 188-type stainless steel, Acta Metallurgica. 20 (1972) 759–767. https://doi.org/10.1016/0001-6160(72)90104-6.
[162] J.W. Brooks, M.H. Loretto, R.E. Smallman, In situ observations of the formation of martensite in stainless steel, Acta Metallurgica. 27 (1979) 1829–1838. https://doi.org/10.1016/0001-6160(79)90073-7.
[163] H.I. Aaronson, J.M. Howe, M.G. Hall, T. Furuhara, J.P. Hirth, Mobility of structural ledges, Scripta Materialia. 37 (1997) 1301–1307. https://doi.org/10.1016/S1359-6462(97)00202-9.
[164] O. Blaschko, G. Krexner, J. Pleschiutschnig, G. Ernst, C. Hitzenberger, H.P. Karnthaler, A. Korner, Coherent Modulated Structure during the Martensitic hcp-fcc Phase Transition in Co and in a CoNi Alloy, Phys. Rev. Lett. 60 (1988) 2800–2803. https://doi.org/10.1103/PhysRevLett.60.2800.
[165] P. Tolédano, G. Krexner, M. Prem, H.-P. Weber, V.P. Dmitriev, Theory of the martensitic transformation in cobalt, Phys. Rev. B. 64 (2001) 144104. https://doi.org/10.1103/PhysRevB.64.144104.
[166] N. Li, S.K. Yadav, X.-Y. Liu, J. Wang, R.G. Hoagland, N. Mara, A. Misra, Quantification of dislocation nucleation stress in TiN through high-resolution in situ indentation experiments and first principles calculations, Sci Rep. 5 (2015) 15813. https://doi.org/10.1038/srep15813.
[167] M. Tamaki, H. Kuwahara, Y. Tomii, N. Yamamoto, An Investigation of Titanium Nitride Prepared by a DC Arc Plasma Jet, Journal of Materials Synthesis and Processing. 6 (1998) 215–219. https://doi.org/10.1023/A:1022681922140.
[168] A.G. Evans, G.B. Crumley, R.E. Demaray, On the mechanical behavior of brittle coatings and layers, Oxid Met. 20 (1983) 193–216. https://doi.org/10.1007/BF00656841.
[169] N.R. McDonald, G.R. Wallwork, The reaction of nitrogen with titanium between 800 and 1200°C, Oxid Met. 2 (1970) 263–283. https://doi.org/10.1007/BF00614621.
[170] R.A. Brockman, A.L. Pilchak, W. John Porter, R. John, Estimation of grain boundary diffusivity in near-α titanium polycrystals, Scripta Materialia. 65 (2011) 513–515. https://doi.org/10.1016/j.scriptamat.2011.06.015.
[171] S.V. Rempel, A.A. Rempel, A.A. Valeeva, Effect of Stoichiometry and Ordering on the Microstructure of Titanium Monoxide TiOy, ACS Omega. 5 (2020) 22513–22519. https://doi.org/10.1021/acsomega.0c03122.
[172] B.M. Moshtaghioun, D. Gómez-García, A. Domínguez-Rodríguez, Spark plasma sintering of titanium nitride in nitrogen: Does it affect the sinterability and the mechanical properties?, Journal of the European Ceramic Society. 38 (2018) 1190–1196. https://doi.org/10.1016/j.jeurceramsoc.2017.12.029.
[173] F.B. Kværndrup, M.A.J. Somers, T.L. Christiansen, Extreme Expansion and Reversible Hydrogen Solubility in h.c.p. Titanium Stabilized by Colossal Interstitial Alloying, Metallurgical and Materials Transactions A. 52 (2021) 4997–5003. https://doi.org/10.1007/s11661-021-06444-w.

[174] H. Okamoto, N-Ti (Nitrogen-Titanium), J. Phase Equilib. Diffus. 34 (2013) 151–152. https://doi.org/10.1007/s11669-012-0153-6.
[175] V. Ern, A.C. Switendick, Electronic Band Structure of TiC, TiN, and TiO, Phys. Rev. 137 (1965) A1927–A1936. https://doi.org/10.1103/PhysRev.137.A1927.
[176] J. Graciani, S. Hamad, J.Fdez. Sanz, Changing the physical and chemical properties of titanium oxynitrides ${\text{TiN}}_{1\ensuremath{-}x}{\text{O}}_{x}$ by changing the composition, Phys. Rev. B. 80 (2009) 184112. https://doi.org/10.1103/PhysRevB.80.184112.
[177] J.L. Endrino, C. Århammar, A. Gutiérrez, R. Gago, D. Horwat, L. Soriano, G. Fox-Rabinovich, D. Martín y Marero, J. Guo, J.-E. Rubensson, J. Andersson, Spectral evidence of spinodal decomposition, phase transformation and molecular nitrogen formation in supersaturated TiAlN films upon annealing, Acta Materialia. 59 (2011) 6287–6296. https://doi.org/10.1016/j.actamat.2011.06.039.
[178] Z. Liu, G. Welsch, Literature Survey on Diffusivities of Oxygen, Aluminum, and Vanadium in Alpha Titanium, Beta Titanium, and in Rutile, Metallurgical Transactions A. 19 (1988) 1121–1125. https://doi.org/10.1007/BF02628396.
[179] J.R. Akse, H.B. Whitehurst, Diffusion of titanium in slightly reduced rutile, Journal of Physics and Chemistry of Solids. 39 (1978) 457–465. https://doi.org/10.1016/0022-3697(78)90022-7.
[180] R.A. Perez, H. Nakajima, F. Dyment, Diffusion in α-Ti and Zr, Materials Transactions. 44 (2003) 2–13. https://doi.org/10.2320/matertrans.44.2.
[181] M. Batzill, E.H. Morales, U. Diebold, Influence of Nitrogen Doping on the Defect Formation and Surface Properties of ${\mathrm{TiO}}_{2}$ Rutile and Anatase, Phys. Rev. Lett. 96 (2006) 026103. https://doi.org/10.1103/PhysRevLett.96.026103.
[182] S. Sahoo, S.P. Alpay, R.J. Hebert, Surface phase diagrams of titanium in Oxygen, Nitrogen and Hydrogen environments: A first principles analysis, Surface Science. 677 (2018) 18–25. https://doi.org/10.1016/j.susc.2018.05.007.
[183] E. Stoyanov, F. Langenhorst, G. Steinle-Neumann, The effect of valence state and site geometry on Ti L3,2 and O K electron energy-loss spectra of TixOy phases, American Mineralogist. 92 (2007) 577–586. https://doi.org/10.2138/am.2007.2344.
[184] T.M. Sabine, D.J.H. Corderoy, A.E. Jenkins, The observation of interstice lattice stacking faults in αTi-O alloys, Acta Metallurgica. 15 (1967) 519–523. https://doi.org/10.1016/0001-6160(67)90085-5.
[185] A. Jostsons, P.G. McDougall, Fault Structures in Ti2O, Physica Status Solidi (b). 29 (1968) 873–889. https://doi.org/10.1002/pssb.19680290240.
[186] L. Germain, S.R. Dey, M. Humbert, N. Gey, Determination of parent orientation maps in advanced titanium-based alloys, Journal of Microscopy. 227 (2007) 284–291. https://doi.org/10.1111/j.1365-2818.2007.01812.x.
[187] V.M. Ievlev, K.A. Solntsev, S.A. Soldatenko, L.Yu. Leonova, P.V. Novikov, E.V. Golosov, A.A. Sinel'nikov, A.M. Vozgor'kov, Orientation, substructure, and optical properties of rutile films, Inorg. Mater. Appl. Res. 3 (2012) 282–287. https://doi.org/10.1134/S2075113312040053.
[188] H.M. Flower, P.R. Swann, An in situ study of titanium oxidation by high voltage electron microscopy, Acta Metallurgica. 22 (1974) 1339–1347. https://doi.org/10.1016/0001-6160(74)90034-0.

[189] E. Anastassakis, A. Pinczuk, E. Burstein, F.H. Pollak, M. Cardona, Effect of static uniaxial stress on the Raman spectrum of silicon, Solid State Communications. 88 (1993) 1053–1058. https://doi.org/10.1016/0038-1098(93)90294-W.
[190] D. Tuschel, Stress, strain, and Raman spectroscopy, Spectroscopy. 34 (2019) 10–22.
[191] L. Ma, W. Qiu, X. Fan, Stress/strain characterization in electronic packaging by micro-Raman spectroscopy: A review, Microelectronics Reliability. 118 (2021) 114045. https://doi.org/10.1016/j.microrel.2021.114045.
[192] S.C. Jain, B. Dietrich, H. Richter, A. Atkinson, A.H. Harker, Stresses in strained GeSi stripes: Calculation and determination from Raman measurements, Phys. Rev. B. 52 (1995) 6247–6253. https://doi.org/10.1103/PhysRevB.52.6247.
[193] T. Etzelstorfer, A. Wyss, M.J. Süess, F.F. Schlich, R. Geiger, J. Frigerio, J. Stangl, Determining the directional strain shift coefficients for tensile Ge: a combined x-ray diffraction and Raman spectroscopy study, Meas. Sci. Technol. 28 (2017) 025501. https://doi.org/10.1088/1361-6501/aa5372.
[194] R.J. Betsch, H.L. Park, W.B. White, Raman spectra of stoichiometric and defect rutile, Materials Research Bulletin. 26 (1991) 613–622. https://doi.org/10.1016/0025-5408(91)90104-T.
[195] J.C. Parker, R.W. Siegel, Calibration of the Raman spectrum to the oxygen stoichiometry of nanophase TiO2, Appl. Phys. Lett. 57 (1990) 943–945. https://doi.org/10.1063/1.104274.
[196] G.M. Raynaud, R.A. Rapp, In situ observation of whiskers, pyramids and pits during the high-temperature oxidation of metals, Oxid Met. 21 (1984) 89–102. https://doi.org/10.1007/BF00659470.
[197] D.R. Askeland, P. Fulay, W. Wright, The science and engineering of materials 6th edition, Cengage Learning Inc. (2010) 889.
[198] M.W. Barsoum, E.N. Hoffman, R.D. Doherty, S. Gupta, A. Zavaliangos, Driving Force and Mechanism for Spontaneous Metal Whisker Formation, Phys. Rev. Lett. 93 (2004) 206104. https://doi.org/10.1103/PhysRevLett.93.206104.
[199] P. Jagtap, P. Kumar, Whisker Growth in Sn Coatings: A Review of Current Status and Future Prospects, Journal of Electronic Materials. 50 (2021) 735–766.
[200] T. Hurlen, On the defect structure of rutile, Acta Chem Scand. 13 (1959) 365.
[201] F. Motte, C. Coddet, P. Sarrazin, M. Azzopardi, J. Besson, A comparative study of the oxidation with water vapor of pure titanium and of Ti-6Al-4V, Oxid Met. 10 (1976) 113–126. https://doi.org/10.1007/BF00614241.
[202] D.J. Rose, Titanium oxidation kinetics and TiO2 growth effects, Retrospective Theses and Dissertations, 1919-2007. (1966). https://circle.ubc.ca/handle/2429/37085 (accessed May 13, 2016).
[203] H. Lee, S. Dregia, S. Akbar, M. Alhoshan, Growth of 1-D TiO2 Nanowires on Ti and Ti Alloys by Oxidation, Journal of Nanomaterials. 2010 (2010) 503186. https://doi.org/10.1155/2010/503186.
[204] X. Peng, A. Chen, Aligned TiO 2 nanorod arrays synthesized by oxidizing titanium with acetone, Journal of Materials Chemistry. 14 (2004) 2542–2548.
[205] University of Cambridge DoITPoMS, Interactive Ellingham diagram., (n.d.).
[206] JANAF, Titanium nitride (TiN) thermodynamic table, (n.d.). https://janaf.nist.gov/tables/N-014.html (accessed January 11, 2022).

[207] G. Bertrand, K. Jarraya, J.M. Chaix, Morphology of oxide scales formed on titanium, Oxid Met. 21 (1984) 1–19. https://doi.org/10.1007/BF00659464.
[208] M.R. Begley, J.W. Hutchinson, The mechanics and reliability of films, multilayers and coatings, Cambridge University Press, 2017.
[209] M.R. Begley, LayerSlayer Multilayer Analysis Suite, (n.d.). https://sites.engineering.ucsb.edu/~begley/LayerSlayer.html.

10 Copyright permissions

When using figures from journal articles or textbooks as-is or as adaptations, permissions were sought from the relevant publishers or authors to re-use in this thesis. The sources are always cited within the figure captions in the thesis itself. Specific wording is included in this section to satisfy the requirements of the provided licenses.

From the American Physical Society (APS) - https://www.aps.org/:

- **Figure 2.4, Figure 2.6, Figure 2.7.** Reprinted adaptations of Figures 1, 3, 7, and 9 with permission from Gunda, N. S. H., Puchala, B. & Van der Ven, A. Resolving phase stability in the Ti-O binary with first-principles statistical mechanics methods. Phys. Rev. Materials 2, 033604 (2018). Copyright 2018 by the American Physical Society.
- **Figure 2.11.** Reprinted adaptation of Figure 8 with permission from Gunda, N. S. H. & Van der Ven, A. First-principles insights on phase stability of titanium interstitial alloys. Phys. Rev. Materials 2, 083602 (2018). Copyright 2018 by the American Physical Society.
- **Figure 2.3.** Reprinted adaptation of Figure 3 with permission from Wu, H. H. & Trinkle, D. R. Direct Diffusion through Interpenetrating Networks: Oxygen in Titanium. Physical Review Letters 107, (2011). Copyright 2011 by the American Physical Society.

From Springer - https://www.springer.com/us:

- **Figure 2.11.** Reprinted adaptation of Figure 7 by permission from Springer: Khidirov, I. Revision of the Ti-N phase diagram as probed by neutron diffraction. Russian Journal of Inorganic Chemistry 56, 298–303 (2011).
- **Figure 2.11.** Reprinted adaptation of Figure 1 by permission from Springer: Wriedt, H. & Murray, J. The N-Ti (nitrogen-titanium) system. Bulletin of Alloy Phase Diagrams 8, 378–388 (1987).
- **Figure 2.4.** Reprinted adaptation of Figure 1 by permission from Springer: Okamoto, H. O-Ti (Oxygen-Titanium). Journal of Phase Equilibria and Diffusion 32, 473–474 (2011).
- **Figure 2.1.** Reprinted adaptation of Figures 1 and 2 by permission from Springer: Lütjering, G. & Williams, J. C. Titanium. vol. 2 (Springer, 2003).
- **Figure 2.4.** Reprinted adaptation of Figure 1 by permission from Springer: Murray, J. & Wriedt, H. The O- Ti (oxygen-titanium) system. Journal of Phase Equilibria 8, 148–165 (1987).
- **Figure 2.20.** Reprinted adaptation of Figure 2 by permission from Springer: Gomes, J. E. L. & Huntz, A. M. Correlation between the oxidation mechanism of titanium under a pure oxygen atmosphere, morphology of the oxide scale, and diffusional phenomena. Oxid Met 14, 249–261 (1980).
- **Figure 2.19.** Reprinted Figure 5 by permission from Springer: Gomes, J. E. L. & Huntz, A. M. Correlation between the oxidation mechanism of titanium under a pure oxygen atmosphere, morphology of the oxide scale, and diffusional phenomena. Oxid Met 14, 249–261 (1980).

- **Figure 2.20.** Reprinted adaptation of Figure 5a by permission from Springer: Bertrand, G., Jarraya, K. & Chaix, J. M. Morphology of oxide scales formed on titanium. Oxid Met 21, 1–19 (1984).
- **Figure 2.21 and Figure 2.22.** Reprinted Figure 2 by permission from Springer: Göbel, M., Haanappel, V. a. C. & Stroosnijder, M. F. On the Determination of Diffusion Coefficients of Oxygen in One-Phase Ti (α-Ti) and Two-Phase Ti–4Nb (α- and β-Ti) by Micro-Hardness Measurements. Oxidation of Metals 55, 137–151 (2001).
- **Figure 2.26.** Reprinted Figure 1 by permission from Springer: Desmaison, J., Lefort, P. & Billy, M. Oxidation mechanism of titanium nitride in oxygen. Oxid Met 13, 505–517 (1979).

From Taylor & Francis - http://www.tandfonline.com/:

- **Figure 2.27a.** Reprinted Figure 6a from Robertson, I. M. & Wayman, C. M. Tweed microstructures I. Characterization in β-NiAl. Philosophical Magazine A 48, 421–442 (1983) by permission from Taylor and Francis.

From AIP Publishing - https://publishing.aip.org/:

- **Figure 2.3.** Reprinted adaptation of Figures 5 and 6 from Scotti, L. & Mottura, A. Interstitial diffusion of O, N, and C in α -Ti from first-principles: Analytical model and kinetic Monte Carlo simulations. The Journal of Chemical Physics 144, 084701 (2016), with the permission of AIP Publishing.

From Elsevier - https://www.elsevier.com/:

- **Figure 2.10.** Reprinted Figure 3 from Walsh, F. C. & Wills, R. G. A. The continuing development of Magnéli phase titanium sub-oxides and Ebonex® electrodes. Electrochimica Acta 55, 6342–6351 (2010). Copyright 2010, with permission from Elsevier.
- **Figure 2.11.** Reprinted adaptation of Figure 1 from Lengauer, W. Properties of bulk δ-TiN1-x prepared by nitrogen diffusion into titanium metal. Journal of Alloys and Compounds 186, 293–307 (1992). Copyright 1992, with permission from Elsevier.
- **Figure 2.16, Figure 2.25, Figure 5.12, Figure 5.24, Figure 6.25.** Reprinted adaptations of Figures 3 and 16 from Dupressoire, C. et al. The role of nitrogen in the oxidation behaviour of a Ti6242S alloy: a nanoscale investigation by atom probe tomography. Acta Materialia 216, 117134 (2021). Copyright 2021, with permission from Elsevier.
- **Figure 2.24.** Reprinted Figure 2 from Zhecheva, A., Sha, W., Malinov, S. & Long, A. Enhancing the microstructure and properties of titanium alloys through nitriding and other surface engineering methods. Surface and Coatings Technology 200, 2192–2207 (2005). Copyright 2005, with permission from Elsevier.
- **Figure 2.27b.** Reprinted portion of Figure 1 from Laughlin, D. E., Sinclair, R. & Tanner, L. E. Comments on “the early stages of the transformation in dilute alloys of titanium in nickel”. Scripta Metallurgica 14, 373–376 (1980). Copyright 1980, with permission from Elsevier.
- **Figure 2.28.** Use of Figure 3 from Ekoi, E. J., Gowen, A., Dorrepaal, R. & Dowling, D. P. Characterisation of titanium oxide layers using Raman spectroscopy and optical

profilometry: Influence of oxide properties. Results in Physics 12, 1574–1585 (2019). permitted under CC license reproduced after this section.

- **Figure 5.18.** Reprinted portion of Figure 2b from Ma, X., Guo, X., Fu, M. & Qiao, Y. In-situ TEM observation of hcp-Ti to fcc-Ti phase transformation in Nb-Ti-Si based alloys. Materials Characterization 142, 332–339 (2018). Copyright 2018, with permission from Elsevier.